uOttawa

# Consolidation of Cermet Coatings by Cold Gas Dynamic Spraying

A thesis submitted to the Faculty of Graduate and Postdoctoral Studies in conformity with the requirements for the degree of

**Doctor of Philosophy**

in Mechanical Engineering
Ottawa-Carleton Institute for Mechanical and Aerospace Engineering
University of Ottawa

Ottawa, Canada

## Abstract

Metal-ceramic (Cermets) materials that combine properties of both: high hardness, high wear resistance, and high working temperatures of ceramics and the ductility, toughness, and heat conductance of metals. Cold gas dynamic spraying, or simply cold spray, is a solid state thermal spray process that has been in development for the last 25 years. In the cold spray process, ductile materials are accelerated in a supersonic flow. These particles impact a substrate and adhere by plastic deformation. The continuous accumulation of these particles covers the substrate and creates a dense coating.

The cold spray process is beginning to become a popular method to consolidate some select cermet materials into coatings. This technique can be advantageous when an erosion and wear resistant coating is required. During the deposition of these coatings, researchers have shown that the ceramic particles have a dramatic influence on the deposition behavior by causing an increase in deposition efficiency and coating adhesion. These effects have been presented in several experiments but have yet to be thoroughly explained.

The goal of this investigation is to increase the knowledge, on a fundamental level, with regards to the deposition behavior of metal-ceramic blending and cermet powders. Ultimately, the focus is to prove the feasibility of these coatings for the requirements needed in the engineering industry.

The first part of the investigation is a fundamental study on the deposition behavior of metal-ceramic blends with different compositions. Three theories that aim to explain the increase in deposition efficiency were proposed in the literature and further investigated in this study. One proposed mechanism for the increase in deposition efficiency was established by probability analysis to be too unlikely to contribute to the increment in deposition efficiency. The other two proposed mechanism, the presence of asperities caused by ceramic particles, and the oxide removal produced by the impact of ceramic particles, shown to play a major role in increasing the deposition efficiency. The effect of the ceramic particle morphology on the deposition behavior of metal-ceramic blending was studied in the second part of the investigation. This study greatly complements the previous one adding more depth to the investigation and confirming results. The increment in deposition efficiency normally seen with the addition of small amounts of angular alumina was not seen when spherical alumina was added instead. The creation of asperities during deposition was explored for the two morphologies and was determined that spherical alumina does not produce the same asperities at the surface. In addition, the coating sprayed with spherical alumina showed very little ceramic retention compared with the ones sprayed with angular alumina. These results have a direct impact on the mechanical properties of the coatings. Wear resistance for coatings sprayed with spherical alumina showed no improvement compared with pure aluminum coating due to the low ceramic content. Hardness was lower

in coatings sprayed with spherical alumina for the same feedstock powder composition but was harder when the final coating composition was considered. Adhesion strength significantly increases with the addition of ceramic content in the feedstock powder; this increase was greater for coating sprayed with spherical alumina.

The third part of the investigation focuses on understanding the mechanism of deposition for cermet particles with various morphologies. Six commercially available CrC-NiCr powders were studied, varying in morphology and metal/ceramic ratio. Spherical powders led to the erosion of the substrate and no coating was formed. Porous agglomerated and sintered powder lead to severely cracked coatings. For dense agglomerated and sintered powders, the outcome of powder depended on the initial metal/ceramic ratio, powders with 25%wt.NiCr led to erosion while 35%wt.NiCr powders led to a dense coating. Finally blended ceramic metal powders also lead to a successful coatings. All coatings obtained had lower ceramic content than the initial feedstock powder. Interrupted deposition tests, FEA analysis, and SEM observation were used to draw conclusions on the deposition behavior and explain the results.

Finally, the last part of this investigation aims to apply the knowledge learned to an applied engineering problem. The problem that is targeted is the replacement of chrome plating for the aerospace industry. A commercially available cermet powder CrC-NiCr (65/35) was proposed as a replacement of chromium plating as well as a restoration for this coating and its alternatives (electroless nickel-plating, and WC-Co-Cr HVOF). The coatings and restoration were analyzed by SEM and tested by strip rupture rest, neutral salt spray fog, and fluid immersion testing. The adhesion strength, porosity, and hardness of the cold spray coating was also tested. The deposition and restoration of coatings were successful; a hard and dense coating was obtained with good adhesion strength. The process of restoration chromium-plating and its alternatives was also developed with a clean interface was achieved in each case. Coatings and restoration passed strip to rupture rest as well as fluid immersion test in two selected industry fluids. Neutral salt spray fog test revealed that the cold spray coating and repairs may have a path that allows the solution to penetrate the substrate and start the corrosion process. This behavior was found in a few select spots and should be further investigated. Overall, the coating proved to have potential as an alternative of chromium-plating or to restore damaged hard coatings.

# Acknowledgement

First, I would like to thank my supervisor, Professor Bertrand Jodoin, for all the opportunities that have open to me, his valuable engagement throughout my research work and for being not just a mentor but also a friend. I am more than grateful for his insightful guide, encouragement and continuing support. I consider myself very privileged to have had him as a mentor during my studies, and I am looking forward to keeping collaborating in the future.

I am very grateful to have worked with industrial partners during my studies. I would like to offer my particular thanks to Stephen Gaydos and all of our collaborators at the Boeing Company, Centerline, NWMO, VLN, and Mitacs.

I wish to acknowledge the help provided the technicians from the machine shop at the University of Ottawa. Having access to skilled technicians was crucial in completing this research, thank you for the excellent support you constantly provide.

I would also like to thank my colleagues for making this an amazing experience both in and outside of the lab. Dr. Mohammed Yandouzi, Daniel MacDonald, Aleksandra Nastic, Deliang Guo, Antoine Bacciochini, Tyler Samson, Patrick Trahan, Francesco Delloro, Mathieu Bolduc, Jean-Louis Pelletier, Samuel Leblanc Robert, Guillaume Archambault, Daniel Cormier, Yannick Cormier, Philippe Dupuis. I will miss our endless meetings, discussion and laughs.

Finally, I wish to thank Fabiola for showing me so much support, patience and encouragement during all these years. I couldn't have done it without you.

To all of you, I am sincerely grateful.

# Contents

# List of Tables

# List of Figures

# Chapter 1

# Introduction

## 1.1 Background

Cermet materials are composite materials composed of metal and ceramics. They are designed to possess the best properties of each [25]. Cermets possess the high hardness, high wear resistance, and high working temperatures found in ceramics with the ductility, toughness and heat conductance found in metals. This gives cermets a wide range of applications in the engineering industry, including electronic components, biomedical implants, armor, and any application where abrasion resistance is required. There are several methods to manufacture cermets which can be divided into three categories: liquid state, vapor deposition, and solid state. These different processes produce different microstructures and, in consequence, different properties of the material obtained [4].

Cold Gas Dynamic Spraying, or simply cold spray, is a thermal spray deposition method that has been developed in recent decades. Unlike other thermal spray methods that rely on the thermal energy to melt and deposit particles, cold spray relies on the kinetic energy of the particle to deposit and adhere to the substrate through plastic deformation [6, 26]. Since the particles are never melted, the process is considered a solid state process. Since the process relies heavily on plastic deformation to obtain the adherence of particles, ductile materials may be deposited and hard brittle particles can embed as long as there is a ductile phase in the substrate. The main focus of the literature has been on the deposition of metallic particles, but the deposition of polymers and ceramic-metals has also been investigated [21, 27]. The addition of ceramic particles to metals increases the properties of the obtained coatings. But it also can improve the deposition process by increasing the

deposition efficiency and lowering the porosity of the coatings [21]. These changes in deposition behavior of cermets have been demonstrated in several experiments, but the phenomenon has yet to be explained.

In a related narrative, the industry has been pushing to eliminate the use of hard chrome coatings due to the hazardous side-products of its production [28]. Hard chrome coatings are a thick layer of chromium normally deposited on steel to improve durability (through abrasion tolerance and wear resistance), to minimize seizing of parts, and to improve corrosion resistance. The coatings rely on the inherent hardness and inertness of the chromium layer [29]. The major drawback of the coating is in its production; the plating process uses hexavalent chromium $Cr_6$, which is the most toxic form of chromium. This toxicity has forced the industry to find a suitable replacement (and repair method) for hard chrome plating. Only a few alternatives that have shown some potential as a replacement; such as electroless nickel plating and High-Velocity Oxygen Fuel (HVOF) coatings (usually with WC-Co). These alternatives have disadvantages; low building rate and low hardness in the case of electroless Nickel and lack of reparability in the case of HVOF.

Based in the prior discussion, the purpose of this investigation is to shed light on the deposition mechanism of cermets using Cold Gas Dynamic Spraying. It is hypothesized that the properties obtained in the coatings may also resemble those obtained by chromium plating. Therefore, it is proposed that the deposition of cermets by cold spray may be a suitable replacement (and restoration method) for the hard chrome plating process.

## 1.2 Motivation and Objectives

The motivation for this research lays in the potential that cold spray has in consolidating cermets. While the majority of cold spray applications are focused on producing coatings with soft materials for corrosion applications, there is great potential in the production of hard and wear resistant coatings. The deposition of hard particles can be challenging, but the addition of ceramic particles may help to reach the density and deposition efficiency required. The consolidation of these ceramic particles in the coating also has the potential of improving the wear properties of the coating. To achieve a complete understanding of the mechanism of deposition of this mixture of material, it is important to weight the influence of each characteristic the powder has in the deposition mechanism. Characteristics such as composition (blending of ceramic-metal), size distribution, and morphology

have shown to be of great importance in the deposition behavior. Another benefit that cold spray has compared with other thermal spray techniques is related to the reparability and residual stress remaining in the coating after deposition. It is known and well documented that regular thermal spray techniques such as plasma spray or HVOF induce tensile stresses in the coating due to the thermal mismatch between the sprayed particle (hot and melted) and the substrate (cold). These tensile stresses may be very harmful if the pieces will be subjected to fatigue or when the goal of the spray is the restoration of a pre-existing coating, the tensile stresses pull the coating away of the pre-existing coating, leaving weak interface that can be subjected to corrosion or abrasion. Since cold spray is a solid state process with low working temperatures (compared to the ones in HVOF or Plasma spray) and the deposition mechanism is based on deformation (and not melting), the resulting residual stress is compressive instead of tensile [30]. This stress makes cold spray ideal for the restoration of coatings. The deposited coatings will push against the preexisting coating, closing any gap and sealing the repair. This also provides the coating, and by extension to the piece, a longer fatigue life. Under the framework of this research is worth mentioning that the addition of ceramic particles induces further deformation which brings the compressive stresses to an even higher level.

As was mentioned in the previous section. For this reason, it is suggested that cermet coatings produced by cold spray could be an alternative to traditional hard chromium plating. The application will help to extrapolate the results of the present study to a real life engineering application.

In order to achieve the goals exposed previously the following objectives were proposed:

1. Study the effect of ceramic content in a ceramic-metal blending on the cold spray deposition process.
2. Study the effect of ceramic morphology in a ceramic-metal blending on the cold spray deposition process.
3. Study the effect of cermet powder morphology on the deposition cold spray deposition process.
4. Consolidation of cermet coating by cold spray for an engineering application

## 1.3 Outline of the Thesis

The presented thesis has been formulated in six chapters. The present chapter (Chapter 1) describes the relevant background information for the study. It also presented the motivation for the investigation and the main objectives of the research.

In Chapter 2 the process of cold spray is reviewed, an explanation of the fluid dynamics of the process is presented and a detailed review of the current theories of adhesion and deformation upon impact are described. Concepts such as critical velocity, phase transformation, and bonding are presented. Secondly, a review of ceramic metal composites, describing consolidation techniques are presented. A detailed review of the studies of cermets in cold spray is reviewed detailing the proposed theory of the effects observed with the addition of ceramic into the feedstock powder. Lastly, a brief description of chromium plating is presented.

Chapter 3 describes in detail the main and specific objectives of this investigation. It is presented the research interest of the study as well as the importance of the possible applications. Chapter 4 provides a detail of the methodology followed and the research approach of the study. The research design is described, showing constants, variables and expected results of the experiments. The equipment for the production and characterization of samples are defined as well as the conditions for their analysis. The selection of the materials (powders, substrates, and its providers) are presented along with a list of experiments and a detailed description of the steps to follow in the study.

Chapter 5 of this thesis shows the results and discussions of each experiment. This chapter is structured in the form of four different self-contained investigations. Each investigation addresses one of the main research objectives described before. Each section is written as an independent research article to allows the reader to easily follows the experiment methodology and to understand quickly the results and conclusion obtained from each investigation.

Finally, chapter 6 gathers the main conclusion obtained in the investigations, highlighting the most important results and outcomes of the study. Multiple suggestions for future work are also presented in this chapter with the goal to facilitate future studies in the area of deposition behavior of cermet and to provide a guideline to future investigations needed to validate these coatings for use in the industry.

# Chapter 2

# Literature review

## 2.1 Cold gas dynamic spraying

### 2.1.1 Background

The cold spray process is a solid-state deposition process that was re-discovered in the mid-1980 at the Institute of Theoretical and Applied Mechanics of the Siberian Division of the Russian Academy of Science in Novosibirsk. While they were conducting studies in a supersonic flows in a wind tunnel. The researchers observed that when increasing the velocity of the flow, the metallic tracer particles will stop eroding the leading edges of the models and will rather build up a coating [26, 31, 32]. They identified the potential and develop a device to test the phenomenon and produced further studies in different metals proving the feasibility of the process. A United States patent was issued in 1994 [5] and the European patent in 1995 [33]. Even though the cold spray process was materialized by Alkhimov et al. [32] the concept of it was conceptualized over a century ago in 1900 by Thurston [34] as a metallic blasting process in order to obtain embedment of metallic particles. Further progress in the design was made by Rocheville in 1958 [35] with the introduction of a supersonic nozzle. The concept was never materialized and now is proved that even though the concept was in the right direction, it lacked enough of velocity in the particle to produce a coating [5]. A schematic of the device envisioned in the patent by Alkhimov et al. [32] can be seen in Figure 2.1.

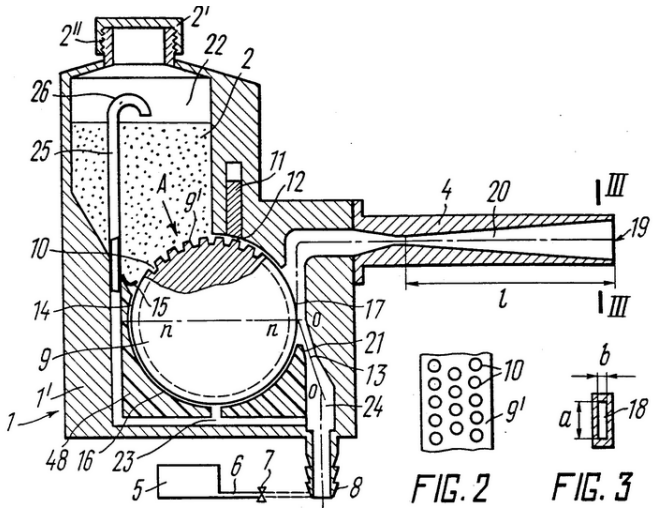


Figure 2.1: Schematic in the patent, by Alkhimov et al. [5]

When cold spray was re-discovered, it opened a new field of investigation in solid-state deposition. Solid-state processes offer great advantages over processes where melting is required, the main advantage is the possibility to control the microstructure of the material [36]. Processes where fusion is required lead to difficulties in controlling the cooling rate and solidification, therefore the microstructure may have heterogeneous properties. Solid-state processes as the name suggests are processes where the materials used are always in a solid state. Therefore, the microstructure obtained in the final form will have a strong resemblance to the original microstructure of the material [6]. The most common example of solid state processes is machining, but maybe the clearest example of the potential of solid-state processes is powder metallurgy, where the microstructure can be controlled very finely and properties can be achieved that surpass other processes.

Cold spray is in the family of thermal spray processes, same as plasma spray and HVOF [6]. Cold spray operate in the realm of *low temperatures* and *fast velocities* compared with the other thermal spray depostion. Figure 2.2 helps comparing cold spray with other thermal sprays processes. Cold spray, relies on plastic deformation in order to build up the coating. This gives the advantages of a solid state process but also limits the variety of material than can be sprayed with this technique [37]. For this reason, cold spray works almost exclusively with metals, polymers or composites where one of the components can offer some degree of plasticity.

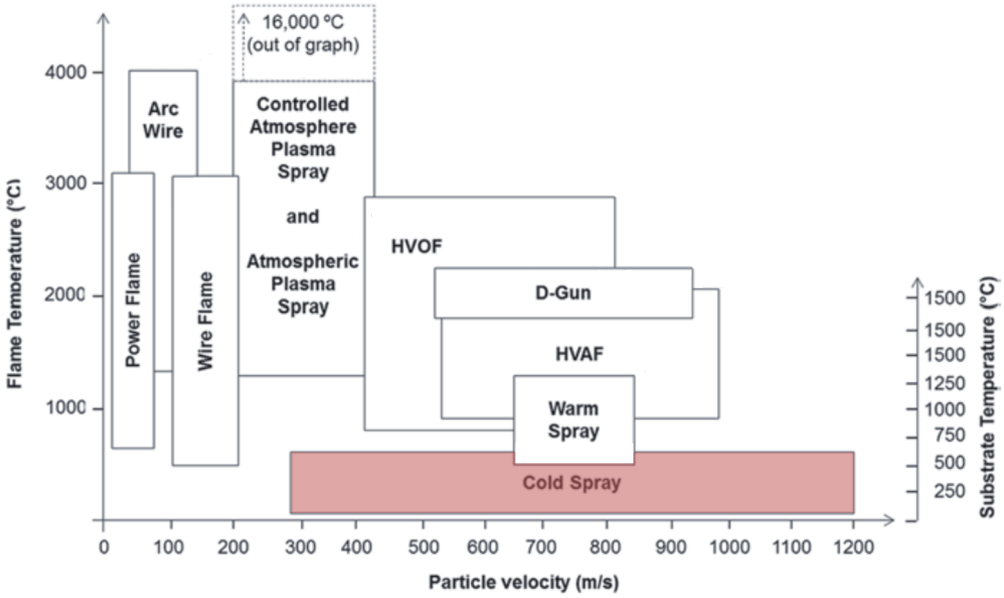


Figure 2.2: Cold spray velocity and temperature vs other thermal spray processes [6].

Since cold spray was discovered an increasing amount of studies have been done on the topic every year. These studies vary from fundamental studies to applications of cold spray in the industry. Even though the process of cold spray appears to be simple, the phenomenon is extremely complex; it is a multidisciplinary endeavor to fully understand the process to a fundamental level. It includes phenomena of gas dynamics, heat transfer, mechanics of solids, and surface and material science, of which, not all aspects are fully understood (such as, extreme rates of deformation and bonding mechanism).

### 2.1.2 Process Overview

A simple schematic used to describe the process is shown in Figure 2.3. The process begins with the driving gas at high pressure. The high pressure gas is connected to a pressure regulator where the process pressure is set. The regulated gas then passes through a heater where it reaches the process temperature. The gas is then accelerated through a convergent-divergent nozzle (de-Laval) to convert the thermal energy of the gas into kinetic energy; bringing the gas into supersonic velocities typically (400 m/s - 1000 m/s), depending on the nature of the gas and temperature used [36]. The powder is then fed into the gas stream. The injection can be done before the throat of the nozzle, referred as high pressure cold spray, or downstream the throat, known as low-pressure cold spray. The particles are accelerated by the gas and exit the nozzle at a high velocity. The particles impact

the material to be coated and adhere through plastic deformation. In order to fully understand the phenomenon present in cold spray, the process can be analyzed in different sections: The gas dynamics, the particle journey, the impact, and the bonding to the substrate. These will be detailed in the following sections.

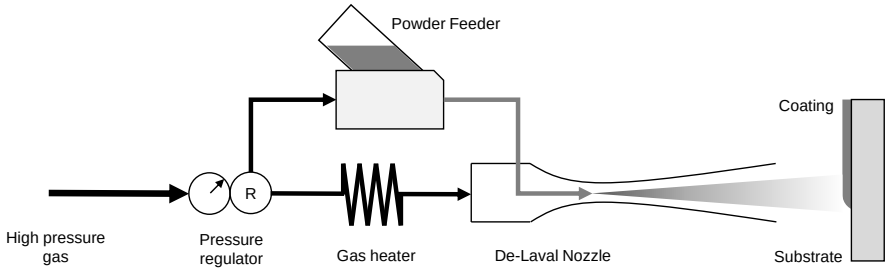


Figure 2.3: Cold spray diagram.

### Gas dynamics of Cold Spray

The cold spray process produces coating using the kinetic energy imparted to the particles. In order to obtain a dense coating, it is necessary to produce a high velocity impact to deform the particles and obtain an intimate contact between the particles and the substrate (particle-substrate) and between different particles (particle-particle). The particles are propelled solely by the gas. Thus, it is important to transform the energy stored in the gas at high pressure and temperature (enthalpy) into kinetic energy. For this purpose, a de-Laval nozzle is used. This nozzle will efficiently convert enthalpy to kinetic energy with the condition of having the right pressure ratio between the ends of the nozzle. In order to understand the process, a gas dynamic analysis will be done starting from basic concepts.

The speed of sound, $c$, of a material is the distance traveled per unit time by a pressure wave propagating through it. It is defined for any material as the square root of the stiffness of a material over the density, or more formally as the instantaneous change in elastic stress due to a change in density [38].

$$c = \sqrt{\frac{K}{\rho}} = \sqrt{\left(\frac{\partial P}{\partial \rho}\right)_s} \tag{2.1}$$

This could be written in a different way for an ideal isentropic gas:

$$\frac{P}{\rho^{\gamma}} = \text{Constant} \qquad \text{Deriving} \qquad \frac{\partial P}{\partial \rho} = \frac{\gamma P}{\rho} \qquad \text{Then} \qquad c_{gas} = \sqrt{\frac{\gamma P}{\rho}} \tag{2.2}$$

Where $\gamma$ is the adiabatic coefficient $\gamma = C_p/C_v$. Is also possible to see that the stiffness for an ideal gas is defined as $\gamma P$. Using the ideal gas law $P = \rho RT$, we obtain that for an ideal gas the speed of sound is also define as:

$$c_{gas} = \sqrt{\gamma RT} \tag{2.3}$$

where $R$ is the specific gas constant. From this equation, it is possible to see that the only variable that controls the speed of sound in an ideal gas is the temperature and the nature of the gas (by $\gamma$ and $R$). Therefore, the best candidate for cold spray to achieve high velocities are the gases with a higher $\gamma R$ and thus a higher speed of sound. Table 2.1 shows the speed of sound of various common gases at standard pressure and temperatures. It can be seen that the speed of sound of hydrogen and helium have outstanding values compared with other gases. From a practical point of view, hydrogen is too dangerous to be used due to its reactivity. Helium is used mainly when higher velocities are required, but it is avoided in the industry due to its price and because it is a non-renewable resource. The most common gas in use in cold spray is nitrogen, although the speed of sound in mitrogen is considerably lower that in helium, its price, availability and its low reactivity makes it ideal for cold spray in industrial applications.

Table 2.1: Speed of Sound of Common Gases at Standard Pressure and Temperature [1]

| **Gases** | **Speed of sound** |
|---|---|
| Carbon dioxide | 269 $m/s$ |
| Argon | 322 $m/s$ |
| Air | 346 $m/s$ |
| Nitrogen | 351 $m/s$ |
| Helium | 1016 $m/s$ |
| Hydrogen | 1315 $m/s$ |

After the gas pressure is regulated and after passing the heater, there is not other source of energy or work. Assuming the heat and friction losses are negligible, the process could be assumed to be adiabatic and the flow of gas to be in steady state. Under these assumptions, we can write the first law of thermodynamics as the stagnation enthalpy of a control volume.

$$h_0 = h + \frac{V^2}{2} = constant \tag{2.4}$$

Where $h_0$ is the enthalpy of the fluid when velocity is equal to 0. Assuming a constant specific heat capacity at constant pressure ($dh = C_p dT$), using the ideal gas specific heat definition: $C_p = \gamma R/(\gamma - 1)$ and the Equation 2.3. It is possible to rearrange Equation 2.4 to obtain:

$$\frac{T_0}{T} = 1 + \frac{\gamma - 1}{2} M^2 \tag{2.5}$$

Where $M$ is the Mach number $M = V/c$; the ratio of velocity over speed of sound. It is easy to see that if $M$ increases (increase in velocity), the temperature of the gas decreases. This is a clear implication that enthalpy is being converted to kinetic energy. From isentropic flow relations and Equation 2.5 we can also write the pressure $P$ and density $\rho$ as a function of Mach number $M$ and stagnation properties, obtaining:

$$\frac{P_0}{P} = \left(1 + \frac{\gamma - 1}{2} M^2\right)^{\frac{\gamma}{\gamma - 1}} \tag{2.6}$$

$$\frac{\rho_0}{\rho} = \left(1 + \frac{\gamma - 1}{2} M^2\right)^{\frac{1}{\gamma - 1}} \tag{2.7}$$

From these two equations, it can be seen that if the Mach number increases the pressure and density of the gas decreases. It is important to note that the concept of the convergent-divergent nozzle has not been introduced yet. The equations listed above are valid for any isentropic flow of an ideal gas. If the law of conservation of mass is introduced with conservation of momentum, and the relations of the Equations 2.2 are used again, the following can be obtained:

$$\left.\begin{aligned} \dot{m} &= \rho V A \\ -\partial P &= \rho V \partial V \\ \partial P &= c^2 \partial \rho \end{aligned}\right\} \quad \left(1 - M^2\right) \frac{\partial V}{V} = -\frac{\partial A}{A} \tag{2.8}$$

This equation, however simple, has profound implications for the design of nozzles [38]. If gas is moving slower than its speed of sound $M < 1$, then the only possible way to accelerate the gas $\partial V > 0$ is by reducing the cross sectional area in the direction of the flow $\partial A < 0$. This implication is intuitive. If the area keeps reducing, the velocity will keep increasing but this increment will be lower as the velocity gets closer to the speed of sound, due to the term $\left(1-M^2\right)$ (where $M^2$ increases with velocity). For $M \geq 1$, the only possible way to keep increasing the velocity of the gas is by increasing $\partial A > 0$. Therefore, to obtain the highest velocity, a convergent divergent nozzle is needed. With this, the gas can be accelerated from stagnation values in the convergent zone until it reaches the throat, where, if the properties of the gas satisfy the required conditions, the Mach number of the gas will reach $M = 1$ and will keep accelerating in the divergent portion.

In the same way, from conservation of mass, there are other important equations that can be derived. Using ideal gas relations and the definition of Mach number, it is possible to rewrite conservation of mass as,

$$\dot{m} = \rho V A \qquad \Longrightarrow \qquad \dot{m} = \frac{P}{RT} M \sqrt{\gamma R T} A$$

Using Equations 2.6 and 2.5 we also can write conservation of mass as,

$$\dot{m} = \left(1 + \frac{\gamma - 1}{2} M^2\right)^{\frac{-\gamma}{\gamma - 1}} P_0 M \sqrt{\frac{\gamma}{RT_0}} \sqrt{1 + \frac{\gamma - 1}{2} M^2} A \tag{2.9}$$

As it was mentioned previously if the condition permit it, the Mach number of the gas will be $M = 1$ at the throat, and since the mass flow rate is constant throughout the nozzle, it is possible to write the mass flow of gas as a function only of stagnation properties and nozzle throat area:

$$\dot{m} = P_0 \gamma A_t \sqrt{\frac{1}{\gamma R T_0} \left(\frac{2}{\gamma + 1}\right)^{\frac{\gamma+1}{\gamma-1}}} \tag{2.10}$$

Also, since Equation 2.9 is valid to any isentropic flow of an ideal gas and the mass flow rate $\dot{m}$ is constant, it is possible to write an equation of area based as a function of Mach number, or more practically an equation that gives the Mach number ratio by a certain area ratio,

$$\frac{A_2}{A_1} = \frac{M_1}{M_2}\sqrt{\left(\frac{1+\frac{\gamma-1}{2}M_2{}^2}{1+\frac{\gamma-1}{2}M_1{}^2}\right)^{\frac{\gamma+1}{\gamma-1}}} \tag{2.11}$$

more specifically assuming $M_1 = 1$ and therefore $A_1 = A_t$.

$$\frac{A}{A_t} = \frac{1}{M}\sqrt{\frac{2}{\gamma+1}\left(1+\frac{\gamma-1}{2}M^2\right)^{\frac{\gamma+1}{\gamma-1}}} \tag{2.12}$$

This equation is convenient for designing nozzles; it provides the area ratio needed in order to obtain the desired Mach number. Since a cold spray nozzle has a specific area ratio, the maximum Mach number that can be achieved is set. However,the maximum gas velocity can be increased with the gas temperature as it can be seen in the Equation 2.3. The maximum Mach number can be achieved as long as the pressure ratio between the chamber and the exit is higher than a certain value. The different cases of gas properties depending on pressures ratios are explained below and illustrated in Figure 2.4.

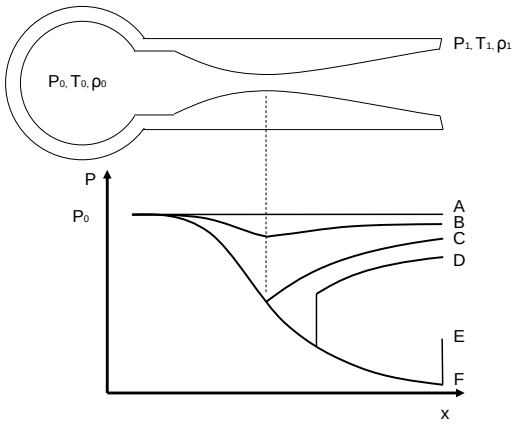


Figure 2.4: Nozzle schematic with pressure distribution assuming one dimensional isentropic flow.

- If the exit pressure is equal to the stagnation pressure as in case A, the absence of $\Delta P$ will result in a static gas and no acceleration will occur, therefore, no transformation from enthalpy to kinetic energy.
- If the exit pressure is lower than the stagnation pressure but, still not low enough to produce

a Mach number $M = 1$ at the throat, as in case B, the gas will accelerate up to the throat and then decelerate in the divergent zone of the nozzle.

- There is a critical pressure where the gas moves at the sonic speed at the throat ($M = 1$), but is not low enough to sustain the acceleration in the divergent zone, as illustated by case C. In this case, the gas will also decelerate in the divergent part of the nozzle, reconverting the kinetic energy into enthalpy.

- If the exit pressure is below case C and above a critical value, such as in case D then a supersonic flow will be achieved after the throat, but at some point inside the nozzle the gas will be forced to raise its pressure drastically in order to equalize the gas pressure with the exit pressure creating a shock wave, and followed by a deceleration of the flow. When the gas experiences this change of pressure the temperature and density increase and the gas velocity decreases drastically. The lower the exit pressure, the farthest downstream this shock wave will occur, until the shock wave is at the exit of the nozzle. As illustrated by case E

- If the exit pressure is below this critical point it is said to be over-expanded. The gas reaches the end of the nozzle moving at supersonic velocities, but the pressure of the gas is lower than the exit pressure. The same pressure discontinuity will happen outside the nozzle creating oblique shock in order to balance the pressure of the gas with the exit pressure.

- If the pressure of the gas at the exit of the nozzle is exactly the exit pressure, then it is said that the nozzle is working at its designed pressure. The gas will reach the exit of the nozzle moving at supersonic speed and no shock wave will be generated due to the balance in pressures, as is shown in case F.

- The last case that can happen occur when the exit pressure is lower that the design pressure. In this case, the gas exits the nozzle at supersonic speed, but then since its pressure is higher than the exit pressure, expansion fans will be produced. In this case, it is said the gas is under-expanded.

Cold spray nozzles normally operated in the two last regimes, where the nozzle operates at is design pressure or when it is under-expanded. This way, shock-waves in the nozzle can be avoided and the highest gas velocities can be obtained.

Even though shock waves can be avoided with a good nozzle design, they cannot be completely eliminated from the cold spray process. The gas exits the nozzle at supersonic velocities and is directed to the substrate. The surface of the substrate is normal to the direction of the flow, redirecting the gas radially and creating a *stagnation bubble* at the center of the gas flow at the substrate, see Figure 2.5. In this zone, the properties of the gas change abruptly to properties similar to stagnation as the velocity reduces [39]. This high density static gas creates a high drag force on the particles (moving at high speed) slowing them down. This affects mainly the low momentum particles reaching the substrate at hindered velocities. The standoff distance between the nozzle exit and the substrate can be critical as it determines the size of the stagnition bubble. As was studied by Pattison et al. [7], when stand off distance is reduced, the deposition performance was reduced as a result of the bow shock.

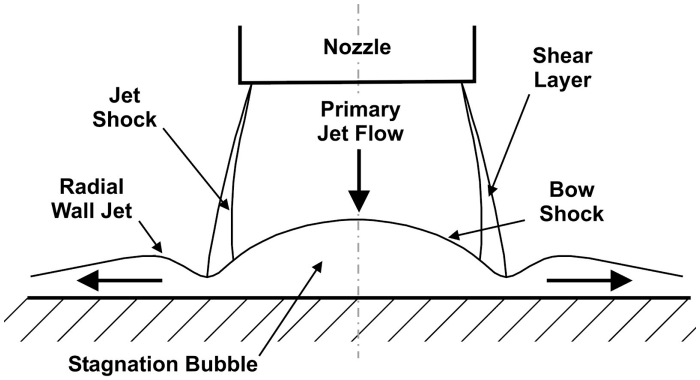


Figure 2.5: Schematic diagram of the supersonic impingement zone at the substrate [7].

As the gas expands in the nozzle and $M$ increases, the density of the gas decreases rapidly as Equation 2.7 mandates. Also, as will be explained in the next section, the drag of the gas on the particles decreases when the gas density decreases. Consequently, there is little gain in expanding the gas more than necessary, as such higher Mach numbers (and, therefore, gas velocities) may not result in higher particle velocities. In addition, higher gas velocities increase the strength of the bow shock, which have been shown to have an important effect on small particles [39]. For this reasons nozzles designed for cold spray tend to be in the supersonic regime optimally around $M = 2-3$, rather than the hypersonic regime [6].

It is important to notice that the analysis done previously is based on an isentropic state of the flow. This is not the case in reality as some irreversibilities occur during the process, mainly due to friction, heat losses, and viscous effects. This will result in a reduction of the gas velocity.

According to Alkhimov et al. [40] boundary layers produced in the nozzle walls can decrease the velocities of the gas up to 67% of the isentropic value, this reduction is improved in nozzles with higher area/length ratio where the boundary layers produce lower disturbances in the flow.

**Particle Journey**

The previous section described the gas dynamic principles of cold spray. The objective is to accelerate the particles to obtain a high velocity impact. From the particle injection at the nozzle to the impact with the substrate, the particles experience a variety of interaction with the gas, nozzle, and with other particles. The velocity of the particles is achieved by the acceleration given by the drag force with the gas. The particle instantaneous acceleration is determined by the balance of the forces given by the drag,

$$m_p a_p = \frac{1}{2}\rho_g \Delta V^2 C_d A_p$$

Where the subindex $p$ and $g$ are used to identify particle and gas respectively, $a_p$, and $m_p$ are the acceleration and mass of the particles, $C_d$ is the drag coefficient $\Delta V$ is the difference of velocities between the gas and the particle and $A_p$ is the cross sectional area of the particle. Using the definition of Mach number and equation 2.3. Is possible to rewrite this equation as,

$$m_p a_p = \frac{1}{2}\rho_g \left(M\sqrt{\gamma R T_g} - V_p\right)^2 C_d A_p$$

Then, using equations 2.5, 2.7 and ideal gas law we can express the acceleration of the particle depending of the Mach number and stagnation properties,

$$a_p = \frac{P_0}{2RT_0}\left(1+\frac{\gamma-1}{2}M^2\right)^{\frac{-1}{\gamma-1}}\left(M\sqrt{\gamma R T_0\left(1+\frac{\gamma-1}{2}M^2\right)^{-1}} - V_p\right)^2 C_d \frac{A_p}{m_p}$$

Finally using $m_p = \rho_p Vol_p$ we can rewrite the equation highlighting the influences of different parameters in it,

$$a_p = \frac{P_0}{2RT_0}\left(1+\frac{\gamma-1}{2}M^2\right)^{\frac{-1}{\gamma-1}}\left(M\sqrt{\gamma RT_0\left(1+\frac{\gamma-1}{2}M^2\right)^{-1}}-V_p\right)^2 \overbrace{C_d\frac{A_p}{Vol_p\rho_p}}^{\text{Particle dependent}} \tag{2.13}$$

It can be seen that the acceleration of the particles highly depends on the Mach number, the stagnation properties $P_0$ and $T_0$ and gas nature $\gamma$. It also depends on the geometry of the particle by the cross sectional area and its volume. In addition the acceleration also depends on the nature of the particle, as the equation is inversely proportional to its density $\rho_p$. The drag coefficient $C_d$ is related to both gas dynamics and particle morphology as this value dependency on the pressure drag and friction drag. This makes the drag coefficient difficult to estimate as it constantly changes as the particle accelerates and spins [41]. In Equation 2.13 it is also clear that the acceleration of the particle will depend on its instantaneous velocity, making the calculation of final velocity a non-linear equation. All of this makes the computation of the final velocity of the particle difficult to achieve through analytical models, thus to estimate this velocity, numerical methods are preferred [42–45].

From a practical point of view, the mean particle size selected to work with cold spray ranges between $10\mu m$ to $50\mu m$ . Particles this size are small enough to obtaining particle velocities high enough for deposition in most of the commercially available systems, yet are large enough to have the momentum to pierce the bow shock and still have high velocity upon the impact with the substrate. [2, 39, 46]. Particle velocities achieved in cold spray greatly depends on the gas used and stagnation properties as is was presented in Equation 2.13. Typical velocity values obtained ranged between 300 $m/s$ to 600 $m/s$ when using Nitrogen and up to 800 $m/s$ for Helium [47, 48]

Beside experiencing an increase in velocity, the particles may also experience a change in temperature due to heat transfer with the gas. Even though the gas cools as it expands, it still may heat the particles and affect the coating produced. The instant temperature of the particles is extremely difficult to measure (if not impossible) due to the velocities and size of the particles. Analytically it is very difficult to estimate, due to the constantly changing convection coefficient as the particle accelerates. Numerical methods are currently the only alternative to estimate the temperatures of the particles and these techniques are widely used among researchers [2, 49]. It has been estimated, that depending on the particles used, stagnation temperature of the gas and location of particle injections, the temperature upon impact can range from room temperature to $800°C$ [2]. For example Schmidt

et al. [2] in their research showed the effect of particle size on the temperature of the particle. Two copper particles 50 $\mu m$ and 5 $\mu m$ injected at the same point showed a difference in temperature of 130°$C$. Whereas the temperature of the 50 $\mu m$ particle was estimate at 180°$C$, the 5 $\mu m$ particles was estimated at a much lower temperature of 50°$C$. This effect is owing to the thermal inertia of the particles. The larger particle was heated by the gas in the high temperature zone, but when the gas expands and the gas lowers its temperature the particle have enough thermal inertia to stay at high temperature. On the other hand, while the small particle is heated in the same zone it can quickly reach a temperature very close to the gas temperature and even higher than the larger particle, but as the gas expand and cools the particle cools down as fast as the gas reaching the exit with a temperature cooler than its bigger counterpart, see a) in Figure 2.6. Schmidt et al. [8] also shows in their simulations that when changing the injection point of a 50 $\mu m$ copper particle from 20 *mm* from the exit of the nozzle to 150 *mm* the temperature estimated upon the impact increased form 180°$C$ to 350°$C$ [8], b) in Figure 2.6. This increase is due to the fact that a particle injected upstream will interact with a hotter gas and for a longer time than a particles injected close to the exit.

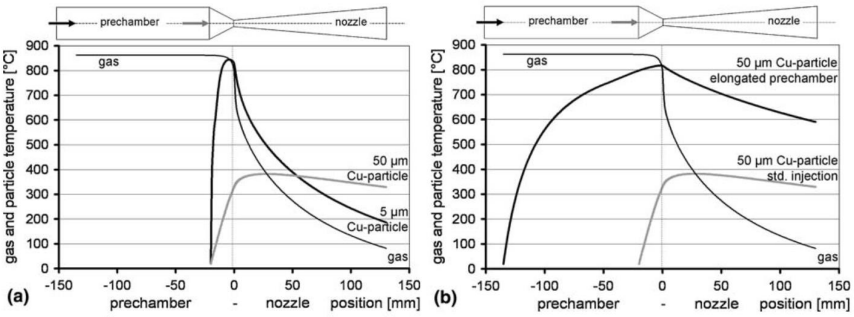


Figure 2.6: Particle temperature of copper particles at a) different particle size, and b) different injection points [8].

Particles can experience other interactions in the travel before the deposition at the substrate; it has been documented that, in most of the cases, the particle interacts with the nozzle walls. These interactions last a short period of time but, depending on the material involved, can affect drastically the velocity and the temperature of the particle. Due to the high velocities involved, particles can smear against the wall and deform prior to the impact, the effect that this deformation has in the building of a coating is not clear [50]. The particles can also interact with each other during flight. Even though this interaction is expected to be rare, it still may have an impact on the overall process.

All these interactions, accelerations, temperature changes, impacts, etc. occur in a short period of time but have an enormous impact on the state of the particles before reaching the substrate. The

state of the particles has a direct effect on the deformation and bonding to the substrate. The process of cold spray depends directly on how these interactions occur.

**Particle Impact and Deformation**

Once the particle impacts the substrate, the high kinetic energy stored in the particle results in a high plastic deformation of both, the substrate and the particles. During the impact, all the plastic energy used by the deformation gets dissipated into heat [2, 51, 52]. This heat increases the temperature of the substrate and the particles in the deformation zone. Some investigations suggest that the heat could even lead to a melting process of some zones of the particle [13, 53, 54]. However, other researches state that the material always stays below melting point, making it a solid state process [2, 51, 52]. There is a consensus that the highest heating occurs in the high deformation zone where the particle and the substrate interact. Assadi et al. [51] applied the theory of adiabatic shear instability to explain this localized heating.

Adiabatic shear instability is a thermo-viscoplastic instability. In simple words, it refers to the localization of deformation due to thermal softening when a material cannot dissipate heat. In a quasistatic (isothermal) deformation a material dissipates the energy of plastic deformation in the form of heat into the environment, then the flow stress that the material perceived only change by work hardening (Figure 2.7 *isothermal*). If the process is considered adiabatic, meaning it cannot dissipate this heat to the environment nor to the rest of the material, then the energy get transformed into an increase of temperature of the material, as the material heats the flow stress needed for plastic deformation will be reduced due to thermal softening. In an ideally homogeneous material, the material will homogeneously deform, heat and soften, leading to completely homogeneous deformation (Figure 2.7 *Homogeneous adiabatic*). But in the case of real materials, any discrepancies in the microstructure or small gradient of temperature or stress will create a heterogeneity in the softening and therefore in the deformation. Since the system is adiabatic, an instability is created, as a specific zone gets more deformed, then a higher heating will occur in this zone leading to an even higher softening with respect to the rest of the material. Therefore localizing the stress in this section (Figure 2.7 *Adiabatic unstable*).This process is called adiabatic shear instability [51] [55]. This phenomenon is seen in metals only at high strain rates. The deformation rate has to be high enough to counteract the high heat conductivity and obtain this quasi-adiabatic process.

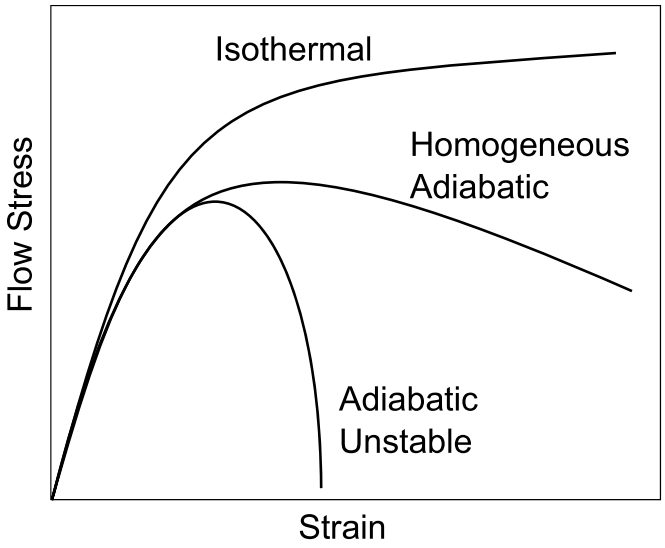


Figure 2.7: Schematic curve explaining the deformation behavior under isothermal conditions, ideal homogeneous adiabatic, and adiabatic instability

An experimental way to characterize deformation is by single particle impact experiments, also called wipe tests. In this tests the morphology of a single deformed particle is studied. This experiment gives some insight into the process of deformation of a particle but if fails to explain the coating formation after several impact events. The study of these tests have shown that depending on the kinetic energy prior to impact, the deformation can show jetting (see Figure 2.8), which is a violent ejection of the material due to rapid plastic flow. The existence or absence of jetting had been linked with the adhesion strength of the coating to the substrate [56]. This is attributed to the deformation localization of the adiabatic shear instability. Some researcher claim that jetting is caused by melting upon impact, this argument is still open to debate [13, 57].

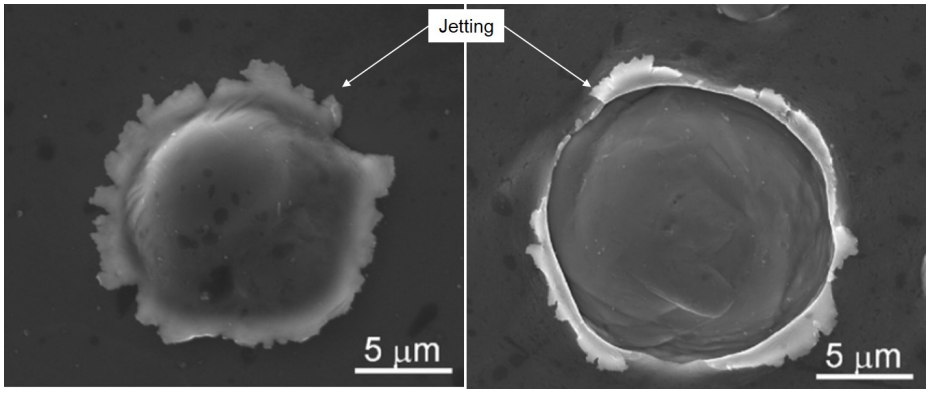


Figure 2.8: Jetting of titanium cold sprayed particle and substrate in wipe test [9]

The nature of the strain produced by the impact and deformation falls in the range of the ultra-high strain rate ($> 10^6\ mm/mm$) at the first nanosecond of the impact, and it decreases as the material slows down. The constitutive behavior of materials at this rate of strain is not well understood. At strain rates higher than $10^{-3}$, the flow stress follow at dependence $\sigma_f(\varepsilon, \dot{\varepsilon}, T)$ where $\varepsilon$, $\dot{\varepsilon}$, $T$ are the strain, the strain rate and the temperature of the material respectively [58].

In cold spray, it is extremely difficult to experimentally characterize the deformation of a particle in situ, due the short time frame at which the impact occurs (tens of nanoseconds), and to the dimensions involved (tens of micrometers). As a result of these limitations, numerical models are preferred to study the process of deformations and have been widely used to identify the deformation mechanism in cold spray [2, 51, 59]. These methods are useful, but researchers have to be very careful confirming hypotheses base on models since the constitutive equation are still not clear at this deformation rates. Therefore, not all the results of numerical simulations might be accurate. For example, the most commonly used equation to simulate impacts by cold spray is *Johnson-Cook's* equation [60]. This equation very accurately predicts the flow stress for different conditions of materials.

$$\sigma_f(\varepsilon, \dot{\varepsilon}, T) = [A + B(\varepsilon)^n] \left[1 + C \ln\left(\frac{\dot{\varepsilon}}{\dot{\varepsilon}_0}\right)\right] \left[1 - \left(\frac{T - T_0}{T_m - T_0}\right)^m\right]$$

Where $A, B, C, m, n$ are material properties related with strain hardening, strain rate hardening and temperature softening. $\dot{\varepsilon}_0$ is the quasistatic strain rate used to determined the constants and $T_m$ is the melting point of the material. Even though this equation can accurately represent the flow stress in some conditions, it was designed for low, high and very high strain rate regimes ($< 10^6\ mm/mm$) [58]; which is still below the strain rate observed in cold spray in the first instant of the impact. This leads to a calculated flow stress lower than the experimentally measured flow stress at these strain rates [59]. Other equations exist to fit better the behavior at this range of strain rates but there are not reliable at lower strain rates, or the data is limited to very few materials [61].

### Particle Bonding

Once the particle hits and deforms with the substrate, it can adhere to it and be part of the coating, or it can bounce back. The conditions necessary to produce bonding in cold spray are very complex

and not well understood. Some researchers have proposed some theories [26,51,56], but there is no consensus on a single dominant mechanism acting to produce bonding. In all cases, literature agrees that the principal types of bonding mechanisms present in cold spray deposition are: *Mechanical* and *Metallic* bonds. The types of bonding generated and the strength of the bond depends strongly on the condition of the impact, such as temperature, topology, velocity and also the materials involved.

Mechanical bonding or anchoring is the physical bond produced by mechanically interlocked structures. A clear example of this type of bonding mechanism is *hook and loop fasteners* commonly known as *Velcro*, Figure 2.9a. This kind of bonding has been seen in metals in processes such as explosive welding [57], where vortex-like structure are seen between the materials. Cold spray has also shown this kind of rolled structures, Figure 2.9b. It is easy to see how jetting can lead to mechanical bonding, as the particle and substrate deform and jet it can get interlocked creating these anchoring points [56], Figure 2.10. In order to produce jetting severe deformation must occur in the particle as well as in the substrate. Thus, it is expected that higher mechanical anchoring should occur at higher impact velocities and in materials with similar hardness. In the case of dissimilar materials hardness, this anchoring can be artificially induced in the substrate by creating the anchoring point prior to deposition, Samson et al. [62] roughened the surface of a substrate by a novel method of surface preparation, *Pulsed Water Jet*, and saw an increase in the adhesion compared with polished substrates. This increase is expected to happen by increasing the mechanical anchoring between the coating and the substrate [62].

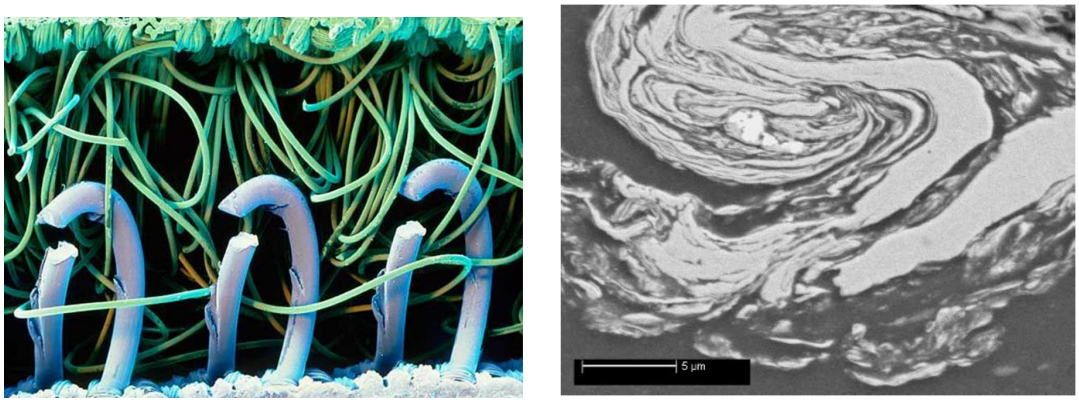


(a) (b)

Figure 2.9: (a) Mechanical bonding of Velcro [10], and (b) Vortex like structure observed in cold spray interface [11]

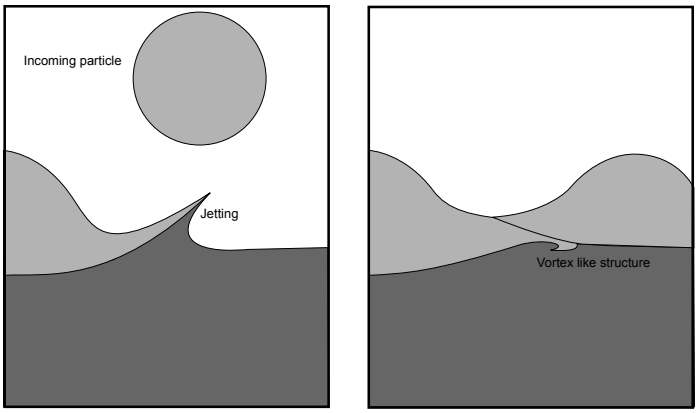


Figure 2.10: Schematic of Vortex like structure produced by jetting

Metallic or Metallurgical bonding is the chemical bond between atoms sharing a cloud of delocalized electrons. The forces involve are electrostatic between the positive cations and the negative charge of the electron cloud. It is what keeps a metal together as a bulk material. In theory, if two perfectly smooth and clean pieces of the same metal come in contact, they should adhere, and it should be impossible to identify one piece of the metal from the other one [63, 64]. The attraction between the metals start becoming important at around 5 Å depending of the material and the orientation of the lattice [64]. This process of metal sticking is known as *Cold Welding* and it has been proven at the nano scale under vacuum [65]. Cold welding has become a problematic issue in space components while in vacuum, deformation due to fretting and galling can lead to cold welding of metallic components [66]. With common metals under normal condition, Cold Welding, is more complicated due to the presence of nano-roughness, oxides, greases and other foreign elements in the surface of the metals that obstruct a clean contact of the metallic pieces. In metals with negative potential (the vast majority), an oxide layer exists on the surface. The thickness of this oxide layer may vary drastically between metals and environmental conditions (up to 50 Å for aluminum). In theses cases, a large amount of pressure between the metallic elements is needed to break the oxide layer and to achieve enough plasticity to obtain a clean contact and Cold weld the materials [65]. In cold spray various researchers affirm that this is the main adhesion mechanism as well as being the strongest [52, 53, 57, 67]. The theory of how this bond is formed is based on the high deformation of the particles, which leads to the breaking and cleaning of the oxides at the surface of particle and substrate while the inert gas inhibits the formation of new oxides. This allows a clean and intimate contact between the elements creating the metallic bond [31, 52, 53, 57, 67]. The main parameters that have shown an influence in the formation of this kind of bonding in cold spray are tempera-

ture and velocity of the particles. These parameters directly influence the amount of deformation in the particles. Of course, deformation cannot guarantee the formation of this bonding, the exact conditions to create the bond are still unclear and appears to be highly material dependent. Another mechanism such as solid diffusion or localize melting are believed to have a minimal effect due to the time frame at which this bonding has to occur [57].

**Concept of Critical Velocity**

In order to simplify the complexity of the phenomenon of bonding in cold spray, researchers have proposed the concept of critical velocity [26, 68, 69]. It has been shown that above a particular velocity the Deposition Efficiency (DE, the ratio between the amount of material impacting and the amount of material bonded) increases drastically. It was theorized that if the particles achieve this velocity or higher, they have enough kinetic energy to bond with the substrate (either mechanically or metallurgically). There have been a series of attempts to propose an equation of critical velocity [2, 37, 51]. These empirical equations consider a series of properties of the particle material, as well as the temperature of impact [70, 71]. In these studies, they define the critical velocity as the velocity when the DE reaches 50% [72]. The existence of another critical velocity has also been theorized, which if reached result in coating erosion [2]. Figure 2.11 shows a schematic of these two processes. A rapid increase in DE can be seen at a certain velocity, followed by a slow decay due to the erosion of the coating. Critical velocities show a large variation depending on the material sprayed [2, 3]. Table 2.2 shows the critical velocity range for several materials. This variation has been attributed to the differences in the material proprieties such as crystallographic structures, hardness, density, melting point and mechanical strength [3]. There are other parameters that also influence critical velocity, such as particle size [69] and thickness of the oxide layer in the particles [73, 74].

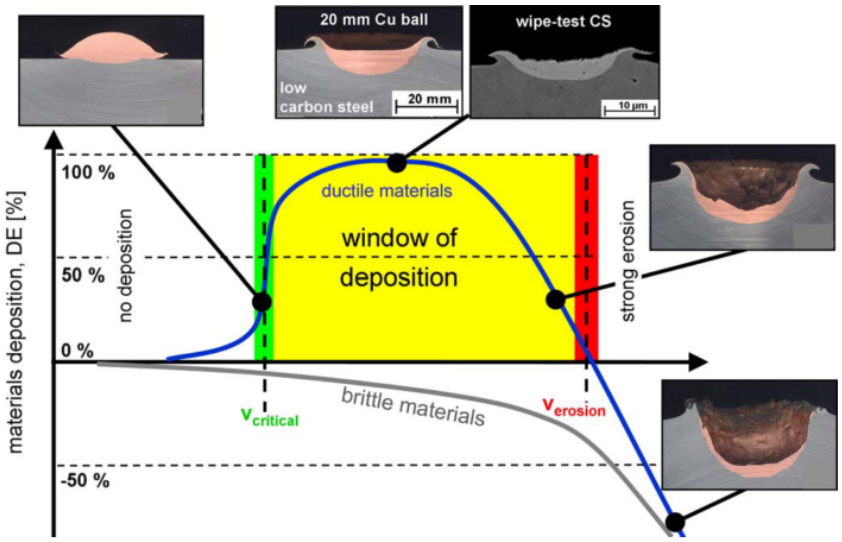


Figure 2.11: Schematic of window of deposition in cold spray [2].

Table 2.2: Critical Velocities for Different Materials [2, 3]

| Material | Critical Velocity |
|---|---|
| Aluminum | 620 - 660 $m/s$ |
| Titanium | 700 - 890 $m/s$ |
| Tin | 160 - 180 $m/s$ |
| Zinc | 360 - 380 $m/s$ |
| Stainless Steel 316L | 700 - 750 $m/s$ |
| Copper | 460 - 500 $m/s$ |
| Nickel | 610 - 680 $m/s$ |
| Tantalum | 490 - 650 $m/s$ |
| CoNiCrAlY | 850 - 900 $m/s$ |

### 2.1.3 Microstructure of Cold Spray Coatings

The main difference between cold spray and other thermal spray processes relies on the fact that is a solid-state process (or very localized melting). This ensures a retention of the main features of the microstructure of the feedstock powder. Thus, the process allows a better control of the microstructure of the coating. For example, some researchers have deposited a coating using metallic glasses obtaining a bulk metallic glass as a coating [12, 75], as is shown in the diffused XRD pattern in Figure 2.12. These type of materials are often obtained just as a powder form due to the large cooling rate needed to freeze the structure from the liquid state.

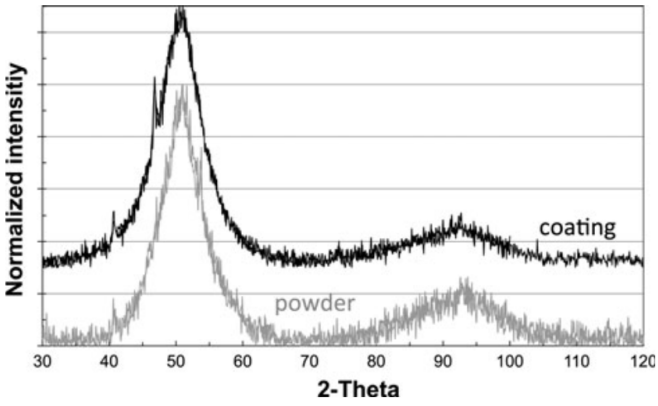


Figure 2.12: XRD patterns of Fe-Based metallic glass, powder v/s Coating [12].

Although the main microstructure is conserved and depends on the feedstock powder, there are still a few characteristics that most of cold spray coatings have in common. As was discussed before, the particles undergo a large degree of deformation to achieve bonding. This deformation, is common for all cold spray coating and, as a result, it creates a microstructure dense in dislocations in crystalline metals [76–79]. This zone of high density of dislocation, combined with the temperature of the spray can lead to phenomenon such as dynamic recrystallization at severely deformed zones such as the particle interface [80], as is shown in Figure 2.13 where a smaller grain size can be found in the particles interfaces of a cold spray coating .

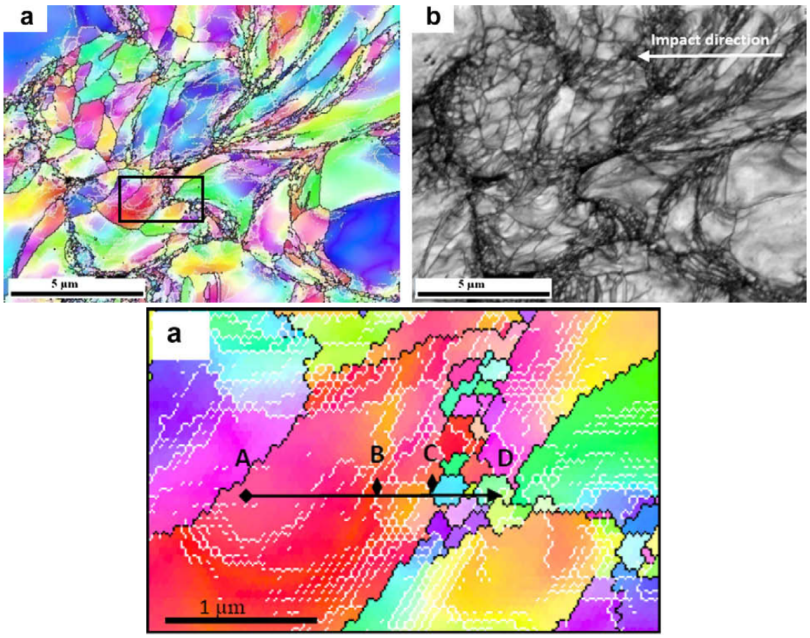


Figure 2.13: EBSD analysis in cold spray coating showing dynamic recristallization in the particle interface [12].

Another important feature of the microstructure of cold spray coatings is the porosity level. In general cold spray coatings have a low degree of observable porosity ($< 2\%$). This is due to the severe deformation of particles during deposition. While nanoporosity between particle is not visible and is difficult to detect, it is believed that it exists and can be responsible for behavior as permeability through coatings [81]. Despite the porosity levels being low, pores can still play an important role in the behavior of the coatings under different conditions. For example, porosity hinders grain growth in an annealing process [82] or can be a crack nucleation point that leads to fracture. Other microstructural features that can be observed are material dependent, for example, twinning and shear banding have been seen in titanium deposits, These phenomena are usually seen in heavily deformed HCP structure, see Figure 2.14. The high deformation seen in particles during cold spray can lead to large changes in microstructure in some sensitive materials. For example, Richer et al. [83] showed that CoNiCrAlY coating deposited by cold spray leads to grain refinement of the $\gamma$-phase matrix down to the nanometer scale as well as dissolution of $\beta$-phase precipitates that were present in the powders before spraying.

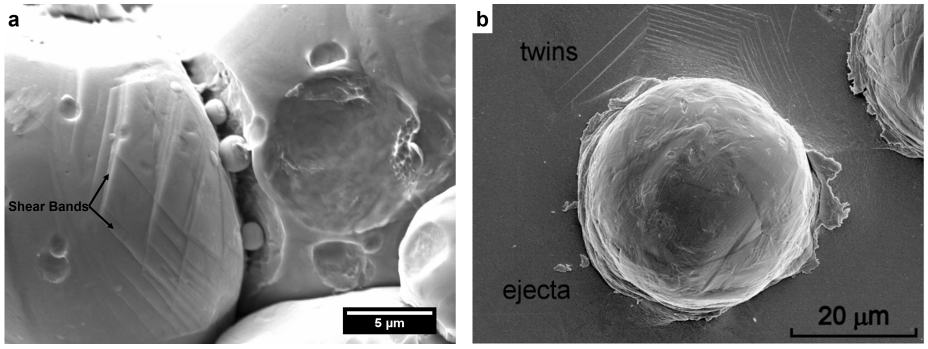


Figure 2.14: SEM images of Titanium powder showing (a) Shear banding and (b) Twinning in the substrate [13]

### 2.1.4 Properties and Applications of Cold Spray Coatings

Similar to the microstructure of cold spray coatings, most of the coating properties depend on the feedstock material used [48]. However, there are still some properties that can be consistently found in the coatings. Due to the high deformation during impact, coatings are heavily cold worked, meaning that they normally present high hardness levels and low ductility [6, 19, 48].

Depending on the properties needed in the coatings the powders to be sprayed are selected accordingly. For example, some corrosion protection coating has been sprayed with aluminum powder

or copper powder to improve the corrosion resistance of the base material component [14,15,84–86]. The high deformation of the particle leads to low porosity, sealing the piece and providing protection against the harsh environment. Trahan [14] improved the corrosion resistance of friction stir welded joints by coating the junction with a thin layer of pure aluminum, see a) in Figure 2.15. Also Cold Sprayed copper coatings have been proposed for the long term corrosion resistance for nuclear waste canisters [15, 86], b) in Figure 2.15.

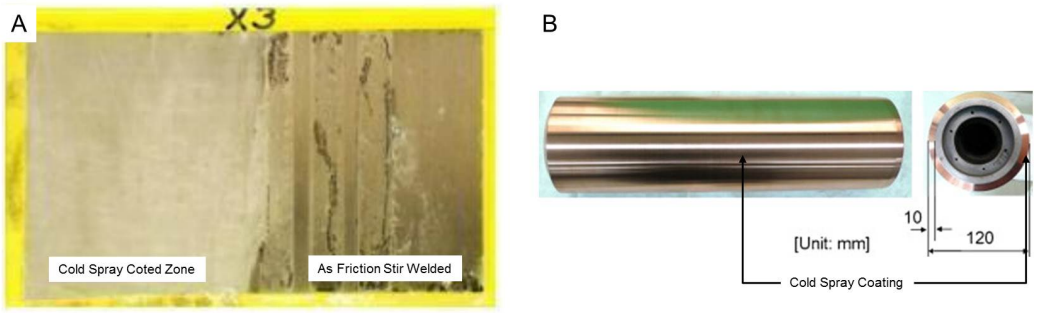


Figure 2.15: (a) Aluminum coating protection friction stir welded joint [14]. (b) Copper canister prototype for long term corrosion protection of nuclear waste [15]

Wear resistance is another property that can be achieved with cold spray coatings. Tungsten carbide-based cermet powders have been proven to be sprayable [87–91], creating a thin but very hard coating onto a substrate. Through this method, it is possible to improve the wear performance of a component drastically.

Another property that is important to mention is the adhesion of the coating to the substrate, which is directly related to the bonding mechanism. Depending on the material couple used (Coating - Substrate), and the spray parameters. The adhesion strength may be higher than the coating cohesion or low enough to result in delamination. Most applications look to increase the adhesion strength of the coatings.

Cold spray coatings have been used for dimensional repairs [16, 85, 92–96], Figure 2.16. In these cases, a high adhesion is required to ensure the integrity of the piece. In the same line of repair, the process also had been proposed as a quasi-structural repair such as thread repair method, Figure 2.17.

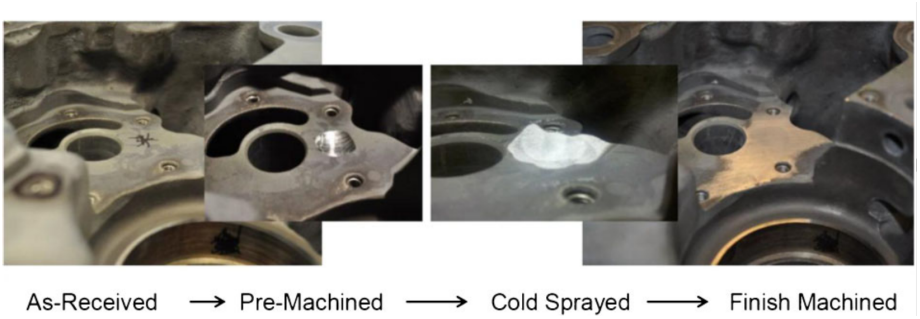


Figure 2.16: Magnesium gearbox repaired by portable cold spray [16]

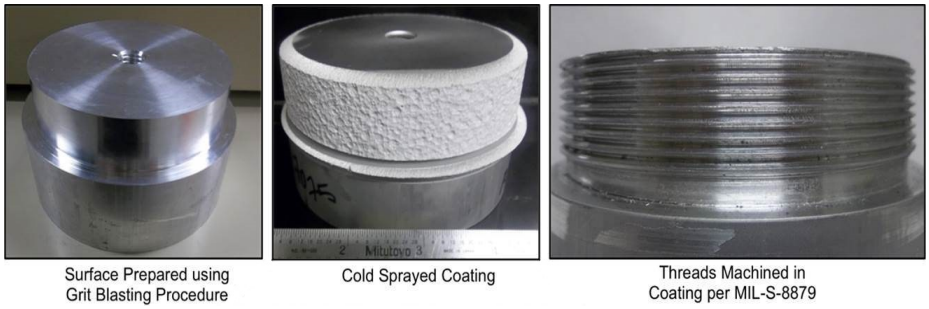


Figure 2.17: Thread repair in aircraft aluminum component [17]

Some applications exist for which low adhesion strength is advantageous. For example, cold spray has been envisioned as an additive manufacturing process [97, 98], where a near to shape piece can be sprayed. In this application, a low adhesion is preferable in order to detach the piece with ease. Another interesting case where low adhesion is needed is the metallization of composite material by inverse molding [18]; where a cold spray coating is sprayed on an Invar mold, composite is built into it, and removed to obtain a metallized composite piece, Figure 2.18.

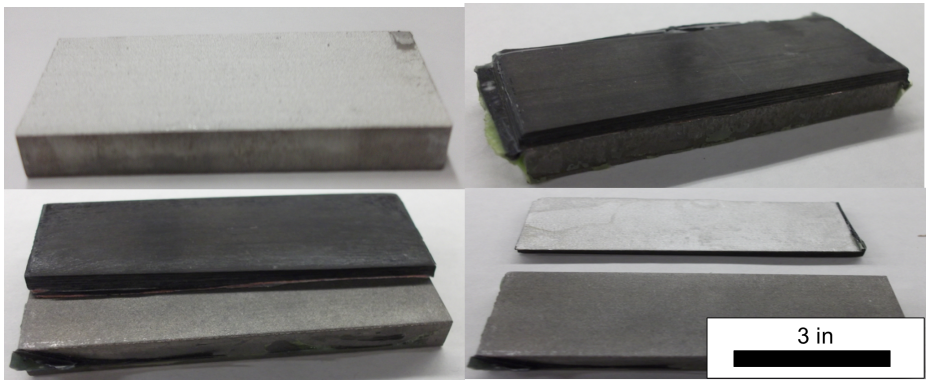


Figure 2.18: Metallization of carbon fiber by inverse molding with cold spray coating [18].

One of the obstacles that cold spray has to encounter is related to the intrinsic brittleness of the coatings. This property makes cold spray unfavorable for structural repairs or applications where stresses can lead to fracture [16]. Some researchers have tried to solve this obstacle by annealing the coating [19, 99]. For example Gärtner et al. [19] studied the effect on annealing time on the mechanical properties of copper coatings; obtaining an increase in ductility and toughness depending of the annealing time, see Figure 2.19 and 2.20. Cold spray also showed to be advantageous over other thermal spray processes in the capability of restoring the mechanical properties of the material after annealing.

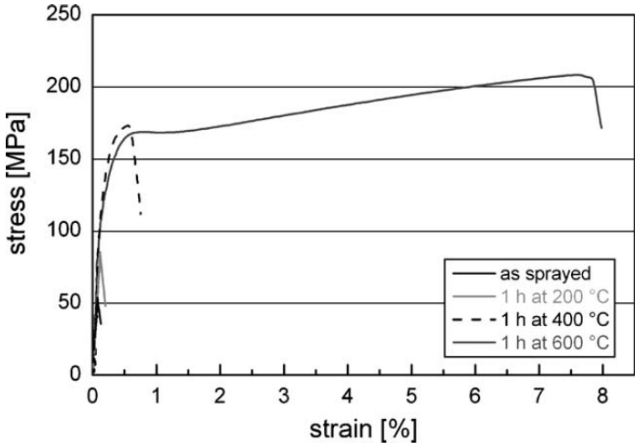


Figure 2.19: Stress-Strain curve of micro flat in copper coatings tensile test, annealed at different conditions [19]

.

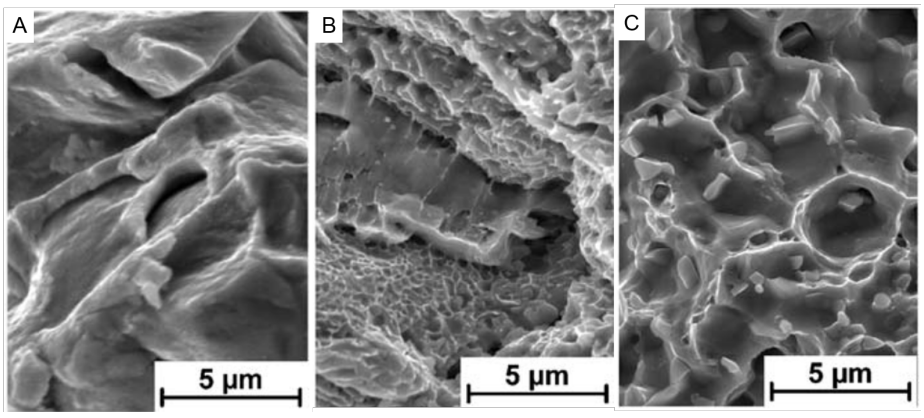


Figure 2.20: Fracture surfaces of Stress-Strain curve of micro flat in copper coatings tensile test. (a) as sprayed (b) annealed for 1 h at 400°$C$ and (c) annealed for 1 h at 600°$C$ [19].

### 2.1.5 Numerical simulations of particle impact in cold spray

Due the extremely short impact time and the small particle size, the study of the deformation of cold spray particle it is practically impossible, and therefore numerical FEA is preferred for this studies. FEA offer a strong tool to investigate the deposition behavior of the particles, by giving the option of calculating the contact pressures between the particle and substrate, plastic deformations, stresses and temperatures created during the impact. Several investigation have benefit with the use single impact simulations [2, 51, 53, 59, 100]. Concepts as adiabatic shear instability have been confirmed, and features as jetting and full coatings can be obtained by simulations [101–105]. Although FEA can be very powerful in obtaining results in cold spray, several input parameters need to be added to the simulation, as several models are being solved. This parameters needed for this models are material dependent. In the following section as a brief summary of the main models normally used in a single particle impact simulation will be described.

#### Plastic Model

When a particle starts its deformation process, the particle will suffer elastic deformation, and plastic deformation in zones where the stress have reach the yield point $\sigma_y$. In a practical approach, this value is not a constant, as it increases due to work hardening or higher strain rates, and can decrease if the temperature of the material increases. The preferred model in cold spray to calculate $\sigma_y$ is Johnson-Cook's equation [60] as it combines a simple approach including work hardening, strain rate hardening and thermal softening, other equations have been studied for the deformation of particles, but its use and parameters are limited to very specific materials [59].

$$\sigma_{JC} = \overbrace{\left[A + B(\varepsilon)^n\right]}^{Work\ hardening} \overbrace{\left[1 + C\ln\left(\frac{\dot{\varepsilon}}{\dot{\varepsilon}_0}\right)\right]}^{Strain\ rate\ Hardening} \overbrace{\left[1 - \left(\frac{T - T_0}{T_m - T_0}\right)^m\right]}^{Thermal\ softening} \tag{2.14}$$

The equation considers a constant value for the undeformed material and a powder law for hardening. This is multiplied by two expressions that consider hardening/softening for the speed of deformation and temperature, each normalized by a reference value.

### Shock Compressed Solid

The equation of state normally used in high velocity impact is the linear Mie-Grüneisen equation. This equation is widely used in simulations of cold spray particles or ballistic analysis. The impact creates shocks that propagate through the material creating an abrupt change in pressure and density and as a consequence material speed and strain. This equation relates pressure and volume at a given temperature in a shock compressed solid. The (Us-Up) Hugoniot form of the equation is normally used in cold spray [2, 51, 53, 59, 100].

$$p = \frac{\rho_0 {c_0}^2 \eta}{(1 - s\eta)^2} \left(1 - \frac{\Gamma_0 \eta}{2}\right) - \Gamma_0 \rho_0 E_m \, , \; \eta = 1 - \frac{\rho_0}{\rho} \tag{2.15}$$

Where $p$ is the hydrodynamic stress, $\rho_0$ is the initial density, $\rho$ is the actual density, $c_0$ is the material speed of sound inside of the material, $s$ is the Hugoniot slope, $\Gamma_0$ is the Grüneisen constant, and $E_m$ is the energy per unit mass.

## 2.2 Ceramic-Metal Composites

Ceramic-Metal composites, most commonly known as cermets, are composite materials composed of a ceramic part and a metallic part. Cermets are designed to have the optimal properties of its components, such as plastic deformation and toughness of metals, and hardness and wear resistance of ceramics [4]. Their development started during the 1930s as cutting tool materials, since then, they have gained popularity due to their potential for high strength and high temperature resistance. The application of cermets has broadened to different fields of engineering, and various types of cermets have been developed. The most common cermets are metal-matrix with ceramic particulates dispersed homogeneously. The particulates can be as coarse as $100\mu m$ or as fine as $2\mu m$ depending on the properties sought and the processing method used to consolidate the cermet [4] .

Cermets are usually categorized by their refractory component, the most common being carbide, nitride, and oxide-based [25]. The metallic binder phase can consist of pure metal, an alloy or combinations of both. Some of the most commonly used metals and alloys are nickel, cobalt, molybdenum, stainless steel and superalloys. The volume fraction of the binder elements depend directly on the properties sought and normally range between 15-85% vol.

The industrial use of cermets cover a broad spectrum of applications, cutting tools being the most common, but cermet can also be used for engine parts, mining components or any application where high wear may be present. In the transportation industry, they are employed in brakes pads and clutches due their high wear resistance. They are also used as biomaterials in hip replacement components [4].

The consolidation methods to produce cermets follow similar processes as powder metallurgy, such as compaction and sintering. Table 2.3 summarize the most common consolidation techniques for cermets. Figure 2.21 shows a schematic of differents manufacturing processes of a cermet [4].

Table 2.3: Various Consolidation Method for Cermets [4]

| Production method | Products |
|---|---|
| 1. Presintering | Cemented-carbide parts and cermets |
| 2. Vacuum sintering | Steel-bonded carbides and cermets |
| 3. Canning | Steel-bonded carbides |
| 4. Hot extrusion | Aluminum cermets with moderate amounts of hard-phase additions |
| 5. Infiltration | TiC parts with nickel-or cobalt-base infiltrants and other cermets with about 55-85 vol% hard phase |
| 6. Warm extrusion | Cemented-carbide rods or other slender cermet parts |
| 7. Slip casting | Cermets with high proportions of hard phase |
| 8. Powder injection molding | A wide variety of cermet compositions |
| 9. Powder rolling | Aluminum, copper, and other nonferrous metals with moderate additions of hard-phase components |
| 10. Hot pressing | A wide variety of cermet compositions |

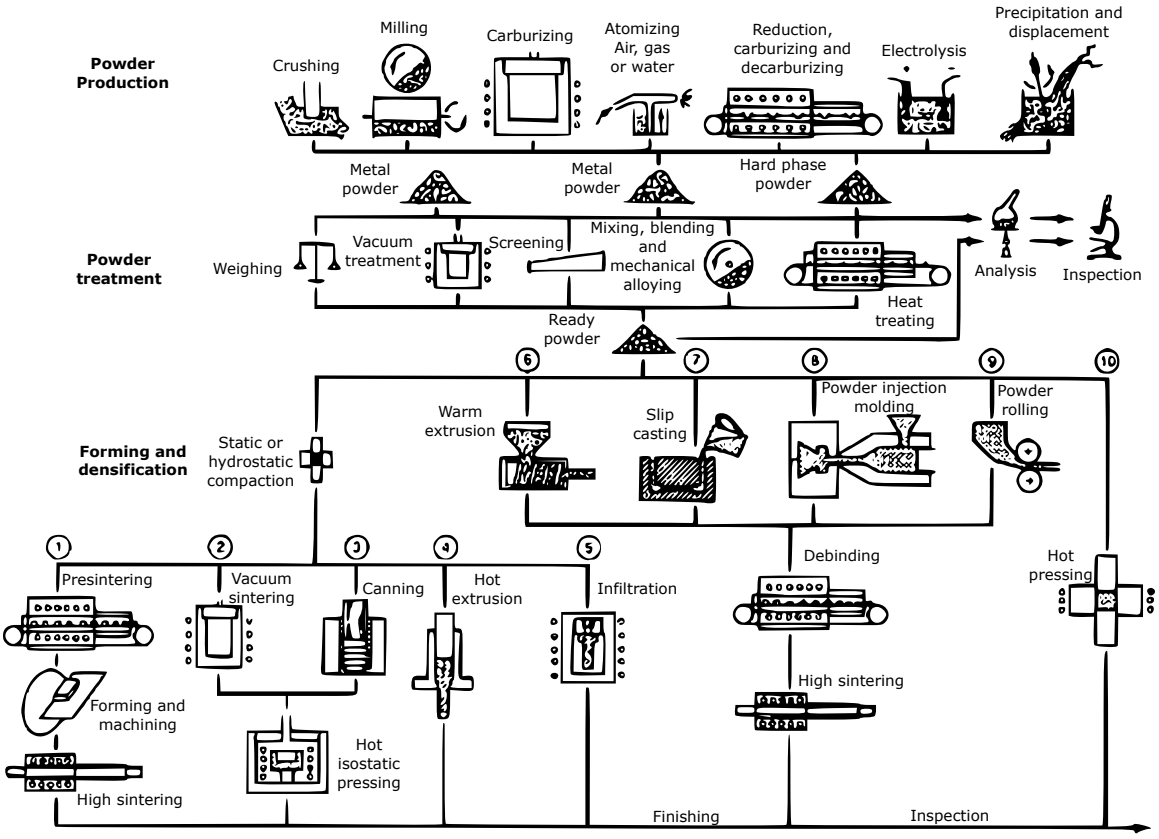


Figure 2.21: Different process of consolidations of Cermets [4].

### 2.2.1 Cermets in Cold Spray

In cold spray, cermet materials have been a subject of interest. Several ceramic metal combinations have been successfully deposited by cold spray with a variety of different powder morphologies [20–22, 106]. The properties and applications closely resemble the ones seen in other thermal

spray processes, principally wear resistance, high hardness, and high temperature applications. The inclusion of ceramic particles is the main responsible for the improvement of these properties [4,25]. The addition of ceramic particle does not just affect the properties of the coating but also have a substantial effect on the deposition behavior [21]. Even though the deposition of ceramics-metals mixtures has been studied in cold spray and the properties and deposition behavior have been established, all the studies done have been exploratory and have used a descriptive approach with a focus on industrial applications. Few studies have been done with the purpose of explaining the behaviors observed. Several theories have been proposed but have not been proven. In this section, the most important studies of cermet in Cold spray are presented, describing the phenomenon seen and the theories proposed.

Some studies have shown that the deposition characteristics of cold spray are dramatically affected by the addition of ceramic particles to the feedstock powder. These effects extend to deposition efficiency, adhesion and porosity of the coatings.

One of the most dramatic changes in behavior that have been seen with the addition of ceramic particles to the feedstock powder is the increase in DE. This behavior was observed in the first studies of deposition of ceramic metal mixtures, and was scientifically reported by Shkodkin et al. in 2006 [20]. In this study, the researchers deposited mixtures of ceramic-metal at different ratios in order to *grit blast* the substrate surface with the abrasive particles. They noticed an increase in DE with the addition of ceramic particles up to 30 wt% and a decrease of DE at higher ceramic contents reaching 0% DE at 95 wt% ceramic, Figure 2.22. The low deposition efficiency at higher ceramic content was expected due to the lack of ductility of ceramics, thus it cannot be deposited; just embedded [20]. Shkodkin et al. [20] mentioned that at lower ceramic content, the roughening of the substrate may have some influence in the DE. The researchers give no further explanation on the behavior observed and mentioned the need for further research to completely understand the role of the abrasive material in the deposition.

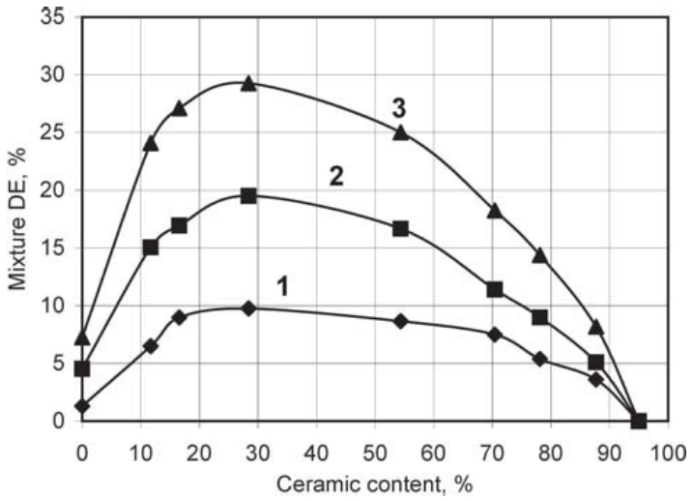


Figure 2.22: Deposition efficiency dependencies on the mass ceramic content in Al-ceramic powder mixture at different air stagnation temperatures 1) 600 K, 2) 700 K, 3) 800 K [20].

Several other investigations have shown similar trends in deposition efficiency [21–23, 106]. Irissou et al. [21] studied the effect of aluminum particle size in the deposition of a mixture of aluminum-alumina. They computed the deposition efficiency of the blend and of the aluminum fraction of the mix. This study demonstrated that the deposition efficiency of the aluminum fraction in the mixture can be increased even though the overall deposition efficiency decreases, Figure 2.23. Irissou et al. [21] explained that this is due to the erosion of the alumina particles when impacting other alumina particles and the lower chances to embed alumina particles versus depositing aluminum. Irissou et al. also proposed an explanation for the change of deposition efficiency. They observed that the interface between the coating and substrate roughens as the percentage of ceramic increases, Figure 2.24. This increase in roughness is expected due to the *grit blasted* effect of the impacting alumina particles in the substrate. At a higher ceramic percentage in the mixtures, more alumina particles blast the substrate. Irissou et al. proposed that these *asperities* are the ones helping to bond more particles, increasing the deposition efficiency of the mixture. This theory has been used as a possible explanation in other investigations [106, 107] but it had not been proven or further explored.

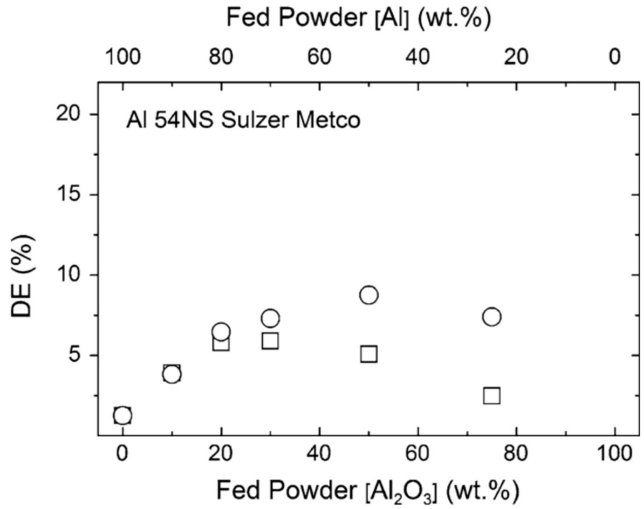


Figure 2.23: Deposition efficiencies of (□) the blended Al-$Al_2O_3$ powder and (◯) the Al content of the powder. [21]

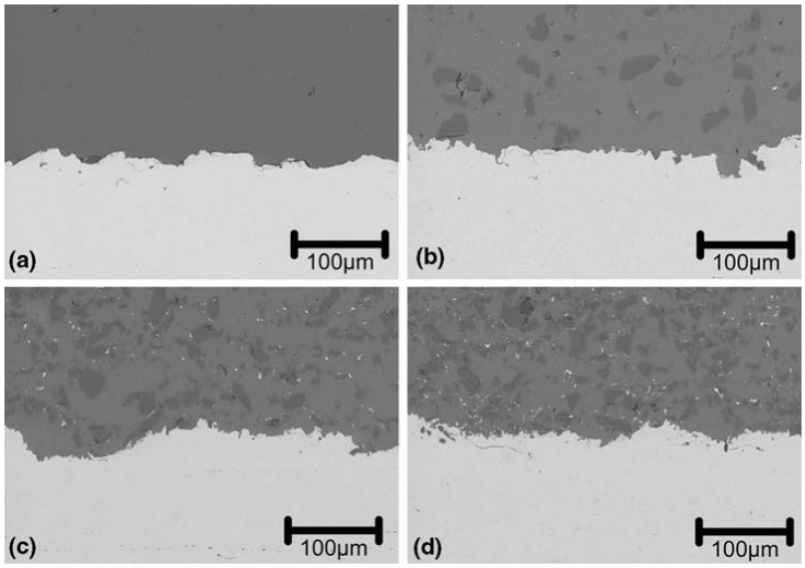


Figure 2.24: Back-scattered electron micrographs showing roughness and asperities at different $Al_2O_3$ content in the starting powder: (a) 0 wt.%, (b) 10 wt.%, (c) 50 wt.%, and (d) 75 wt.% [21].

Besides this theory about roughening, two alternate possible explanations have been proposed to explain the change in deposition efficiency. One theory explains that during the deposition, the ceramic particles deform the substrate and clean its oxide film but do not adhere, preparing the substrate for the arrival of the subsequent metallic particles. Even though the oxide layer of the incoming particle still exists, this could lead to the increase of deposition efficiency observed. This theory is still to be proven and has not been investigated

Finally, the third explanation that can be found in the literature is referred as the peening or impingement effect of ceramic in the metallic particles [22, 23, 108]. It was first proposed by Maev and Leshchynsky [108] in their work about the deposition of powder mixtures where they spray different metals and ceramics. They proposed, that a hard particle act as *Shot Balls*, peening the soft particles in front of it, increasing the deformation and as a consequence increasing the deposition efficiency. Like the other theories, this one has not been proven yet. It is important to consider, that in order for this theory to be true, a ceramic particle will need to impact the metallic particle immediately after the metallic particle arrives at the substrate, increasing the deformation and the probability to stick to the substrate. If this condition is not met, the incoming particle will be gone (due to the lower deposition efficiency) before the ceramic particle arrives at the substrate.

Another property that benefits from the addition of ceramic particles is the adhesion of the coating to the substrate. It has been reported that the addition of ceramic particles to the feedstock powder can lead to a dramatic increase in adhesion [21, 22, 109], Figure 2.25. This behavior has been explained by the same principles than the effect in deposition efficiency:

- The increase in roughness of the substrate can lead to more anchoring points, increasing the mechanical bonding between the coating and the substrate. This effect has been seen in cases where the substrates have been artificially roughen [62], and higher values of adhesion have been observed.
- The addition of ceramics might promote the oxide film removal of the substrate surface, increasing chances of obtaining metallurgical bonding between the particles and the substrate [56].
- Finally, peening of the particles leads to higher deformation and can help to consolidate the coating. This can lead to higher metallurgical bonding, and therefore to an increase of adhesion.

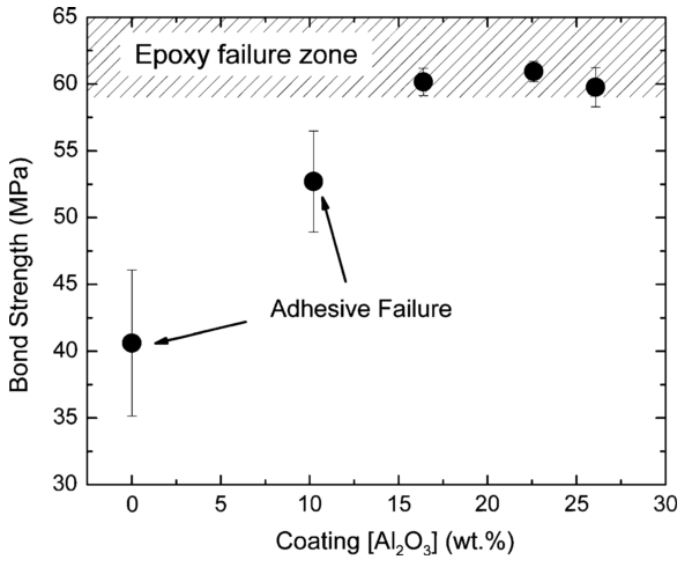


Figure 2.25: Adhesion strength of Aluminum-$Al_2O_3$ coating at various ceramic contents [21].

It is important to note that all the behavior previously mentioned occurs with a mixture of metal-ceramic in the feedstock powder. Therefore, the initial condition of the feedstock material is not a cermet but a mix of powders. The consolidation to a cermet occurs during the deposition process where ceramic particles deform the substrate and embed into the coating with metallic particle forming the matrix. This can lead to inconsistencies in the microstructure of the cermet and discrepancies between the ceramic content of the feedstock powder and the resulting coating. For this reason, various researchers have reported the ceramic content of the coating obtained versus the original composition of the feedstock powder. [21–23, 110]. As is expected, the composition of ceramic is always lower in the coating than the initial composition, Figure 2.26. This is due to the lower chances of embedding ceramic particles compared to the chances of adhering the metallic particle during deposition. Ceramics can be incorporated into the coating just after they get surrounded by the metallic phase [22]. Some researchers have shown that the relative percentage of ceramic retention is stable, e.g. a)in Figure 2.26. Wang et al. [22] found that the amount of ceramic retained in the coating was consistently 50% of the amount of ceramic present in the feedstock powder, and this value was independent of the process temperature. Shockley et al. [23] found a different percentage of retention and this value differs with the ceramic morphology, b) in Figure 2.26. This suggests that the percentage of ceramic retention depends on the particle size, morphology, and material, and not on the process parameters.

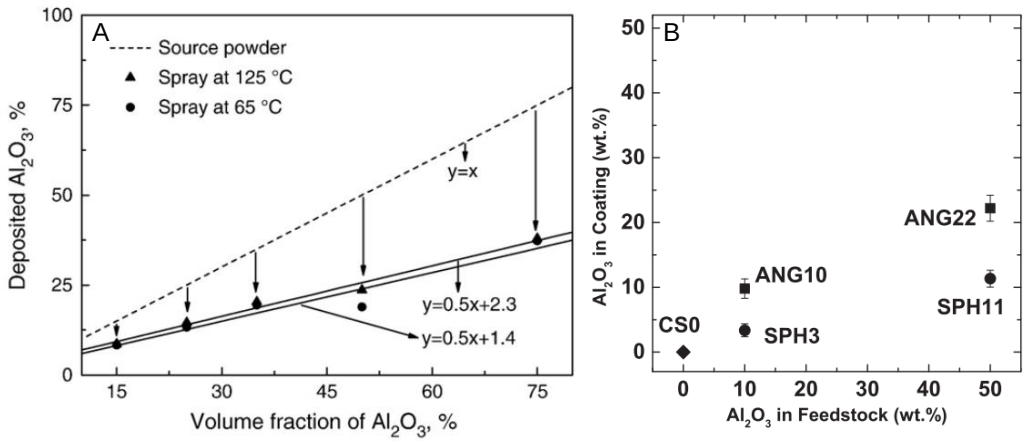


Figure 2.26: Ceramic retention of $Al - Al_2O_3$ produced by different researchers, a) Wang et al. [22], and b) Shockley et al. [23] with different morphology of $Al_2O_3$ ANG:angular and SPH:Spherical .

These discrepancies in ceramic retention lead to inconsistencies in properties and behavior of the coatings. A way to address these inconsistencies is by avoiding using a metal-ceramic mixture as feedstock powder, and instead using a pre-consolidated cermet powder. Manufacturers produce different kinds of cermet powders, but its production is intended to be used on others thermal spray processes, such has HVOF or plasma spray [24]. In these *hotter* thermal spray processes, the metallic phase is intended to melt during the deposition process to achieve a coating. Some examples of these kinds of powder are *agglomerated*, *agglomerated and sintered*, and *mechanically cladded*, Figure 2.27. Since the metal-ceramic composition is intrinsic to each particle in the powder, this composition remains similar in the coating [87]. Even though these kinds of powder were not originally intended to be sprayed by cold spray, researchers had been able to deposit them under different conditions [88, 111–113]. The deposition behavior of these particles differs depending on the initial morphology, composition and sizes [87, 111, 112, 114].

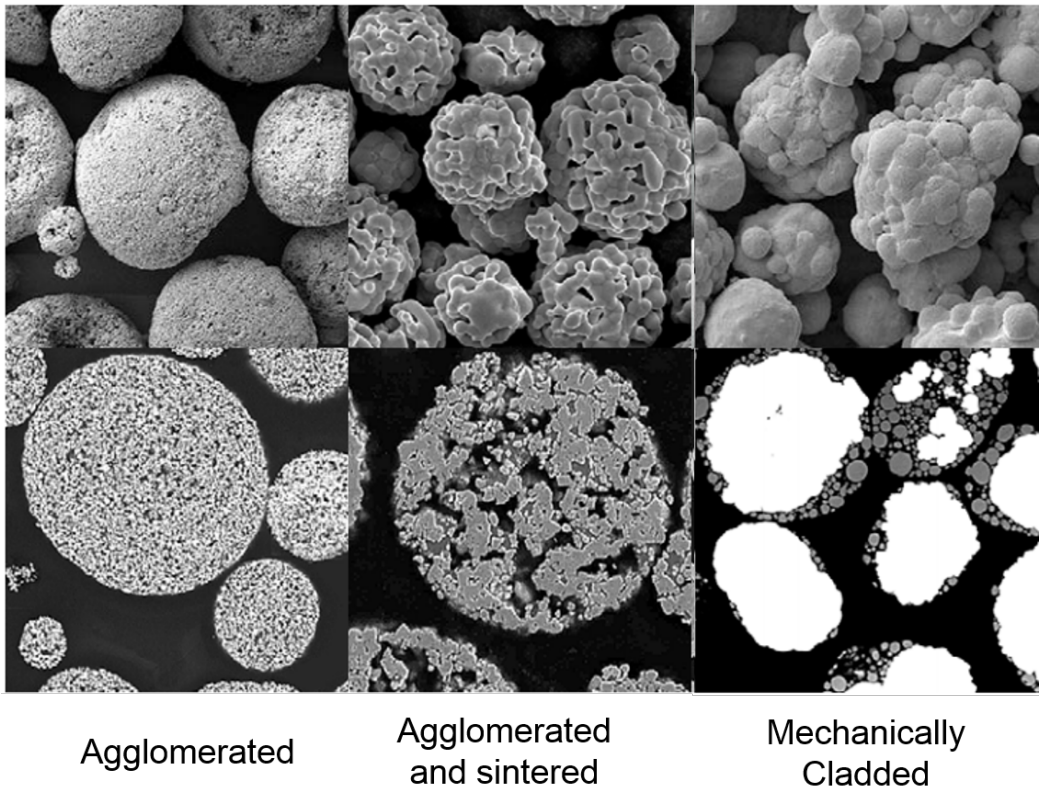


Figure 2.27: Examples of consolidated cermet powders [24] .

The properties of cermet coatings produced by cold spray are similar to traditionally manufactured cermets, such as high hardness and excellent wear and abrasion resistance, Figure 2.28. They also share properties of cold spray coatings. The ductile phase has gone through a severe plastic deformation in order to consolidate the coating. This leads to a higher hardness of the material at the same ceramic-metal ratio. In addition, since the consolidation of the coating happens at low temperature, some unwanted reactions are avoided. For example, in the production of $WC-Co-Cr$ coatings by other thermals spray processes such as HVOF, decarburization of the tungsten carbide. $WC$ reacts and form $W_2C$ and $W_3C$, which are fragile phases compared against $WC$ therefore, decreasing the properties of the coating [114, 115]. In cold spray, this decarburization can be avoided completely, giving a higher potential for better properties [93, 112, 114]. However, since the ductile phase does not undergo melting, there are some limitations in the amount of ceramic retention that can be obtained.

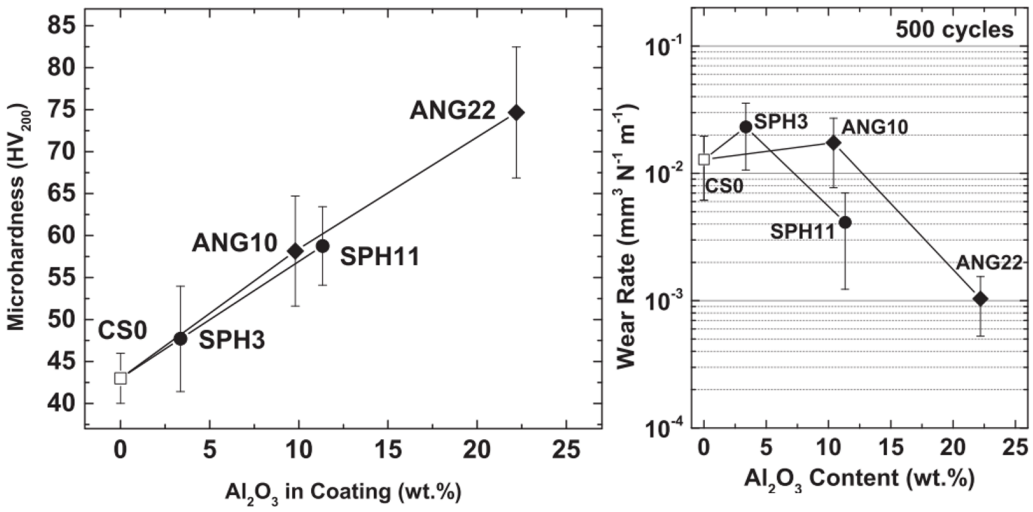


Figure 2.28: Hardness and wear rate at different ceramic content in the coating with different morphology of $Al_2O_3$ ANG:angular and SPH:Spherical [23].

## 2.3 Chromium Plating

Chromium plating is a process heavily used in the engineering industry as a surface finish and protective coating that prevents corrosion and increases durability of a piece. It can be divided in decorative plating and hard (wear resistant) plating. Decorative chrome plating is used mainly in consumer goods. This thin coating ($0.5\mu m$ to $5\mu m$) is primarily designed to be aesthetically pleasing, but it also improves the durability and corrosion resistance of the coated piece. Hard plating is a thicker chrome layer than decorative plating, between $8\mu m$ to $250\mu m$ [116, 117]. Due to its thickness, it shows the inherent hardness of chromium and improves the erosion resistance of the piece [116, 117]. Its value for engineering applications relies on its hardness which ranges from 800HV to 1000HV, and its low friction coefficient. These coatings are also used for minimizing the seizing of parts and improving the corrosion resistance of the piece.

In a different perspective, the industry has been pushed to eliminate the use of hard chrome coatings due to the hazardous side products of its production. The plating process uses hexavalent chromium $Cr_6$, which is the most toxic form of chromium [29, 116, 118]. The use of hexavalent chromium has been banned in the European Union since 2006 [28], it lists in the group 1 in the international agency for research on cancer (IARC) [119]. In the U.S. the Environmental Protection Agency (EPA) identifies Hexavalent Chromium as 1 of 17 *high-priority* toxic chemicals and it is regulated heavily. It also lists a *priority pollutant* under the Clean Water Act [120] and a *haz-*

*ardous constituent* under the Resource Conservation and Recovery Act [121]. In Canada hexavalent chromium figures between the toxic substances regulated by Canadian Environmental Protection Act since 1999 [122].

Currently, the electroplating industry is focusing its efforts on changing the plating process to use Trivalent Chromium $Cr_3$, this component is less toxic than $Cr_6$ and the compound has the potential of replacing $Cr_6$ but the coatings produced have proven to be more expensive, difficult to control and have not reached the same performance than $Cr_6$ [116, 123].

Another disadvantage of this plating process is its inability to be repaired. If a chrome plated part gets damaged, it is necessary to remove the coating completely from every part of the piece. The piece is then cleaned and plated again [116]. This restoration method is highly inefficient, time consuming and expensive. For these reasons, there is a need to find a suitable replacement and repair method for hard chrome plating. Researchers have been studying different alternatives for its replacement, and have found just a few alternatives that have some potentials such as electroless nickel plating [124, 125], HVOF coatings (usually with WC-Co) [29, 118] and PVD coatings [126]. These alternatives have their own disadvantages, such as low building rate and low hardness in the case of electroless nickel. HVOF coatings have the same lack or repairability as **chromium** plating, and PVD coatings are still far from becoming industrial application with the production rate necessary to replace chromium plating.

# Chapter 3

# Description of Research Objectives

The main purpose of this research is to make an assessment of the deposition mechanisms of blended ceramic-metal and cermet powders by cold spray. The understanding of these mechanisms and their effect on the microstructure and properties of the coating can help to better tailor the feedstock powder for different applications where hard coatings are needed.

Ultimately the study aims to apply the discoveries made in the investigation to a real engineering application where a hard coating is needed. As is was mention in the previous chapter, deposition of cermets by cold spray has been documented in the last decade and general trends have been established such as the increase of DE with the addition of ceramic particles in the feedstock powder, or the reduction of the ceramic-metal ratio in the coatings versus the feedstock powder [21]. These phenomena, have not been completely explained. The objective of this investigation is to shine some light on the mechanisms of deposition and explain these phenomena through a comprehensive study. A set of objectives have been defined to address each of the phenomena described previously:

1. Study the effect of ceramic content in a ceramic-metal blending on the cold spray deposition process.
2. Study the effect of ceramic morphology in a ceramic-metal blending on the cold spray deposition process.
3. Study the effect of cermet powder morphology on the cold spray deposition.
4. Consolidation of cermet coating by cold spray for an engineering application

## 3.1 Study the Effect of Ceramic Content in a Ceramic-Metal Blending on the Cold Spray Deposition Process

Most of the studies in cermet deposition by cold spray are based on blended powder. This kind of powders allows for the easy modification of their ceramic-metal ratio. As was discussed in the previous chapter, most of the phenomena found in the deposition of cermets by cold spray shows a strong influence of the content of ceramic in the feedstock powder. Previous studies show changes of deposition efficiency with ceramic content, changes of wear properties with the ceramic embedding the coating, and changes in adhesion. Understanding the different behavior of deposition with a change of ceramic content reveals the mechanisms acting during the deposition and helps understand the influence of each parameter on the coating properties. These objectives will serve as a guideline to obtain a strong understanding of the effect of ceramics on the deposition of blended cermets.

### 3.1.1 Evaluate the Erosion Rate of Angular Ceramics vs. the Deposition Rate of Metallic Particles in Cold Spray

As was discussed before, researchers have shown a strong influence of the percentage of ceramic in the feedstock powder on the deposition efficiency. The general trend shows an increase of the overall DE with the inclusion of some ceramic particles leading to a peak in DE at a specific ceramic-metal ratio. Followed by a consistent decrease of DE with a higher ceramic content, reaching a point where no coating is built [20–23, 106]. On a different note, the erosion of ceramic particles in a metallic substrate has been intensively studied by several researchers [127–129]. Neilson and Gilchrist [129] studied the erosion mechanism in ductile metals and showed the effect at the initial stages of the impact. Initially the ceramic embeds into the ductile metal. This is followed by fracturing of the ceramic and erosion of the substrate caused by the next impacting particles. This process suggests that the ceramic particles could act as an erosion agent, and the metal as an additive material to the substrate. Thus, there are two mechanisms competing, erosion and deposition. Considering that both processes occur at the same time, the erosion process does not occur as in Neilson and Gilchrist experiment, but a *fresh* substrate is constantly forming as the metallic particles are deposited. Therefore, the overall process depends mainly on the number of incoming ceramic impact against the adhering metallic particles. Based on this, it is proposed to study the decrease in DE during the spray at high ceramic content.

### 3.1.2 Evaluate and Explain the Effect on DE with the Addition of Ceramic Particles in Cold Spray

In the previous section, the effect of ceramic particles on the erosion of the coating during the deposition was discussed. This effect has been shown when there is a high ceramic content of the feedstock powder. A different effect has been shown with a low addition of ceramic in the powder. Several studies have described that the DE increases with the addition of ceramic particles [21], This behavior suggests that the presence of ceramic particles in the feedstock powder promotes the adherence of metallic particles. The influence of ceramic particles on metallic ones can happen in three instances: during flight, during impact or ceramic interaction with substrate followed by a metallic particle interacting with the altered substrate. It is generally accepted that the interaction of particles during flight is negligible. Three theories have been suggested as explanations for the increment in DE: by introduction of asperities into the substrate, by removing the oxide layer of the substrate, or by impingement of a ceramic with the impacting particles. None of this theories have been (dis-)proved or further explored. This objective seeks to clarify these processes. The explanation of this phenomenon not only benefits the understanding of deposition of cermets but also can help to clarify some of the fundamentals of the adhesion mechanism of cold spray.

### 3.1.3 Evaluate the Retention of Ceramic Particles on a Cold Spray Coating

In the literature, it has been demonstrated that most of the desirable properties of cermets depend strongly on the ceramic-metal ratio of the coating. During the consolidation of cermet by cold spray, it has been shown that the ceramic-metal ratio in the coatings obtained is lower than in the feedstock powder. Even though this behavior is expected, it generates issues obtaining a coating with a target ceramic-metal ratio. These inconsistencies in the ceramic-metal ratio make it difficult to accurately predict the properties of the resulting coating before deposition; wasting time and resources in the process of optimization. In this investigation, the process of adherence of the ceramic particle, as well as the identification of how ceramic is lost are assessed. This objective aims to shed some light on the process and parameters of ceramic inclusions and how it affects the deposition.

## 3.2 Effect of the Ceramic Morphology in a Ceramic-Metal Blending On the Cold Spray Deposition Process

The ceramic morphology is a characteristic that has been overlooked in cold spray research. In the literature, there are just one example that use a ceramic different than angular [23]. It is expected that the morphology of the ceramic plays a major role in the deposition process as well as in the effects such as erosion, impingement, embedment, and asperities created. In this investigation two ceramics were used in order to assess the effect of the morphology of the ceramic: angular ceramic are compared with spherical.

### 3.2.1 Evaluate the Effect of Ceramic Morphology on the DE of Cold Spray Coatings, Comparison between Spherical Ceramic and Angular Ceramic

If the increase in DE seen with the addition of ceramics in cold spray occurs due to the promotion of asperities as one theory suggests, then it is expected to have a change in behavior if the ceramic morphology changes. Spherical alumina should promote a smoother surface than angular ceramic. Therefore, the increase of DE should be less significant. If the increase in DE occurred by the breaking of surface oxides by plastic deformation, the morphology of the ceramic should not be that influential and, the DE should not have a major change with the change of morphology. In any case, the study of DE with different ceramic morphology will give important guidelines to the explanation of the phenomenon of DE in the deposition of blended cermet.

### 3.2.2 Evaluate the Effect of Ceramic Morphology on the Inclusion of Ceramic in Cold Spray Coatings

The morphology of the ceramic is expected to have a large influence on the inclusion during the deposition of blended cermet by cold spray. The embedding of ceramic depends mainly on the anchoring points of the ceramics. Angular ceramics are expected to have more chances to embed, whereas spherical ceramics should be more prone to bouncing and not sticking. Even though the benefit of ceramics in the coatings has been discussed, there is also interest in obtaining ceramic free coatings. The coatings would have all the benefit obtained with the addition of ceramics in the flow, such as low porosity, high deformation, and high adhesion. This section of the investigation

aims to provide a deep understanding of the inclusion of ceramic particles during the deposition of blended cermets. And how the morphology of the ceramic particles could affect the inclusion in the coating, identifying the key parameters that influence this phenomenon.

## 3.3 Effect of Cermet Powder Morphology on the Cold Spray Deposition

In this section of the investigation, the effect of non-blended cermet is addressed. Most of the studies in the literature investigate the effect of blended cermets during deposition, which may lead to difficulties in the ceramic retention of the obtained coating. However, there is a variety of cermet powders being produced that are not blended, but rather agglomerated or sintered. The use of these morphologies have some benefits and drawbacks in cold spray. For example, the ceramic-metal ratio in the coating is expected to have the same ratio that the one in the feedstock powder, which is a great advantage, because it permits to estimate the properties of the coating before the deposition. However, it is expected to have lower deposition efficiency than blended powder, since the particles are more prone to cracking during impact. From a research point of view, the composition of the powders is limited to the manufacturers production. In the literature, some investigation has been done with this kind of particles, but most of it are sprayed using high pressure systems with extremely high parameters (high pressures, temperatures and using He as process gas). This investigation aims to understand the mechanism of deformation and deposition for cermet powders of diverse morphology using a Low Pressure cold spray system using $N_2$ as process gas. This makes these coatings more attractive for industrial application. The focus of this objective is to obtain a strong understanding of how the different morphology of cermets powders affect the deposition and properties of the resulting coating.

## 3.4 Consolidation of Cermet Coating by Cold Spray for an Engineering Application

Finally, one of the objective for this investigation aims to apply the knowledge learned to an applied engineering problem. The problem targeted is the replacement of chrome plating. As it was mentioned in the previous chapter, there is a strong interest in the replacement of this coating for health and environmental reasons. The objective are to select a material, produce a dense coating

and obtain the properties desired. Test designed for the aerospace industry were used to assess the performance of the coating.

# Chapter 4

# Methodology and Research Approach

The present chapter explains the proposed research approach to achieve the goals previously outlined in the last chapter. A precise experimental plan, as well as the methodology for the deposition and analysis of the coatings is described. The feedstock powders, the equipment to produce and analyze the coatings are defined as well as the parameters needed for the deposition and testing of the coatings.

## 4.1 Experimental Design

### 4.1.1 Effect of Ceramic Content in a Ceramic-Metal Blending on the Cold Spray Deposition Process

To understand the effect of ceramic content in blended ceramic-metal powder on the deposition mechanisms in cold spray, ductile metallic powders were mechanically blended with crushed ceramic particles at different compositions. These batches of powders were sprayed using a low pressure cold spray system. For each composition of feedstock powder, the process and coatings were characterized using the techniques shown in Table 4.1.

**Constants of the Experiment**

- Powders blended: Aluminum was used as the ductile metallic particles and $Al_2O_3$ as the crushed ceramic powder. The same provider and item number was used, to ensure consistency

Table 4.1: Summary of analysis techniques for powders, coatings, wipe tests and Spray.

| Analysis Techniques | Powders | Coating | Wipe Test | Spray |
|---|---|---|---|---|
| SEM Topology | | ✓ | ✓ | |
| SEM Morphology | ✓ | | | |
| SEM Cross section | ✓ | ✓ | ✓ | |
| Etched samples SEM | ✓ | ✓ | ✓ | |
| EDS | ✓ | ✓ | | |
| Particle Size distribution | ✓ | | | |
| Micro Hardness | | ✓ | | |
| Adhesion test | | ✓ | | |
| Wear rate | | ✓ | | |
| Particle Velocity | | | | ✓ |
| Deposition efficiency | | | | ✓ |
| Gain/loss weight | | | | ✓ |
| FEA | | | | ✓ |

in the powder.

- The process of blending: The blending conditions were kept constant throughout the study.
- Low Pressure Cold Spray: The spray system used and the input parameters were kept constant throughout the investigation.
- The same substrate material was used in all depositions.

### Variable of the Experiment

- The ceramic content of the feedstock powders was varied. Eleven different composition were used $Al_2O_{3x} - Al_{(1-x)} (x_{wt} = 0,\ 0.1,\ 0.2,\ 0.3,\ 0.4,\ 0.5,\ 0.6,\ 0.7,\ 0.8,\ 0.9,\ 1)$

### Expected Results

- As the ceramic content increases in the feedstock powder, it was expected that the deposition efficiency increases to a maximum, and then decreases until obtaining erosion of the substrate.
- The erosion rate of the coating was assessed based on the powder flow rate along with the gain/loss of mass measurement of the substrate.
- With the EDS of powders and coatings was possible to explore the ceramic content of powders vs. the ceramic content of the coatings. This determines the percentage of ceramic particles that get embedded and the percentage that rebound during the deposition process.

- Etched analysis of powder and coatings determined if any structural changes occur in the powder during deposition at the grain level and the influence of ceramic content in this change.
- Adhesion strength of the coatings gave insight on the influence of ceramic particles on the substrate-coating interface during deposition.
- Porosity, hardness, and wear rate results gave a notion of the mechanical properties of the coating, and the influence of the ceramic content on these properties. It was expected that as the amount of ceramic increases in the coating, the hardness increases as well as the wear resistance.
- Single particle impacts (Wipe test) helped to elucidate the mechanism of the deposition of the blended powder, specifically the phenomenon of DE increment.
- Finally, the analysis of non-consolidated powders provided a good notion of the process required for the adhesion or embedment of metallic or ceramic powders respectively.

### 4.1.2 Effect of Ceramic Morphology in a Ceramic-Metal blending on the Cold Spray Deposition Process

For the study of the effect of morphology of the ceramic in blended ceramic-metal powders, the same ceramic material used in the previous section was procured with spherical morphology, the availability of the ceramic in this two morphologies was key in selecting the ceramic material to be used. This powder was characterized, blended and sprayed under the same conditions as the previous section to ensure a consistent comparison.

**Constants of the Experiment**

- Powder blended: Same aluminum powder as the previous section was used. Plasma spherodized $Al_2O_3$ powder was procured.
- The process of blending: The blending conditions were kept constant throughout the study.
- Low Pressure Cold Spray: The cold spray system used and the input parameters were kept constant throughout the investigation.
- The same substrate material was used in all experiments.

**Variable of the Experiment**

- The composition of spherical ceramic on the feedstock powder was varied in six different compositions $Al_2O_{3x} - Al_{(1-x)}(x_{wt} = 0,\ 0.2,\ 0.4,\ 0.6,\ 0.8,\ 1)$.
- The composition of crushed ceramic on the feedstock powder was varied in six different compositions $Al_2O_{3x} - Al_{(1-x)}(x_{wt} = 0,\ 0.2,\ 0.4,\ 0.6,\ 0.8,\ 1)$(These results were extracted from the previous section).

**Expected results**

- As the amount of ceramic content increases in the feedstock powder, it was expected that the deposition efficiency increases to a maximum and then decrease until obtaining erosion of the substrate. It was expected that the increment in DE with spherical ceramic to be lower than with crushed ceramic.
- EDS and contrast image analysis provided data to plot ceramic content in the coatings vs the ceramic content in the feedstock powders. This plot was compared with the one obtained with crushed powder. It was expected to obtain a lower amount of embedded particles with the spherical ceramic.
- In coatings sprayed with spherical ceramic, it was expected have higher deformation of the ductile metal that the ones sprayed with crushed ceramic. Hardness analysis helped to provide an insight of the amount of cold work in the coating.
- Comparison between adhesion strength between coatings sprayed with both ceramic morphologies gave a notion of the influence of the shape of the ceramic in the substrate-coating interfaces.
- Mechanical testing showed the influence of the morphology of the ceramic on the properties of the coatings. For the same ceramic composition in the coatings, it was expected that the coatings with spherical ceramic particles would have higher hardness and similar wear resistance than the crushed ceramic particles.
- Wipe test analysis helped to understand the increase in DE with the addition of ceramic particles into the feedstock powder and the influence of the ceramic particle morphology on this

phenomenon.

### 4.1.3 Effect of Cermet Powder Morphology on the Deposition Cold Spray Deposition Process

To study the effect of the cermet feedstock powder morphology on the deposition of cold spray coatings, different cermet powders were procured, each produced by different processes. These powders were characterized following the steps presented in Table 4.2. Coatings were sprayed and also characterized following this Table.

Table 4.2: Summary of analysis techniques for powders, coatings, wipe tests and Spray.

| Analysis Techniques | Powders | Coating | Wipe Test | Spray |
|---|---|---|---|---|
| SEM Topology | | ✓ | ✓ | |
| SEM Morphology | ✓ | | | |
| SEM Cross section | ✓ | ✓ | ✓ | |
| EDS | ✓ | ✓ | | |
| Micro Hardness | | ✓ | | |
| Adhesion test | | ✓ | | |
| Particle Velocity | | | | ✓ |
| Deposition efficiency | | | | ✓ |
| Gain/loss weight | | | | ✓ |
| FEA | | | | ✓ |

**Constants of the Experiment**

- Low Pressure cold spray were used and the input parameters were kept constant in all the sprays.
- The substrates material to be used in the study was kept constant.

**Variable of the Experiment**

- Four morphologies of powders were used: a blended powder, two different agglomerated and sintered powders, and a atomized powder.
- composition used in the experiment may vary depending of the provider.

**Expected Results**

- It was expected that varying the morphology of the cermet powders result in a different ceramic retention in the coatings. In particular, the more consolidated (densified) the cermet, the closer to the original composition was expected to be found in the coatings.
- It was expected that changing the morphology of the cermet powders affects the DE of the process. In particular, the more consolidated (densified) the cermet, the lower the DE obtained.
- Mechanical testing was expected to show the influence of the cermet morphology on the mechanical properties of the coating.
- SEM analysis were expected show the influence of the original structure of the powder in the consolidated coatings.
- Particle velocity analysis gave some insights into the influence of the morphology of the particles in the velocity achieved in the nozzle.
- SEM analysis of powder, recovered powder, and Wipe test gave insights in the deposition mechanism of each of the different morphology of the cermet.
- FEA of the powders and wipe test was expected to give some insight in the deposition behaviour of the powders.

### 4.1.4 Consolidation of Cermet Coating by Cold Spray for an Engineering Application

Finally to validate cold spray as a suitable process to produce high performance cermet coatings, a specific engineering application was selected. Based on the studies performed a feedstock powder composition and a morphology was chosen. Sets of coatings were sprayed and tested under a strict engineering testing plan. The engineering application selected is the replacement and repair of Chrome plating steel. The testing plan used allowed to validate the coating under requirements needed in the aerospace industry and is detailed in the following sections. The feedstock powder composition and morphology was selected based in the previous results, as well as the parameters used to deposit the coating.

## 4.2 Equipment and Sample Preparation

### 4.2.1 Low Pressure Cold Spray

The commercially available SST Series EP Cold Spray system built by CenterLine SST (Canada) was used for this study. The maximum operational pressure is 3.45 $MPa$ and the maximum temperature 500 $°C$.

#### System description

The system consists of a safety cabinet, a control system, a filtration system (Figure 4.1a), a gas heater, a nozzle, an XY robot and an optional powder heater (Figure 4.1b). The bulk gas is connected to the control system where the pressure is regulated. The gas then travels to the heater mounted on the robot inside the safety cabinet. The temperature is digitally controlled by the electronics in the control system; the temperature control is based on a PID controller with feedback coming from a thermocouple in the inlet of the nozzle and regulated trough a PWM. The powder is injected at the nozzle location after the throat. The deposition process happens in the safety cabinet and the excess of powder goes through a water filter. This avoids contamination into the environment and protects the user from possibly hazardous powders. The movement of the nozzle is driven by the XY Robot and controlled by an external computer. This allows the user to program different nozzle paths.

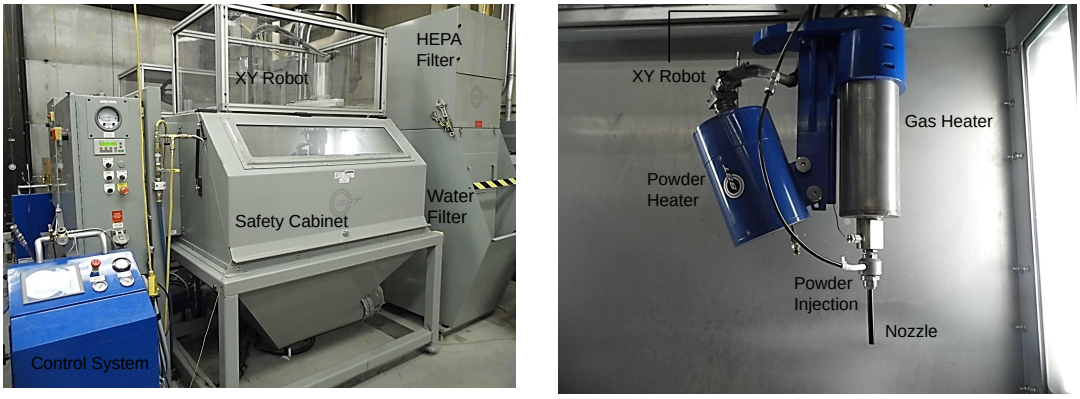


(a) (b)

Figure 4.1: Overview of EP-LPCS Centreline Canada SST division.

**Powder Feeding**

The powder injection was done using a volumetric rotatory powder feeder (Thermach AT-1200). In this feeder the amount of powder is controlled by a perforated wheel rotating at a constant angular velocity. The powder rests in the canister on the wheel and fills the perforations as the wheel turns. The powder is then pushed by a stream of gas (the flow rate of this gas is also controlled). The fluidized powder travels to the nozzle injection point where the powder is fed. The EP-series system also allows for an optional preheat of the powder. In this powder heater, the powder travels through a coiled stainless steel tube wrapped with an electrical heater, the temperature of this heater is controlled by the main control system getting feedback by two thermocouples located between the coiled tube and the heater.

### 4.2.2 Sample Preparation for Optical and SEM Analysis

The sample preparation used for optical microscopy and for SEM is a standard preparation for metallurgical samples. The specimen was cut into several sections, with a precision wet saw SECOTOM-10 Struers. The cut specimen or powder was then mounted in Bakelite in a mounting press LABOPRESS-3 Struers. This machine allows the control of the heating and cooling times, temperatures and pressure. Finally, the mounted sample was polished under several steps in a TEGRAPOL-31 polishing machine. This machine allows to polish six samples at the time. For SEM analysis, the sample went through a sputtering process that covers the sample with a thin layer of gold to make the surface conductive. The equipment used for this purpose is a Denton Vacuum Desk IV. Once the sample was sputtered, the top surface was electrically connected to the bottom by a copper tape which allows for the discharge of electron during the SEM analysis.

### 4.2.3 Scanning Electron Microscope

The SEM used was a Zeiss EVO-10MA. The machine is powered by a $LaB_6$ electron source, has a maximum acceleration voltage of 30 $kV$ and a theoretical maximum resolution of 2 $nm$ point to point. The equipment has secondary and backscatter electron detectors. It is also equipped with capabilities for backscatter electron diffraction (EBSD) with a NordLYS HKL-Technologies from Oxford Instruments. It also has an X-ray detector Energy Dispersive X-Ray Spectrometry (EDS) INCA X-Act also from Oxford Instruments and with X-ray microtomography capabilities with a

SkyScan Micro-CT system.

### 4.2.4 X-ray Diffraction

For X-ray diffraction, an Philips X-Pert PW 1830 diffractometer was used. The equipment operates with wavelength of Cu-k alpha ($\lambda = 0.15406\,nm$), the measurement were taken at an step of $0.02^\circ/s$, between $20^\circ$ to $80^\circ$. The phases were detected with the database PDF4 installed in the software *Jade*. The equipment is designed to work with powders and flat polycrystalline samples, therefore the sample preparation method for coating consisted of simply polishing the surface of the coating, to obtain a flat surface.

### 4.2.5 Hardness

The hardness equipment used in this study was Duramin-10 Struers equipped with a Vickers indenter. The equipment allows the user to vary the load from 0.05 $kgf$ to 2 $kgf$. The indentation time can be set in the machine. The load values used in this study are: 0.1 $kgf$, for soft materials, 0.3 $kgf$ and 0.5 $kgf$ for hard materials. The loading time was set at 10 $s$. To obtain a reliable value of hardness a minimum of five test were done.

### 4.2.6 Particle Size Distribution

The particle size distribution was analyzed using laser diffraction instruments (Microtrac particle size analyzer S3500, Nikkiso, Japan). The proceadure is as follows, a sample of the powder is first left for 12 *hrs* in a solution for deagglomeration of the particles. The samples are then vibrated and mixed in an aqueous solution in the delivery controller. This solution was directed to the dynamic image analyzer. The software Microtrac FLEX was used to retrieve the data.

### 4.2.7 Optical Microscopy

Optical microscopy was used for overall assessment of the coatings. The microscope used was VHX-2000 from Keyence. The apparatus has an automated XY stage, and gives a magnification up to 1000X through a digital camera. A computer controls the stage and the focus. The built-in software allows to autofocus, stitching images, compose fully-focus 2D images at different depths. It also can produce 3D imaging by focus depth composition. These capabilities became very useful

to extract topology of samples and compute roughness that are too high to be measured with regular roughness testers. Porosity values were processed using the software *ImageJ* and computed by contrast areas.

### 4.2.8 Adhesion Strength

To evaluate the adhesion strength of the coatings, the ASTM-633C standard was followed. The deposition was done on $1''$ diameter cylindrical coupons with a length of $1.5''$ . The coatings were machined down to a thickness of 380 $\mu m$. The coatings then were glued to a counter coupon using FM-1000 glue. The glue was cured at $190°C$ for 1 hour. Finally the glued coupons were pulled in a universal testing machine Instron Model 4202 at a rate of 0.02 $mm/min$. The force needed to separate the coupons is obtained from the machine load cell. The load then can be used to calculate either the adhesion value (if the coating failed in the interface) or the cohesion value (if the coating failed internally). In order to obtain a reliable value of strength and its dispersion, a minimum of three coupons were tested per condition.

### 4.2.9 Wear Test

To quantify the wear resistance of the coatings the ASTM G133-05 standard was followed. The equipment consists of a rail where the samples are positioned. A $3/16''$ alumina ball slides on top of the sample with a load applied of 25 $N$. The sliding length is 10 $mm$ at a velocity of 10 $mm/s$. The wear test was measured by calculating the volume loss of the trace at a specific travel distance of the alumina ball. The voulme was calculated by optical 3d imaging by depth composition. In addition, the wear trace was analyzed by SEM to evaluate the wear behavior of the material.

### 4.2.10 Particle Velocity Measurement

The in-flight particle velocity were measured with the equipment DPV-2000 from Tecnar Automation Ltd, St-Bruno, Quebec, Canada. The system illuminates the particles in flight with a laser and captures the reflection with a light sensor. The sensor is covered with a two slits mask with a precise distance between these slits. The velocity of the particles is computed with this distance and the time within the two light peaks sensed by the detector. The detector head was positioned at the same standoff distance used during the deposition. The flow of powder was reduced in order to

make the measurements.

### 4.2.11 Deposition Efficiency Measurement

In order to compute the deposition efficiency of the spray, the feed rate of powder injected into the nozzle was measured. This measurement was done weighing the powder injected in the nozzle for a specific amount of time. This was compared with the weight gain of the substrate due to the coating. A ratio was calculated for weight gain over the weight of powder fed, to give the deposition efficiency.

### 4.2.12 Other Relevant tools and Equipment

#### Precision Balance

In order to calculate the deposition efficiency or the gain/loss of weight of a sample, a Sartorius Extend - model ED124S precision balance was used. This balance has a resolution of 100 $\mu g$.

#### Roughness Meter

To measure surface roughness a stylus tester Phase II SRG-4000 was used. The machine has a 5 $\mu m$ diamond tip at 90°. It have a range up to 80 $\mu m$ in height, a tracing length of 1.3 $mm$ and a display resolution of 0.001 $\mu m$. The machine is capable to give values of Ra, Rz, Rq and Rt. For the study the measurement were taken a minimum of three times in order to obtain a reliable value.

#### Finite Element Analysis

To perform the FEA simulation of impacting particles the commercial software Abaqus/Explicit version 6.12 was used. The morphology of the particles was digitized with the software *ImageJ* and a software developed in the open-source Simple Morphological Image Library (SMIL) software. The data points were then exported using a Python-Abaqus script into a sketch to proceed with the simulation. Any particular inconsistency in the sketch creation process was fixed manually.

## 4.3 Feedstock Materials and Experimental Procedure

### 4.3.1 Effect of Ceramic Content in a Ceramic-Metal Blending on the Cold Spray Deposition Process

Aluminum is a material that has been widely studied using cold spray due to its importance in engineering applications and its low melting point. This makes it appropriate to understand the full range of possibilities that Cold spray have to offer. Alumina ($Al_2O_3$) is known by its high hardness, stability, and abrasion resistance. It makes it suitable as abrasive materials or to produce cutting tools and can be found in angular and spherical morphology. In cold spray, these properties can be exploited to ease the understanding of the effect on the deposition of a hard ceramic particle blended with a soft ductile phase. Powders with an appropriate particle size for cold spray ($10\ \mu m - 50\ \mu m$) were procured. Once received, the powders were characterized using microscopy and particle sizes distribution analysis.

**Materials**

- **Ductile metallic powder:** Atomized aluminum powder AA5001 - Centerline. Figure 4.2a.
- **Ceramic powder:** Crushed Al2O3 G0001 - Centerline. Figure 4.2b.
- **Substrate:** Al6061-T6 bar $1'' \times 1/4''$ and $1''$Adhesion strength coupons Al6061-T6.

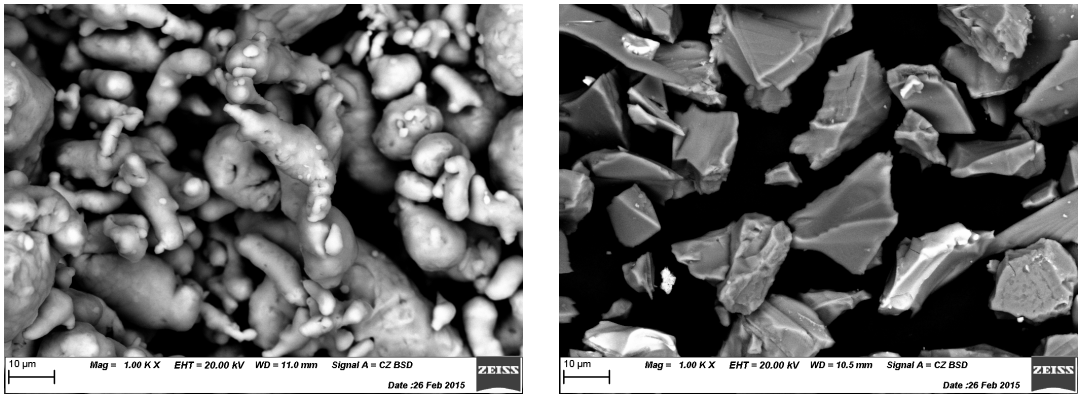


(a) (b)

Figure 4.2: Overview of powder used in current experiment, a) Atomized aluminum powder AA5001 - Centreline, b) Crushed alumina powder Al2O3 G0001 - Centerline.

### Blending Conditions and Composition

To obtain the sprayed blendings, the powder was weighed with a high precision scale, then it was placed in a container and was mechanically blended until a homogeneous mixture was obtained. Table 4.3 summarize the partial weight used for the different blendings.

Table 4.3: Partial Weight Composition to Blend $Al - Al_2O_3$.

| **Code Name** | $Al$ **wt %** | $Al_2O_3$ **wt%** | $Al$ $g$ | $Al_2O_3$ $g$ | **Total weight** $g$ |
|---|---|---|---|---|---|
| 01-Blend-10-00 | 100 | 0 | 200 | 0 | 200 |
| 01-Blend-09-01 | 90 | 10 | 180 | 20 | 200 |
| 01-Blend-08-02 | 80 | 20 | 160 | 40 | 200 |
| 01-Blend-07-03 | 70 | 30 | 140 | 60 | 200 |
| 01-Blend-06-04 | 60 | 40 | 120 | 80 | 200 |
| 01-Blend-05-05 | 50 | 50 | 100 | 100 | 200 |
| 01-Blend-04-06 | 40 | 60 | 80 | 120 | 200 |
| 01-Blend-03-07 | 30 | 70 | 60 | 140 | 200 |
| 01-Blend-08-02 | 20 | 80 | 40 | 160 | 200 |
| 01-Blend-09-01 | 10 | 90 | 20 | 180 | 200 |
| 01-Blend-00-10 | 0 | 100 | 0 | 200 | 200 |

### Spray Conditions

Table 4.4 summarize the spray condition used in this study.

Table 4.4: Spray Conditions for Spray of Blended $Al - Al_2O_3$

| **Parameter Selection** | **Value** |
|---|---|
| Powder | Blend |
| Gas Temperature | $300°C$ |
| Gas Pressure | 1.37 $MPa$(200 $psi$) |
| Gas Nature | Nitrogen |
| Standoff Distance | 10 $mm$ |
| Traverse Speed | 50 $mm/s$ |
| Step Size | 2 $mm$ |
| Number of Cycles | 1 |
| RPM Feeder | 8 $rpm$ |
| Feed Wheel Type | 240 holes |
| Powder Feeder Gas Flow Rate | 30 $SCFH$ |
| Powder Feeder Gas Nature | Nitrogen |
| Nozzle Type | Stainless Steel |
| Orifice Diameter | 2 $mm$ |

## 4.3.2 Effect of Ceramic Morphology in a Ceramic-Metal blending on the Cold Spray Deposition Process

As is was mentioned before, the metallic powders used in this part of the research were the same as the last section. This condition was compulsory for this study to link the results of the previous

section with this one. In this section, the effect of two different morphologies of ceramic powders are shown. The results obtained in the previous section was compared with depositions made with spherical $Al_2O_3$.

### Materials

- **Ductile metallic powder:** Atomized aluminum powder AA5001 - Centreline. Figure 4.3a.
- **Spherical Ceramic powder:** Plasma spheroidized alumina powder AL2O3-2N-45 Tekna Advances Materilas Inc. Figure 4.3b.
- **Substrate:** Al6061-T6 bar $1'' \times 1/4''$ and $1''$Adhesion strength coupons Al6061-T6.

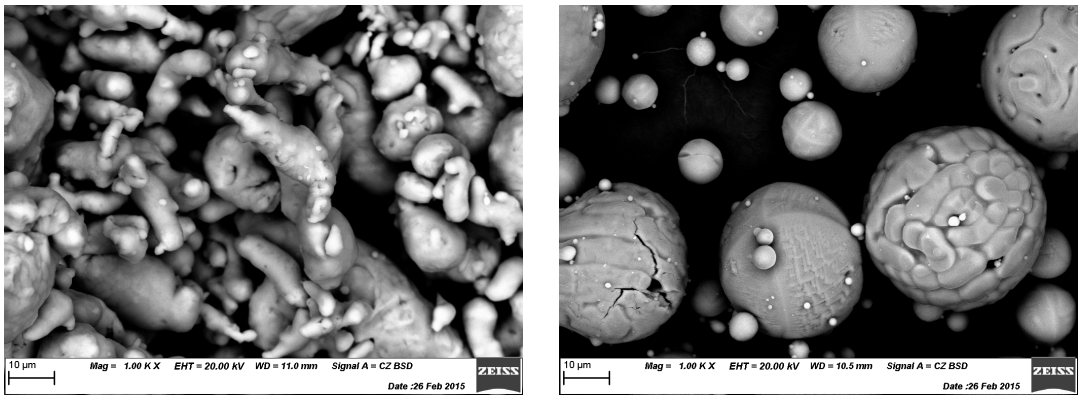


(a) (b)

Figure 4.3: Overview of powder used in current experiment, a) Atomized aluminum powder AA5001 - Centreline, b) Plasma spherodize alumina powder.

### Blending Conditions and Composition

As before, the blending process was achieved by weighing the powders and by mechanically blend them together. Table 4.5 summarize the partial weight used for the blending process.

Table 4.5: Partial Weight Composition Blended of $Al$ and Spherical $Al_2O_3$.

| **Code Name** | $Al$ **wt %** | $Al_2O_3$ **wt%** | $Al$ $g$ | $Al_2O_3$ $g$ | **Total weight** $g$ |
|---|---|---|---|---|---|
| 02-Blend-10-00 | 100 | 0 | 200 | 0 | 200 |
| 02-Blend-08-02 | 80 | 20 | 160 | 40 | 200 |
| 02-Blend-06-04 | 60 | 40 | 120 | 80 | 200 |
| 02-Blend-04-06 | 40 | 60 | 80 | 120 | 200 |
| 02-Blend-08-02 | 20 | 80 | 40 | 160 | 200 |
| 02-Blend-00-10 | 0 | 100 | 0 | 200 | 200 |

**Spray condition**

To obtain a comparison point with the study described previously, the spray conditions used in this section were the same as in Table 4.4.

### 4.3.3 Effect of Cermet Powder Morphology on the Deposition Cold Spray Deposition Process

For this section of the research, different morphologies of powders were selected. The ductile metallic phase used was $Ni-20Cr$, and the ceramic phase $Cr_3C_2$. $Ni-20Cr$ is a metal known for its high hardness, good corrosion resistance and its high melting point. This makes it a great candidate for several engineering application where high performance under harsh environments is required. In addition, $Cr_3C_2$ is a ceramic with outstanding hardness, is commonly mix with $Ni-20Cr$ to produce cermets. This mixture provides exceptional wear resistance. The composition used in this investigation are based in the commercially available compositions, which vary between $(Cr_3C_2)_{65}(Ni-20Cr)_{35}$ to $(Cr_3C_2)_{75}(Ni-20Cr)_{25}$

**Materials:**

- **Blended powder:**
  Sulzer Metco Diamalloy 3004 $(Cr_3C_2)_{75}(Ni-20Cr)_{25}$ Figure 4.4a.
- **Agglomerated and sintered powder 1:**
  HCStark Amperit 584 $(Cr_3C_2)_{75}(Ni-20Cr)_{25}$ Figure 4.4b.
- **Agglomerated and sintered powder 2:**
  Praxair CRC-300 $(Cr_3C_2)_{75}(Ni-20Cr)_{25}$ Figure 4.4c.
- **Atomizated powder:**
  Praxair CRC-410 $(Cr_3C_2)_{75}(Ni-20Cr)_{25}$ Figure 4.4d.
- **Substrate:**
  4140 Steel bar $1'' \times 1/4''$ and $1''$Adhesion strength coupons 4140 Steel bar.

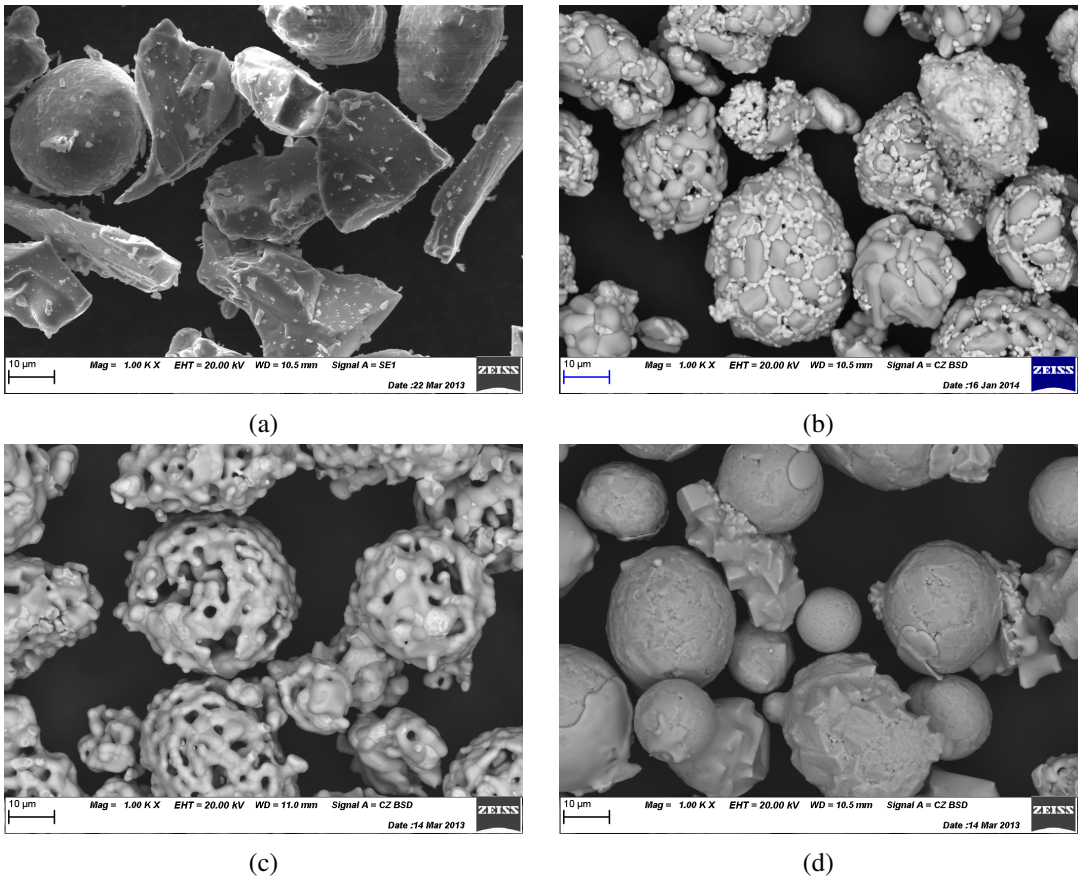


Figure 4.4: Overview of powder to used in current experiment, (a)Sulzer Metco Diamalloy 3004, (b)HCStark Amperit 584, (c)Praxair CRC-300, (d)Praxair CRC-410.

## Spray condition

Table 4.6 summarize the spray condition used in this study.

Table 4.6: Spray Conditions for $(Cr_3C_2)-(Ni-20Cr)$

| Parameter Selection | Value |
|---|---|
| Powder | Variable |
| Gas Temperature | $500^{\circ}C$ |
| Gas Pressure | 3.44 $MPa$(500 $psi$) |
| Gas Nature | Nitrogen |
| Standoff Distance | 10 $mm$ |
| Traverse Speed | 5 $mm/s$ |
| Step Size | 2 $mm$ |
| Number of Cycles | 3 |
| RPM Feeder | 5 $rpm$ |
| Feed Wheel Type | 240 holes |
| Powder Feeder Gas Flow Rate | 30 $SCFH$ |
| Powder Feeder Gas Nature | Nitrogen |
| Nozzle Type | UltiLife Nozzle |
| Orifice Diameter | 2 $mm$ |

### 4.3.4 Consolidation of Cermet Coating by Cold Spray for an Engineering Application

As it was discussed, the importance of hard chromium coatings replacement has increased due to the highly toxic hexavalent chromium salts. These hard coatings are heavily used in aerospace applications for their corrosion resistance as well as their low wear rate. These coatings can be found in gears, turbine engines and landing gears. Some promising alternatives have been researched, HVOF WC-Cr-Co and electroless Nickel being the most promising option in wear and corrosion resistance respectively. In addition, once the hard chromium coating is damaged it cannot be repaired. This inconvenience is also present in coating produced by WC-Co-Cr HVOF and electroless nickel. Needless to say, the focus of this section was testing a cermet coating under a strict qualification plan for hard chromium replacing and repair.

#### Materials and Spray Conditions

Due to the hardness of $Cr_3C_2 - Ni20Cr$ powder and by the experience obtained with the mixtures, the most promising coating obtained in the last section was used to performed the test for replacement and repair of hard chromium coating. Also the condition of spray found in the last section were also used

#### Test Plan

The testing plan focuses not only on the replacement and repair of hard chromium coating but also its alternatives such as HVOF and electroless nickel. The qualification plan and materials were selected in order to meet the requirement of the aerospace industry. The plan consist of the following tests:

#### Adhesion and Metallurgy

Porosity, roughness and micro-hardness of base material and repairs were measured. Coatings had to meet the standard DPS 9.89 or MIL-STD-865C. These tests were performed on $1'' \times 6'' \times 0.25''$ samples of bare steel and damaged materials (chromed plated steel, HVOF coated steel, and nickel plated steel). The principal requirement were:

- Hardness of at least 700 Hv.
- Porosity values of less than 1%.
- The Strip rupture testing were performed and inspected for evidence of peeling and flaking of the coating.

To facilitate the bending process on 0.25" steels in the strip to rupture test, a V-notch were machined on the back.

**Corrosion**

Corrosion test was performed following ASTM B117-16 standard. Cold sprayed coatings and repair performances were compared with an electroless Ni plate as control. These tests were performed on $4'' \times 6'' \times 0.25''$ samples of damaged materials (chromed plated steel, HVOF coated steel and nickel plated steel). Three sample of each were tested for 168, 336, 504, and 672 hours.

**Fluid Immersion**

Fluid immersion tests were performed using a modified version of ASTM F483, The fluid immersion test measures the compatibility for cold spray coatings and Ni brushing coatings, with two selected aircraft maintenance chemicals. Visual inspection of the samples were done after an exposure of 24 and 168 hours. Any differences were recorded between the exposed and unexposed specimen with regard to staining, discoloration, corrosion, pitting, blistering, peeling, flaking or any other surface condition. The cold spray repair performance were compared with an electroless Ni plate baseline. These tests were performed on $1'' \times 6'' \times 0.25$ in samples of bare steel and damage materials (chromed plated steel, HVOF coated steel and nickel plated steel).

# Chapter 5

# Results and Discussion

The results presented in this chapter are structured in the form of four different self-contained investigations. Each investigation addresses one of the main research objectives described in Chapter 3. Each section is written as a research article and have been or will be submitted as four peer-reviewed journal papers. This presentation should allow the reader to easily follow the experimental methodology and to quickly understand the results and conclusion obtained from each investigation as well to a fast link with the references needed.

## 5.1 Cold Spray Aluminum-Alumina Cermet Coatings: Effect of Alumina Content

This section address the first research objective "Study the effect of ceramic content in a ceramic-metal blending on the cold spray deposition process". The investigation discusses in depth the effects of ceramic content on the deposition efficiency of metal-ceramic mixtures. An experiment was designed to isolate the various potential mechanisms proposed in the literature. FEA simulations, as well as a probabilistic analysis were used to dismiss one of the effects proposed (peening effect). Both of the other two effects were shown to have a major role in increasing the deposition efficiency of the aluminum particles. A novel test was designed to assess the effect of the asperities created by the ceramic particles while eliminating the effect of oxide removal. The erosion rate of the aluminum coating by the ceramic particles was assessed, and it was determined that all feedstock powder compositions were not in a state of erosion. The ceramic retention in the coatings

was assessed by EDS and showed that the coatings have nearly half of the ceramic content of the feedstock powder. Some mechanical properties of the coatings were also tested. Tests showed an increase of the coating hardness with the coating alumina content. Adhesion strength also showed a steady improvement with increasing alumina content in the feedstock powder, reaching the upper limit of the test with coatings sprayed with the highest alumina content.

# Cold Spray Aluminum-Alumina Cermet Coatings: Effect of Alumina Content.

Ruben Fernandez, Bertrand Jodoin

University of Ottawa Cold Spray Research Laboratory, Ottawa, ON, Canada.

## Abstract

Deposition behavior and deposition efficiency were investigated for several aluminum-alumina mixture compositions sprayed by cold spray. An increase in deposition efficiency was observed. Three theories postulated in the literature, explaining this increase in deposition efficiency, were investigated and assessed. The interaction between a ceramic particle peening an aluminum particle at the impact time of the latter was found through finite element analysis to be a possible mechanism to increase the deposition efficiency of aluminum particles, but a probability analysis demonstrated that this peening event is too unlikely to contribute to the increment in deposition efficiency observed. The presence of asperities at the substrate and deposited layers was confirmed by a single-layer deposition efficiency measurement and proven to be a major mechanism in the increment of deposition efficiency of the studied mixtures. Finally, oxide removal produced by the impact of ceramic particles on substrate and deposited layers was evaluated as the complement of the other effects and found to also play a major role in increasing the deposition efficiency. It was found that the coatings retained approximately half of the feedstock powder alumina content. Hardness tests have shown a steady increase with the coating alumina content. Dry wear tests have revealed no improvement in wear resistance in samples with an alumina content lower than 22wt.% compared to pure aluminum coatings. Adhesion strength showed a steady improvement with increasing alumina content in the feedstock powder from 18.5 MPa for pure aluminum coatings to values above 70 MPa for the ones sprayed with the highest feedstock powder alumina content.

*Keywords: Deposition Efficiency, Cermet, Aluminum-Alumina, Cold Spray.*

## Introduction

Ceramic-metal composites, most commonly known as cermets, are composites materials made of ceramics and metals. Cermets are designed to retain the optimal properties of its components, such as ductility and toughness of metals, along with the hardness and wear resistance of ceramics [1–4]. Typical production methods used to consolidate cermets include compaction and sintering, hot

extrusion, and infiltration [2, 4]. Thermal spray processes have also been used for the production of cermet materials by spray deposition. A recent proposed alternative is the deposition by cold gas dynamic spraying, more often referred to as cold spray. The cold spray process accelerates feedstock powders (usually metals) using a supersonic gas stream generated by a De Laval-type nozzle [5–7]. Due to the relatively low gas temperatures resulting from the rapid gas expansion in the nozzle, the feedstock powders remain solid throughout their flight [8–10]. When the particles impact the substrate, they experience extensive plastic deformation [8, 11]. These particles adhere to the substrate either by mechanical anchoring or, if enough plastic deformation is obtained, by metallurgical bonding [5, 8, 12–15]. To cold spray cermets, reinforcement particles are mixed with ductile metallic feedstock powders. During deposition, a fraction of the reinforcement particles is retained into the final coating [16–19]. Hard reinforcement particles do not experience severe plastic deformation such as the ones observed in the ductile materials, but rather induce more plastic deformation of the ductile phase [16, 17]. These particles adhere to the coating, normally by embedding themselves in the coating producing the cermet [19, 20].

Several ceramic-metal combinations have been successfully deposited by cold spray with a variety of powder morphologies[16, 17, 21–25]. The applications and sought coating properties closely resemble the ones seen in other thermal spray processes, principally wear resistance, high hardness, and high temperature applications. The inclusion of ceramic particles is the main cause of improvement of these properties when compared with the ductile metallic phase. The addition of ceramic particles does not just affect the coating properties but also has a substantial effect on the deposition process behavior. Even though the deposition of ceramic-metal mixtures has been extensively studied in cold spray and the properties and deposition behavior have been established, most of these studies have been exploratory and have used a descriptive approach with a focus on industrial applications [18, 26–28]. A few studies have been performed with the purpose of explaining the behavior observed and a few theories have been proposed to account for the effect of ceramic particles in the feedstock powder [16, 17, 19, 26, 29–31].

One of the most dramatic changes in deposition behavior observed with the addition of ceramic particles to ductile feedstock powder is the increase in deposition efficiency (DE). This behavior was first reported in a study where mixtures of Al-$Al_2O_3$ at different weight ratios were deposited [19]. They noticed an increase in DE with the addition of $Al_2O_3$ particles with a peak at 30 wt.% $Al_2O_3$ and a decrease of DE at higher feedstock powder ceramic contents, eventually reaching 0% DE at 95 wt.% ceramic. Several other investigations have shown similar trends in deposition efficiency [16, 29].

This increase in DE was not initially expected, as the cold spray of ceramics only leads to substrate erosion [32, 33]. Another study used the coating ceramic content to compute the partial deposition efficiency of both the metallic and ceramic particles [16]. This showed that the DE increase could not be solely attributed to ceramic particles embedding into the coating, but rather to an interaction between the ceramic and the metallic powder particles, with the DE of the aluminum particles increasing with the addition of ceramic particles into the feedstock powder [16]. Consequently, aluminum particles have an increased probability to adhere to the substrate when they are in the presence of ceramic particles. This increase in partial DE of aluminum is observed up to high wt.% of ceramic in the feedstock powder. Therefore, the decrease in the overall DE at higher wt%. of ceramic is the result of the low DE of ceramic particles, and its influence gets more relevant as its weight contribution in the feedstock powder increases.

Investigations have provided some explanations for the observed DE increase with the addition of ceramic particles into the feedstock powder. The peening or impingement effect was described in one study, in which they sprayed different metals and ceramics [31]. They proposed that a hard ceramic particle acts as shot balls, peening the soft particles in front of it, increasing its deformation, and as a consequence, increasing the softer metallic particles deposition efficiency. This proposed mechanism has been mentioned in other investigations but has never been verified [18, 29].

Another mechanism was proposed in two separate studies [16],[19]. In their investigations, it was observed that the interface between the coating and substrate roughens as the percentage of ceramic in the feedstock mixture increases. This increase in roughness is expected due to the grit blasting effect of the impacting alumina particles onto the substrate. At a higher ceramic percentage in the mixture, more alumina particles blast the substrate/coating. It was suggested that these asperities are helping bonding more particles, increasing the deposition efficiency of the mixture due to a higher probability of obtaining mechanical anchoring [16]. This potential mechanism has been used as an explanation in other investigations as a possible mechanism but has never been verified [17, 21].

Finally, the last potential mechanism suggested in the literature is referred to as the oxide cleaning effect of ceramic particles impacting the metallic particles/substrate. This explanation describes the ceramic particles deforming and removing the native oxide film of the metallic particles/substrate upon impact, exposing new fresh metal surfaces and leaving them ready for the impact of the next metallic particle for the creation of a favorable metallurgical bonding site. This effect might also be achieved by pure deformation, as the oxide layer is brittle and may crack leaving oxide free

locations that could lead to the increase of DE observed [34]. This effect has been described before in cold spray, but it has not been proven to be the responsible in increasing the DE [9, 35, 36]. These three mechanisms potentially explaining the increase in DE are illustrated in Figure 1.

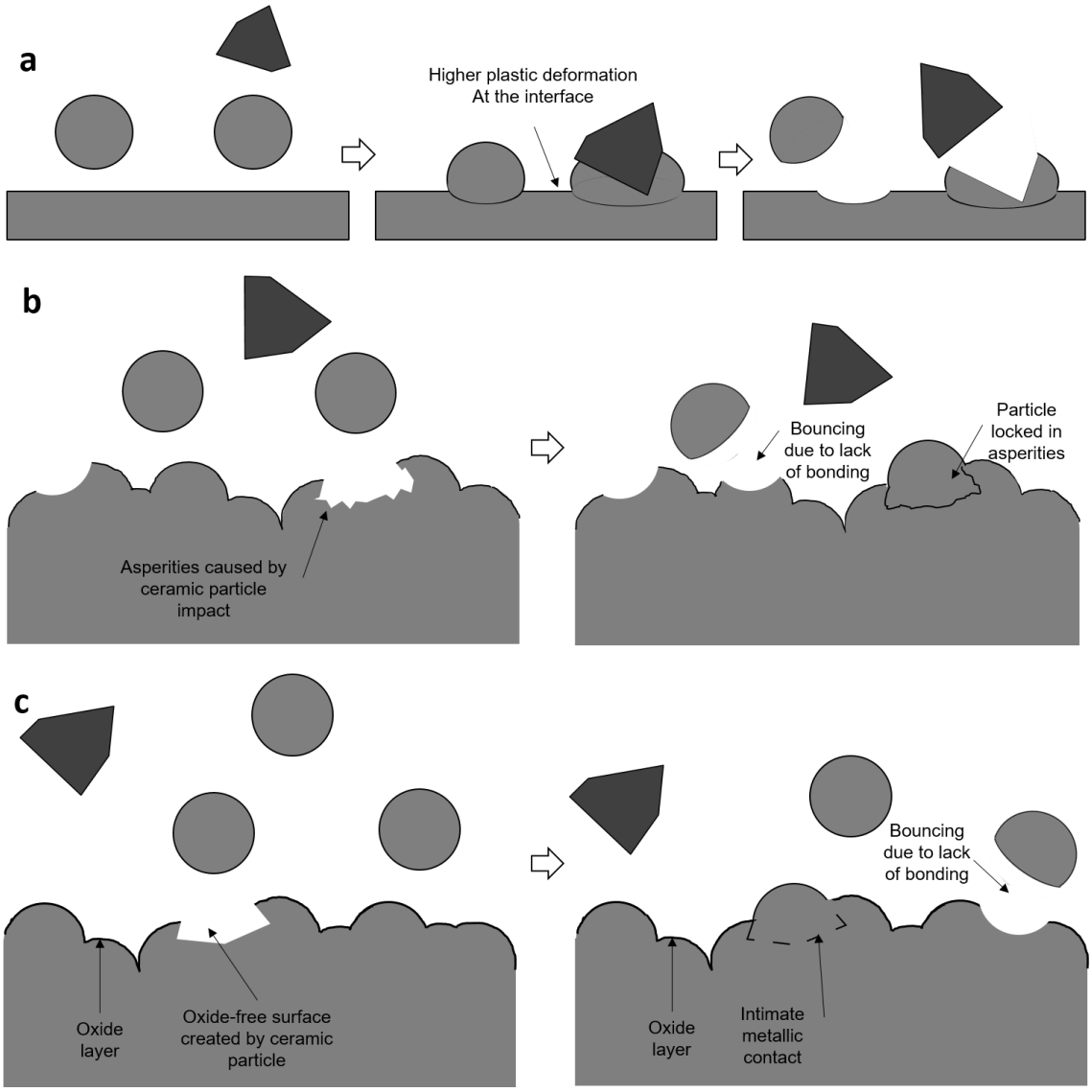


*Figure 1:Three mechanisms proposed in the literature for the DE increase in metal-ceramic mixtures: a) Metallic particles adhere due to peening of ceramic particles upon impact; b) Metallic particles adhere mechanically due to the asperities created by previous ceramic particle impacts; c) Metallic particles adhere to oxide-free surfaces cleaned by previous ceramic particle impacts.*

Another important point to take into account when ceramic particles are added to the feedstock powder is that erosion might occur to the substrate/metallic particles. Erosion by solid particles has been extensively studied [20, 32, 33, 37]. They described the different steps of erosion caused by hard angular particles impacting and cutting on a metallic surface. As explained, the process starts with a combination of embedment of the ceramic particles in the metal and cutting of the metal by the ceramic particles. Initially, the rate of embedment is higher than the rate of cutting, leading to a mass gain. This is followed by a saturation of the surface by the embedding particles. Then, the impacts break some of the superficial ceramic stabilizing its content; at this point, the embedment rate reaches zero, and the cutting rate leads to a mass loss in the entire substrate. Figure 2 shows an extract of the investigation, showing surface mass change caused by the impacting ceramic particles at different speeds.

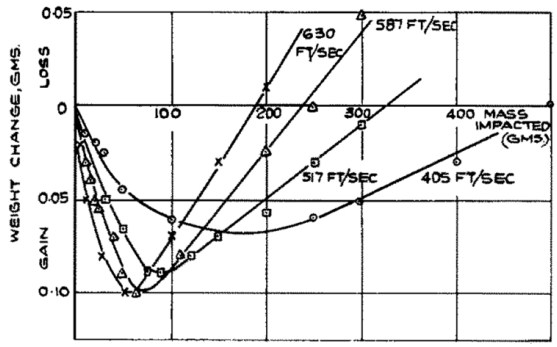


*Figure 2: Weight change for aluminum plates vs. mass impacted grit [33].*

In these studies, the substrate is impacted solely by ceramic particles while in the case of cold spray, the substrate is bombarded by a combination of both, metallic and ceramic particles. While the ceramic particles initially embed and eventually act towards erosion, the metallic particles that adhere will build a coating renewing the surface by a new non-eroded surface. Therefore, depending on the DE and the ceramic/metal ratio of the powder mixture, it is possible that the erosion state is never reached.

The focus of the present study was to verify and asses the fundamental mechanisms responsible for the increment in DE seen by the addition of ceramic particles in the feedstock powder. Commercially, pure aluminum and alumina were mixed and the influence of $Al_2O_3$ content on the DE was measured. The three potential mechanisms proposed in the literature for the increase of DE with the addition of ceramic particles investigated were: (i) the interaction between ceramic and

the metallic particles upon impact, (ii) the effect of the asperities created by the ceramic particle impacts, and (iii) the effect of the oxide removal from the substrate. The effect of the interaction between ceramic and metal upon impact was analyzed by finite element analysis combined with a probabilistic analysis. For the effect of the asperities, the DE of a single layer of aluminum particles was. Finally, the effect of the oxide cleaning was evaluated as the complement of the other two effects.

# Experimental Procedures

## Materials and mixtures

Commercially available pure aluminum powder (SST-A5001) (Centerline (Windsor) Ltd. Windsor, Ontario, Canada) was used. This is a gas atomized powder with an irregular shape, as seen in Figure 3 (a).

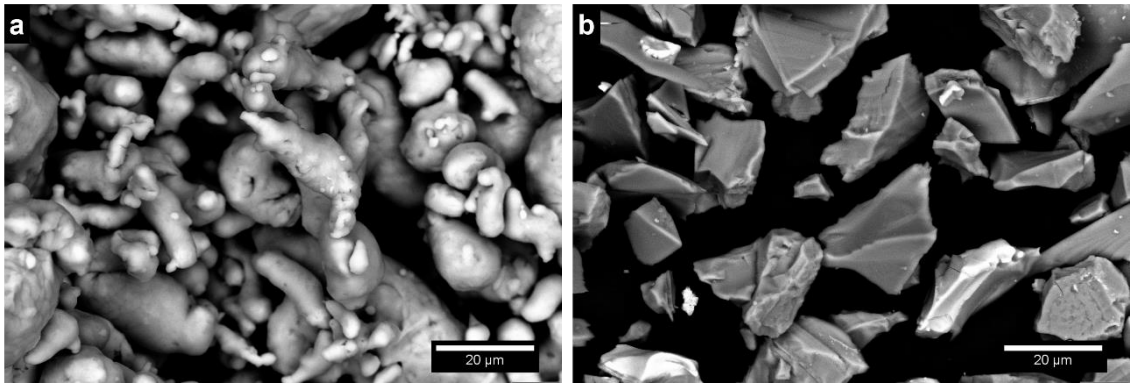


*Figure 3: Overview of feedstock particles used : (a) Aluminum particles (b) Alumina particles.*

Figure 4 (a) presents the particle size distribution of this powder (measured using a Microtrac Particle Size Analyzer S3500, Nikkiso, Japan), revealing an average particle size of 26 µm. The ceramic powder utilized for this investigation was alumina powder (G-0001), also from Centerline. Morphology and particle size distribution of this powder can be found in Figure 3 (b) and Figure 4 (b) respectively. The alumina particles are angular and the average particle size is 22 µm. In order to study the effect of different ceramic contents and influence on the deposition behavior during cold spray, a total of eleven aluminum-alumina mixtures were produced. Table 1 shows the samples designation name as well as the weight percentage and the volume proportion of each powder used in this investigation. The powders were weighed and mechanically blended for 10 minutes prior to deposition.

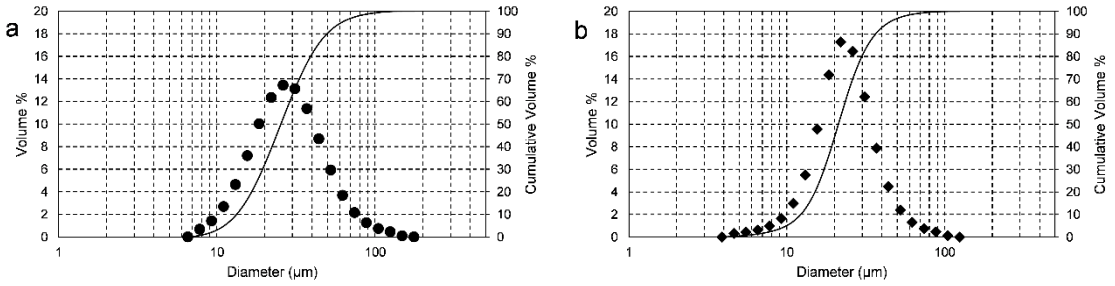


*Figure 4: Particle size distribution: (a) Aluminum particles; (b) Alumina particles*

*Table 1: Feedstock powder compositions*

| **Composition designation** | **Feedstock powder Al wt.%** | **Feedstock powder $Al_2O_3$ wt.%** | **Feedstock powder Al vol.%** | **Feedstock powder $Al_2O_3$ vol.%** |
|---|---|---|---|---|
| Al-00 | 100% | 0% | 100% | 0% |
| Al-01 | 90% | 10% | 93% | 7% |
| Al-02 | 80% | 20% | 85% | 15% |
| Al-03 | 70% | 30% | 77% | 23% |
| Al-04 | 60% | 40% | 69% | 31% |
| Al-05 | 50% | 50% | 59% | 41% |
| Al-06 | 40% | 60% | 49% | 51% |
| Al-07 | 30% | 70% | 39% | 61% |
| Al-08 | 20% | 80% | 27% | 73% |
| Al-09 | 10% | 90% | 14% | 86% |
| Al-10 | 0% | 100% | 0% | 100% |

## Cold Spray Deposition

The cold spray system used to produce the coatings for this work is the commercially available EP Series SST Low Pressure Cold Spray System (Centerline Ltd., Windsor, Ontario, Canada). The system consists of a 15 kW heater with a maximum gas temperature of 500°C and a maximum gas pressure of 3.8 MPa. The De Laval nozzle used for this work has a throat diameter of 2 mm and a diverging section length and exit diameter of 120 mm and 6.6 mm respectively. The mixed powder was fed using a commercially available rotatory powder feeder model AT-1200HP (Thermach Inc., Appleton, WI, USA). All coatings were sprayed using the spray parameters given in Table 2.

*Table 2: Cold spray parameters*

| Parameter | Value |
|---|---|
| Gas Temperature | 250 °C |
| Gas Pressure | 1.65 MPa |
| Gas Nature | Nitrogen |
| Traverse Speed | 20 mm/s |
| Passes | 3 |
| Feed Conditions | 320 holes wheel at 8 RPM |
| Standoff Distance | 15 mm |
| Substrate | Al-6061 |

## Coatings Characterization

The coatings produced with the different mixtures were characterized using several methods. Ceramic content measurements were done using a digital microscope (VHX-1000, Keyence Corporation, Osaka, Japan), and contrast analysis. Imaging was performed on the coatings cross-sections using the scanning electron microscopy (SEM) model EVO MA-10 (Carl Zeiss AG, Oberkochen, Germany), and composition was measured using an energy-dispersive X-ray spectroscopy (EDS) INCA X-Act (Oxford Instruments, Oxford, England ). By using the overall DE, the feedstock powder composition, and the coating composition, it is possible to calculate the partial DE of aluminum and alumina [16]. This allows to draw conclusions related to the increased DE of the metallic particles by segregating them from the effect of the mass contribution of the ceramic phase.

## Erosion Tests

To ensure that the aluminum partial DE is evaluated properly, it is important to consider the effect of erosion that alumina might have on the aluminum particles. At higher alumina content in the feedstock powder, the ceramic particles may erode the aluminum phase, reducing the coating aluminum composition and therefore leading to a perceived lower partial DE of aluminum. If the state of the deposition is in the erosion zone, then the value can be corrected by knowing the erosion rate of the alumina particles in a cold spray aluminum coating. If the state of erosion has not been reached, no correction is needed. A similar approach than the one presented in a previous study [33] was used to determine the initial mass gain and the erosion rate of the deposition. In order to determine the erosion zone of alumina on an aluminum coating, a pure aluminum coating was impacted by a layer of pure alumina. The spray parameters were the same as the ones used to obtain the coatings but with a lower feed rate in order better control the amount of ceramic injected. Since erosion rate is the ratio between mass lost in the substrate and mass of ceramic sprayed (in mg/g),

changing this parameter does not affect the substrate erosion behavior [33]. This test allows assessing the erosion rate of the alumina particles on the deposited aluminum particles. With the erosion curve, the feedstock powder composition and the DE of the spray, it is possible to estimate the amount of ceramic impacting the coatings, and the rate at which the surface is renewed with a new layer of aluminum. This leads to evaluate the erosion state of each feedstock powder during the deposition of the mixture and to assess the impact of erosion on the deposition.

## Assessment of Deposition Efficiency Mechanisms

To evaluate the process DE, the powder feed rate was measured prior to each deposition. These measurements were done three times to ensure consistency. The substrates were also weighed before and after deposition (using a precision scale Sartorius Extend—model ED124S, with a readability of 1mg). The DE was calculated following Equation 1. The standard deviation was calculated using propagation of uncertainty (based on the uncertainty of weight change of the substrate, feed rate values, and weight measurements).

$$DE = \frac{\Delta m_s}{m_i} = \frac{\Delta m_s \cdot v_n}{FR \cdot d} \quad (1)$$

In this equation, DE is deposition efficiency, $m_i$ is the mass of powder injected into the nozzle, $\Delta m_s$ is the change in mass of the substrate after deposition, FR is the feed rate of powder injected, d the distance traveled by the nozzle on top of the substrate, and $v_n$ is the speed of the nozzle relative to the substrate. Beside this overall DE, partial DEs where also calculated. Cross sections of the coatings produced where obtained and ceramic content was computed by contrast analysis and also using EDS. Using the feedstock powder composition and the resulting coating compositions, it is possible to calculate the partial DE of each component.

## Impingement of Ceramic Particles on Metallic Particles upon Impact

This proposed mechanism suggests that the DE increase might be caused by the impingement of the hard phase (alumina) on the soft phase (aluminum) upon impact [31]. The direct observation of this phenomenon is challenging and potentially not currently possible, due to the small dimensional and time scales involved. However, some assumptions can be made in order to estimate the incidence of this phenomenon and its overall effect on DE. For this mechanism to be valid, a ceramic particle should impinge a metallic particle that would otherwise not adhere to the substrate/coating; this impingement makes it possible for the metallic particle to adhere, thus

increasing the DE. The effect of the impingement of an alumina particle on an aluminum particle was studied using finite element analysis. The details of the simulation are explained in the following section. To assess the influence of ceramic particle impingement on the adhesion between aluminum particles and the substrate, the interface elements (aluminum particles-substrate) were analyzed using the outcomes of the simulation that might improve the bonding between them such as the plastic deformation, temperature field and stress produced.

### *Finite Element Analysis*

A 2D finite element analysis was performed in order to evaluate if the impingement of an alumina particle on an aluminum particle leads to phenomena that can promote the adhesion of the latter to the substrate. The software Abaqus/Explicit was used to carry this analysis. The modeling results of the impact of aluminum particles into an Al6061 substrate were compared with the modeling results of the impact of aluminum particles concomitant with an impact with a ceramic particle. Plastic deformation, temperature and contact pressure were compared at the substrate interface to assess if the ceramic particle impact does promote bonding. These properties have been proposed to be indicators for the generation of metallurgical bonding and therefore an increase in DE [9, 36, 38, 39].

Cross sections of representative aluminum and alumina particles were digitalized in order to obtain the geometry required for the simulations. Three aluminum and two alumina particle geometries were chosen, and six different impact configurations were studied. The material properties used in the simulations for aluminum particles, Al6061 substrates, and alumina particles are shown Table 3.

*Table 3: Material properties used in simulations*

| | **Aluminum** | **Al6061-T6** | **$Al_2O_3$** |
|---|---|---|---|
| k (W/m K) | 237 | 167 | 30 |
| ρ (Kg/m3) | 2710 | 2710 | 3900 |
| G (GPa) | 26 | 26 | - |
| E (GPa) | - | - | 300 |
| v | - | - | 0.21 |
| Cp (J/kg K) | 910 | 900 | 700 |

Johnson-Cook constitutive equation (Equation 2) was used to model the plastic behavior of pure aluminum particles and A6061-T6 substrates, and the equation of state used was the linear Us-Up Hugoniot form of Mie-Gruneisen (equation 3). These equations have been used in several investigations to describe cold spray particle and substrate deformations[40–43]. The equations are:

$$\sigma_{eq} = \left[A + B\ \varepsilon_p^n\right]\left[1 + Cln\left(\frac{\dot{\varepsilon_p}}{\dot{\varepsilon_{ref}}}\right)\right]\left[1 - \left(\frac{T - T_{ref}}{T_m - T_{ref}}\right)^m\right] \quad 2$$

$$p = \frac{\rho_0 {c_0}^2 \eta}{(1 - s\eta)^2}\left(1 - \frac{\Gamma_0 \eta}{2}\right) - \Gamma_0 \rho_0 E_m \ , \quad \eta = 1 - \frac{\rho_0}{\rho} \quad 3$$

Where A, B, C, n, m, $\dot{\varepsilon_{ref}}$, and Tref are the Johnson-Cook parameters, $\varepsilon_p$ is the plastic strain, $\dot{\varepsilon_p}$ is the plastic strain rate, T is the temperature of the material, and Tm is the melting point. In equation 3, p is the hydrodynamic stress, $\rho_0$ is the initial density, $\rho$ is the actual density, $c_0$ is the material speed of sound, $s$ is the Hugoniot slope, $\Gamma_0$ is the Gruneisen constant, and $E_m$ is the energy per unit mass. The parameters for the materials used can be found in Table 4.

*Table 4. Johnson-Cook and Mie-Gruneisen parameters used in simulations*

| **Johnson-Cook Parameter** | **Al-1100-H12**[44] | **Al6061-T6**[45] |
|---|---|---|
| A (Mpa) | 148.4 | 324 |
| B (Mpa) | 345.5 | 114 |
| C | 0.001 | 0.002 |
| n | 0.183 | 0.42 |
| m | 0.895 | 1.34 |
| $\dot{\varepsilon_{ref}}$ | 1 | 1 |
| Tm (K) | 925 | 925 |
| Tref (K) | 293 | 300 |
| Gruneisen Constant ($\Gamma_0$) | 1.97 | 1.97 |
| Speed of sound ($^m/_s$) | 5386 | 5240 |
| Hugoniot slope ($s$) | 1.34 | 1.4 |

The particle impact velocities required as model inputs were measured using a Cold Spray Meter (CSM) eVOLUTION (Tecnar Automation Ltd, St-Bruno, Canada). The system performs in-flight diagnostic on individual particles illuminating the particles with a continuous 2.4 W (λ = 810 nm) laser and capturing the reflection through a dual split photomask in order to calculate the velocity. The substrate temperature used in the model was measured using a FLIR i7 Portable Infrared Camera. The particle impact temperature was assumed to be 80% of the gas stagnation temperature, similarly to what has been calculated in previous investigations [46, 47].

A quadratic mesh was used with a coupled temperature-displacement element type (CPE4RT). The maximum element size used was µm. Arbitrary Lagrangian-Eulerian (ALE) adaptive domain was used in the in the substrate and aluminum particle mesh. Equivalent plastic strain (PEEQ), temperature, and contact pressure (CPRESS) were evaluated in the elements at the surface of particle and coating [43]. The results were averaged through the elements, and the maximums were used for the comparison.

### *Probabilistic Analysis*

The FEA analysis results presented later show the possibility of increasing the chances of adhesion of an aluminum particle when a ceramic particle is impacting it. It is important to note that for this interaction to occur, the alumina particle must hit an alumium particle before the latter bounces back. If the ceramic particle arrives too late, the aluminum particle will be long gone, and no impingement would occur. The short time span and narrow area that the ceramic particle has to hit to influence the aluminum particle impact makes this event potentially unlikely. The probability of this event was calculated in order to evaluate the incidence of this potential mechanism on the overall DE. The probability equation used is shown in equation 4:

$$\mathbb{E}_{event}(t) = \left[\mathbb{P}(p_1 = Al) \times [1 - DE(Al)]\right] \times \mathbb{Q}(t) \times \mathbb{P}(p_2 = Al_2O_3) \qquad 4$$

Where $\mathbb{E}_{event}(t)$ is the probability of the event (aluminum particle being impinged by alumina particle while it is impacting the substrate) to happen over a period of time $t$. $\mathbb{P}(p_1 = Al) \times [1 - DE(Al)]$ is the probability of the first impacting particle to be an aluminum particle that wouldn't stick to the substrate. $\mathbb{Q}(t)$ is the probability of at least one of the incoming particles impacting during a time span $t$ to hit the area defined the first particle. Finally $\mathbb{P}(p_2 = Al_2O_3)$ is the probability for that incoming particle to be an alumina particle. It is important to note that $\mathbb{Q}(t)$ takes into consideration the time span that the second particle has to impact the first particle, and the narrow area where it has to hit in order to have an interaction. $\mathbb{Q}(t)$ can also be written as:

$$\mathbb{Q}(t) = 1 - (1 - \mathbb{Z})^{N(t)}$$

This equation gives the probability of at least one of the incoming particles to peen the previous one in a specific time span. $N(t)$ represents the number of particles hitting the substrate in this time span $t$. $\mathbb{Z}$ is the probability of impacting inside a specific zone (in the vicinity of the previous particle). Therefore, $(1 - \mathbb{Z})^{N(t)}$ is the probability of all the incoming particles impacting outside this specific zone. Finally the complement of this term represent the probability of not all the

particles to hit outside this area (thus at least one hits inside this area). It is important to note that $\mathbb{Z}$ represents the likelihood of an impact to happen in a specific area. This probability is different depending on the relative position from the nozzle axis. Directly below the nozzle, a higher flow rate of particles hit the substrate compared with a zone away from the nozzle, therefore $\mathbb{Z}$ is higher at the center of the nozzle and decays towards the periphery.

The probability $\mathbb{P}$ was obtained based on the ceramic content of the feedstock powder. The total number of particles (aluminum and alumina) was calculated per unit mass using the density of the elements as well as the average particle size. For simplicity, the volume of a sphere was used to estimate the number of particles per unit mass. The probability $\mathbb{P}(p = Al)$ was considered as the calculated number of aluminum particles over the total number of particles in an unit mass. Similarly $\mathbb{P}(p = Al_2O_3)$, was considered as the number of alumina particles over the total number of particles.

$N(t)$ was computed using the total number of particles per unit of mass of the powder mixture and the feed rate measured during deposition. A uniform number of particles per unit of time was assumed (constant feed rate). The time span $t$ is the impact time of the aluminum particle from initial contact with the substrate until it has completely bounced back and is not in contact with the substrate anymore and was obtained from FEA simulations. Finally, to obtain the probability $\mathbb{Z}$, it was necessary to obtain the spatial distribution of particles impacting the substrate directly below the nozzle. The distribution of particles in the nozzle was assumed to be axisymmetric with a radial probability distribution profile. This distribution was fitted from a single coating spot produced by the nozzle. This curve was obtained using a 3D depth composition image (VHX-1000, Keyence Corporation, Osaka, Japan). It was assumed that the spot left by the nozzle closely represents the spatial particle distribution. With this radial distribution function, $\mathbb{Z}$ can be defined as the cumulative distribution function expressed by:

$$\mathbb{Z} = f[\,\boldsymbol{x_1} - \Delta_r < \boldsymbol{x_2} < \boldsymbol{x_1} + \Delta_r\,] \times \frac{\Delta_{\boldsymbol{\theta}}}{\pi}$$

where $f$ is the radial distribution of particles below the nozzle, $\boldsymbol{x_1}$ and $\boldsymbol{x_2}$ are the position of impact of the initial particle and second particle, respectively, $\Delta_r$ and $\Delta_\theta$ are ranges of where the second particle can impact and still hit the previous particle. $\Delta_r$ was assumed as the addition of the average aluminum and ceramic radiuses and $\Delta_\theta$ is defined by the tangent arc of $\Delta_r$ and the distance from the nozzle axis. The area of interaction assumed by this equation is shown in Figure 5 (a) as a shaded area. The cumulative area of interaction of the function $f$ is represented in Figure 5 (a), but

this represent a ring around the axis of the nozzle. To consider the angular segment, a section of arc $2\Delta_\theta$ was considered over $2\pi$ section for the full ring, as shown in Figure 5 (b). which is reduced to the term $\frac{\Delta_\theta}{\pi}$, to represent the probability of impact in the angular section of the ring. It is important to note that it creates a larger zone of interaction than in reality (due to the the corners in the figure outside $\boldsymbol{r_2}$) therefore overestimating the probability of the event to happen.

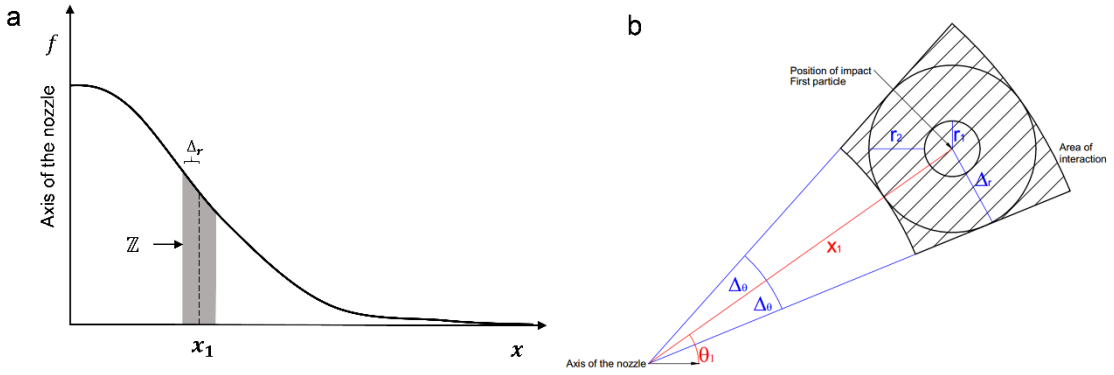


*Figure 5: Schematic of the impact zone for particles interactions: a) Radial distribution; b) Angular section.*

## Effects of Asperities and Oxide Removal on DE

These two effects are closely linked, as both are caused by the impact of ceramic particles. When ceramic particles hit the substrate, it creates craters and new surfaces through deformation and cutting of the soft metallic phase. At the same time, during the impacts, the native surface oxide layer of the substrate breaks exposing oxide-free metallic surfaces, as the oxygen-free gas (working gas) prevents the oxidation of this newly created surface maintaining it clean until the arrival of the next particle. In order to evaluate the effect of surface asperities created during the deposition of ceramic particles, it is important to separate it from the influence of oxide removal occuring during the same process.

To decouple these effects and evaluate independently the effect of the asperities it is imperative to evaluate the DE of the aluminum particles hitting a surface topography identical to the one present during deposition of the mixture. For this reason, a test was designed to calculate the deposition efficiency of a single layer of aluminum particles only. Properly designing this test for just a single layer of aluminum is crucial to evaluate solely the effect of asperities, otherwise, if more than a single layer is deposited, the second wave of particles will encounter a surface without the asperities skewing the measured DE toward the one of pure aluminum. To create the substrates with

asperities, coatings were sprayed with each of the feedstock powder compositions using the parameters presented in Table 2. After deposition, the coatings were exposed to air at standard conditions for 72 hrs in order to develop the surface oxide layer. Particular care was taken in handling the samples in order not to affect the surface topology created during deposition.

Afterward, a single layer of pure aluminum particles was sprayed on top of the previously deposited coating. Spray parameters were kept constant, while feed rate was adjusted in order to obtain a single layer. The coatings were preheated with the working gas in order to closely recreate the same conditions of deposition.

This method allows segregating and assessing the contribution of the surface asperities created by the powder mixture on the DE of pure aluminum and indirectly allows to evaluate the contribution of the oxide layer removal. To directly assess the effect of the oxide-free surfaces without the asperities is a highly challenging task. Maintaining an oxide-free aluminum surface is a highly labor intensive task and has to be done in an entirely oxide-free environment. For this reasons, the contribution of oxide-free surfaces in the DE was measured indirectly by subtracting the effect of the two other mechanisms studied in this investigation to the overall DE gain. It is important to mention that this method considered that the three mechanisms studied are the only ones acting toward the increment in DE in the deposition of ceramic-metal mixture.

## Adhesion Strength and Mechanical Testing

Adhesion strength, hardness, and wear performance were measured for each coating produced. Adhesion strength was determined following the ASTM C-633 standard. A thermally cured elastomeric adhesive (FM-1000) with a tensile strength of 76.9 MPa was used. The samples were placed in an oven at 175°C for 2 hours to ensure the adhesive had properly cured. Testing was done using a universal tensile testing machine that recorded the force needed to remove the coatings. Three samples of each mixture were tested, and the mean and standard deviation of each preparation were computed. Hardness values were obtained using a Duramin-10 (Struers ApS, Denmark) equipped with a Vickers indenter using a load of 0.3 kgf. Wear tests were performed following the ASTM G133-05 standard. This dry slide wear test was conducted at three different travel lengths: 25 m, 50 m, and 100 m or until the wear track reaches the substrate. The load used was 25 N using a 3/16” alumina ball.

# Results and Discussion

## Deposition Efficiency and Coating Characterization

The eleven powder mixtures were sprayed successfully, and DE measurements were completed. Figure 6 shows the DE for each of the powder mixtures. It is important to note that a coating was produced for each mixture where aluminum was present, even in the case of 90 wt.% $Al_2O_3$. This shows that the erosion rate inflicted by the alumina particles is low. The DE of pure aluminum was 11.0% ± 2.1% and increased up to 19.0% ± 2.5% for a 30 wt.% alumina content. From 30 wt.% of $Al_2O_3$, a consistent decrease in DE is observed, reaching zero at 100% $Al_2O_3$. These results are in line with the literature, where similar behavior had been reported [16, 18, 19, 29]. This behavior (increase followed by a decrease) is evidence that there are two mechanisms competing, one to increase the DE of the mixture and another one to decrease it. At 30 wt.% $Al_2O_3$, the decreasing mechanism starts overcoming the increasing one, decreasing the DE.

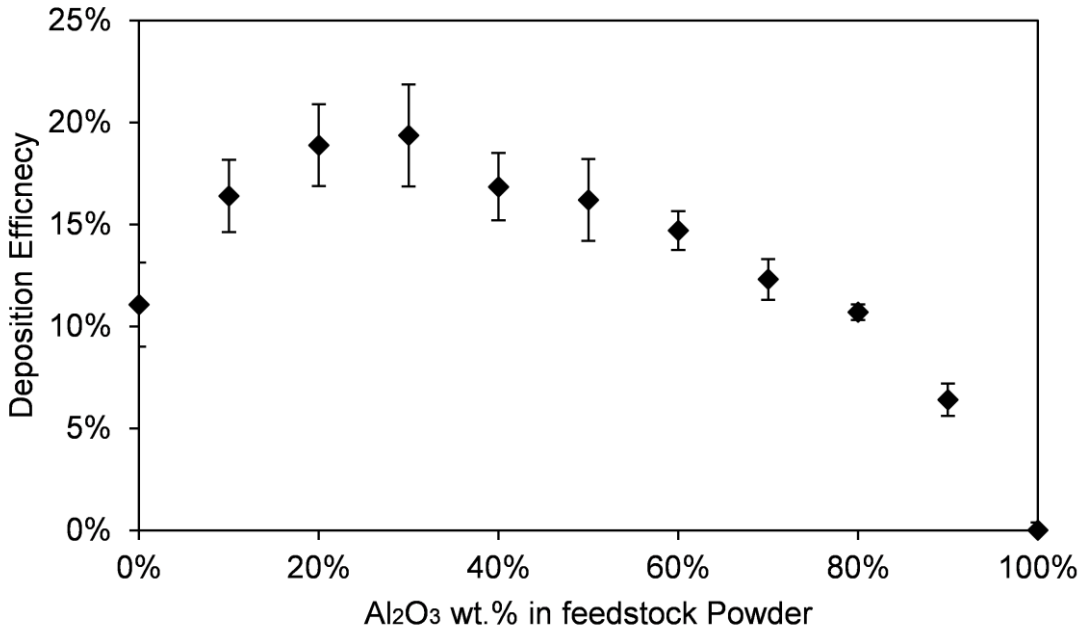


*Figure 6: Measured deposition efficiency of coatings for different feedstock powder compositions.*

Figure 7 shows some selected coatings cross-section images. It can be seen that the coatings are dense and the alumina particles appear to be embedded in the metallic phase.

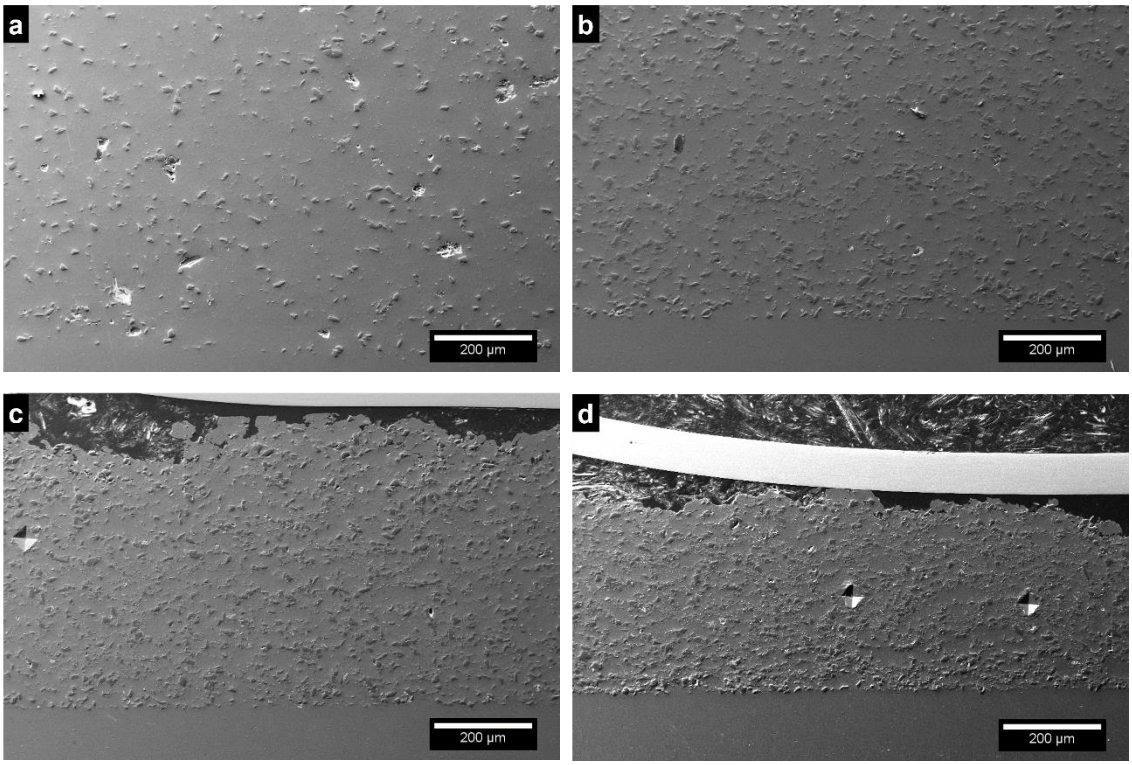


*Figure 7: Overview of coatings cross-sections for feedstock powders containing: (a)10 wt.% $Al_2O_3$; (b) 40 wt.% $Al_2O_3$ ; (c) 60 wt.% $Al_2O_3$ ; (d) 80 wt.% $Al_2O_3$.*

Contrast analysis was used to compute the coatings ceramic content. The measured values were converted to wt.% to have a direct comparison. This analysis was also performed using X-ray spectroscopy (EDS). The values were converted to wt.% based on the oxygen content and assuming there are just aluminum and alumina phases present. Table 5 shows the alumina wt.% found in each of the coatings calculated using these two methods. These results can also be seen in Figure 8, where it can be directly compared with the feedstock powder alumina percentage. It can be seen that the coatings alumina content is always lower than the one of the feedstock mixture. This result was expected due to the lower chances of deposition of alumina compared to the deposition of aluminum. The relation between the injected and deposited alumina appears to be linear, averaging to 51.2% of alumina retained when the coatings are formed. These values are similar to the ones reported in previous investigations [16, 18, 29, 48], despite using different feedstock powders and cold spray systems.

*Table 5: Alumina content in coatings measured by two different methods.*

| Sample | $Al_2O_3$ wt.% in coating measured by contrast | $Al_2O_3$ wt.% in coating measured by EDS |
|---|---|---|
| Al-00 | 0% ± 0% | 1% ± 0% |
| Al-01 | 9% ± 1% | 12% ± 0% |
| Al-02 | 15% ± 1% | 16% ± 0% |
| Al-03 | 22% ± 1% | 21% ± 1% |
| Al-04 | 28% ± 2% | 26% ± 1% |
| Al-05 | 30% ± 2% | 28% ± 3% |
| Al-06 | 33% ± 2% | 30% ± 3% |
| Al-07 | 39% ± 4% | 35% ± 1% |
| Al-08 | 43% ± 4% | 38% ± 4% |
| Al-09 | 51% ± 4% | 46% ± 3% |
| Al-10 | - | - |

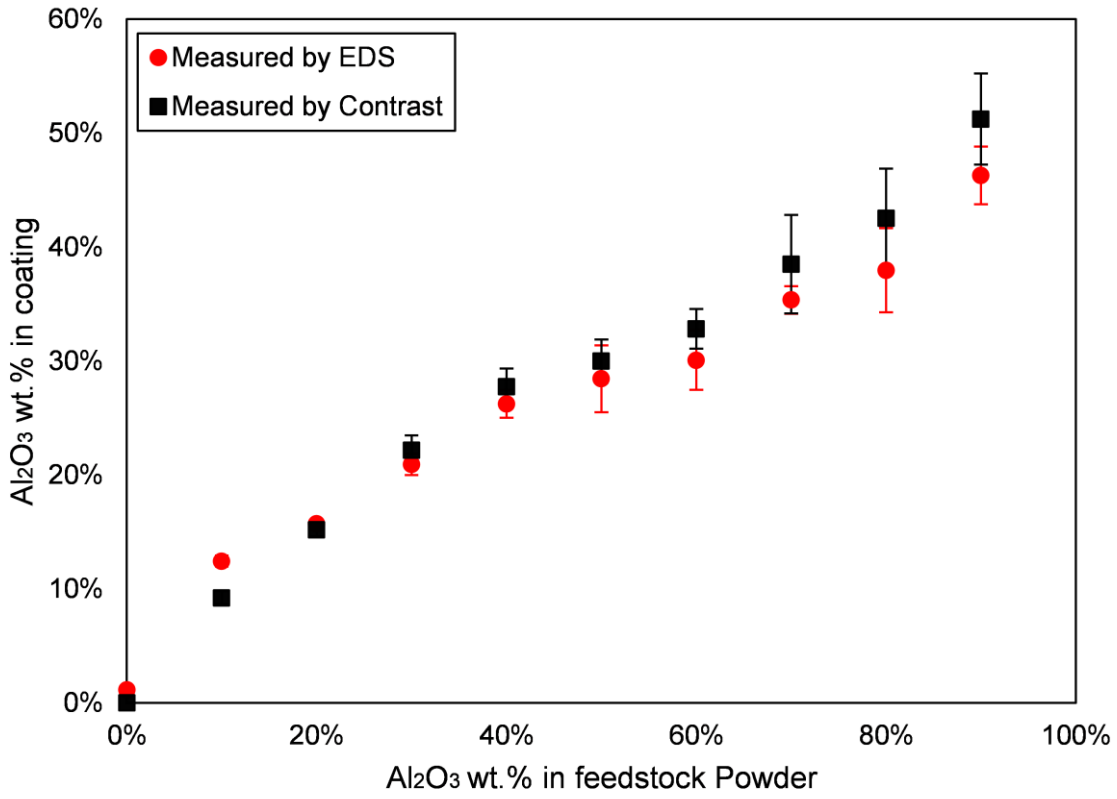


*Figure 8: Alumina content in coatings versus alumina content in feedstock powders, measured by two different methods.*

The results in Table 5 were used to obtain the partial DE of aluminum and of alumina. This result is presented in Figure 9. It is clear that the presence of alumina particles in the feedstock powder results in an increase in DE of the aluminum phase. This improvement increases with the alumina content present increasing the pure aluminum partial DE from 11.0% in pure aluminum to 31.0% for the 90 wt.% alumina mixture. The figure also shows that the alumina partial DE strongly depends on the feedstock powder aluminum content. Pure alumina has a DE of 0% while 10wt.% of alumina with 90% aluminum shows an alumina DE of 15.1%. Both powders get a benefit in DE under the presence of the other one. This interaction leads to a maximum overall DE at 30wt.% alumina. The erosion test gives some insights on reasons behind the increment in alumina partial DE observed at higher aluminum content. The reasons behind the increase in aluminum partial DE are exposed with the assessment of the three potential mechanisms studied.

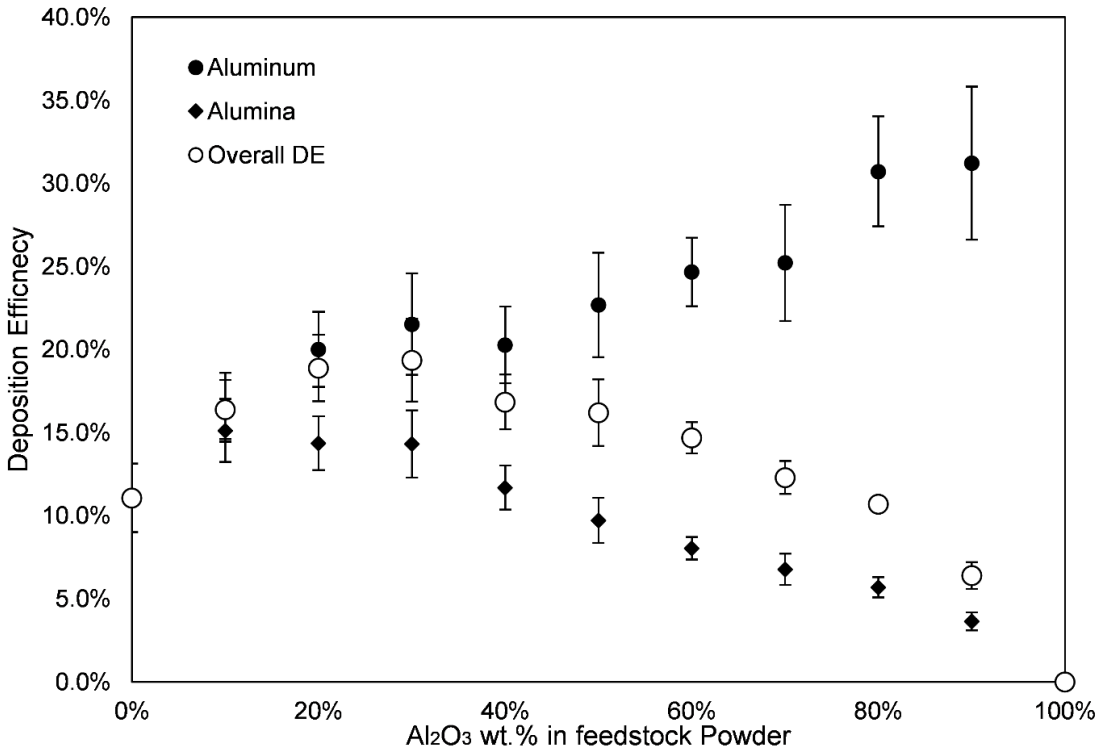


*Figure 9: Partial deposition efficiencies calculated using overall DE and alumina composition in coatings.*

Figure 10 shows the substrate weight gain/loss versus the amount of ceramic impacting per unit area obtained from the erosion test. It can be seen that initially there is a substrate weight gain, reaching a maximum and followed by a constant decrease. This curve is similar to the one obtained

by Neilson and Gilchrist [33] and reveals that before leading to erosion, ceramic particles first embed in the substrate, up to a certain level. The positive side of the curve represents the zone where alumina particles add mass to the substrate by embedding on it, and the negative side represent the cases when the particles erode the substrate, removing material from it. The point when the slope changes from positive to negative occurs when ceramic particles have reached a saturation limit of embedding, as an increase in the amount of particles directed towards the substrate results in removal of previously embedded particles. The slope of the negative side of the curve is the steady-state erosion rate and was evaluated 3.87 mg of eroded aluminum per gram of injected alumina.

The figure also shows an approximation of the erosion state experienced by aluminum while being sprayed for each of the feedstock powder compositions (vertical dotted lines). This is an estimated value based on the feedstock powders compositions, the feed rate and the spray conditions. These values allow to calculate the mass per area of ceramic being sprayed in the time needed to renew a layer of aluminum. This time is calculated with the same values and the DE of aluminum at that composition (i.e. 0.62 $mg/mm^2$ of alumina will be sprayed in the time it takes to the aluminum to renew a $mm^2$ with a new layer)

It can be seen that even for 90 wt% of alumina content, the state is still on the positive side of the curve. This suggests that at the spray parameters used, even the 90 wt% of alumina content in the feedstock powder used does leads to a coating instead of erosion. This estimation is in line with the results obtained in the previous section, where even the 90wt% alumina content powder produced a successful coating. The results also correlate well with alumina content measured by EDS at the surface of the coatings sprayed with each of the compositions, presented in Figure 11. The alumina composition at the surface increases consistently until it reaches a plateau at approximately 70-80wt.% $Al_2O_3$ in the feedstock powder. This plateau could be a result of surface alumina a saturation allowed to embed in the aluminum.

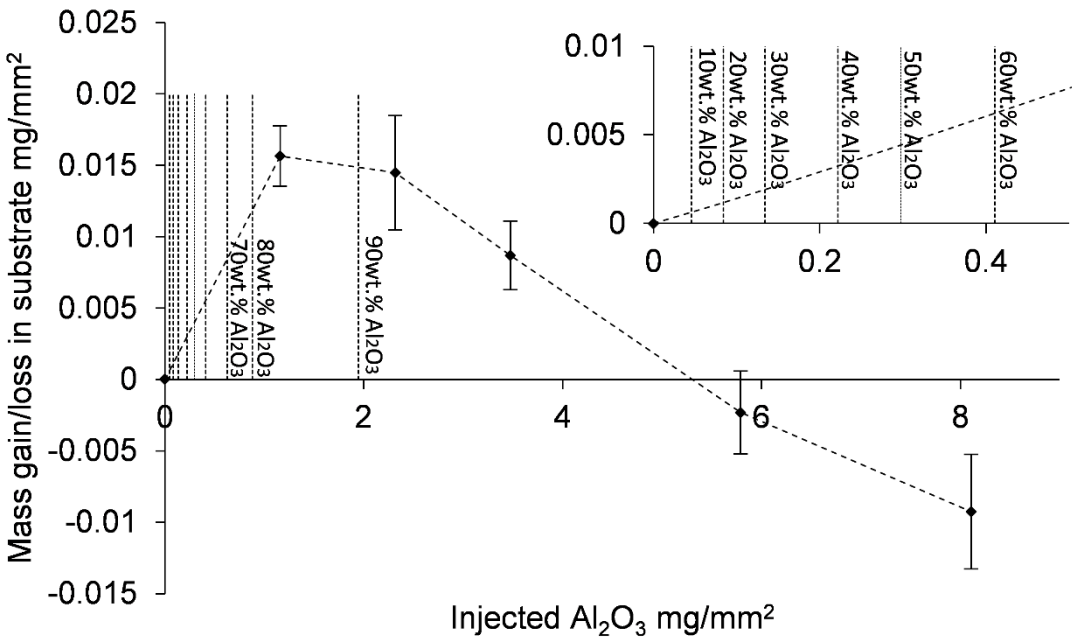


*Figure 10: Substrate mass change vs. alumina mass impacted for aluminum coatings. Vertical lines represent the equivalent erosion state of each feedstock powder mixture.*

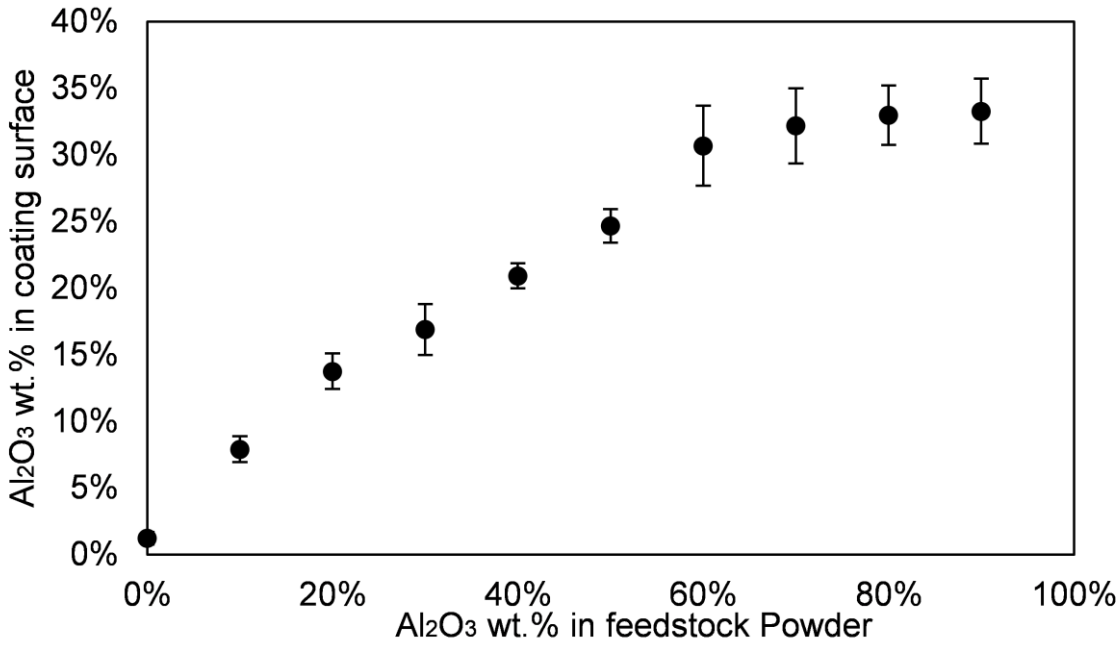


*Figure 11: Surface alumina content in coatings sprayed with different feedstock powder compositions.*

This test helps to explain the reasons behind the increment in DE seen by the alumina particles in the presence of aluminum. At higher aluminum content (lower alumina content) newly deposited metallic phase gets renewed more often than the erosion occurrences, lowering the chances of a ceramic particle to impact another embedded ceramic particle, increasing the chances to embed it in the metallic matrix staying in the coating and therefore increasing its partial DE.

## Interaction Ceramic-Metal upon Impact

*Finite element analysis*

This potential mechanism states that the increase in DE might be due to the peening of a ceramic particle into an impacting metallic particle that otherwise would not adhere. It has been proposed that this interaction will increase the particle/substrate deformation and therefore increase the probabilities of obtaining bonding via more favorable conditions at particle/substrate interface [18, 30, 31]. A finite element analysis was performed to evaluate the potential of this process to increase the DE. Figure 12 shows the particles selected for the simulation and their digitalization. Three aluminum particles and two alumina particles were selected.

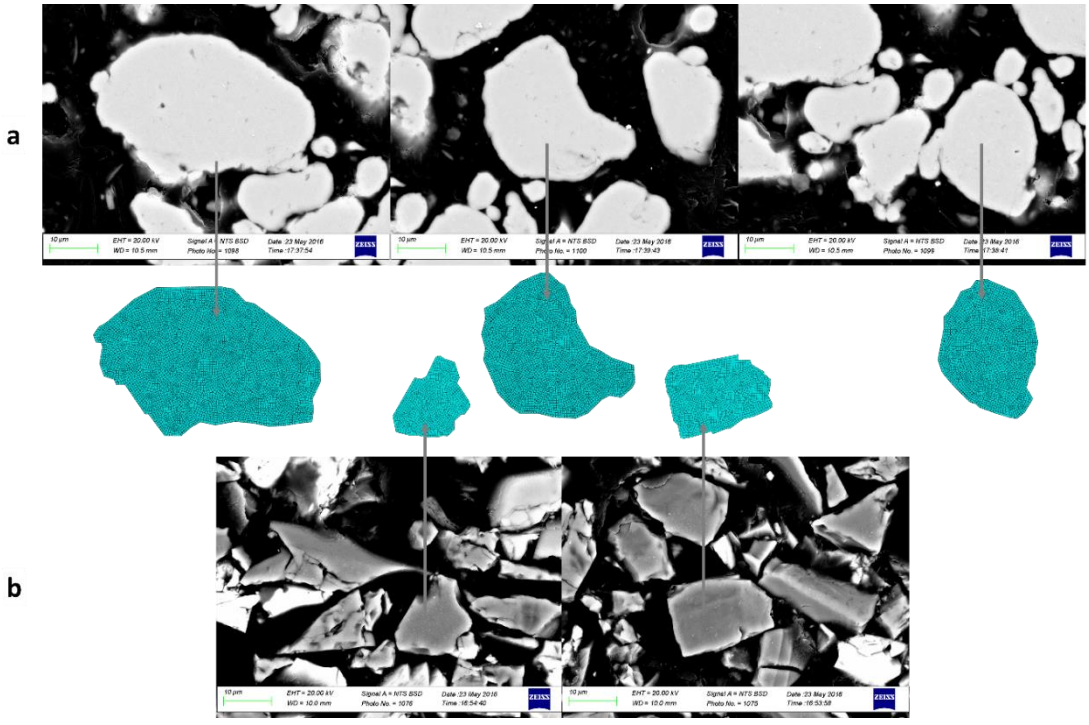


*Figure 12: Digitalized particles: (a) Aluminum and (b) Alumina*

Figure 13 (a) shows an example of one of the layouts used to perform the simulations. Each alumina particle was positioned to impinge each of the three aluminum particle with a total of six different simulations of aluminum-alumina interactions.

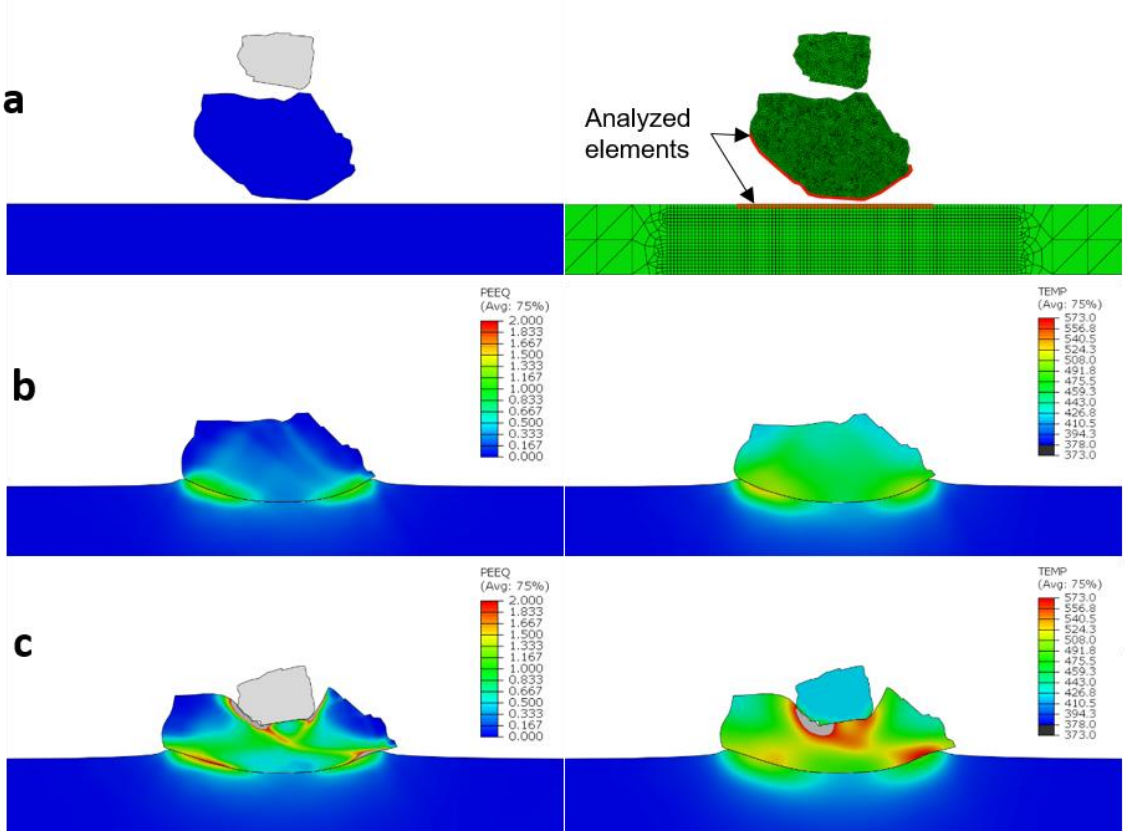


*Figure 13: (a) Layout of the simulations and elements analyze;, (b) Aluminum impact: PEEQ and temperature and (c) Aluminum-Alumina impact: PEEQ and temperature*

Laser diagnostic was used to assess the average particles impact velocities and was evaluated at 457 m/s for the aluminum particles and 451 m/s for the alumina particles. The substrate temperature measured was 105°C, and the particle impact temperature was assessed as 145°C. Figure 13 (b), and (c) show the results of one of the simulations. Table 6 shows the average increase in PEEQ, temperature, and CPRESS at the aluminum and substrate interface as a result of the ceramic particle impingement compared to the values computed in the aluminum particles without impingement of the ceramic particle.

*Table 6: Increases of CPRESS, PEEQ and Temperature over values obtained in single aluminum impact.*

| | **CPRESS** | **PEEQ** | **Temperature** |
|---|---|---|---|
| Aluminum Particle | 30.7% ± 12.7% | 59.6% ± 33.5% | 9.1% ± 4.1% |
| Substrate | 35.7% ± 9.7% | 9.2% ± 2.8% | 8.6% ± 5.9% |

The simulations show that the addition of an impinging ceramic particle increases the three properties. The contact pressure between the substrate and the aluminum particles increased an average of 30% when an impinging alumina particle was added to the simulation. The plastic deformation showed an increment of nearly 60% in the aluminum particle while the increment at the substrate was considerably lower at around 10%. Temperatures appeared to be the least affected by the addition of an alumina particle showing an average increase in the interface between the aluminum particle and substrate of 9%. Considering that the three properties increased with the addition of an alumina particle impinging an aluminum particle, it can be concluded that the conditions to get bonding are enhanced with the presence of an impinging ceramic particle.

## Probability of the event

The FEA results showed that if an alumina particle is peening an aluminum particle, the chances for the latter to adhere to the substrate increases. In this section, the likelihood of this peening event to happen during the impact time (the time the aluminum particle is in contact with the substrate prior to rebounding away if no bonding occurs) is estimated. As described before, the probability of this event is:

$$\mathbb{E}_{event}(t) = \left[\mathbb{P}(p_1 = Al) \times [1 - DE(Al)]\right] \times \left[1 - (1 - \mathbb{Z})^{N(t)}\right] \times \mathbb{P}(p_2 = Al_2O_3)$$

Based on the particle size distribution and mixture composition, the probability $\mathbb{P}$ was calculated. The number of particles impacting the substrate per second was calculated using the feed rate, the density of the materials and the average particle size. These results are shown in Table 7. It is important to specify that the impact rates shown represent the total number of aluminum and alumina particles.

*Table 7: Calculated probabilities* $\mathbb{P}(\boldsymbol{Al})$, $\mathbb{P}(\boldsymbol{Al_2O_3})$ *and impact rate for each feedstock powder composition, fort the specific spray parameters used.*

| Mixture | $\mathbb{P}(\boldsymbol{Al})$ | $\mathbb{P}(\boldsymbol{Al_2O_3})$ | $\boldsymbol{N \times 10^6\, par/_s}$ |
|---|---|---|---|
| AL-00 | 100% | 0% | 5.12 |
| AL-01 | 89% | 11% | 5.32 |
| AL-02 | 78% | 22% | 5.81 |
| AL-03 | 67% | 33% | 5.72 |
| AL-04 | 57% | 43% | 6.19 |
| AL-05 | 47% | 53%c | 6.57 |
| AL-06 | 37% | 63% | 6.97 |
| AL-07 | 28% | 72% | 6.97 |
| AL-08 | 18% | 82% | 6.98 |
| AL-09 | 9% | 91% | 7.06 |
| AL-10 | 0% | 100% | 7.14 |

The radial distribution function $\mathbb{Z}$ was obtained. Figure 14 (a) shows the 3D image of a single coating spot obtained. The height data from the center of the image composition was used to fit a Gaussian distribution [49]. Figure 13 (b) shows the fitted distribution function ($\mu = 0, \sigma = 1.7016\, mm$). Having a normal distribution representing the probability density function of particles has the advantage of simplifying the cumulative function to:

$$\mathbb{Z} = \left[\boldsymbol{erf}\left(\frac{\boldsymbol{x_1} + \Delta_r}{\sqrt{\boldsymbol{2}}\,\boldsymbol{\sigma}}\right) - \boldsymbol{erf}\left(\frac{\boldsymbol{x_1} - \Delta_r}{\sqrt{\boldsymbol{2}}\,\boldsymbol{\sigma}}\right)\right] \times \frac{\Delta_\theta}{\pi} \qquad 5$$

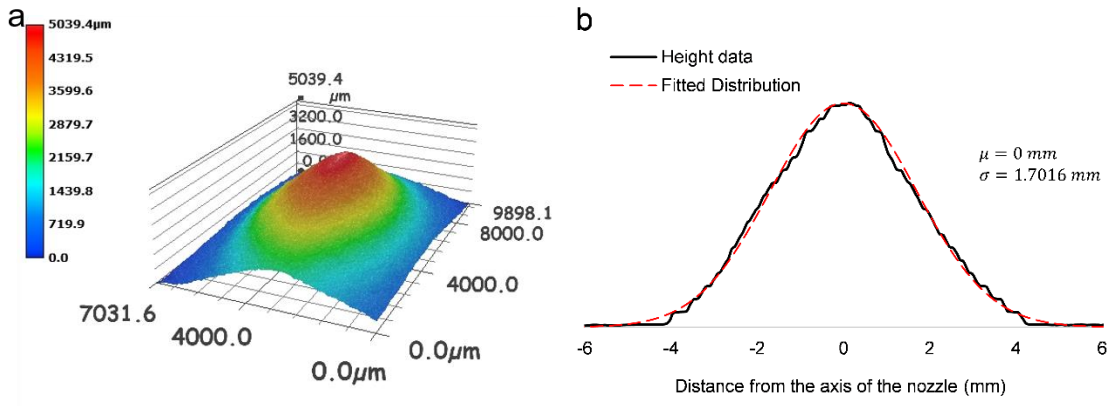


*Figure 14: (a) 3d Image composition of a single spot ; (b) adjusted distribution of particles to the profile.*

The impact time span was estimated, based on the FEA results and evaluated as $t = 0.1\ \mu s$ . This value is considered conservative, as in the simulation the particle is already detached from the surface at that time, as is shown in Figure 15. Finally, the probability to obtain the event for some selected mixture along the spray radius is shown in Figure 16. It is possible to see that the event is most probable at the center of the nozzle, and the highest probability occurs for the feedstock powder AL-05. At composition lower than 50wt% $Al_2O_3$ there are lower chances of getting an alumina particle to peen an aluminum particle, and at higher composition the chances of obtaining the first aluminum particle is also lower. The highest probability value obtained is 0.082%. It is important to note that this event considers the total flow of particles impacting the substrate, and in spite of the 6.5 million particle per second impacting the substrate the short time span for the event and the narrow area keeps the probability value remarkably low.

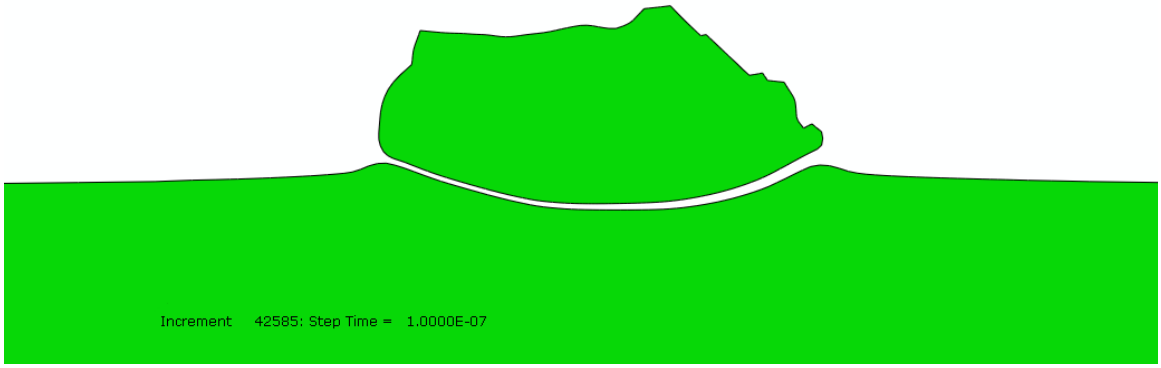


*Figure 15: FEA of Aluminum particle at 0.1 ms after the impact.*

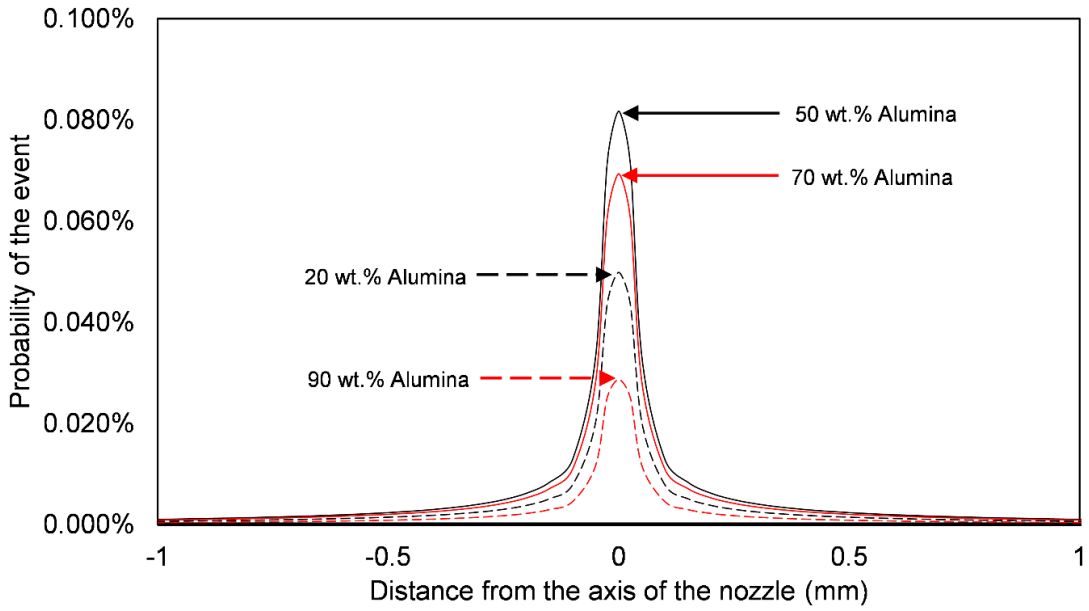


*Figure 16: Selected probability curves of an alumina interacting with aluminum upon impact*

Even though the FEA model shows that this interaction can increase the DE, the likelihood of the event indicates that the effect is negligible. Even with a conservative approach the probability of this event in the most likely scenario is 0.082%. This value also represents the upper limit of the DE increment of this mechanism. Therefore this mechanism cannot explain the increase in DE obtained in this work.

## Effect of Asperities and Oxide Removal

Based on the previous section, it is possible to assume that the contribution of metal-ceramic interaction upon impact is negligible. The remaining possible mechanisms are related to the influence of the ceramic particles into the substrate, specifically, the effect of asperities created by the ceramic particle impacts, and the effect of oxide removal that the ceramic particle induces on the substrate surface once it impacts it. Figure 17 shows representative images of the coatings surfaces produced using feedstock powder with various alumina contents. It shows the creation and evolution of a number of asperities at different compositions. It can also be seen that the asperities are caused by the cutting of the metal and bouncing off of the sharp angular ceramic particles. The asperities dimensions are in the micron-sized range and appear to get smaller and more numerous as the wt.% $Al_2O_3$ of the powder increases, see highlights in Figure 17 . This result is expected as a higher number of ceramic particles impacting the surface leads to an increase in the number of

new surfaces being generated, but these particles also deform asperities created by previous impacts, reducing their size.

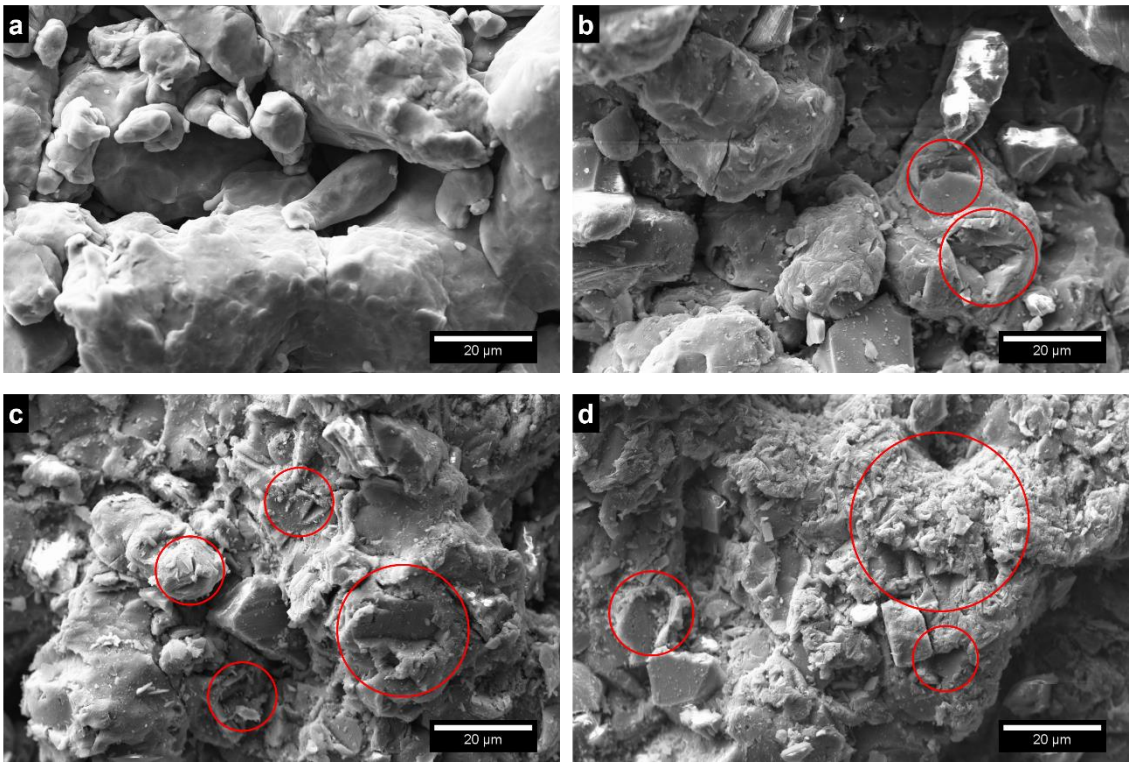


*Figure 17: Coatings surfaces, highlighting asperities in samples (a) Al-00 (b) Al-02 (c) Al-04 (d) Al-06.*

The proposed mechanism states that the increase in DE occurs due to an increase of mechanical bonding between the aluminum particles and the surface due to more preferential sites allowing this to occur. Figure 18 shows an etched cross-section of a coating, where the particles interfaces reveal locations where asperities might have acted to enhance mechanical interlocking.

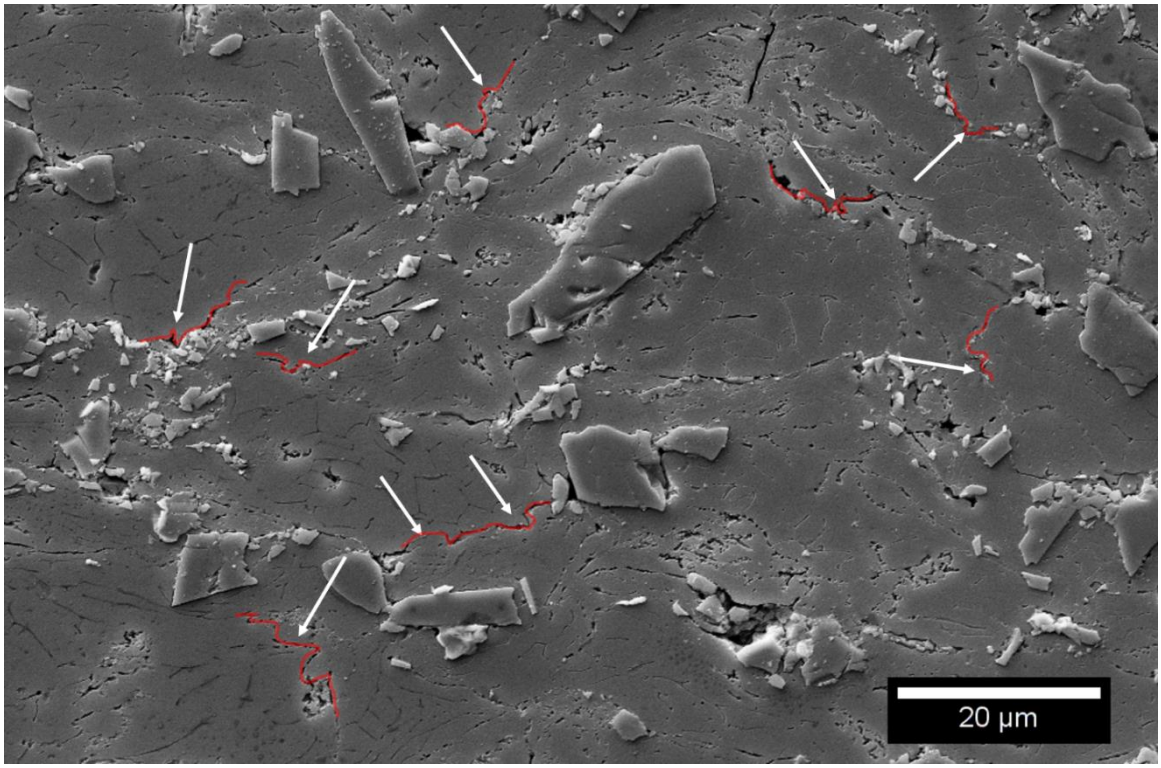


*Figure 18: Etched cross-section of sample Al-06. Possible points of asperities locking particles are highlighted.*

The processes of oxide removal and asperities were decoupled by calculating the DE of a single layer of pure aluminum deposited on a coating surface produced with the different feedstock powders, and therefore with the asperities. The oxide layer was left to grow back on these coatings for 72 hrs. Figure 19 presents selected coatings cross sections showing the single layer of aluminum particles obtained during deposition on the previously sprayed aluminum-alumina coatings. Figure 20 displays the DE of these single layers of aluminum as well as the partial DE of aluminum calculated from overall DE and cross sections. The figure presents a positive influence of the asperities on the DE, increasing to 18%. Due to the exposure to normal conditions, the surface of the coatings is covered by the native oxide present in aluminum materials. Therefore the effect that an oxide-clean surface due to the presence of alumina might have on DE is completely suppressed, and the increment in DE can only be attributed to the presence of those initial asperities. As Figure 17 shows, a higher content of $Al_2O_3$ particles in the feedstock powder leads to a higher density of asperities on the surface of the substrate and already deposited particles; this leads to a higher DE of aluminum particles at higher alumina composition. It is important to note that the effect of

asperities appears to reach a plateau, starting at 50 wt.% of $Al_2O_3$. This can be a result of the reduced asperity size at higher alumina composition.

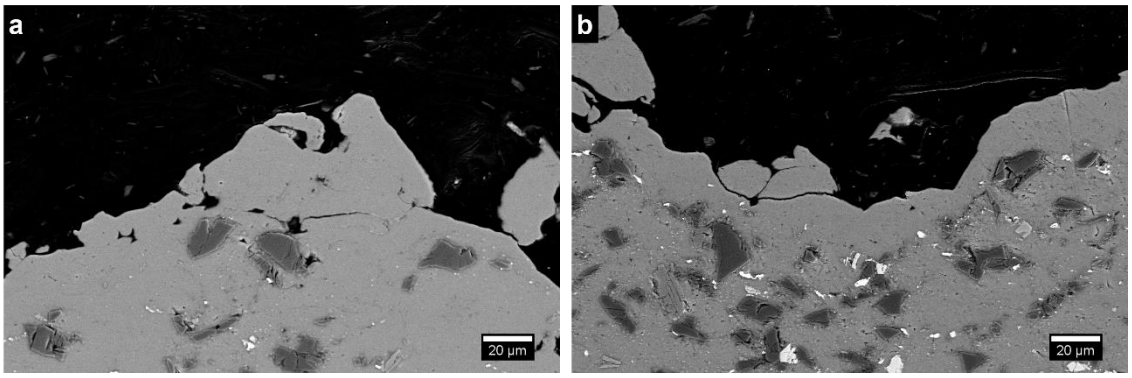


*Figure 19: Selected cross-sections of a single layer of aluminum particles deposited on samples (a) Al-02 and (b) Al-06.*

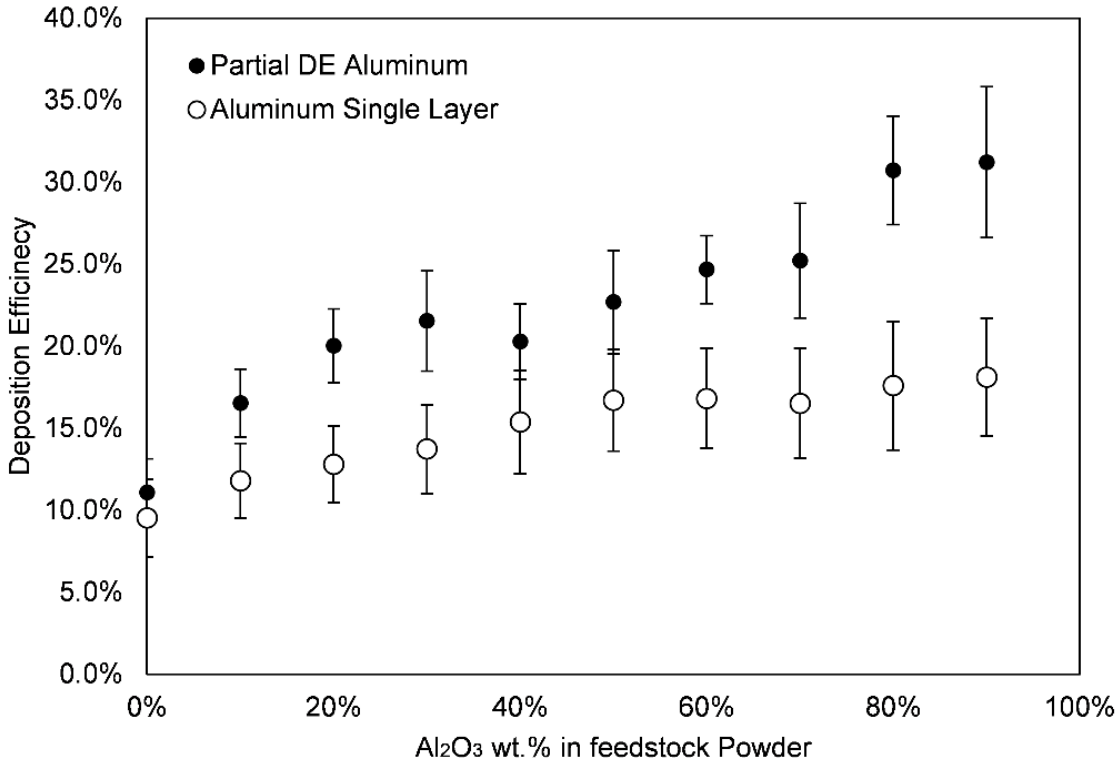


*Figure 20: Partial deposition efficiency of aluminum and of single layer aluminum at different feedstock powder compositions.*

Although the increase in DE due to asperities follows a clear trend, the asperity mechanism does not completely explain the increment of the partial DE of aluminum particles during the deposition of the mixture. The partial DE observed in the deposition of the mixture showed an increment from 11% to 31% while the single layer deposition showed an increment to 18%. Therefore it is evident that the presence of asperities is not the only mechanism acting to increase DE. The remaining increase in partial DE of aluminum particles is attributed to the last proposed mechanism, the oxide removal during deposition. As the number of asperities increases with the alumina content, the effect of oxide removal also appears to be increasing.

Both mechanisms seem to be very relevant in increasing partial DE of aluminum particles in the spraying of these mixtures as it is represented in Figure 21. In this figure, the partial contribution of each mechanism is showed over the base DE seen in the deposition of pure aluminum. It is important to notice that Figure 21 illustrates the contribution of each mechanism brought by the presence of ceramic particles in the feedstock powder.

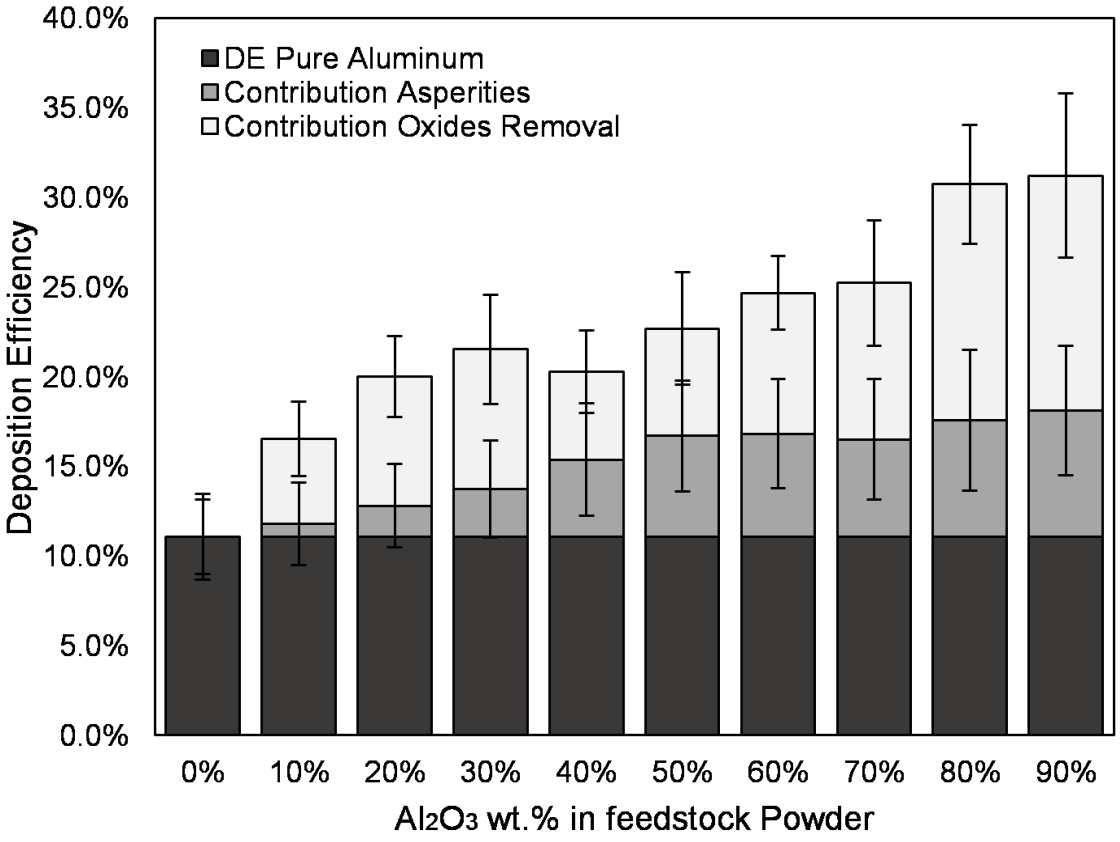


*Figure 21: Partial Deposition efficiency of pure aluminum at different feedstock powder compositions showing the effect on DE of asperities and oxide removal over DE of pure aluminum.*

An aspect to take into consideration is the morphology of the ceramic. In this study crushed alumina particles were used, and this powder has an angular morphology that promotes the creation of asperities. Similar tests should also be performed using spherical alumina, to suppress or change the asperities produced by the ceramic impacts. This is expected to alter the contribution of this aspect on the DE of the feedstock powder. Also, it is important to mention that the oxide cleaning mechanism is proved under the assumption that no other mechanism is acting toward the increment in DE. If another mechanism is discovered in future investigations, then this mechanism should have to be taken into account in order to re-evaluate the effect of oxide cleaning.

## Mechanical properties and Adhesion Strength

Table 8 shows coating hardness, and the estimated hardness based on coatings composition and on the lower bound rule of mixtures, shown in Equation 6, where $H_c$ is the hardness of the coating, $v$ is the alumina volume composition of the coating, $H_{Al_2O_3}$ is the hardness of alumina (2500 Hv), and $H_{Al}$ is the hardness of a pure aluminum coating [48, 50, 51], this relation account for the load sharing of distributed particles in a matrix. As expected, the hardness is strongly related to the coating ceramic composition; this relationship can be easily seen in Figure 22 where coating composition is plotted against the hardness measured. The estimated hardness values were also plotted in this figure. It can be seen that the coating hardness is higher than the estimated value by the lower bound rule of mixture; this difference is expected as cold spray coatings have an intrinsic higher hardness due to cold working. At coatings with higher alumina composition this difference gets larger as more ceramic particles impact and do not adhere into the coating, further increasing coating work hardening.

$$H_c = \left[\frac{1-v}{H_{Al}} + \frac{v}{H_{Al_2O_3}}\right]^{-1} \qquad 6$$

*Table 8: Measured and estimated hardness of coatings.*

| Sample | Hardness $HV_{0.3}$ | Estimated Hardness |
|---|---|---|
| AL-00 | 45.0 ± 8.9 | 45.0 |
| AL-01 | 52.3 ± 1.3 | 48.2 |
| AL-02 | 64.4 ± 1.6 | 50.2 |
| AL-03 | 68.5 ± 2.8 | 53.0 |
| AL-04 | 72.3 ± 7.1 | 54.4 |
| AL-05 | 78.1 ± 5.7 | 56.9 |
| AL-06 | 79.9 ± 4.3 | 59.6 |
| AL-07 | 86.1 ± 8.1 | 64.3 |
| AL-08 | 89.5 ± 3.9 | 65.4 |
| AL-09 | 114.2 ± 12.1 | 78.6 |
| AL-10 | - | - |

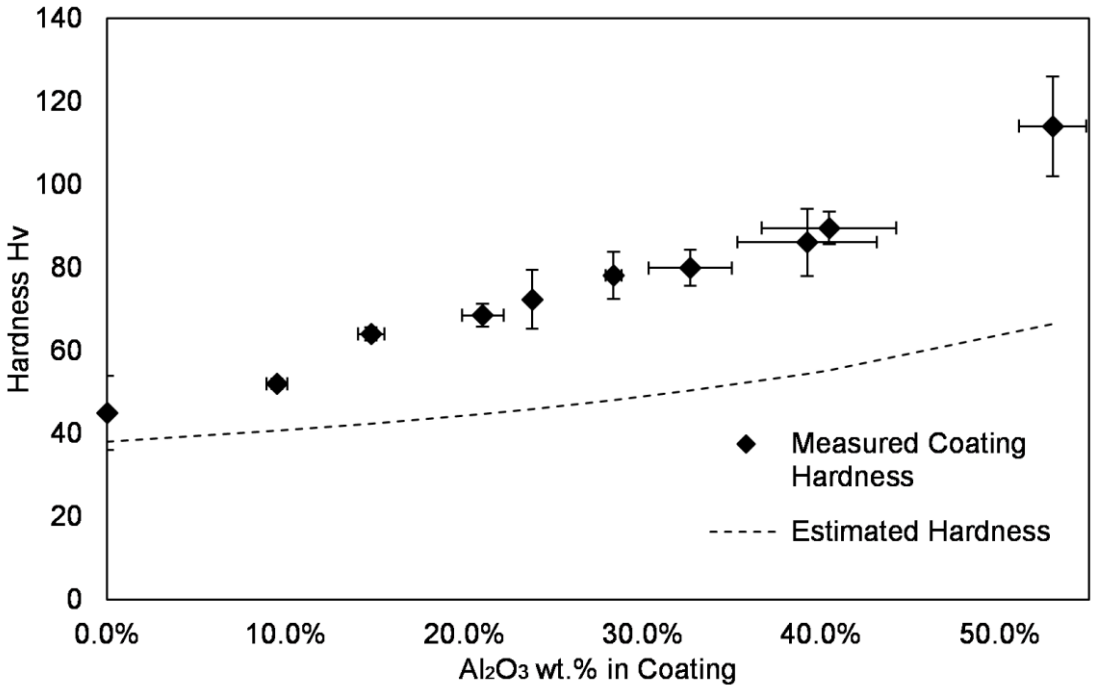


*Figure 22: Measured and estimated hardness of coatings versus coating alumina contents.*

Wear test results are shown in Figure 23. It shows the volume loss of each sample for a travel distance up to 100 m or until the coating was completely worn out. It is easy to see the strong dependence of the ceramic content on the coatings wear resistance. The figure shows three behaviors depending on the coating composition. Coatings with 22wt.% $Al_2O_3$ content or less show almost no benefit in wear resistance compared with the pure aluminum coatings produced. Samples wore to the substrate in a distance travel lower than 5 m. Coatings with composition between

26wt.% $Al_2O_3$ and 33wt.% $Al_2O_3$ showed a sharp increase in wear resistance with ceramic content and extended to 100 m of travel distance without reaching the substrate. Finally, the last behavior seen starts with coating composition of 39wt.% of $Al_2O_3$. These samples showed the highest wear resistance in the study, and no significant increment in resistance is observed in samples with alumina content above 39wt.%. The coatings wear properties appear to have stabilized at this ceramic content level. This wear resistance dependence on the coating composition is common in metal matrix composites [1, 2, 29]. Ceramic particles, besides resisting the wear, help to distribute the stress throughout the material. For compositions with lower ceramic content, this stress distribution does not occur efficiently as the ceramic particles are too spread throughout the coating. The ductile phase deforms excessively and plows the ceramic particles as the wear tip slide through the coating, resulting in little wear resistance provided by the ceramic content. This mechanism changes at higher ceramic content, as the stresses get more distributed and the metallic phase does not suffer as much deformation, and the ceramic can act as a wear resistant material[29, 51, 52].

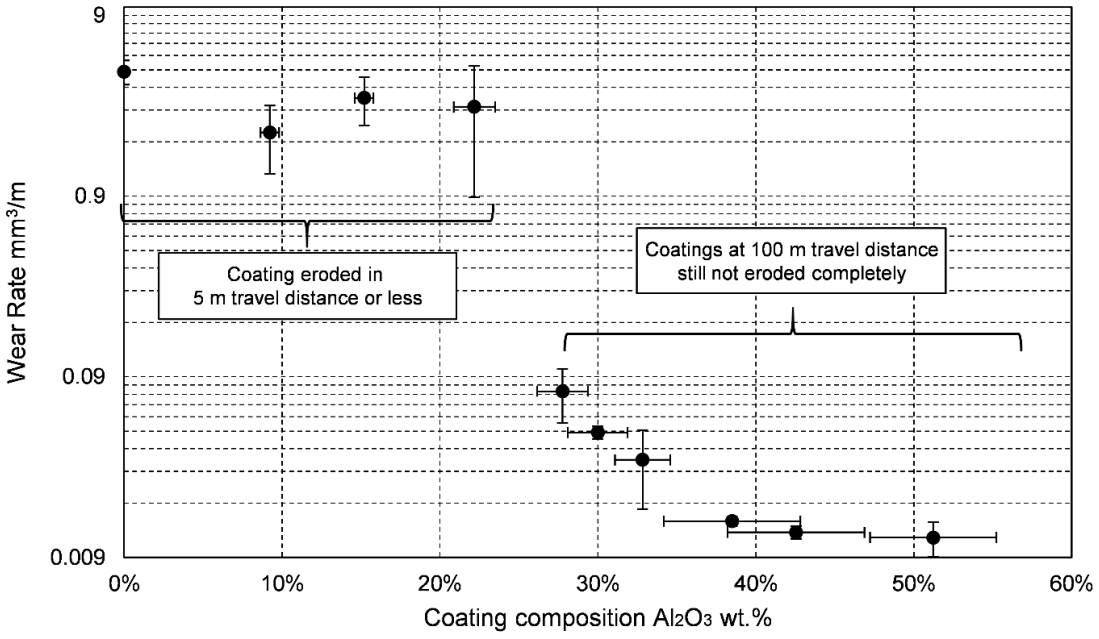


*Figure 23: Wear rate of coatings with different alumina contents, calculated until 100 m or worn to the substrate.*

Finally, the adhesion test results can be seen in Figure 24 where the adhesion strength is shown as a function of the feedstock powder composition. It is clear that the addition of ceramic particles into the feedstock powder greatly increases the coatings adhesion strength. Sample AL-00 showed

an average adhesion strength of 18.6 MPA, and this value increases to values higher than the glue limit (above 70 MPa).

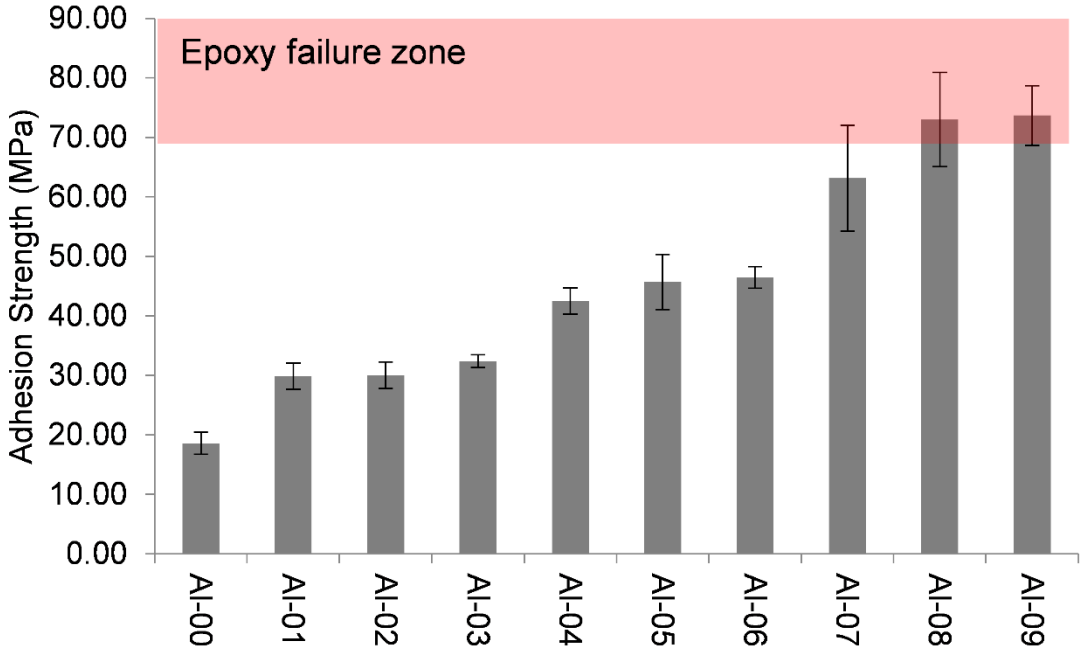


*Figure 24: Adhesion Strength of coatings sprayed with different feedstock powder compositions.*

Irissou et al. have also demonstrated the same behavior as the one seen in Figure 24 [16]. They explained this increase in adhesion by the presence of asperities at the interface, increasing the mechanical bonding between the coating and the substrate. This is supported by this study. However, it is unlikely that mechanical bonding could improve the adhesion strength from 18 MPa to values higher than 70 MPa. It is also important to note that asperities are not the only acting mechanism. It was shown that DE might also be increased by oxide removal, increasing the chances of creating metallurgical bonding. This mechanism also can occur at the coating-substrate interface, considerably increasing the adhesion strength. This result supports the influence of oxide cleaning effect in the increment in DE explained in this study as the combination of these two mechanisms can account for this significant increase in adhesion strength. It is important to note that the adhesion strength appears to have a plateau between specimens Al-04 and Al-06. This behavior is in line with a similar plateau seen in the DE increment related with asperities. These two observations suggest that at higher ceramic compositions, the oxide cleaning effect might be more relevant and that the asperities effect gets saturated.

# Conclusions

This study gives some insights in the production of cermet coatings and helps to understand behaviors previously observed in other investigations. The deposition behavior and effect of feedstock powder ceramic content was analyzed using eleven aluminum-alumina feedstock powder compositions. The DE of each of the composition was measured and revealed an increment of DE with the addition of ceramic content peaking at 30wt.% followed by a consistent decrease reaching 0% DE at 100% $Al_2O_3$. The coatings composition revealed that even though the DE decreased at higher $Al_2O_3$ content, the partial DE of aluminum always increases, confirming that the presence of alumina particles in the flow has a positive effect on the deposition behavior of the aluminum particles. Three different potential mechanisms explaining this behavior were found in the literature and were assessed.

The interaction of ceramic and metallic particles upon impact was studied, showing that an impinging ceramic particle on aluminum particle leads to an increment on pressure, plasticity, and temperature at the aluminum-substrate interface, which might lead to higher chances of deposition of the metallic particle. However, a probabilistic analysis showed that the event is extremely unlikely and thus this effect can be considered negligible. Two other possible mechanisms were studied, namely the effect of asperities and oxide removal. This was done by measuring the DE of a single layer of pure aluminum particles over coatings previously deposited with the different feedstock powder. This showed that both asperity creation and oxide layer removal mechanisms have a major influence in the increment of DE during deposition.

Coatings cross section revealed that almost half of the ceramic content of the feedstock powder is lost but do contribute to coating formation by peening the coating and creating the asperities as well as influencing the coating hardness.Wear resistance was shown to benefit from ceramic content. Three zones of wear resistance were found. In coatings containing 22wt.% of less of alumina, no significant benefit was seen. At higher values, a consistent increase in wear resistance is seen until 39wt.% of $Al_2O_3$. Coating with higher alumina content did not show an increment in wear resistance. Adhesion strength of the coatings also increased with the addition of ceramic particles to the feedstock powder, reaching glue values with coating sprayed with a mixture with 70wt.% of alumina or more. This can be explained by the asperities promoting mechanical bonding Oxide removal are also potentially increasing the adhesion strength by promoting the probabilities of obtaining metallurgical bonding between the particles and the substrate.

# References


1. Tinklepaugh JR (1960) Cermets. Reinhold Publishing Corporation

2. Ellis JL, Goetzel CG (1990) Cermets. In: ASM Handb. Vol. 2 Prop. Sel. Nonferrous Alloy. Spec. Mater. - ASM Int. ASM International, p 1328

3. Bergmann CP, Vicenzi J (2011) Protection against Erosive Wear Using Thermal Sprayed Cermet. Prot against Erosive Wear Using Therm Sprayed Cermet 89. doi: 10.1007/978-3-642-21987-0

4. Evans A, San Marchi C, Mortensen A (Andreas) (2003) Metal matrix composites in industry : an introduction and a survey. Kluwer Academic

5. Dykhuizen RCC, Smith MFF (1998) Gas Dynamic Principles of Cold Spray. J Therm Spray Technol 7:205–212. doi: 10.1361/105996398770350945

6. Tokarev a. O (1996) Structure of aluminum powder coatings prepared by cold gasdynamic spraying. Met Sci Heat Treat 38:136–139. doi: 10.1007/BF01401446

7. Alkhimov AP, Papyrin AN, Kosarev VF, et al (1995) Method and device for coating.

8. Assadi H, Gärtner F, Stoltenhoff T, Kreye H (2003) Bonding mechanism in cold gas spraying. Acta Mater 51:4379–4394. doi: 10.1016/S1359-6454(03)00274-X

9. Schmidt T, Assadi H, Gärtner F, et al (2009) From particle acceleration to impact and bonding in cold spraying. J Therm Spray Technol 18:794–808. doi: 10.1007/s11666-009-9357-7

10. Grujicic M, Saylor JR, Beasley DE, et al (2003) Computational analysis of the interfacial bonding between feed-powder particles and the substrate in the cold-gas dynamic-spray process. Appl Surf Sci 219:211–227. doi: 10.1016/S0169-4332(03)00643-3

11. Grujicic M, Zhao CL, Tong C, et al (2004) Analysis of the impact velocity of powder particles in the cold-gas dynamic-spray process. Mater Sci Eng A 368:222–230. doi: 10.1016/j.msea.2003.10.312

12. Hussain T, McCartney DG, Shipway PH, Zhang D (2009) Bonding mechanisms in cold

spraying: The contributions of metallurgical and mechanical components. J Therm Spray Technol 18:364–379. doi: 10.1007/s11666-009-9298-1

13. Dykhuizen RCC, Smith MFF, Gilmore DLL, et al (1999) Impact of High Velocity Cold Spray Particles. J Therm Spray Technol 8:559–564. doi: 10.1361/105996399770350250

14. Samson T, MacDonald D, Fernández R, Jodoin B (2015) Effect of Pulsed Waterjet Surface Preparation on the Adhesion Strength of Cold Gas Dynamic Sprayed Aluminum Coatings. J Therm Spray Technol 24:984–993. doi: 10.1007/s11666-015-0261-z

15. Koivuluoto H, Vuoristo P (2010) Structural Analysis of Cold-Sprayed Nickel-Based Metallic and Metallic-Ceramic Coatings. J Therm Spray Technol 19:975–989. doi: 10.1007/s11666-010-9481-4

16. Irissou E, Legoux J-G, Arsenault B, Moreau C (2007) Investigation of Al-Al2O3 Cold Spray Coating Formation and Properties. J Therm Spray Technol 16:661–668. doi: 10.1007/s11666-007-9086-8

17. Sova a., Papyrin A, Smurov I (2009) Influence of Ceramic Powder Size on Process of Cermet Coating Formation by Cold Spray. J Therm Spray Technol 18:633–641. doi: 10.1007/s11666-009-9359-5

18. Wang Q, Spencer K, Birbilis N, Zhang M-X (2010) The influence of ceramic particles on bond strength of cold spray composite coatings on AZ91 alloy substrate. Surf Coatings Technol 205:50–56. doi: 10.1016/j.surfcoat.2010.06.008

19. Shkodkin a., Kashirin A, Klyuev O, Buzdygar T (2006) Metal Particle Deposition Stimulation by Surface Abrasive Treatment in Gas Dynamic Spraying. J Therm Spray Technol 15:382–386. doi: 10.1361/105996306X124383

20. Finnie I, McFadden DH (1978) On the velocity dependence of the erosion of ductile metals by solid particles at low angles of incidence. Wear 48:181–190. doi: 10.1016/0043-1648(78)90147-3

21. Sova a., Kosarev VF, Papyrin A, Smurov I (2010) Effect of Ceramic Particle Velocity on Cold Spray Deposition of Metal-Ceramic Coatings. J Therm Spray Technol 20:285–291. doi: 10.1007/s11666-010-9571-3

22. Wang YX, Yang H, Lim G, Li Y (2010) Glass formation enhanced by oxygen in binary Zr–Cu system. Scr Mater 62:682–685. doi: 10.1016/j.scriptamat.2010.01.023

23. Wang Y, Normand B, Mary N, et al (2014) Microstructure and corrosion behavior of cold sprayed SiCp/Al 5056 composite coatings. Surf Coatings Technol 251:264–275. doi: 10.1016/j.surfcoat.2014.04.036

24. Lima R., Karthikeyan J, Kay C., et al (2002) Microstructural characteristics of cold-sprayed nanostructured WC–Co coatings. Thin Solid Films 416:129–135. doi: 10.1016/S0040-6090(02)00631-4

25. Silva FS d., Bedoya J, Dosta S, et al (2017) Corrosion characteristics of cold gas spray coatings of reinforced aluminum deposited onto carbon steel. Corros Sci 114:57–71. doi: 10.1016/j.corsci.2016.10.019

26. Spencer K, Fabijanic DM, Zhang M-X (2009) The use of Al–Al2O3 cold spray coatings to improve the surface properties of magnesium alloys. Surf Coatings Technol 204:336–344. doi: 10.1016/j.surfcoat.2009.07.032

27. Lee HY, Yu YH, Lee YC, et al (2004) Cold Spray of SiC and Al2O3 With Soft Metal Incorporation: A Technical Contribution. J Therm Spray Technol 13:184–189. doi: 10.1361/10599630419355

28. Feng C, Guipont V, Jeandin M, et al (2012) B4C/Ni Composite Coatings Prepared by Cold Spray of Blended or CVD-Coated Powders. J Therm Spray Technol 21:561–570. doi: 10.1007/s11666-012-9774-x

29. Shockley JM, Descartes S, Vo P, et al (2015) The influence of Al2O3 particle morphology on the coating formation and dry sliding wear behavior of cold sprayed Al–Al2O3 composites. Surf Coatings Technol 270:324–333. doi: 10.1016/j.surfcoat.2015.01.057

30. Maev RG, Leshchinsky E (2006) Low Pressure Gas Dynamic Spray : Shear Localization during Particle Shock Consolidation. Therm. Spray 2006 Sci. Innov. Appl.

31. Maev RG, Leshchynsky V (2006) Air Gas Dynamic Spraying of Powder Mixtures: Theory and Application. J Therm Spray Technol 15:198–205. doi: 10.1361/105996306X108048

32. Finnie I (1960) Erosion of surfaces by solid particles. Wear 3:87–103. doi: 10.1016/0043-

1648(60)90055-7

33. Neilson JH, Gilchrist A (1968) Erosion by a stream of solid particles. Wear 11:111–122. doi: 10.1016/0043-1648(68)90591-7

34. Xie Y, Planche M-P, Raoelison R, et al (2016) Investigation on the influence of particle preheating temperature on bonding of cold-sprayed nickel coatings. Surf Coatings Technol. doi: 10.1016/j.surfcoat.2016.09.037

35. Gärtner F, Borchers C, Stoltenhoff T, et al (2003) Numerical and Microstructural Investigations of the Bonding Mechanisms in Cold Spraying. Therm Spray 2003 Avdancing Sci Appl Technol 1–8.

36. Grujicic M, Zhao C. L, DeRosset W. S, Helfritch D (2004) Adiabatic shear instability based mechanism for particles/substrate bonding in the cold-gas dynamic-spray process. Mater Des 25:681–688. doi: 10.1016/j.matdes.2004.03.008

37. Bitter JGA (1963) A study of erosion phenomena. Wear 6:169–190. doi: 10.1016/0043-1648(63)90003-6

38. Wang X, Feng F, Klecka MA, et al (2015) Characterization and modeling of the bonding process in cold spray additive manufacturing. Addit Manuf 8:149–162. doi: 10.1016/j.addma.2015.03.006

39. Bae G, Xiong Y, Kumar S, et al (2008) General aspects of interface bonding in kinetic sprayed coatings. Acta Mater 56:4858–4868. doi: 10.1016/j.actamat.2008.06.003

40. Meng F, Aydin H, Yue S, Song J (2015) The Effects of Contact Conditions on the Onset of Shear Instability in Cold-Spray. J Therm Spray Technol 24:711–719. doi: 10.1007/s11666-015-0229-z

41. WANG X (2007) Adiabatic Shear Localization for Steels Based on Johnson-Cook Model and Second- and Fourth-Order Gradient Plasticity Models. J Iron Steel Res Int 14:56–61. doi: 10.1016/S1006-706X(07)60075-2

42. Liu ZS, Swaddiwudhipong S, Islam MJ (2012) Perforation of steel and aluminum targets using a modified Johnson–Cook material model. Nucl Eng Des 250:108–115. doi: 10.1016/j.nucengdes.2012.06.026

43. Cormier Y, Dupuis P, Jodoin B, Ghaei A (2015) Finite Element Analysis and Failure Mode Characterization of Pyramidal Fin Arrays Produced by Masked Cold Gas Dynamic Spray. J Therm Spray Technol 24:1549–1565. doi: 10.1007/s11666-015-0317-0

44. King PC, Bae G, Zahiri SH, et al (2010) An Experimental and Finite Element Study of Cold Spray Copper Impact onto Two Aluminum Substrates. J Therm Spray Technol 19:620–634. doi: 10.1007/s11666-009-9454-7

45. Saleh M, Luzin V, Spencer K (2014) Analysis of the residual stress and bonding mechanism in the cold spray technique using experimental and numerical methods. doi: 10.1016/j.surfcoat.2014.04.059

46. Papyrin A, Kosarev V, Klinkov S, et al (2006) Cold Spray Technology. Elsevier Science

47. Legoux JG, Irissou E, Moreau C (2007) Effect of Substrate Temperature on the Formation Mechanism of Cold-Sprayed Aluminum, Zinc and Tin Coatings. J Therm Spray Technol 16:619–626. doi: 10.1007/s11666-007-9091-y

48. Hodder KJ, Nychka JA, McDonald A (2014) Comparison of 10 μm and 20 nm Al-Al2O3 Metal Matrix Composite Coatings Fabricated by Low-Pressure Cold Gas Dynamic Spraying. J Therm Spray Technol 23:839–848. doi: 10.1007/s11666-014-0094-1

49. Wu J, Fang H, Yoon S, et al (2005) Measurement of particle velocity and characterization of deposition in aluminum alloy kinetic spraying process. Appl Surf Sci 252:1368–1377. doi: 10.1016/j.apsusc.2005.02.108

50. Hodder K, Izadi H, McDonald A, Gerlich A (2012) Fabrication of aluminum-alumina metal matrix composites via cold gas dynamic spraying at low pressure followed by friction stir processing. Mater Sci Eng A 556:114–121. doi: 10.1016/j.msea.2012.06.066

51. Melendez NM, Narulkar V V., Fisher GA, McDonald A (2013) Effect of reinforcing particles on the wear rate of low-pressure cold-sprayed WC-based MMC coatings. Wear 306:185–195. doi: 10.1016/j.wear.2013.08.006

52. Alidokht SA, Manimunda P, Vo P, et al (2016) Cold spray deposition of a Ni-WC composite coating and its dry sliding wear behavior. Surf Coatings Technol 308:424–434. doi: 10.1016/j.surfcoat.2016.09.089

## 5.2 Cold Spray Aluminum-Alumina Cermet Coatings: Effect of Alumina morphology

The results showed in this section addressed the research objective "Study the effect of ceramic morphology in a ceramic-metal blending on the cold spray deposition process". The main focus was to see the effect of the ceramic morphology in the deposition behavior of metal-ceramic blends. Deposition efficiency tests were done and revealed a different behavior between the two feedstock powder morphologies. Coatings sprayed with spherical alumina do not show a peak in DE as the one seen in coatings sprayed with angular alumina. The reason behind this behavior is attributed to the extremely low partial DE of the spherical alumina particles. Asperities created by the spherical alumina particles proved to have no effect in the partial DE of aluminum proving that this effect is closely related to the morphology of the asperities created. Retention of ceramic particles in the coatings changed drastically with the morphology of the ceramic particles. Interrupted spray tests were performed and helped obtaining insights into the coating building process. Mechanical testing of the coatings showed a strong relationship with the ceramic morphology. Hardness values tended to be higher in coatings sprayed with angular alumina due to their higher ceramic contents, but coatings sprayed with spherical alumina showed to have a higher hardness. Adhesion strength showed to be higher in coatings sprayed with angular alumina. It was hypothesized that the peening done by the spherical alumina particles improved the adhesion of the coatings. Lastly, dry slide wear tests proved to be more related to ceramic content than to the ceramic morphology.

# Cold Spray Aluminum-Alumina Cermet Coatings: Effect of Alumina morphology

Ruben Fernandez, Bertrand Jodoin

University of Ottawa Cold Spray Research Laboratory, Ottawa, ON, Canada.

## Abstract

The effect of alumina morphology on the deposition efficiency and coatings mechanical properties is investigated in the cold spray deposition of aluminum-alumina cermets. Deposition of aluminum mixed with spherical alumina and angular alumina are compared for six different feedstock powder compositions for each alumina morphology. The addition of small amounts of angular alumina particles in the feedstock powder induces an increase in deposition efficiency followed by a decrease as the alumina composition increases. This effect is not observed when spherical alumina is used. The creation of asperities during deposition was explored for the two morphologies and it was determined that spherical alumina does not produce intricate asperities at the coating surface explaining the difference in deposition efficiencies between the powders. The coatings sprayed with spherical alumina showed very little ceramic retention compared with the ones sprayed with angular alumina. These results have a direct impact on the coatings mechanical properties and wear resistance. Hardness was lower in coatings sprayed with spherical alumina for the same feedstock powder composition but were harder when the coating composition is considered. Adhesion strength of coatings significantly increases with the addition of ceramic in the feedstock powder. This increment was greater for coatings sprayed with spherical alumina, reaching the test limit with coatings sprayed with 40wt.% alumina. Deposits sprayed with angular alumina also achieved this limit but for powder with composition higher than 80wt.% $Al_2O_3$. It was determined that these differences in hardness and adhesion were due to a larger amount of plastic deformation in coatings sprayed with spherical alumina due to the lower deposition efficiency of the ceramic particles.

*Keywords: Deposition Efficiency, Cermet, Aluminum-Alumina, Cold Spray, Ceramic Morphology.*

## Introduction

Ceramic-metal composites (cermets) are materials that combine the best properties of metals and ceramics. These composite materials are valued for their hardness, wear resistance, and toughness [1–4]. In the case of aluminum-based cermets, they also show excellent corrosion protection and

low density. The reinforcement material used in aluminum cermets typically consist of SiC or $Al_2O_3$ [5]. Several techniques are used to produce cermets, such as bulk processing, sintering, and more recently cermets have been used as coatings [5–8]. Thermal spray processes are often used to obtain cermet coatings and have shown potential to be used as additive manufacturing processes [9, 10]. Cold gas dynamic spraying, also known as cold spray, has shown great potential in obtaining hard and dense cermet coatings [5–7].

The cold spray process accelerates feedstock powders using a supersonic gas stream produced by a de Laval nozzle [11–13]. Particles are accelerated and impact the substrate in solid state (due to the low process temperatures) and experience severe plastic deformation [14–16]. The particles (usually metallic) adhere to the substrate either through mechanical or metallurgical bonding [11, 14, 17–20]. In order to deposit cermets, reinforcement and matrix particles are mixed as feedstock powder [21–28]. During deposition, a fraction of the reinforcement particles are retained in the coating [21, 24]. These particles (ceramics) do not experience plastic deformation, but rather embed themselves between the ductile particles, consolidating the cermet into coatings [24, 29].

The coatings ceramic content is the primary cause of the mechanical properties improvement, such as hardness and wear resistance. In addition, the ceramic particles also affect the deposition behavior in cold spray as demonstrated in several investigations [21–25, 30]. Deposition efficiency (DE) was shown to increase with relatively small amounts of ceramic in the feedstock powder. Furthermore, the coatings adhesion strength have been shown to increase dramatically with feedstock powder ceramic content. Several hypotheses have arisen to explain these behaviors and have been proposed by several researchers. In previous work, the influence of feedstock powder ceramic content on the deposition behavior and the effect on mechanical properties was investigated [21, 23–25, 31]. Three proposed mechanisms were assessed. One of these mechanisms stating that the increment in DE is due to the peening of ceramic particle on the metallic phase upon impact was invalidated. The other two mechanisms, namely the creation of surface asperities and the oxide cleaning effect caused by the ceramic particles impacting the surface of the substrate proved to be relevant in the increment of the DE.

Investigation of the effect of $Al_2O_3$ morphology in Al-$Al_2O_3$ cold spray coatings with a focus on wear resistance was performed [25]. That study used two feedstock powder compositions (10wt%, and 50 wt.% of $Al_2O_3$) and showed that spherical $Al_2O_3$ morphology was associated to improved tribological properties compared to the angular $Al_2O_3$ morphology for similar $Al_2O_3$ coating

contents. The investigation also considered tests to investigate the deposition behaviors, but no clear trend could be observed using just two feedstock powder compositions.

The ceramic morphology can have a strong influence on the deposition behavior of cold spray coatings. It was shown that one of the largest cause of the change in DE with feedstock powder ceramic content was due to the creation of asperities by the ceramic particles used (crushed alumina) [21, 24]. The morphology of these asperities was attributed to the sharp edges of the crushed alumina indenting the metallic particles. These asperities were correlated with a DE increment as well as with an increase in adhesion strength. Another effect of the ceramic morphology is its retention level in the coating. A high ceramic retention in coatings is obtained when angular ceramics such as crushed alumina are used, due to the locking of the angular edges of the ceramic particles in the metallic phase [32]. The utilization of different ceramic particle morphologies may alter these effects, changing the deposition behavior and the coating mechanical properties [25][32].

In this study, the effect of ceramic particles morphology on the deposition behavior and mechanical properties of cold spray cermet coatings is explored. Spherical alumina particles are mixed with pure aluminum particles to produce the feedstock powders and sprayed. The results are compared with results obtained using angular crushed alumina particles and aluminum particles. The effect of the ceramic particles morphology on the asperities created on the coatings surface is explored, and its influence on deposition efficiency and coatings mechanical properties is assessed. This investigation contributes in widening the understanding of the deposition of cermet powders by cold spray.

# Experimental procedure

Different tests were performed in order to assess the influence of the ceramic particles morphology on the deposition efficiency, as well as coatings hardness and adhesion strength.

## Materials and mixtures

Three different powders were used to produce two different feedstock powders. The metallic powder was a commercially pure aluminum powder (SST-A5001, Centerline Ltd., Windsor, Ontario, Canada). It is an irregular shaped gas atomized powder, as shown in Figure 1 (a), with an average particle diameter of 26 µm. The detailed particle distribution is shown in Figure 2 (a). The ceramic particles used in this study were two different $Al_2O_3$ powders: a crushed powder with angular morphology (referred to as angular alumina), and a plasma spheroidized powder (referred

to as spherical alumina). The angular alumina powder selected was the G-0001 (also from Centerline), and is shown in Figure 1 (b). It has an average particle size of 22µm. The spherical alumina used was the Al2O3-2N-45 (Tekna Advance Materials Inc, Sherbrooke, Quebec, Canada), shown in Figure 1(c). It has an average particle size of 32µm.

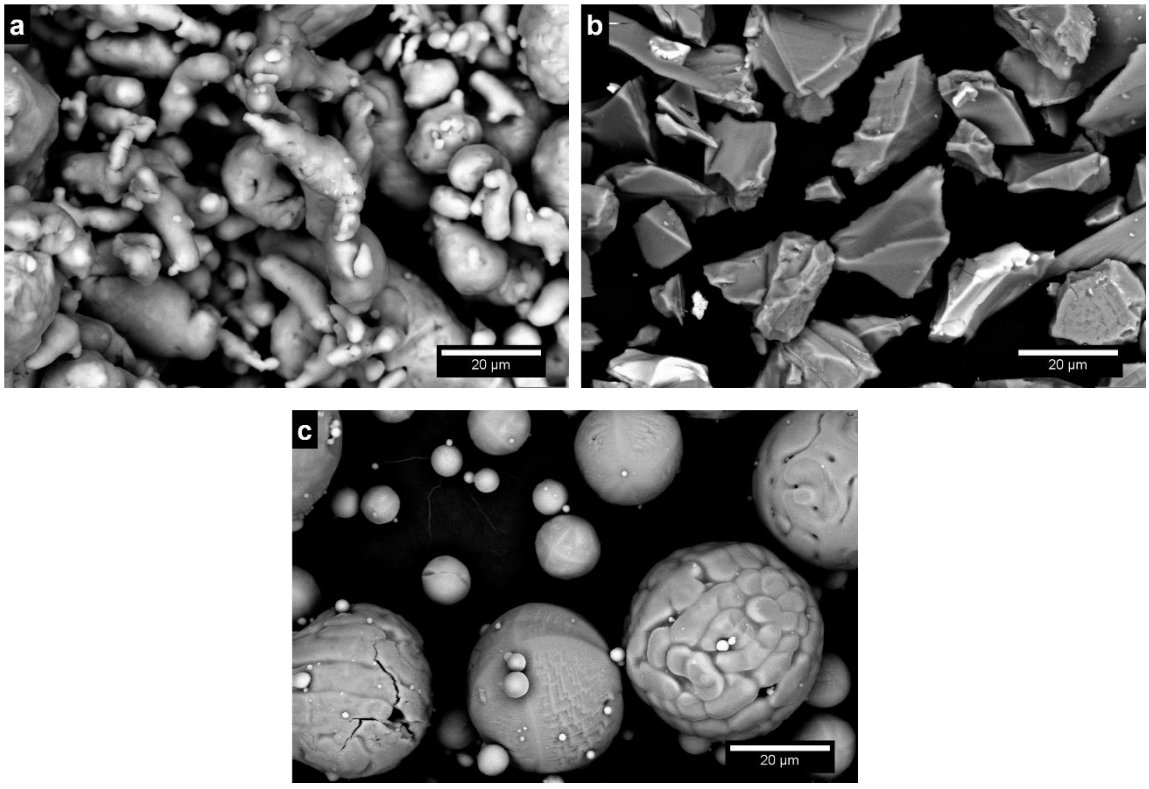


*Figure 1: Overview of particles used : (a) Aluminum particles; (b) Angular $Al_2O_3$ particles (c) Spherical $Al_2O_3$ particles.*

Particle size distribution of both ceramic powders can be seen in Figure 2 (b) and (c). Aluminum 6061-T6 was used as the substrate material. Even though the average particle size of the two alumina powders are not the same, these values are just a reference as the average particle size does not represent the angular powder accurately. Furthermore, both are in the same size range and this difference should not influence the mechanisms being studied. Six different compositions of aluminum-alumina were mixed for each of the alumina particle morphology and used as feedstock powder for this work. Table 1 shows the feedstock powder compositions used.

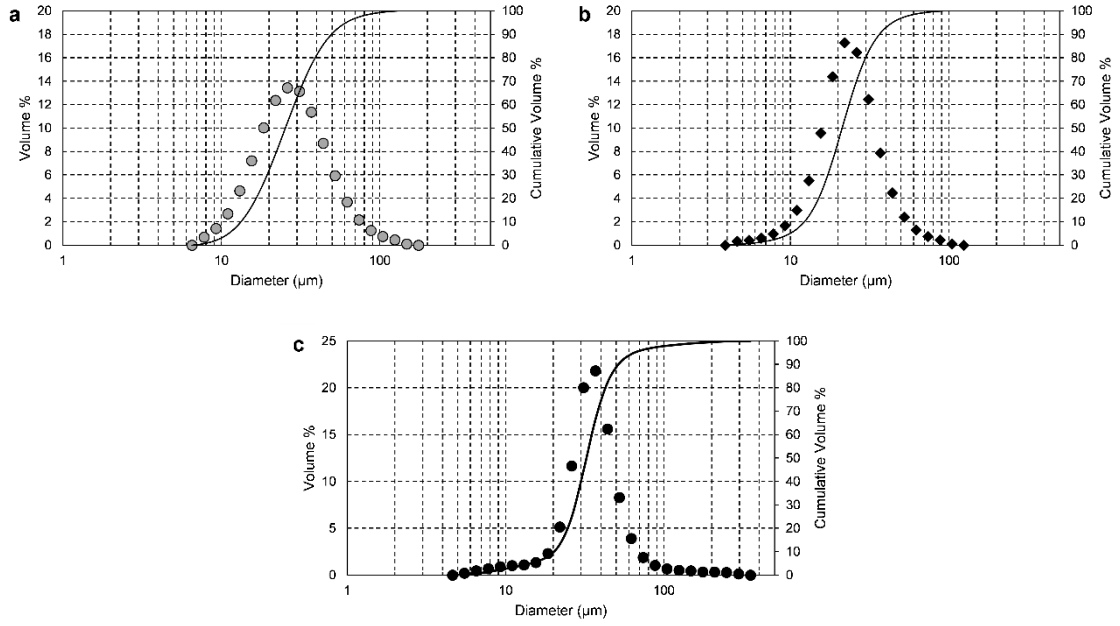


*Figure 2: Particle size distribution: (a) Aluminum particles; (b) Angular $Al_2O_3$ particles; (c) Spherical $Al_2O_3$ particles.*

*Table 1: Feedstock powder composition.*

| **Composition designation** | **Feedstock powder Al wt.%** | **Feedstock powder $Al_2O_3$ wt.%** |
|---|---|---|
| Ang-00 / Sph-00 | 100% | 0% |
| Ang-02 / Sph-02 | 80% | 20% |
| Ang-04 / Sph-04 | 60% | 40% |
| Ang-06 / Sph-06 | 40% | 60% |
| Ang-08 / Sph-08 | 20% | 80% |
| Ang-10 / Sph-10 | 0% | 100% |

## Cold Spray Deposition

A low-pressure cold spray system was used to deposit the coatings. The commercially available EP Series SST Low Pressure Cold Spray System (Centerline Ltd., Windsor, Ontario, Canada) consists of a 15 kW heater with a maximum gas temperature of 500°C and a maximum gas pressure of 3.8 MPa. The De Laval nozzle used for this work has a throat diameter of 2 mm and a diverging section length and exit diameter of 120 mm and 6.6 mm respectively. The feedstock powders were fed using a commercially available rotatory powder feeder. All coatings were sprayed using the spray parameters given in Table 2.

*Table 2: Cold Spray Parameters Used*

| Parameter | Value |
|---|---|
| Gas Temperature | 250 °C |
| Gas Pressure | 1.65 MPa |
| Gas Nature | Nitrogen |
| Traverse Speed | 20 mm/s |
| Passes | 3 |
| Feed conditions | 320 holes Wheel at 8 RPM |
| Standoff Distance | 15 mm |

## Coating Characterization

Coatings were cross-sectioned and analyzed with an optical microscope (VHX-1000, Keyence Corporation, Osaka, Japan), and with and scanning electron mycoscopy (SEM) model EVO MA-10 (Carl Zeiss AG, Oberkochen, Germany). The ceramic composition was measured by contrast imaging and by energy-dispersive X-ray spectroscopy (EDS) using an INCA X-Act (Oxford Instruments, Oxford, England). To assess the process deposition efficiency, the powder feed rate was measured prior and post deposition as well as the substrate weight, using a Sartorius Extend—model ED124S scale, with a readability of 1 mg.

Partial deposition efficiencies were also calculated for aluminum and alumina particles in order to compare the effect of the different alumina morphologies. This was calculated based on the coatings ceramic composition measured by optical contrast and by EDS. The DEs of single layers of pure aluminum sprayed on coatings produced were also measured to assess the effect of surface asperities by different alumina morphologies. This test consist in spraying a single layer of aluminum on top a coatings previously deposited using the various feedstock powder mixtures. This coating keeps the original surface morphology (asperities) but the native oxide layer has grown as it has been exposed to standard conditions for a long period of time (72 h) prior to the pure aluminum layer deposition. Special care is taken in handling the sample to maintain the surface morphology intact. To spray the single layer, the same spray conditions as those shown in **Error! Reference source not found.**Table 2 were used. However, a lower feed rate was used in order to obtain a single particle layer to study solely the surface topology effect.

In order to visualize the deposition behavior of particles impacting the substrate, interrupted deposition tests were done (wipe tests). To perform this test, a deposition was made under the same spray conditions as a regular coating, but the powder feed rate is intermittently interrupted mid-spray. This test creates zones without particle impact, zones where individually discernable

particles impacted and adhered, zones where the first layer of the coating is being formed and zones where a coating at full thickness is produced. This test allows analyzing the deposition process and understanding particle deformation and bonding mechanisms.

### Adhesion Strength and Mechanical Testing

The coatings adhesion strength were measured following ASTM C-633 standard. Cylinders made of aluminum 6061 T6 were coated, and a thermally cured elastomeric adhesive (FM-1000) was used to glue the coatings to counter cylinders. The samples were placed in an oven at 175°C for 2 hours to ensure the adhesive had properly cured. The testing was done using a universal tensile testing machine. The average and standard deviation of each preparation were computed. Vickers microhardness was also measured; values were obtained using a Duramin-10 (Struers ApS, Denmark) equipped with a Vickers micro indenter applying a load of 0.3 kgf. Ten indentations were performed per sample. Finally, dry slide wear tests were carried out on the coatings following the ASTM G133-05 standard. This test was conducted at three different travel lengths: 25 m, 50 m, and 100 m or until the wear reached the substrate. The load applied was 25 N using a 3/16” alumina ball.

## Results and Discussion

### Deposition Behavior

Successful coatings were produced for all the feedstock powders used except for the ones containing pure $Al_2O_3$. Figure 3 and Figure 4 show representative coatings cross-sections obtained when using angular and spherical alumina respectively, at various feedstock powder alumina content. It can easily be observed that coatings sprayed with feedstock powders containing spherical alumina particles show less ceramic particles retention. All deposits were dense, and the coating thickness was the lowest at the highest alumina content in the feedstock powder.

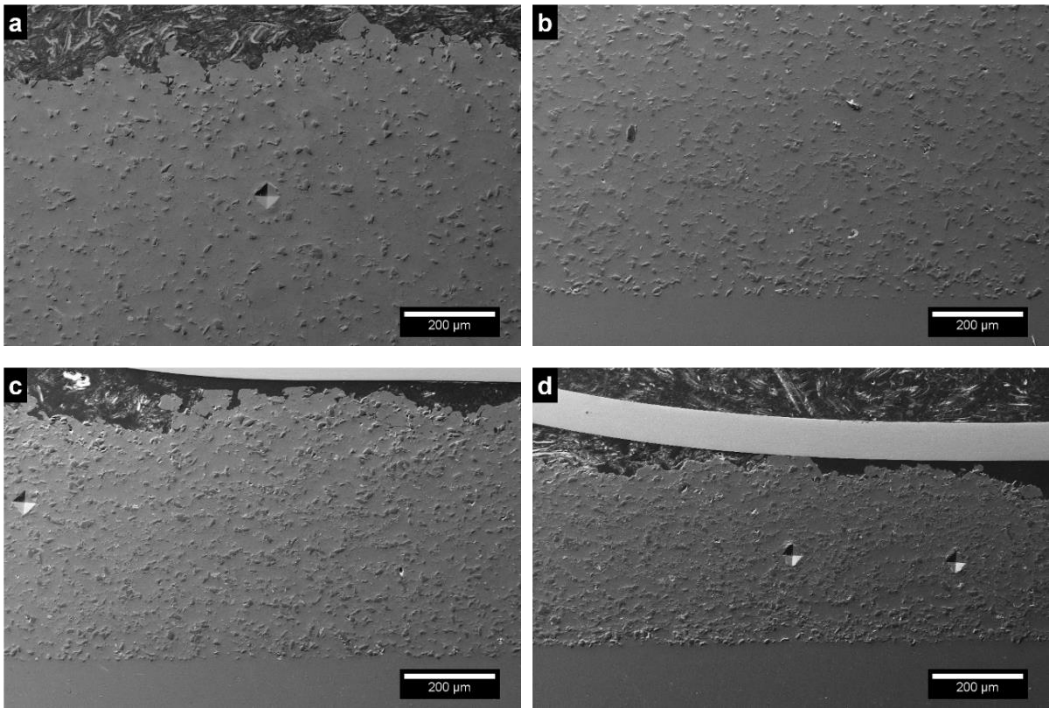


*Figure 3: Cross-sections of coatings sprayed with feedstock powder mixtures containing angular alumina particles: (a) 20 wt.% $Al_2O_3$; (b) 40 wt.% $Al_2O_3$ ; (c) 60 wt.% $Al_2O_3$ ; (d) 80 wt.% $Al_2O_3$.*

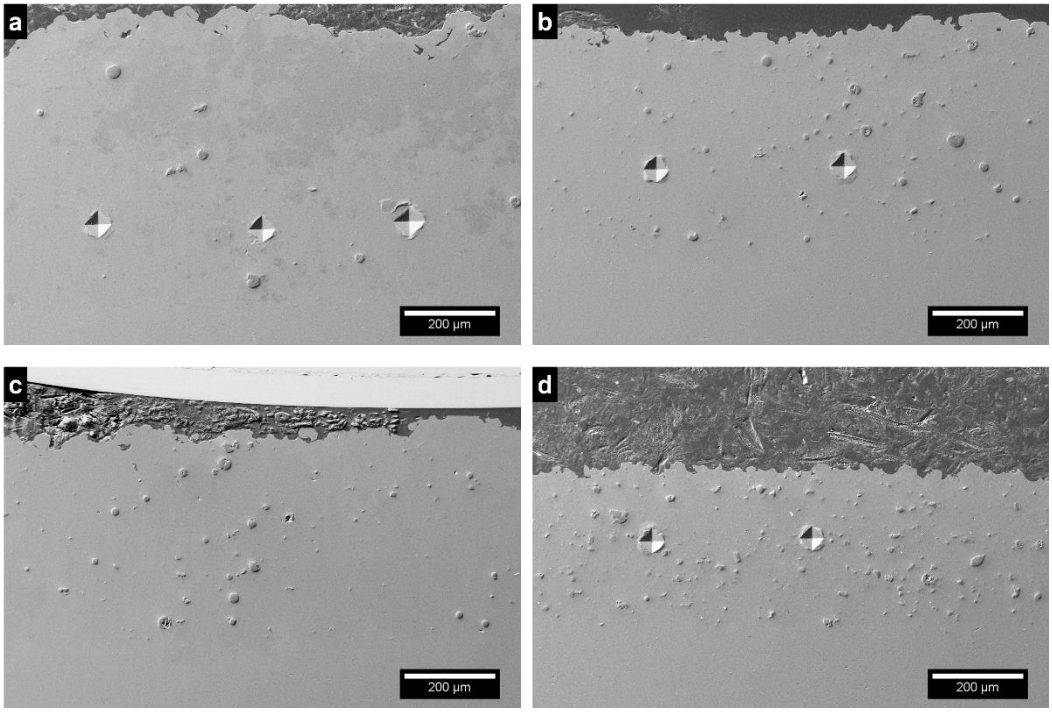


*Figure 4: Cross-sections of coatings sprayed with feedstock powder mixtures containing spherical alumina particles:(a) 20wt.% $Al_2O_3$; (b) 40wt.% $Al_2O_3$; (c) 60wt.% $Al_2O_3$; (d) 80wt.% $Al_2O_3$.*

Deposition efficiency of each mixture is shown in Figure 5. It clearly exhibits differences in the deposition behavior of feedstock powders containing angular ceramic particles versus feedstock powders containing spherical ceramic particles. Aluminum powder mixed with angular $Al_2O_3$ powder presents an increase in DE. The DE rose from 11% to 19% when the feedstock powder composition changed from 0 wt.% $Al_2O_3$ to 20 wt.% $Al_2O_3$. In comparison, feedstock powder made of aluminum mixed with spherical alumina particles showed a continuous decreased in DE, showing no benefits from the presence of the spherical ceramic particles.

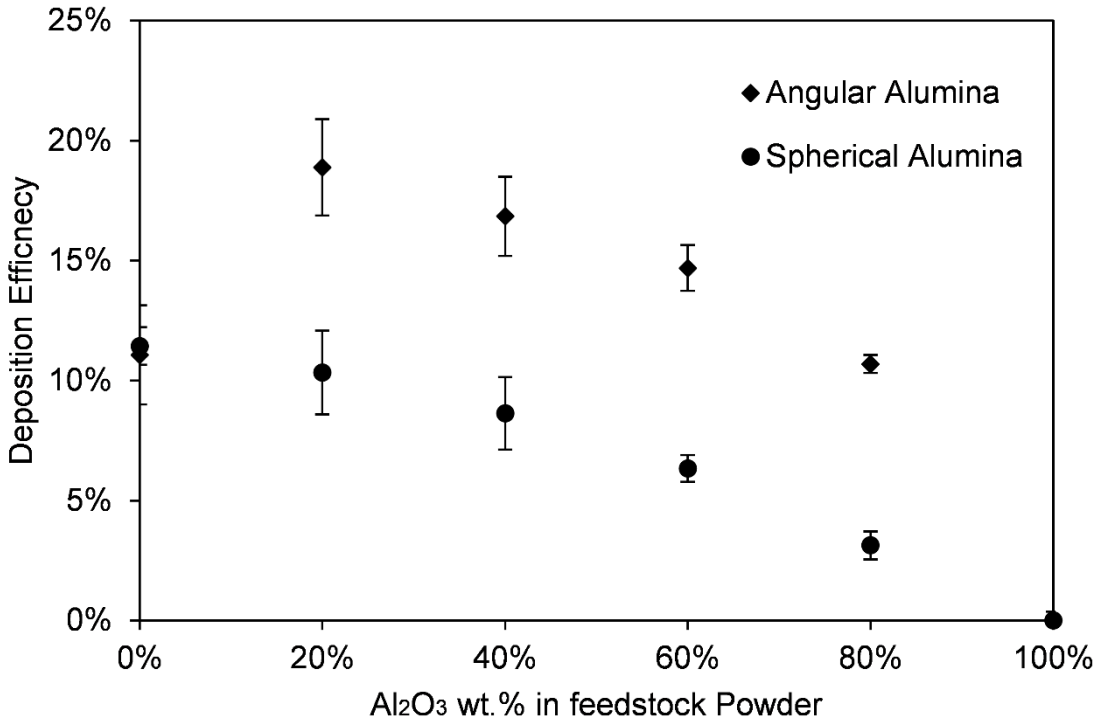


*Figure 5: Measured deposition efficiency of different feedstock powder compositions and alumina morphology.*

The retention of ceramic particles in the coatings is another significant difference observed between the deposits produced. Figure 6 shows the ceramic retention in coatings for both spherical and angular alumina powders at different feedstock powder compositions. The ceramic content was measured by optical contrast and by EDS. While the amount of alumina content in the coatings sprayed with angular ceramic particles is approximately half of the one in the feedstock powder, the amount seen in coatings sprayed with spherical alumina particle showed less than 10% retention of the ceramic particles.

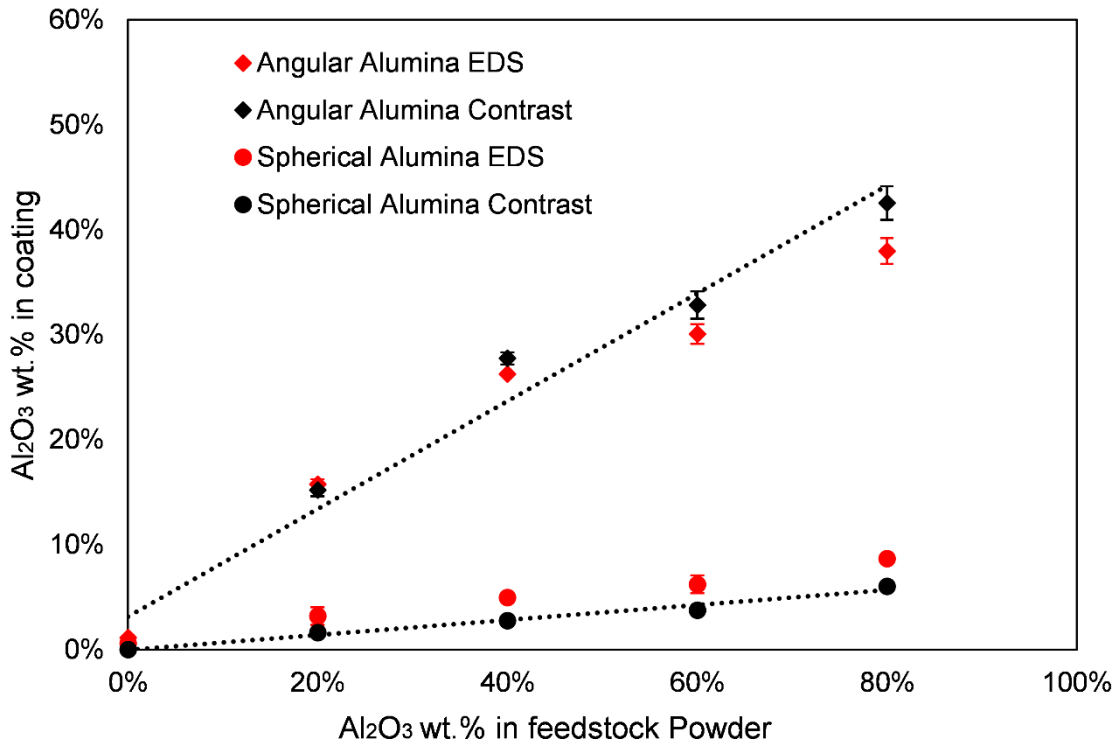


*Figure 6: Alumina content in coatings versus feedstock powder alumina content, as measured by two different methods.*

These drastic differences in the deposition behavior can clearly be attributed to the difference in the ceramic particle morphology of the feedstock powder. The higher retention of angular ceramic particles can be explained by a higher probability of embedding (mechanically anchering) an irregular particle into the coating over a spherical one. Figure 7 compares the coatings surface sprayed with feedstock powder for samples produced with 20 wt.% of $Al_2O_3$ in the feedstock powder, for both alumina morphologies. It is evident from the images that the alumina retention mechanisms are different depending on its morphology. The sharp edges of angular alumina help to lock the particles in the aluminum upon impact. As Getu et al. concluded in their work about embedment of angular materials [33], the embedment of ceramic in a plastic material will depend mainly on the impact velocity, angularity (how sharp is the incident edge) and the friction coefficient between the substrate and the ceramic. Hadavi and Papini demonstrated using numerical simulations that this is also true for aluminum substrates [34]. Both alumina particle types have the velocity needed to embed, and the friction coefficient is similar in both cases, but just the angular alumina has the angularity to embed in the aluminum and lock itself in it while the spherical

alumina has to get trapped between aluminum particles in order to adhere to the coating. Figure 7 shows this trapped alumina but also shows several places where spherical alumina particles peened the deposited aluminum particles and did not get embedded and just deformed the substrate.

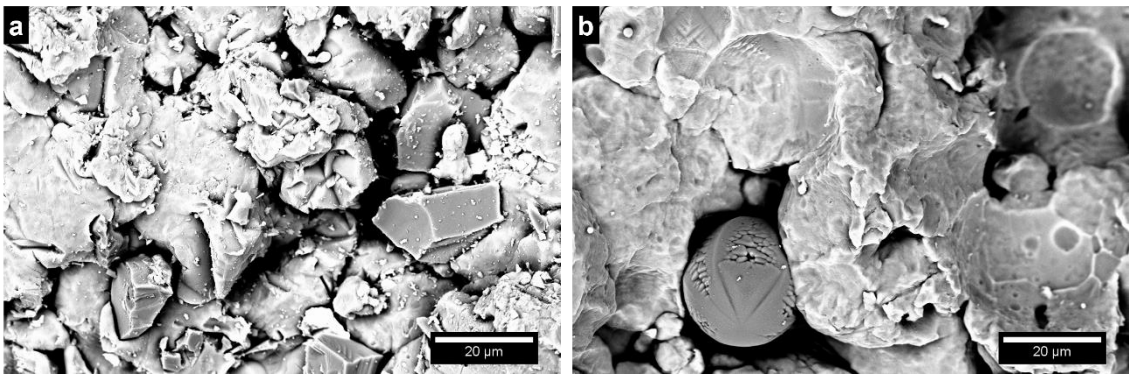


*Figure 7: Top view of coatings sprayed using feedstock powders with 20wt% $Al_2O_3$ detailing the embedding mechanisms of alumina: (a) Angular alumina ; (b) Spherical alumina.*

The physics behind the differences in DEs of the two feedstock powder mixtures is not as straightforward as several mechanisms might be acting to alter it. The partial DE of aluminum particles in the feedstock mixture can be affected by the amount and geometry of asperities caused by the alumina particles impacting the deposited layer as well as the amount of oxide removal resulting from the alumina particles impacts. In addition, the DE will be affected by the amount of alumina in the deposit, as alumina cannot deposit on itself due to lack of ductility.

The partial DE of aluminum and $Al_2O_3$ particles are shown in Figure 8 for each alumina morphology, as a function of alumina content of the feedstock powder. Figure 8(a) shows that the partial DE of aluminum increases considerably as the angular alumina content increases in the feedstock powder, going from 11% in pure aluminum to 30% in the case of the powder with 80wt.% of angular alumina. In addition, it also shows the partial DE of angular alumina also increases with the presence of aluminum. As more aluminum is mixed in the feedstock powder, more chances are for the alumina particles to embed into the coating, increasing the partial DE of angular alumina. Therefore, two competing effects of partial DEs are acting as the alumina content increases. At low alumina content, the increasing partial DE of aluminum particles and the higher aluminum content in the powder results in an increase of the overall DE. But, as the alumina composition increases, its decreasing partial DE overcomes the effect of the increase of aluminum partial DE, resulting in a decrease of the overall DE at high alumina content.

Figure 8(b) shows a different scenario. The partial DE of pure aluminum also shows an increase when the spherical alumina content in the feedstock powder increases, but this increase is considerably lower than the one observed for angular alumina. Partial DE of spherical alumina particles shows a negligible increment with the aluminum content (below 1%). This effect results in an overall DE that is constantly decreasing. As the alumina content increases, its low partial DE dominates and overcomes the slight increase seen in partial DE of aluminum.

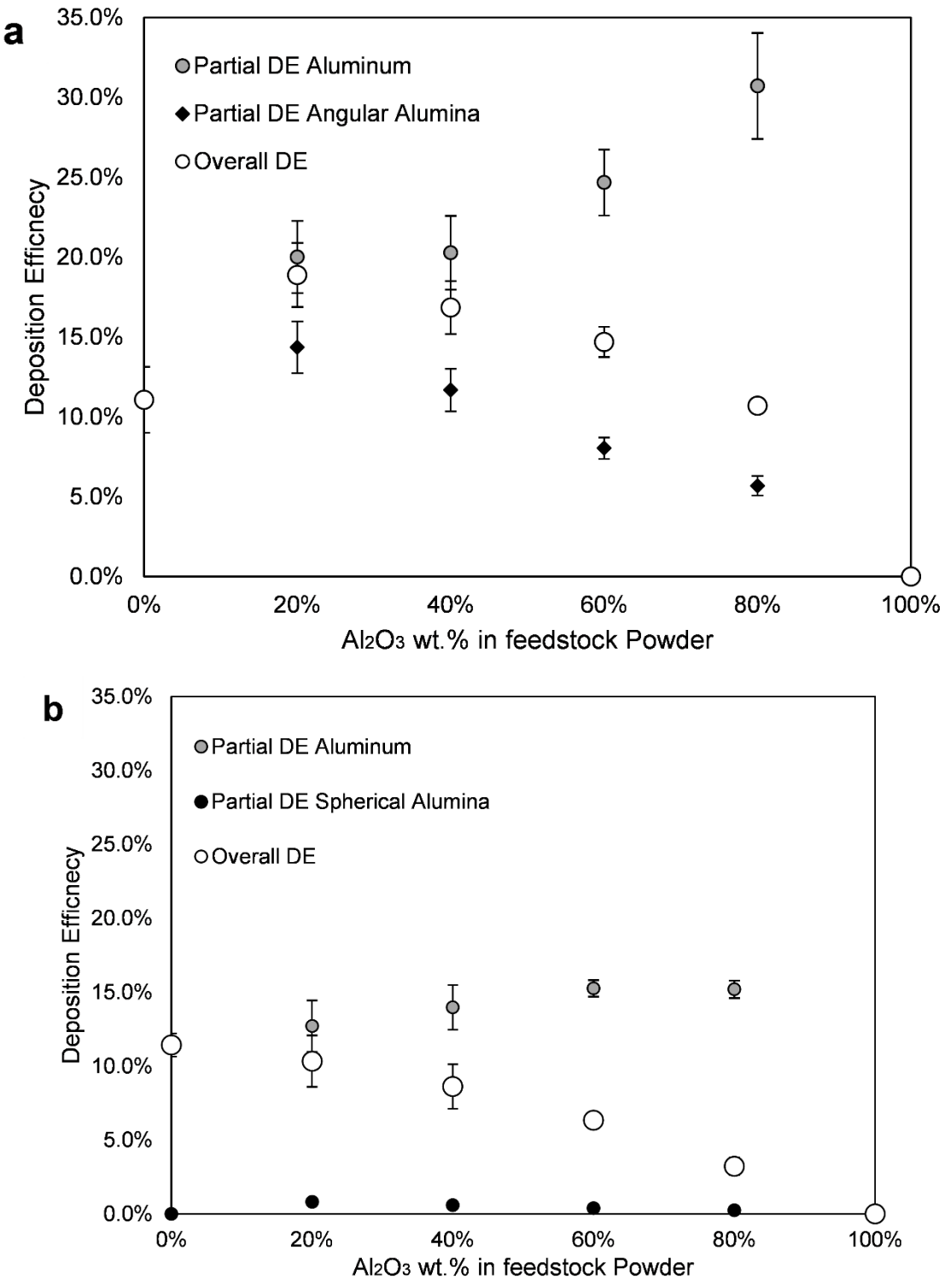


*Figure 8: Partial and overall deposition efficiency for each feedstock powder composition and morphology: (a) Angular alumina ; (b) Spherical alumina.*

It was suggested in a previous study that the increment in partial DE of the aluminum particles when mixed with angular alumina particles is due mainly to 2 mechanisms: The creation of new surface asperities and the removal of superficial oxides [21, 31, 35–37]. It was shown that asperities are created by the impact of angular alumina particles on previously deposited aluminum particles and that these asperities are increasing the probabilities of an aluminum particle to adhere mechanically to the coating. Furthermore, where alumina particles create these asperities, they also clean the superficial oxide by cutting and deforming the surface of the previously deposited aluminum particles. These oxide-free surfaces enhance the probability of metallurgical bonding due to the intimate contact they can provide to the impacting particles and therefore contribute to increasing the DE of aluminum particles.

In the case of spherical alumina particles, the oxide removal effect due to the deformation inflicted upon impact is also expected. However, the morphology of asperities resulting from spherical alumina impacts is anticipated to be different from angular particles due to the absence of sharp edges. Figure 9 shows a comparison of the coatings surfaces sprayed with feedstock powders containing 80 wt.% of $Al_2O_3$. Coatings sprayed with feedstock powder containing angular alumina particles (Figure 9(a)) exhibit a surface covered with asperities and present a high amount of embedded ceramic particles. However, the surfaces of coatings sprayed with feedstock powder containing spherical alumina particles (Figure 9(b)) show a completely different topology, with limited presence of asperities and a high amount of large craters as a result of plastic deformation of the surface.

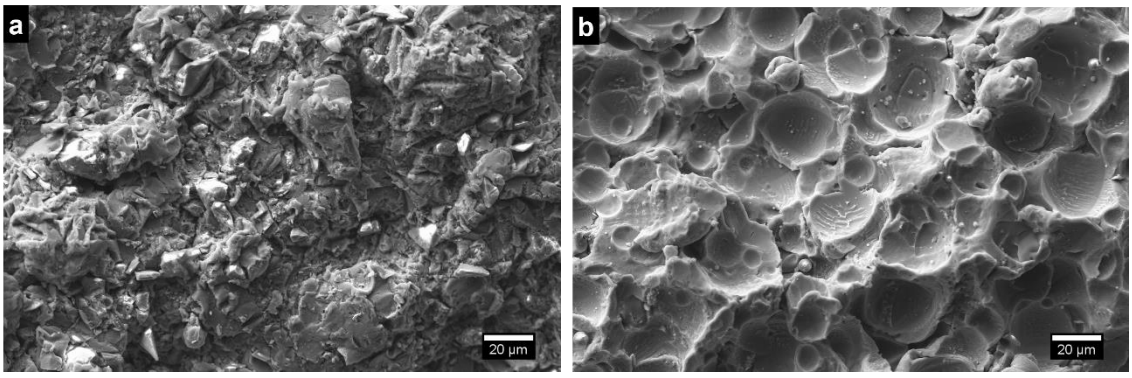


*Figure 9: Top view of coatings surface when using feedstock powder with 80wt% $Al_2O_3$, detailing surface morphology: (a) Case when angular alumina is used showing asperities; (b) Case when spherical alumina is used showing large crater-like deformation.*

An aluminum single layer DE test was performed on the surface of previously deposited coatings. This test allows separating the effects of oxide removal and surface asperities creation, by evaluating just the contribution of the asperities on the DE of aluminum. Figure 10(a) shows the results of the aluminum single layer test on coatings sprayed with feedstock powders containing angular alumina particles. It shows that the DE of aluminum particles increases as the alumina content increases. This increment is lower than the one measured in the partial DE of the coating, and is attributed solely to the presence of asperities at the surface as this test suppresses the oxide removal effect. As the ceramic content in the feedstock powder increases, the density of asperities at the surface leads to an increment in the DE. The coatings sprayed with feedstock powder containing spherical alumina particles (Figure 10(b)) showed no significant increase of DE for the single layer tests. This result confirms the effects previously seen in Figure 9 where limited presence asperities and a different surface topology were observed at the surface of theses coatings. The remaining of the increment in DE seen between the aluminum partial DE and the single layer test (the difference between the two curves in Figure 10(a) and in Figure 10(b)) is attributed to the oxide cleaning effect of the ceramic particles. From Figure 10(a) and (b) it is easy to see that this effect is more important in coating with angular alumina particles than in the ones with spherical alumina particles. It is possible that the oxide-free surface area created by the angular alumina is larger than the one produced by spherical alumina. Further studies are needed in order to understand the reason behind this effect.

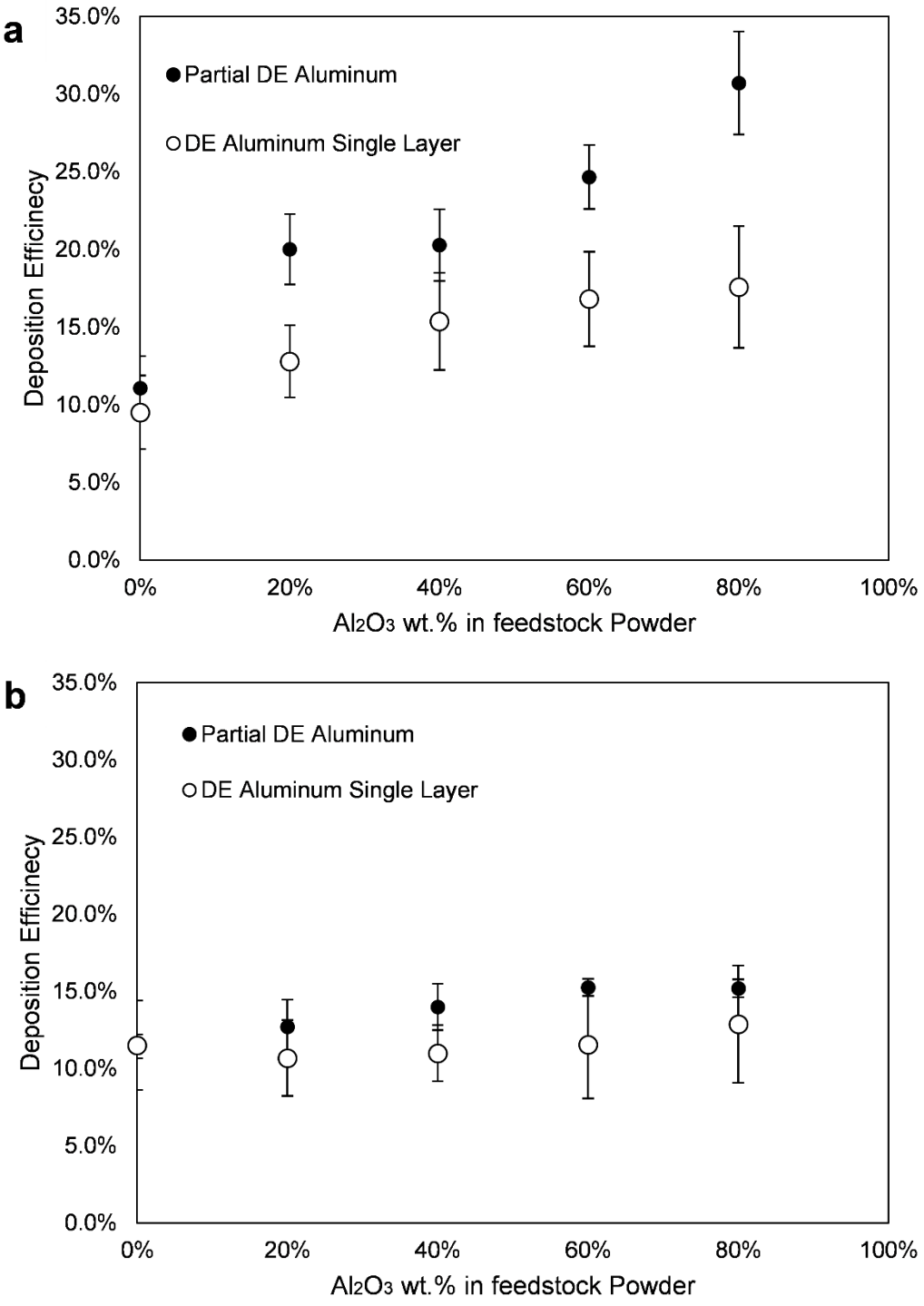


*Figure 10: Deposition efficiency of pure aluminum (partial DE) and of single layer pure aluminum at different feedstock powder compositions for different alumina morphologies: (a) Angular alumina ; (b) Spherical alumina.*

## Mechanical properties

The coatings hardness of each samples is reported as a function of the feedstock powder ceramic content in Figure 11. It can be seen that the coatings hardness increases with the feedstock powder alumina content for both alumina morphologies. Samples sprayed with feedstock powder containing angular alumina particles are harder than the ones sprayed with feedstock powder containing spherical alumina particles. This result is a direct consequence of the different ceramic retention level, caused by the alumina morphology. The ceramic content strengthens the material making it harder to deform therefore increasing the hardness.

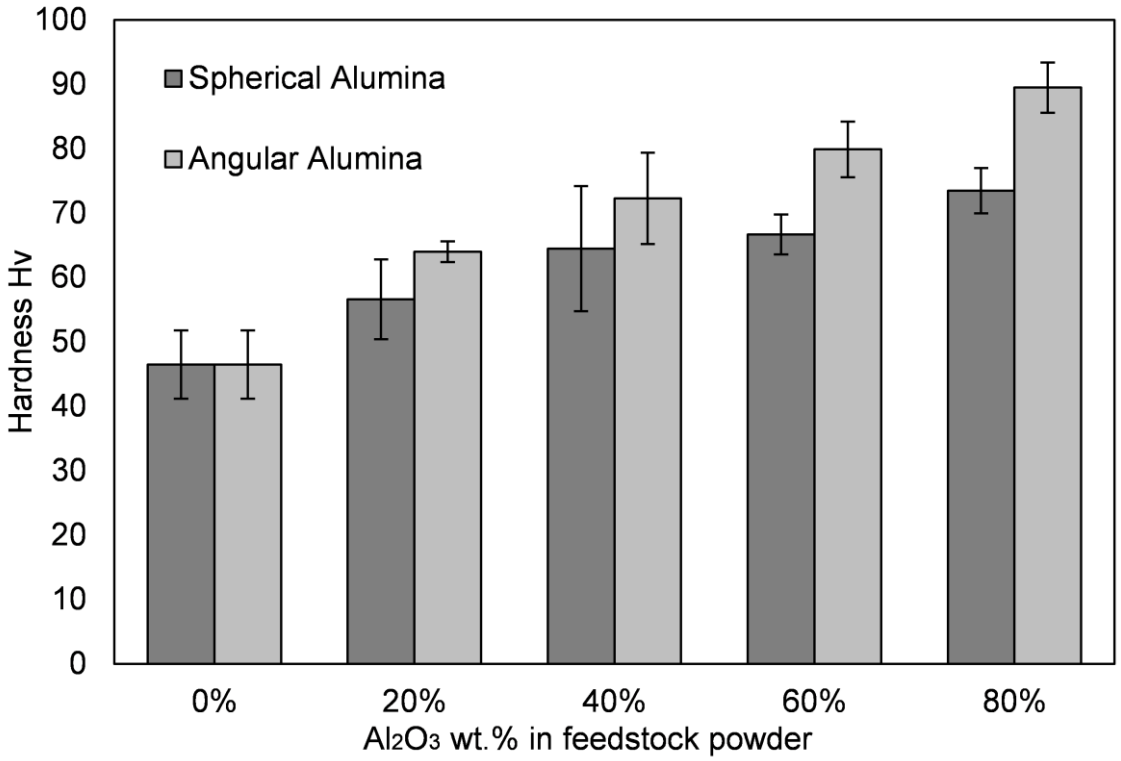


*Figure 11: Hardness of coatings versus feedstock powder composition and alumina morphology.*

In Figure 12, coatings hardness is plotted against coatings ceramic content. It is easy to see the positive influence of the coatings ceramic content on the coatings hardness. The figure shows that for both feedstock powders, as the coatings ceramic content increases the coatings hardness also increases. The hardness of pure aluminum was measured at 45 Hv, while the coating with the highest angular ceramic content reached 89.5 Hv and the one with the highest spherical alumina content reached 73.5 Hv. More remarkable is that even though the hardness of the coatings sprayed

with spherical alumina particles are softer than the one sprayed with angular alumina particles (for the same feedstock powder composition), if ceramic content in the coating is considered, it is easy to see that the coatings sprayed using spherical $Al_2O_3$ particles lead to harder coatings than the ones sprayed with angular alumina particles for the same alumina content. A coating with 14% alumina content sprayed with angular alumina particles in the feedstock powder reached a hardness value of 64 Hv while a coating with slightly less than half of the ceramic composition sprayed with spherical alumina particles reached 73.5 Hv.

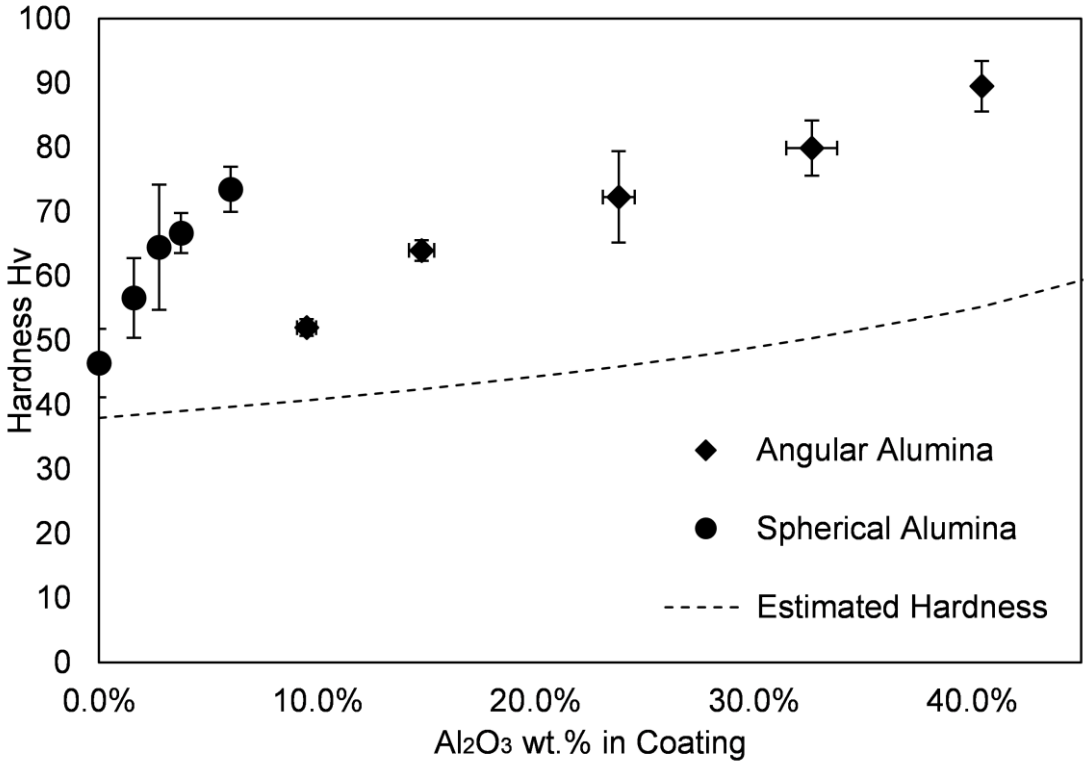


*Figure 12: Measured and estimated coating hardness versus coating composition.*

Even though the ceramic content is very influential on the hardness of cermets coatings [1, 38], it is not the only mechanism acting to strengthen it. Due to the nature of the cold spray process, the particle consolidation is driven by severe deformation which leads to work hardening of the coatings [39]. In addition, a cold sprayed coating with low DE will have even higher plastic deformation as particles that do not adhere to the substrate will impact the surface and impart energy on the surface conveying severe deformation to the coating. This process gets repeated accumulating plastic deformation until the next bounding particle hits, and the process starts over.

This accumulation of severe deformation goes even further when ceramic particles are mixed in the feedstock powder. Ceramic particles will not deform upon impact, thus imparting almost all its kinetic energy into deformation of the coating, conveying even more plastic deformation. Figure 12 also displays an estimated coating hardness based on the lower bound rule mixture of aluminum and alumina ($Al_20_3$=2500Hv). This rule is widely used in particulate strengthened cermets and gives and estimation of the ceramic content effect on the hardness increase [38, 40]. The work hardening caused by cold spray can clearly be seen in coatings sprayed with angular alumina particles with a measured hardness higher than the predicted value. This deviation from predicted values is even more pronounced in coatings sprayed with spherical alumina particles. Since feedstock powder containing spherical alumina particles show a lower DE compared to the one containing angular alumina particles, the aluminum particles have experienced more impacts, and therefore more plastic deformation. This leads to an accumulation of work hardening and a low percentage of ceramic content.

Figure 13 shows an etched cross-section of coatings sprayed without alumina, with angular alumina particles and spherical alumina particles. Higher deformation of the aluminum particles in coatings sprayed with spherical alumina particles is observed compared to the ones sprayed with angular alumina particles. The pure aluminum coatings show minor deformation level, comparable to the ones seen in coatings sprayed with angular alumina particle.

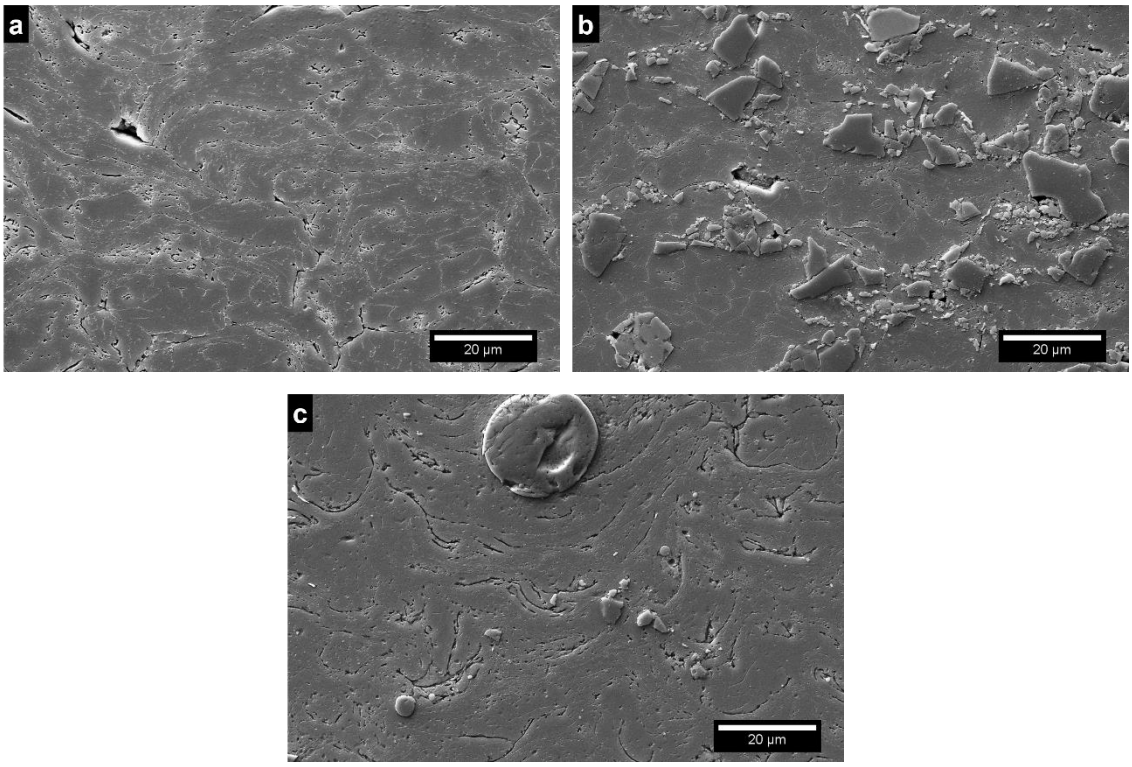


*Figure 13: Etched cross-sections of selected coatings showing different degrees of plastic deformation of the aluminum particles: (a) Pure aluminum; (b) 60wt% angular alumina particles in the feedstock powder; (c) 60wt% spherical alumina particles in the feedstock powder.*

Adhesion test results as a function of feedstock powder composition are shown in Figure 14. As can be observed, the addition of ceramic particles has an important influence on the coatings adhesion strength. Coatings sprayed with the feedstock powders containing angular alumina particles show a steady increase in adhesion strength, from pure aluminum coatings showing an adhesion strength of 25 MPa up to values in the range of the glue strength limit (≈70 MPa) in coatings sprayed with 80 wt.% of alumina. This behavior is even more remarkable for deposits sprayed with feedstock powder containing spherical alumina particles; these coatings reached the glue strength limit at a feedstock powder composition as low as 40 wt.% of alumina.

For coatings sprayed with angular alumina the significant increment in adhesion strength is explained based on the same effects causing the increase in DE: oxide removal and asperities at the surface resulting from the impacts of ceramic particles. These two mechanisms increase the chances of obtaining a higher metallurgical and mechanical bonding respectively [17, 21, 37, 41]. Coatings sprayed with feedstock powder containing spherical alumina particles show a faster increase in adhesion strength than the ones seen with angular alumina. It has been demonstrated that these

coatings exhibit limited surface asperities and the lower increase in DE lead to conclude that the oxide removal effect might not be as high as the case when using angular alumina particles. Therefore another effect might be acting to enhance the adhesion strength of these coatings.

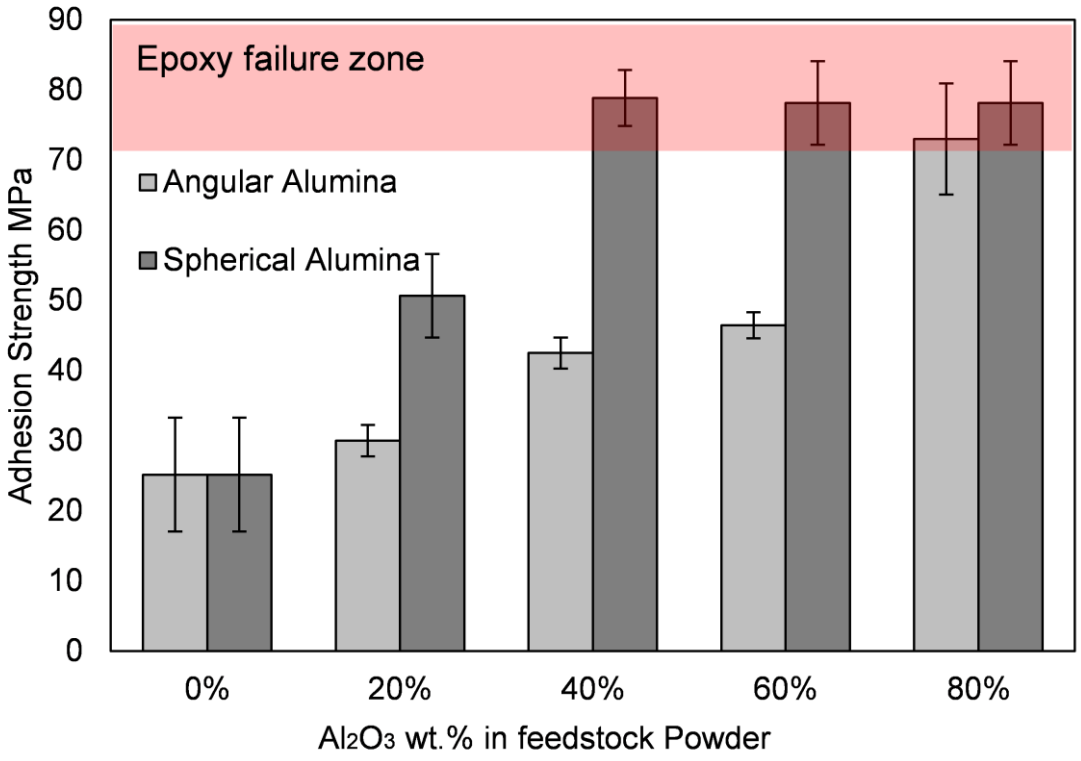


*Figure 14: Adhesion Strength of coatings sprayed versus feedstock powder composition.*

It is important to note that all coatings that did not fail at the glue, failed in adhesion between the coatings and the substrates, therefore in these coatings, the cohesive strength between particles is higher than the strength between the coatings and the substrates. As such, in order to better understand the trends observed for the adhesion strength, single particle impact tests have been performed.

Single particle impact test images show how the first deposited layer of coating is formed. The understanding of the formation of this layer is essential to understand the coatings adhesion strength mechanism. Figure 15, Figure 16 and Figure 17 show the formation of the first deposited layer in coatings sprayed with pure aluminum, mixed with angular alumina particles and mixed with spherical alumina particles respectively.

In Figure 15, the consolidation of the first layer of pure aluminum starts with several impacts of particles with no successful bonding (Figure 15(a)). These particles roughen and prepare the substrate for the arrival of the next particles; this effect has been referred to in other investigation as surface activation [24, 42, 43]. The substrate gets activated by similar principles mentioned previously: the repetitive impingement of particles may lead to oxide cleaning at the surface of the substrate and create some surface topology, both potentially more favorable for bonding that the initial surface easing the deposition of the incoming particles [42, 44] (Figure 15(b)). This is followed by several particles sticking to the substrate. It was observed that aluminum particles appear to be prone to stick to other deposited aluminum particles rather than adhering to the substrate, creating clumps of particles. One of these clumps is shown in Figure 15(c). It is possible that when a particle bonds it acts as a bonding point, increasing the changes of the new incoming aluminum particles to adhere to the substrate, forming these clumps. The reason behind these bonding points is not clearly identified, but might be caused by the impact angle seen by the incoming particles hitting the edges of adhered particles. It has been reported that the angle of impact might be relevant in increasing the adhesion strength in cold spray particles [10]. Finally, the first layer is formed, as shown in Figure 15(d). The surface of this layer shows moderate deformation caused by the impact of not-adhered pure aluminum particles.

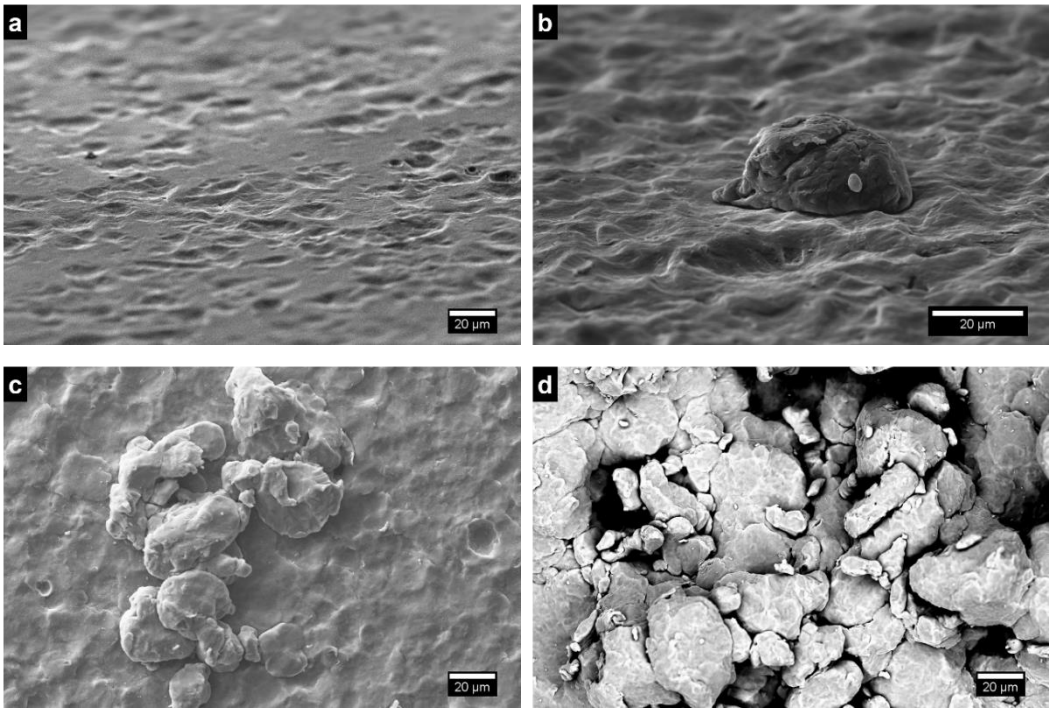


*Figure 15: Deposition progression for pure aluminum (top views): (a) impacts without bonding; (b) first particles adhering ; (c) clumping of particles; (d) first layer surface.*

For coatings deposited with a mix of aluminum and angular alumina particles, the process starts in similar conditions with several particles impacting the substrate without bonding as shown in Figure 16 (a). However, the surface morphology is different from the one of pure aluminum. In this case, the creation of sharper and deeper craters is observed, created by the ceramic particles as a result of their smaller contact points and higher hardness. These sharper craters are the asperities responsible for the increasing DE and adhesion strength. It is important to note that higher alumina content in the feedstock powder results in more of these asperities. The process leads to the first aluminum particles adhering and alumina particles locking into the substrate, as shown in Figure 16 (b). It is important to notice that these mixtures did not show the same behavior of clumping seen in coatings sprayed with pure aluminum. Particles appear to adhere independently of the presence of other particles, as seen in Figure 16 (c). It is possible that the presence of deeper and larger asperities act in a similar way than the bonding points in the case of a pure aluminum deposition, and since these craters are distributed more uniformly in the substrate, the particles do not appear to clump. As more metallic and ceramic particles adhere to the substrate eventually the first layer is formed, as seen in Figure 16 (d). This surface shows some embedded alumina particle, and aluminum particles exhibit in general moderate deformation levels with zones of localized heavy impacts where alumina particles did not bond.

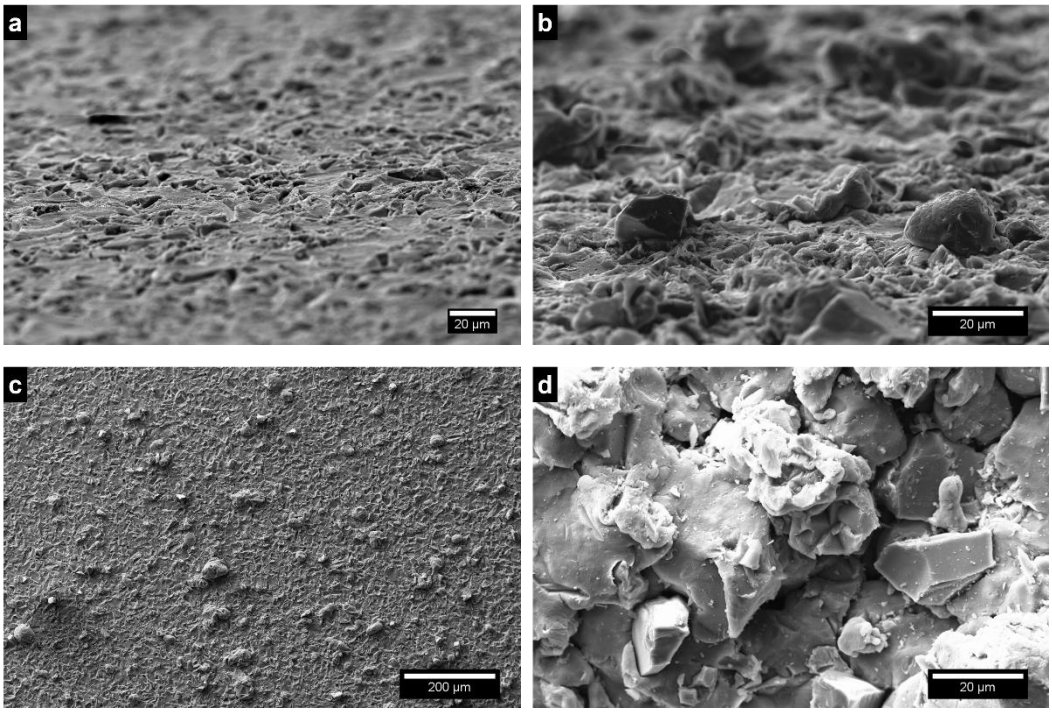


*Figure 16: Deposition progression for aluminum-60wt.% angular $Al_2O_3$ in feedstock powder: (a) Impacts without bonding; (b)First particles adhering; (c)Surface overview; (d)First layer surface.*

Finally, for the deposition of feedstock powders containing spherical alumina particles, the first particles hitting the substrate do not adhere but deform the substrate, as shown in Figure 17(a). It is clear that spherical alumina particles inflict a higher degree of deformation of the substrate surface than angular alumina or pure aluminum particles, creating deeper and wider indentations. After the creation of these craters, the aluminum particles start sticking to the substrate, as seen in Figure 17 (b). It is noted that the first particles to adhere are always contiguous to the indentations left by the spherical alumina. Similarly to the case of feedstock powder using angular alumina particles, the aluminum particles did not adhere in clumps. It is likely that these indentations caused by the alumina particles also promote the bonding of the new incoming aluminum particles. As the deposition progresses the first aluminum particles get heavily deformed by the following alumina particles, severely flattening them and inflicting a higher amount of plastic deformation compared to the two other feedstock powder types, as can be observed from Figure 17(c). This is a direct result of the low DE of spherical alumina particles, leading to increased deformation of the adhered aluminum particles. This effect is evident when the first layer completely covers the substrate, as shown in Figure 17(d). Severe peening is seen on the aluminum particles, and very limited amount of alumina particles can be found in the first deposited layer.

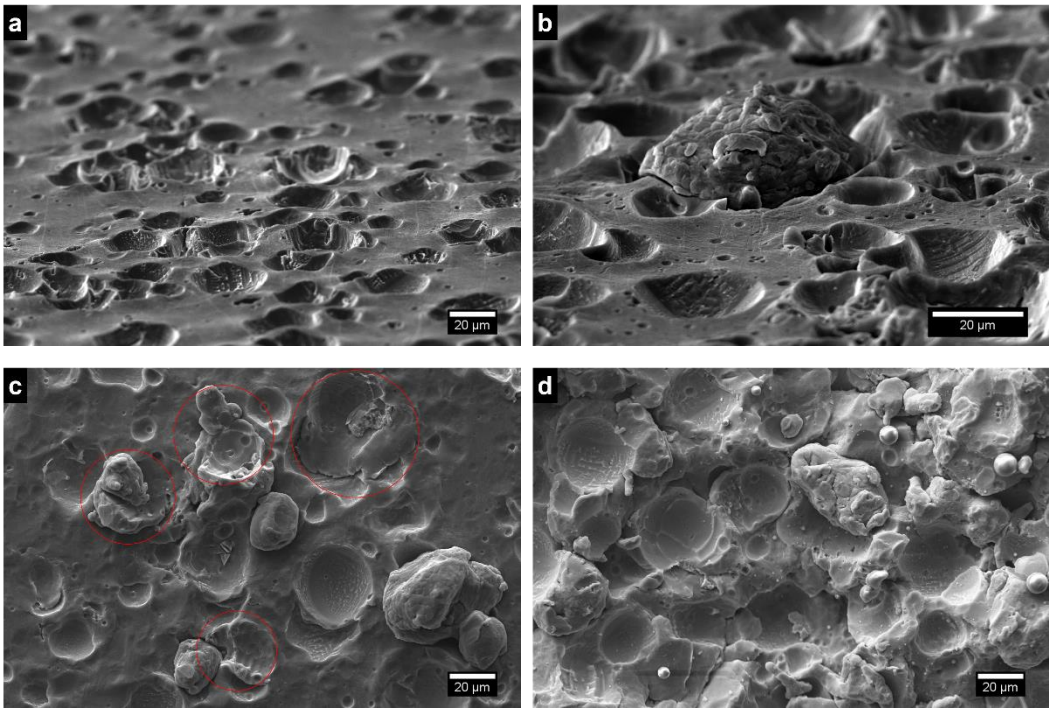


*Figure 17: Deposition progression for aluminum-60wt.% spherical $Al_2O_3$ in the feedstock powder: (a) Impacts without bonding; (b) First particles adhering; (c) Particle deformation ; (d) First layer surface.*

From these results, it is possible to deduce that two mechanisms could be acting to promote the adhesion strength of coatings produced with feedstock powder containing spherical alumina particles over those produced with angular alumina particles. First, the initial layer between the coating and the substrate appears to be more severely deformed in the coatings sprayed with spherical alumina particles. This shot-peening effect can increase the contact area between the particles and the substrate and the increased plastic deformation at the interface can lead to an improvement in the bonding between the particles and the substrate by increasing the chances of metallurgical bonding [10, 17, 37, 45]. Second, the larger amount of alumina particles present at the substrate/coating interface in deposition done with angular alumina particles could also play a role. Even though these particles are responsible for the increased adhesion compared to pure aluminum coatings, by promoting the production of asperities and oxide cleaning at the surface, their embedment at the interface lowers the contact area between the aluminum and the substrate, thus potentially affecting negatively the substrate/coating bonding [19]. These effects are easier to see in Figure 18 where etched cross-sections of the different interfaces are shown. The interface in the pure aluminum coating in Figure 18 (a) shows a flat, not very deformed interface. The interface of the coatings sprayed with angular alumina particles in Figure 18 (b) shows some of the asperities responsible for the increment in DE and adhesion. It also shows some of the embedded ceramic particles that might be detrimental to the adhesion strength by promoting crack propagation. Finally, the interface of the coating sprayed with spherical alumina particles, shown in Figure 18 (c), reveals a severely deformed interface with deep indentations in the substrate. Aluminum particles are also severely deformed and appear to swirl with the substrate. This kind of swirling is usually an indication of good bonding between coatings and substrates [46]. This difference at the interface created by each of the different feedstock powder is expected to be the reason for the different adhesion strength.

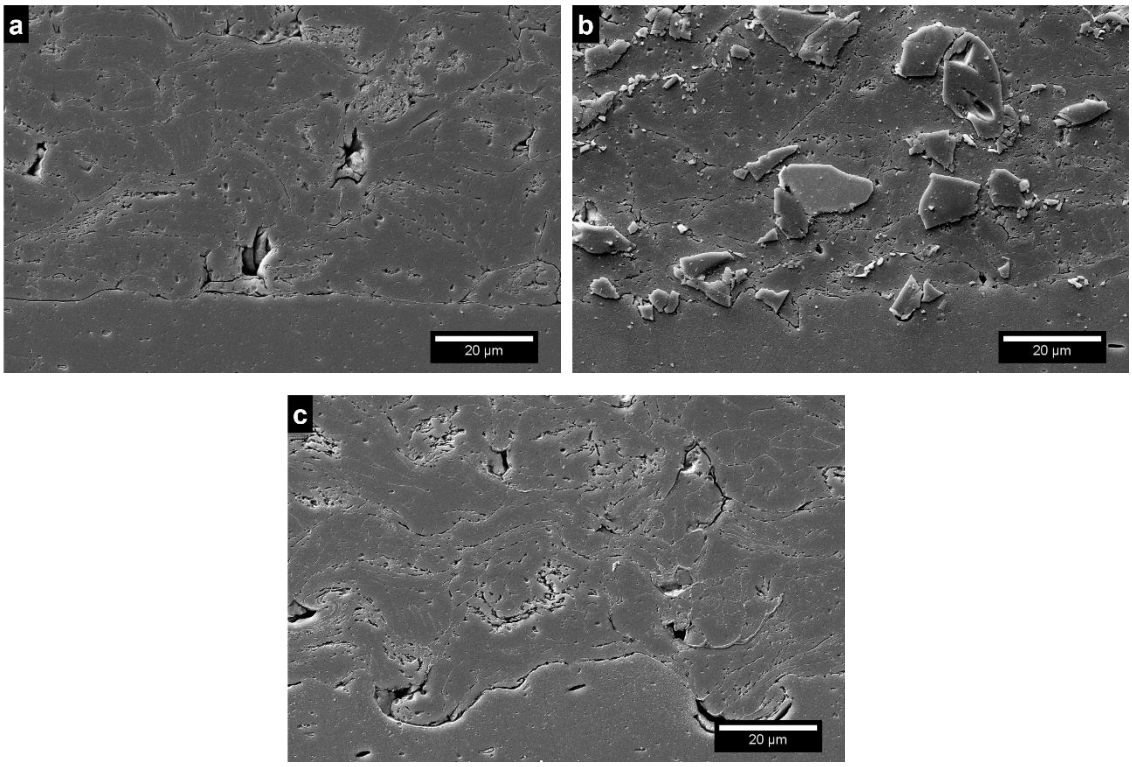


*Figure 18: Etched cross section of selected coatings showing different degrees of plastic deformation of the aluminum particles: (a) Pure aluminum; (b) 60wt% angular alumina particles in the feedstock powder; (c) 60wt% spherical alumina particles in the feedstock powder.*

Wear test results versus coating composition are shown in Figure 19. Different behaviors were observed depending on the coating ceramic content. For deposits containing 15wt.% alumina or less, no significant benefit was seen in wear resistance compared with pure aluminum coatings. At higher ceramic content the wear resistance showed dramatic increase from 28wt.% of alumina and higher. All the coatings with high alumina content were produced with angular alumina particles as the low partial DE of spherical alumina did not allow to obtain coatings with an alumina content higher than 6%wt.

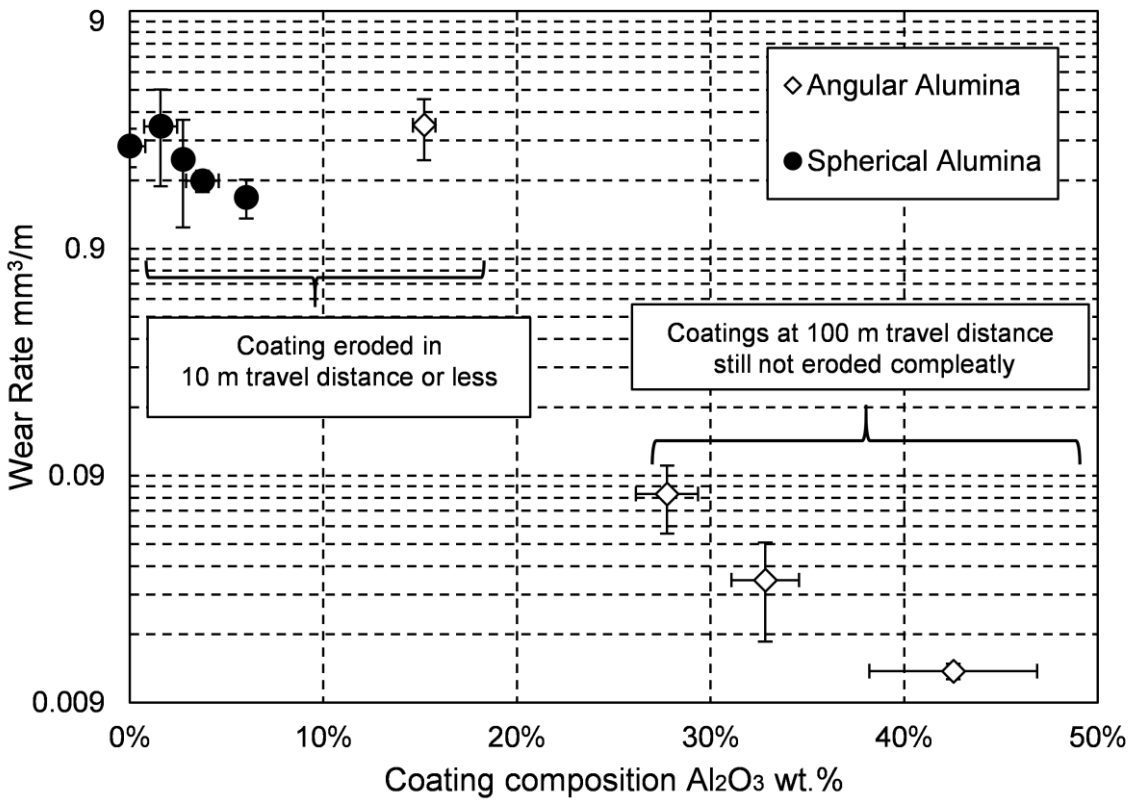


*Figure 19: Wear rate of coatings with different alumina content and morphology, calculated until 100m or worn to the substrate.*

Coatings sprayed with spherical alumina showed no improvement in wear resistance compared with pure aluminum coatings due to the low ceramic composition obtained. In spite of the higher hardness obtained, the alumina content was a dominant factor in the wear resistance of the coatings. This result agrees with the investigation carried by Shockley et al. where limited wear resistance improvement was observed in coatings with alumina content lower than 22%, and no apparent influence of the ceramic morphology was observed in the wear behavior [25].

Figure 20 show the wear track for pure aluminum coating (SPH-00), for which severe plastic deformation and layered structures are formed. This behavior is characteristic of soft metals and specifically aluminum and it is known as adhesive wear. This behavior occurs by plastic deformation leading to localized smearing and finally to ductile failure of the soft material.

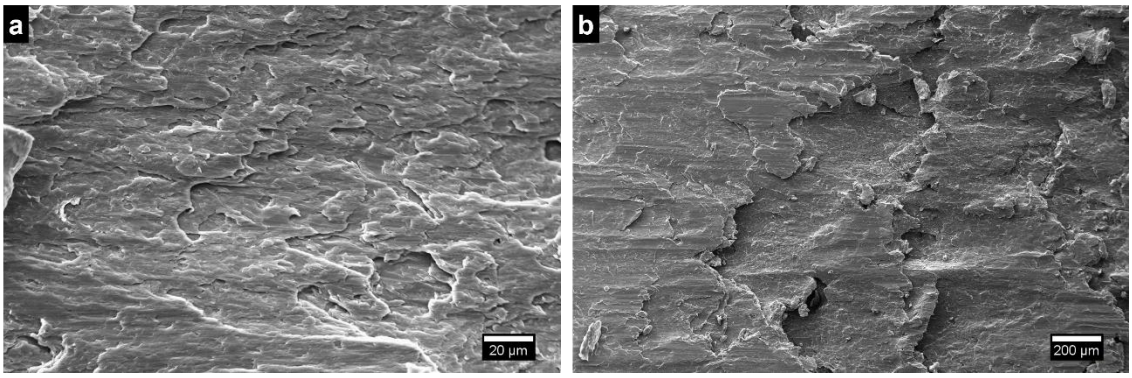


*Figure 20: Overview of wear tracks of pure aluminum coatings.*

Figure 21, shows the wear track of the sample SPH-08, containing 6%wt. spherical $Al_2O_3$ in the coating. A similar layered structure to pure aluminum is seen, but less local smearing is observed. The debris left by the breaking of the ceramic particles can lead to third body abrasion [47]. Scratch traces can be seen in Figure 21(b) as well as fractured ceramic particles. This scratching is characteristic of hard debris acting as a third body during the wear. At this ceramic composition, the ceramic particles are too distant from each other to offer a benefit in wear resistance [40]. In order to increase the wear resistance in a cermet, it is necessary to have enough ceramic particles to spread the stress throughout the material. If not enough particles are introduced in the metallic matrix, they cannot act as a reinforcement spreading the stress.

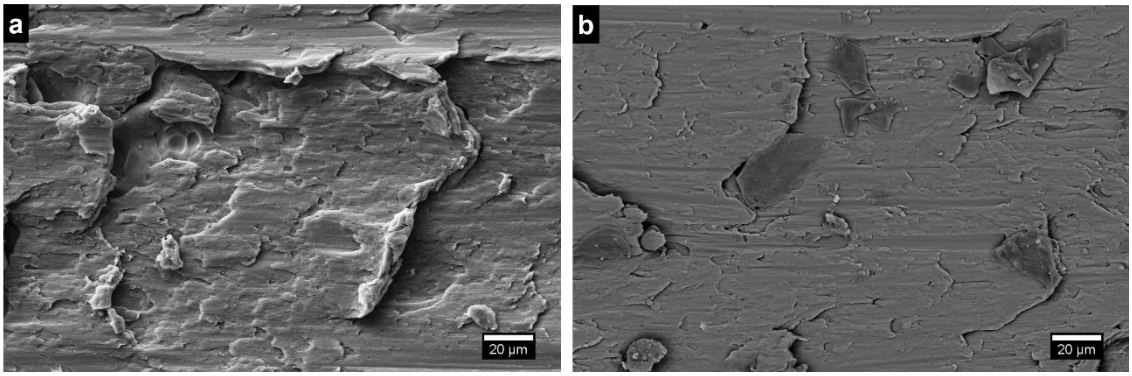


*Figure 21: Overview of wear tracks of coatings sprayed with Aluminum-80wt.% spherical alumina.*

Similar results are seen in Figure 22, where the wear track of ANG-02 sample is shown. This coating has a 15%wt.% of angular $Al_2O_3$ particles. A similar layered structure as the one found in pure aluminum is seen but with limited smearing. Third body scratching is more noticeable in these coatings; this is a result of a higher ceramic content and due to more ceramic debris, leading to

more pronounced scratches. It appears that at this composition, there are still not enough alumina particles to offer an improvement in wear resistance.

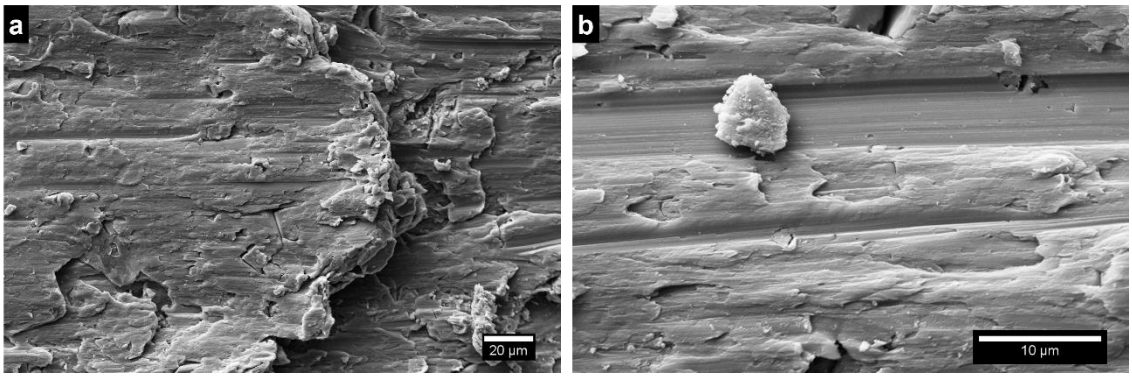


*Figure 22: Overview of wear tracks of coatings of coatings sprayed with Aluminum-20wt.% angular alumina.*

Finally, Figure 23 shows the wear track of sample ANG-08 containing 43%wt.% of angular $Al_2O_3$ particles. The figure shows a smooth and coherent surface characteristic of wear resistant coatings. Shockley et al.g referred to this type of surface as a tribofilm [25, 47, 48], that corresponds to a developed wear resistance surface. As the wear ball presses and slides on the surface, it cannot plastically deform the matrix: the ceramic particles reinforce the material distributing the stresses. This prevents the plowing seen in the previous figures and allows a wear resistant surface.

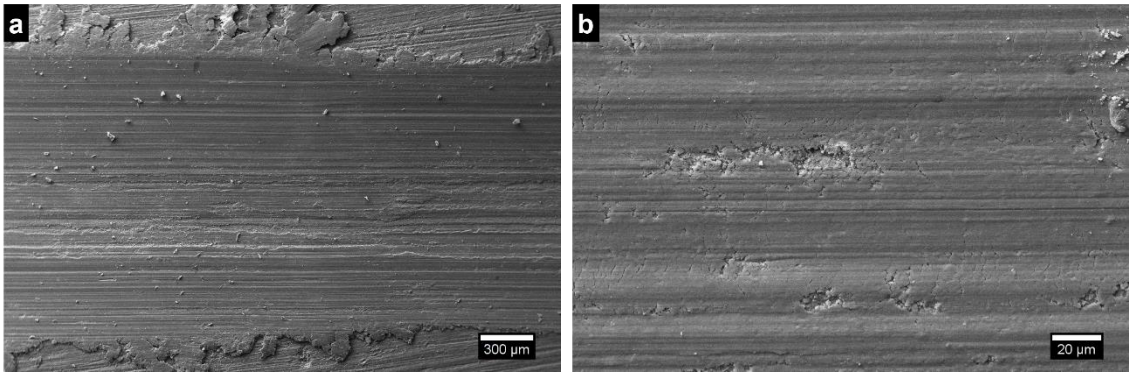


*Figure 23: Overview of wear tracks of coatings sprayed with Aluminum-80wt.% angular alumina.*

# Conclusions

This study focuses on the effect of ceramic morphology in the cold spray deposition behavior and mechanical properties of aluminum-alumina cermets. Aluminum and spherical alumina mixtures

are sprayed and compared to the deposition behavior of aluminum and angular alumina mixtures. The depositions were successful in creating dense coatings for all compositions containing aluminum. The deposition efficiency seen in coatings sprayed with spherical alumina showed a consistent decrease as the alumina content increases. This contrasts with coatings sprayed with angular alumina where an increment in DE is seen in samples with low alumina content, followed by a consistent decrease as the alumina content increases. The reason behind this behavior is attributed to the extremely low partial DE of the spherical alumina particles. Asperities created by the spherical alumina particles proved to have no effect in the partial DE of aluminum proving that this effect is closely related to the morphology of the asperities created. The partial DE of aluminum in coatings sprayed with spherical alumina showed a slight increase when the composition of alumina increases in the feedstock powder. This increase is considerably lower than the one seen with angular alumina even with the effect of asperities removed. This is hypothesized to be due to the effect of oxide-clean surfaces, but no explanation was found to explain why the effect is lower in spherical alumina versus angular alumina. This should be studied further to determine the reasons for the difference.

The retention of alumina in the coatings sprayed with spherical alumina was determined to be considerably lower than the ones sprayed with angular alumina. The retention obtained was assessed to be lower than 10% of the injected amount in the case of spherical alumina and 50% for angular alumina. This low value of ceramic retained in the coating resulted in lower mechanical properties of coatings sprayed with spherical alumina. Wear resistance of coatings sprayed with spherical $Al_2O_3$ showed no improvement when compared with coatings sprayed with pure aluminum. This effect is strictly related to ceramic content as for coatings sprayed with angular alumina with similar ceramic content also showed no improvement in wear resistance. Hardness is also affected by ceramic content, with values for coatings sprayed with 80 wt.% of angular alumina of 89.5 Hv and 73.5 Hv for the ones sprayed with spherical alumina. When coatings $Al_2O_3$ content is taken into account, hardness in coatings obtained with spherical alumina showed to be harder than the ones achieved with angular alumina. At 6wt.% of $Al_2O_3$ in the coating, the hardness achieved was of 73.5Hv in coatings sprayed with spherical alumina and 64Hv was obtained in coatings with 15wt.% of angular alumina. This was determined to be a result of the high deformation of aluminum particles, arising from the low DE seen and resulting enhanced deformation in coatings sprayed with spherical alumina.

Adhesion test showed to increase drastically as the ceramic content increased in the feedstock powder. Coatings sprayed with spherical alumina showed a faster rate of increase than the one

sprayed with angular ceramic. The former reached the limit of the test (Glue Failure) in coatings sprayed with powders containing 40wt.% of spherical alumina, while coatings sprayed with angular alumina also achieved this limit but with powders containing 80wt.%. Cross-sections and single particle impact tests revealed that the adhesion increment are caused by different mechanisms. While it was shown that the presence of asperities and oxide-free surfaces are the mechanism that leads to a higher adhesion in coatings sprayed with angular alumina, in the case of spherical alumina the increase appeared to be driven by a peening effect of the ceramic into the first layer of aluminum particles, this high deformation leading to swirl at the interface strengthening the bonding between the coating and the substrate.

Finally, dry sliding wear tests showed limited improvement over pure aluminum in coatings with low alumina contents. These results were independent of the alumina morphology. At coating alumina content higher than 28wt.% the wear resistance was improved drastically.

# References

1. Tinklepaugh JR (1960) Cermets. Reinhold Publishing Corporation

2. Ellis JL, Goetzel CG (1990) Cermets. In: ASM Handb. Vol. 2 Prop. Sel. Nonferrous Alloy. Spec. Mater. - ASM Int. ASM International, p 1328

3. Bergmann CP, Vicenzi J (2011) Protection against Erosive Wear Using Thermal Sprayed Cermet. Prot against Erosive Wear Using Therm Sprayed Cermet 89. doi: 10.1007/978-3-642-21987-0

4. Evans A, San Marchi C, Mortensen A (Andreas) (2003) Metal matrix composites in industry : an introduction and a survey. Kluwer Academic

5. Lee HY, Yu YH, Lee YC, et al (2004) Cold Spray of SiC and Al2O3 With Soft Metal Incorporation: A Technical Contribution. J Therm Spray Technol 13:184–189. doi: 10.1361/10599630419355

6. Lee HY, Yu YH, Lee YC, et al (2005) Thin Film Coatings of WO3 by Cold Gas Dynamic Spray: A Technical Note. J Therm Spray Technol 14:183–186. doi: 10.1361/105996304523791

7. Vardelle A, Moreau C, Akedo J, et al (2016) The 2016 Thermal Spray Roadmap. J Therm

Spray Technol. doi: 10.1007/s11666-016-0473-x

8. He J, Ice M, Schoenung JM, et al (2001) Thermal Stability of Nanostructured Cr 3 C 2 - NiCr Coatings. 10:293–300.

9. Sova A, Grigoriev S, Okunkova A, Smurov I (2013) Potential of cold gas dynamic spray as additive manufacturing technology. Int J Adv Manuf Technol 69:2269–2278. doi: 10.1007/s00170-013-5166-8

10. Wang X, Feng F, Klecka MA, et al (2015) Characterization and modeling of the bonding process in cold spray additive manufacturing. Addit Manuf 8:149–162. doi: 10.1016/j.addma.2015.03.006

11. Dykhuizen RCC, Smith MFF (1998) Gas Dynamic Principles of Cold Spray. J Therm Spray Technol 7:205–212. doi: 10.1361/105996398770350945

12. Tokarev a. O (1996) Structure of aluminum powder coatings prepared by cold gasdynamic spraying. Met Sci Heat Treat 38:136–139. doi: 10.1007/BF01401446

13. Alkhimov AP, Papyrin AN, Kosarev VF, et al (1995) Method and device for coating.

14. Assadi H, Gärtner F, Stoltenhoff T, Kreye H (2003) Bonding mechanism in cold gas spraying. Acta Mater 51:4379–4394. doi: 10.1016/S1359-6454(03)00274-X

15. Grujicic M, Zhao CL, Tong C, et al (2004) Analysis of the impact velocity of powder particles in the cold-gas dynamic-spray process. Mater Sci Eng A 368:222–230. doi: 10.1016/j.msea.2003.10.312

16. Alkhimov AP, Kosarev VF, Papyrin AN (1990) A method of “cold” gas dynamic deposition. Sov Phys Dokl 35:1047–1049.

17. Hussain T, McCartney DG, Shipway PH, Zhang D (2009) Bonding mechanisms in cold spraying: The contributions of metallurgical and mechanical components. J Therm Spray Technol 18:364–379. doi: 10.1007/s11666-009-9298-1

18. Dykhuizen RCC, Smith MFF, Gilmore DLL, et al (1999) Impact of High Velocity Cold Spray Particles. J Therm Spray Technol 8:559–564. doi: 10.1361/105996399770350250

19. Samson T, MacDonald D, Fernández R, Jodoin B (2015) Effect of Pulsed Waterjet Surface Preparation on the Adhesion Strength of Cold Gas Dynamic Sprayed Aluminum Coatings. J Therm Spray Technol 24:984–993. doi: 10.1007/s11666-015-0261-z

20. Koivuluoto H, Vuoristo P (2010) Structural Analysis of Cold-Sprayed Nickel-Based Metallic and Metallic-Ceramic Coatings. J Therm Spray Technol 19:975–989. doi: 10.1007/s11666-010-9481-4

21. Irissou E, Legoux J-G, Arsenault B, Moreau C (2007) Investigation of Al-Al2O3 Cold Spray Coating Formation and Properties. J Therm Spray Technol 16:661–668. doi: 10.1007/s11666-007-9086-8

22. Sova a., Papyrin A, Smurov I (2009) Influence of Ceramic Powder Size on Process of Cermet Coating Formation by Cold Spray. J Therm Spray Technol 18:633–641. doi: 10.1007/s11666-009-9359-5

23. Maev RG, Leshchinsky E (2006) Low Pressure Gas Dynamic Spray : Shear Localization during Particle Shock Consolidation. Therm. Spray 2006 Sci. Innov. Appl.

24. Shkodkin a., Kashirin A, Klyuev O, Buzdygar T (2006) Metal Particle Deposition Stimulation by Surface Abrasive Treatment in Gas Dynamic Spraying. J Therm Spray Technol 15:382–386. doi: 10.1361/105996306X124383

25. Shockley JM, Descartes S, Vo P, et al (2015) The influence of Al2O3 particle morphology on the coating formation and dry sliding wear behavior of cold sprayed Al–Al2O3 composites. Surf Coatings Technol 270:324–333. doi: 10.1016/j.surfcoat.2015.01.057

26. Wang Y, Normand B, Mary N, et al (2014) Microstructure and corrosion behavior of cold sprayed SiCp/Al 5056 composite coatings. Surf Coatings Technol 251:264–275. doi: 10.1016/j.surfcoat.2014.04.036

27. Wang Q, Spencer K, Birbilis N, Zhang M-X (2010) The influence of ceramic particles on bond strength of cold spray composite coatings on AZ91 alloy substrate. Surf Coatings Technol 205:50–56. doi: 10.1016/j.surfcoat.2010.06.008

28. Silva FS d., Bedoya J, Dosta S, et al (2017) Corrosion characteristics of cold gas spray coatings of reinforced aluminum deposited onto carbon steel. Corros Sci 114:57–71. doi:

10.1016/j.corsci.2016.10.019

29. Finnie I, McFadden DH (1978) On the velocity dependence of the erosion of ductile metals by solid particles at low angles of incidence. Wear 48:181–190. doi: 10.1016/0043-1648(78)90147-3

30. Spencer K, Fabijanic DM, Zhang M-X (2009) The use of Al–Al2O3 cold spray coatings to improve the surface properties of magnesium alloys. Surf Coatings Technol 204:336–344. doi: 10.1016/j.surfcoat.2009.07.032

31. Sova a., Kosarev VF, Papyrin A, Smurov I (2010) Effect of Ceramic Particle Velocity on Cold Spray Deposition of Metal-Ceramic Coatings. J Therm Spray Technol 20:285–291. doi: 10.1007/s11666-010-9571-3

32. Verajankorva S, Lagerbom J, Vuoristo P (2006) Influence of powder type and properties on ceramic layer deposition by cold spraying. Therm Spray 2006 Build 100 Years Success 2–7.

33. Getu H, Spelt JK, Papini M (2012) Conditions leading to the embedding of angular and spherical particles during the solid particle erosion of polymers. Wear 292:159–168. doi: 10.1016/j.wear.2012.05.017

34. Hadavi V, Papini M (2015) Numerical modeling of particle embedment during solid particle erosion of ductile materials. Wear 342:310–321. doi: 10.1016/j.wear.2015.09.008

35. Gärtner F, Borchers C, Stoltenhoff T, et al (2003) Numerical and Microstructural Investigations of the Bonding Mechanisms in Cold Spraying. Therm Spray 2003 Avdancing Sci Appl Technol 1–8.

36. Schmidt T, Assadi H, Gärtner F, et al (2009) From particle acceleration to impact and bonding in cold spraying. J Therm Spray Technol 18:794–808. doi: 10.1007/s11666-009-9357-7

37. Grujicic M, Zhao C. L, DeRosset W. S, Helfritch D (2004) Adiabatic shear instability based mechanism for particles/substrate bonding in the cold-gas dynamic-spray process. Mater Des 25:681–688. doi: 10.1016/j.matdes.2004.03.008

38. Hodder K, Izadi H, McDonald A, Gerlich A (2012) Fabrication of aluminum-alumina metal

matrix composites via cold gas dynamic spraying at low pressure followed by friction stir processing. Mater Sci Eng A 556:114–121. doi: 10.1016/j.msea.2012.06.066

39. Hall a. C, Cook DJ, Neiser R a., et al (2006) The Effect of a Simple Annealing Heat Treatment on the Mechanical Properties of Cold-Sprayed Aluminum. J Therm Spray Technol 15:233–238. doi: 10.1361/105996306X108138

40. Melendez NM, Narulkar V V., Fisher GA, McDonald A (2013) Effect of reinforcing particles on the wear rate of low-pressure cold-sprayed WC-based MMC coatings. Wear 306:185–195. doi: 10.1016/j.wear.2013.08.006

41. Xie Y, Planche M-P, Raoelison R, et al (2016) Investigation on the influence of particle preheating temperature on bonding of cold-sprayed nickel coatings. Surf Coatings Technol. doi: 10.1016/j.surfcoat.2016.09.037

42. Klinkov S V., Kosarev VF (2012) Cold spraying activation using an abrasive admixture. J Therm Spray Technol 21:1046–1053. doi: 10.1007/s11666-012-9778-6

43. Donner K-R, Gaertner F, Klassen T (2010) Metallization of Thin Al2O3 Layers in Power Electronics Using Cold Gas Spraying. J Therm Spray Technol 20:299–306. doi: 10.1007/s11666-010-9573-1

44. Papyrin AN (2007) Preface. In: Cold Spray Technol. Elsevier, pp x–xii

45. Cormier Y, Dupuis P, Jodoin B, Ghaei A (2015) Finite Element Analysis and Failure Mode Characterization of Pyramidal Fin Arrays Produced by Masked Cold Gas Dynamic Spray. J Therm Spray Technol 24:1549–1565. doi: 10.1007/s11666-015-0317-0

46. Ajdelsztajn L, Jodoin B, Kim GE, et al (2005) Cold Spray Deposition of Nanocrystalline Aluminum Alloys. Metall Mater Trans A 36A:657–666. doi: 10.1007/s11661-005-0182-4

47. Sannino AP, Rack HJ (1995) Dry sliding wear of discontinuously reinforced aluminum composites: review and discussion. Wear 189:1–19. doi: 10.1016/0043-1648(95)06657-8

48. Wesmann JAR, Kuroda S, Espallargas N (2017) The Role of Oxide Tribofilms on Friction and Wear of Different Thermally Sprayed WC-CoCr. J Therm Spray Technol 1–11. doi: 10.1007/s11666-017-0522-0

## 5.3 Effect of particle morphology on the deposition behavior of Chromium carbide-Nickel chromium cermet powders sprayed with low-pressure cold spray

This section of the investigation addresses the objective "Effect of cermet powder morphology on the process cold spray". Six commercially available CrC-NiCr powders with different morphologies, and metal/ceramic ratio were studied. Studies of this kind of powders on low-pressure cold spray were not found in the literature, which makes this investigation more appealing for widening the spectrum of powders in cold spray. Powder analysis, as well as interrupted spray tests and FEA were used to investigate the deposition behavior. To closely represent the powder in the FEA, cross-sections of the powders were taken and digitized. This process is new in cold spray simulations, and the simulations of cermet powders in this way has not been done before. The modeling aspect of this investigation can help to guide future research in the simulations of impacts of irregular particles. The investigation showed that spherical powders led to substrate erosion and no coating was formed. The reason of this behavior was due to the limited ductility of the particles. Porous agglomerated and sintered powder lead to successful coatings but were severely cracked. For dense agglomerated and sintered powders, the outcome was dependent on the initial metal/ceramic ratio. Powders with 25%wt. NiCr leads to erosion while 35%wt. NiCr powders lead to successful dense coatings. Finally, blended ceramic-metal powders also lead to successful coatings. All coatings obtained had lower ceramic content than the original feedstock powder. This investigation provided a detailed approach on the deposition of different powder morphology and can help to guide future investigation in tailoring cermet powder production for cold spray.

# Effect of Particle Morphology on the Deposition Behavior of Chromium Carbide-Nickel Chromium Cermet Powders Sprayed with Low-Pressure Cold Spray

Ruben Fernandez, Bertrand Jodoin

University of Ottawa Cold Spray Research Laboratory, Ottawa, ON, Canada.

## Abstract

Nickel chromium-chromium carbide coatings provide good corrosion and wear resistance at high temperatures, making them ideal for applications where a harsh environment and high temperatures are expected. Thermal spray processes are preferred as deposition technique of cermets, but the high process temperatures can lead to decarburization and reduction of the coatings properties. Cold spray uses lower temperatures preventing decarburization. Since the metallic phase remains solid, the feedstock powder morphology becomes crucial on the deposition behavior. Six commercially available powders were studied, varying in morphology and metal/ceramic ratios. The powders were categorized into 4 groups depending on their morphology. Spherical powders lead to substrate erosion due to their limited overall ductility. Porous agglomerated and sintered powders lead to severely cracked coatings. For dense agglomerated and sintered powders, the outcome depended on the initial metal/ceramic ratio: powders with 25%wt.NiCr led to substrate erosion while 35%wt.NiCr powders led to dense coatings. Finally, blended ceramic-metal mixtures also lead to dense coatings. All coatings obtained had lower ceramic content than the initial feedstock powders. Interrupted spray tests, combined with FEA helped drawing conclusions on the deposition behavior to explain the obtained results.

*Keywords: Cold Spray, CrC-NiCr, Deposition behaviour, Finite element analysis, Cermet.*

# Introduction

Chromium carbide based cermets are materials generally employed for wear, abrasion and erosion protection due to their high hardness [1–4]. Nickel alloys are often used for the matrix material to provide good corrosion/oxidation protection in high temperature environments [3, 5]. Investigations have shown that they can operate in harsh environments at temperatures up to 900°C [6–10]. These properties make cermets ideal for operating conditions where erosion is expected as well as corrosive environments, such as combustion chambers and high temperature turbines [11, 12]. These materials also find applications at ambient temperature where corrosion and erosion resistance are required [7].

Chromium carbide-nickel chromium cermets (CrC-NiCr) are normally applied as coatings on top of a base material. Thermal spray processes are the preferred manufacturing methods to produce these coatings, with HVOF and plasma spraying being the most commonly used. The high temperature involved in these processes allows melting the NiCr phase and obtaining low porosity coating with a high deposition efficiency. The main drawback of these high temperature spraying processes is related to the sensitivity of chromium carbides to high temperatures. The elevated gas process temperatures (3000°C for HVOF and 10000°C for plasma spraying) can lead to decarburization which results in reduced coating properties [6]. This drawback of thermal spray processes is present for other cermet coatings as well such as WC-Co [13–15]. Cold spray has been explored as an alternative process to overcome this drawback [14, 16].

The cold spray process accelerates feedstock powders (usually metals) in a supersonic gas stream produced by a convergent-divergent nozzle (De Laval) [17–19]. Due to the low gas temperatures used in addition to the rapid gas expansion in the nozzle, the feedstock powders remain solid throughout their flight making cold spray a solid state process [20–22]. The particles impact the substrate and experience extensive plastic deformation, bonding the particles to the substrate either mechanically or if enough plastic deformation is obtained metallurgically [20–25]. Cermet coatings have been produced by cold spray by blending ceramic particles into the feedstock metallic powders [26–29]. For these cases, the ceramic particles do not experience plastic deformation upon impact and only a fraction of the ceramic particles present in the feedstock powder are retained in the coating [29, 30]. Powders prepared with different techniques have been sprayed, such as agglomerated and sintered WC-Co powders [31–33]. In these cases, higher velocities are needed to obtain a coating, as the particles are difficult to deform [31–33]. The production of a successful coating using these powders typically requires higher operating temperatures and pressures and often helium as main gas, making the process less appealing for industrial applications. Due to the operating temperatures in cold spray

decarburization can be avoided. As such, when a coating is obtained, it normally possesses higher wear resistance and denser microstructures than coatings produced by other thermal spray processes [31–33].

The deposition of the initial layer of CrC-NiCr powders by cold spray has not been extensively studied, although important studies have been performed to address the potential of several CrC-NiCr powders in producing wear and corrosion resistance coatings [34, 35]. Since cold spray is a solid state process, the powder morphology becomes a key factor in the deposition behavior of these particles, in particular of the first layer on the substrate. In this investigation, six different commercially available CrC-NiCr powders were studied. These powders presented different morphologies and ceramic/metal ratios. The powders deposition behavior was investigated by assessing deposition efficiency, observing single-particles impacts and by FEA modeling of the particle impacts. The goal of this study is to assess with a descriptive approach the effect of the cermet morphology on the cold spray deposition behavior of the initial layer of chromium carbide-nickel chromium powders and subsequent built and support the studies previously done with these materials [34].

# Experimental Procedures

## Materials and Production Methods

Six different commercially available CrC-NiCr feedstock powders were studied. The powders were produced by four different production methods. CRC-410 and CRC-425 powders (Praxair Surface Technologies, Indianapolis, IN, USA) were used. They are atomized powders with 30wt.% and 40wt.% NiCr respectively. Three agglomerated and sintered powders were also used: CRC-300 (Praxair Surface Technologies, Indianapolis, IN, USA), Amperit 584 and Amperit 587 (H.C. Starck,Munich, Germany). CRC-300 and Amperit 584 have a composition of 25%wt NiCr and Amperit 587 has a composition of 35%wt NiCr. Finally, the commercially available blended powder Diamalloy 3004 (Oerlikon Metco Inc., Westbury, NY, USA) was also used. This powder is made of crushed chromium carbide and atomized NiCr with a composition of 25%wt NiCr. Table 1 summarizes the feedstock powders used, detailing the production method, composition and powder size range. The selected material for the substrate was AISI 4340 steel with a hardness of 340 Hv.

*Table 1: Summary of Powders Used.*

| Commercial name | Production method | Composition wt.% CRC/Metal | Particle size | Feed rate g/min | In-flight velocity m/s |
|---|---|---|---|---|---|
| Praxair CRC-410 | Atomized | 70/30 | -45 µm/+11 µm | 32.7 ± 3.7 | 435 ± 92 |
| Praxair CRC-425 | Atomized | 60/40 | -45 µm/+11 µm | 31.8 ± 4.3 | 430 ± 85 |
| Praxair CRC-300 | Agglomerated and sintered | 75/25 | -45 µm/+11 µm | 13.5 ± 2.2 | 451 ± 98 |
| H.C. Starck Amperit 584 | Agglomerated and sintered | 75/25 | -45 µm/+10 µm | 21.1 ± 1.2 | 499 ± 143 |
| H.C. Starck Amperit 587 | Agglomerated and sintered | 65/35 | -45 µm/+10 µm | 17.0 ± 2.7 | 509 ± 151 |
| Oerlikon Diamalloy 3004 | Atomized with crushed | 75/25 | -45 µm/+5 µm | 21.3 ± 3.3 | 471 ± 175 |

## Cold Spray Deposition

The cold spray system used was the commercially available EP Series SST Low Pressure Cold Spray System (Centerline Ltd., Windsor, Ontario, Canada). The system consists of a 15 kW heater with a maximum gas temperature of 500°C and a maximum gas pressure of 3.8 MPa. The De Laval nozzle used for this work has a throat diameter of 2 mm and a diverging section length and exit diameter of 120 mm and 6.35 mm respectively. The powder was fed using a commercially available powder feeder (Model AT-1200HP, Thermach Inc., Appleton, WI, USA). All sprays were performed using the spray parameters given in Table 2. It is important to mention that the maximum gas temperature and pressure that can be reached by the system were used in the experiments.

*Table 2: Cold Spray Parameters Used.*

| Parameter | Value |
|---|---|
| Gas Temperature | 500 °C |
| Gas Pressure | 3.8 MPa |
| Gas Nature | Nitrogen |
| Traverse Speed | 5 mm/s |
| Passes | 5 |
| Feed Conditions | 240 holes wheel at 5 RPM |
| Standoff Distance | 10 mm |

The deposition efficiency (DE) of each feedstock powder was calculated. The powder feed rate and the substrate weight were measured prior and post-deposition. A precision scale Sartorius Extend—model ED124S, with a readability of 1mg was used for weighing the substrate. Table 1 presents the feed rates measured in each powder.

Interrupted spray tests were performed to evaluate individual particle deposition. They consist in interrupting the powder feeding while continuing the raster pattern with the spray nozzle. It produces traces on the substrate with zones where no particle have hit, zones where single impacts have occurred, zones where the first complete layer of coating has been produced and zones where a full coating is formed. These tests help to give insights into the powders deposition behavior.

## Powders and Coatings Characterization

The as-received feedstock powder morphology was analyzed through secondary and backscattered electron modes using a scanning electron microscope (SEM, model EVO MA-10, Carl Zeiss AG, Oberkochen, Germany). Powders were also cross-sectioned and analyzed in order to observe the ceramic and metal distributions inside the feedstock particles. The powders composition was evaluated using energy-dispersive X-ray spectroscopy (EDS, model INCA X-Act, Oxford Instruments, Oxford, England).

To get a better insight of the deposition process, as-sprayed not adhered particles were also analyzed by SEM. These particles were recovered by locating an adhesive carbon tape in the vicinity of the substrate during deposition and were analyzed under SEM. The coatings and interrupted spray test samples produced were cross-sectioned and examined using an optical microscope (VHX-1000, Keyence Corporation, Osaka, Japan), and a SEM. The powder and coating compositions were evaluated using EDS.

## Finite Element Analysis

A plane strain 2D finite element analysis was performed in order to evaluate and understand the powder deformation dynamics upon impact. Since different powder morphologies may potentially lead to different deformation mechanisms, powder particle cross-sections were digitalized in order to obtain the proper morphology required for the simulations. The digitalization of the images were based on the contrast of the cross-sectioned images. BSD images were used to obtain different contrasts for the different material phases. This allowed to differentiate the metal and the ceramic phases in the particle. A software was developed in the open-source Simple Morphological Image Library (SMIL) software to process these images and extract the morphology of the particles and the ceramic content. The data points were then exported using a Python-Abaqus script into a sketch to proceed with the simulation. Any particular inconsistency in the sketch creation process was fixed manually. The material properties used were determined by the nature of the phase identified. It is important to mention that irregular particles are rarely modeled in cold spray simulation as it is a labor intensive process [36] and FEA analysis of cermet particles have not been found in the literature. It

is expected that the impact modeling proposed in this work will help to explain the different impact and build up behaviors of the different powders examined. The software Abaqus/Explicit was employed to carry out these analyses. A quad-dominated mesh was used based on 4-node coupled temperature-displacement elements (CPE4RT). Although a 2D simulation presents the limitation of not perfectly representing the particles, the modeling strategy used allows to incorporate the material inhomogeneity in a simple morphological representation. This allows studying the interaction between the metallic and ceramic phases during the particle impacts. The modeling results obtained were compared with the interrupted spray tests in order to validate the results.

For the simulations, the Johnson-Cook constitutive equation (equation 1) was used to model the plastic behavior of the metallic phases [37]. The state equation used was the linear Us-Up Hugoniot form of Mie-Gruneisen (equation 2). These equations have been used in several investigations to describe particles and substrates deformations in cold spray [38–43]. It is important to mention that no damage criteria was included in the analysis.

$$\sigma_{eq} = \left[A + B\,\varepsilon_p^n\right]\left[1 + C ln\left(\frac{\dot{\varepsilon_p}}{\dot{\varepsilon_{ref}}}\right)\right]\left[1 - \left(\frac{T - T_{ref}}{T_m - T_{ref}}\right)^m\right] \quad 1$$

$$p = \frac{\rho_0 {c_0}^2 \eta}{(1 - s\eta)^2}\left(1 - \frac{\Gamma_0 \eta}{2}\right) - \Gamma_0 \rho_0 E_m \ , \quad \eta = 1 - \frac{\rho_0}{\rho} \quad 2$$

*A, B, C, n, m,* $\dot{\varepsilon_{ref}}$, and $T_{ref}$ are the Johnson-Cook parameters, $\varepsilon_p$ is the plastic strain, $\dot{\varepsilon_p}$ is the plastic strain rate, $T$ is the temperature of the material, and $T_m$ is the melting point. In equation 2, $p$ is the hydrodynamic stress, $\rho_0$ is the initial density, $\rho$ is the actual density, $c_0$ is the material speed of sound, $s$ is the Hugoniot slope, $\Gamma_0$ is the Gruneisen constant, and $E_m$ is the energy per unit mass.

NiCr material properties were used for the metallic phase, while steel AISI 4340 was used for the substrate and the elastic properties of $Cr_3C_2$ were employed for the ceramic phase. A summary of those properties is presented in Table 3. It is important to mention that for the plastic behavior of the metallic phase, the NiCr properties were approximated as those of nickel alloy (Inconel 718), due to the unavailability of required NiCr properties in the literature. This alloy was chosen since its chemical composition resembles the one of the NiCr metallic phase. Although this change in the properties can slightly alter simulation results, the overall effect of the cermet morphology on the deformation behavior is expected to remain valid. A similar obstacle was encountered for the equation

of state. In that case, the parameters of Monel were used for the metallic phase. The parameters used can be found in Table 4 and Table 5.

*Table 3: Material Properties Used in FEA Simulations*

| | **Ni20Cr** [44] | **Steel AISI 4340** [37] | **$Cr_3C_2$** [45–47] |
|---|---|---|---|
| k (W/m K) | 11.3 | 16 | 12 |
| ρ (Kg/m3) | 8400 | 7830 | 6600 |
| G (GPa) | 87 | 79.6 | - |
| E (GPa) | - | - | 373 |
| v | - | - | 0.21 |
| $C_p$ (J/kg K) | 450 | 477 | 551.66 |

*Table 4. Johnson-Cook Parameters Used in Simulations*

| **Johnson-Cook Parameter** | **Inconel 718** [48] | **Steel AISI 4340** [37] |
|---|---|---|
| A (MPa) | 450 | 792 |
| B (MPa) | 1700 | 510 |
| C | 0.017 | 0.033 |
| n | 0.65 | 0.26 |
| m | 1.3 | 1.03 |
| $\dot{\varepsilon_{ref}}$ | 0.001 | 1 |
| $T_m$ (K) | 1570 | 1793 |
| $T_{ref}$ (K) | 298 | 293 |

*Table 5. Mie-Gruneisen Parameters Used in Simulations*

| **Parameters** | **Monel** [49] | **Steel AISI 4340** [49] |
|---|---|---|
| Gruneisen Constant ($\Gamma_0$) | 1.95 | 1.67 |
| Speed of sound ($^m/_s$) | 4190 | 4578 |
| Hugonit slope ($s$) | 1.54 | 1.33 |

The particle velocities required for the model inputs were measured using a Cold Spray Meter (CSM) eVOLUTION (Tecnar Automation Ltd, St-Bruno, Canada). This system performs in-flight diagnostic by illuminating the particles with a continuous 2.4 W ($\lambda$ = 810 nm) laser and capturing the reflection through a dual split photomask in order to calculate the particles velocity, the obtained velocities per powder can be found in Table 1. The substrate temperature used in the model was measured using a FLIR i7 portable infrared camera. Finally, the particle impact temperature was assumed to be 80% of the gas stagnation temperature, similar to values calculated in previous investigations [50]. For

particles and substrates a quadratic mesh was used with a coupled temperature-displacement element type (CPE4RT). The maximum element size of 0.5 μm was used. Arbitrary Lagrangian-Eulerian (ALE) adaptive domain was used for the substrates and metallic phase mesh. The results were directly compared to the interrupted spray test results to evaluate the deposition behavior of the particles.

# Results and Discussion

Powder morphology was observed for the six different feedstock powders studied. Four distinctive morphology categories were defined based on what was observed: CRC-410 and CRC-425 were categorized as spherical, CRC-300 as porous agglomerated and sintered, Amperit 584 and Amperit 587 as dense agglomerated and sintered, and finally Diamalloy 3004 as blended. In the following section, the description of the results of deposition behavior, interrupted spray tests as well as the FEA are separated according to the powder categories.

## Spherical Morphology

Both CRC-410 and CRC-425 atomized powders were categorized as spherical. These powders are morphologically similar, presenting a spherical structure characteristic of atomized powders. The powders show several ceramic particles inside a metallic matrix. Figure 1 (a) and (b) show the CRC-410 and CRC-425 powders respectively, establishing their morphological similarities. Figure 1 (c) shows details at the surface of the CRC-425 powder where ceramic phases can be observed. Figure 1 (d) shows a representative cross-section of one CRC-410 particle, showing the carbide distribution, represented as the darker particles in the BSD image, and the NiCr represented as the whiter matrix. It can be seen that the powder particles are dense and that the ceramic is uniformly distributed inside the particles. It can be noted that some of the particles appear to have a smooth coat at the surface, as can be observed in Figure 1 (b). This was identified as NiCr. It is possible that during the atomization, some of the droplets had no ceramic particles suspended in the liquid metallic phase and some of them impacted and solidified on other particles, coating them with a thin metallic layer.

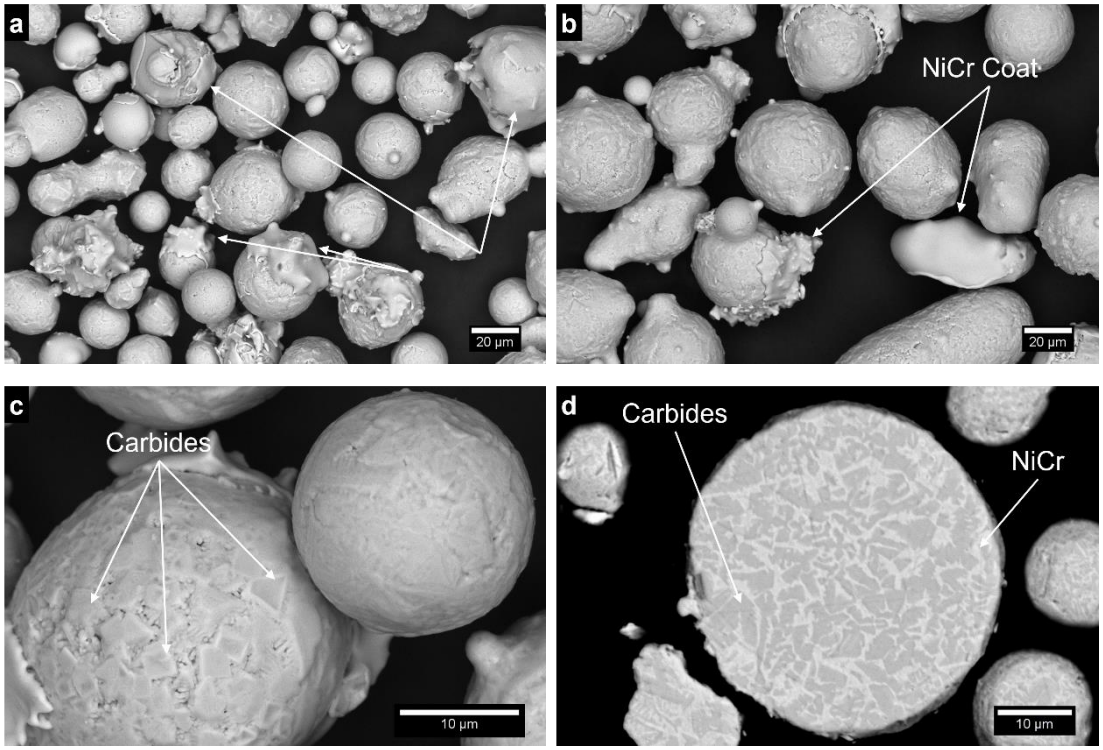


*Figure 1: Overview of powders: a) CRC-410; b) CRC-425; c) Details of CRC-425; d) Cross-section of a CRC-410 particle.*

Neither of these powders resulted in a successful coating. The spray process rather led to erosion of the steel substrate. This was corroborated by the DE measurement, yielding for CRC-410 and CRC-425 values of -0.6% and -0.4% respectively. The interrupted spray tests gave some insights into the spray process of these powders with results that were similar for both spherical powders. Figure 2 shows an overview of the tests results. Clear indentations of the cermet particles are observed on the substrates, and a few adhered particles are observed at the substrates surface.

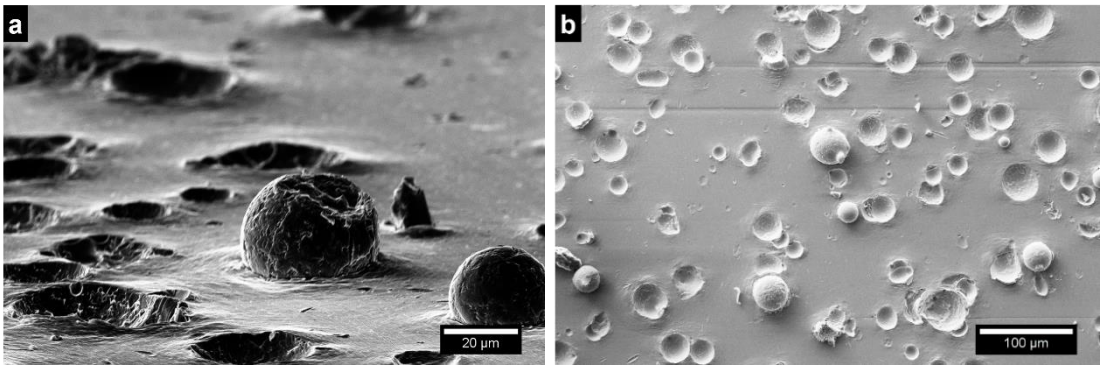


*Figure 2: Overview of interrupted spray test for: a) CRC-410 powder; b) CRC-415 powder.*

Examination of Figure 3 (a) reveals some details about the powders deposition behavior. Mutiple deep spherical indentations in the steel substrates are visible with a clear imprint of the particles surface. The presence of severe material jetting can be found in the craters surroundings. EDS analysis identified that this jetting occurred solely in the substrate. Even though the high strength steel substrates show these signs of severe deformation, the cermet particles show a complete lack of deformation, demonstrating the high hardness of these cermet powders. This lack of deformation is shown in cross-section images of the interrupted spray tests, such as Figure 3 (b). It reveals that the particles are still spherical even below the substrate surface. This result is also confirmed when analyzing the recovered powder particles after the spraying process. Figure 4 (a) and (b) show representative powder particles recovered, illustrating that the particles have not experienced deformation upon impact.

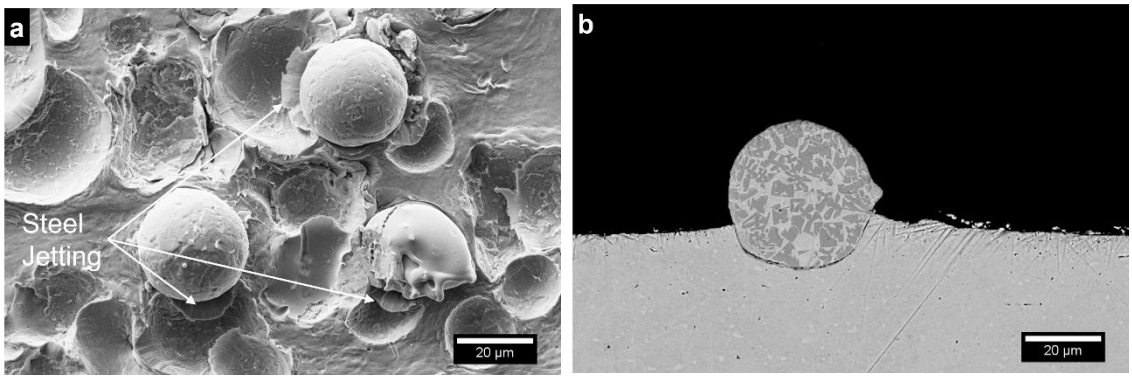


*Figure 3: a) Details of interrupted spray test of CRC-410 powders, showing jetting of the steel substrate; b) Cross-section of a CRC-415 deposited particle.*

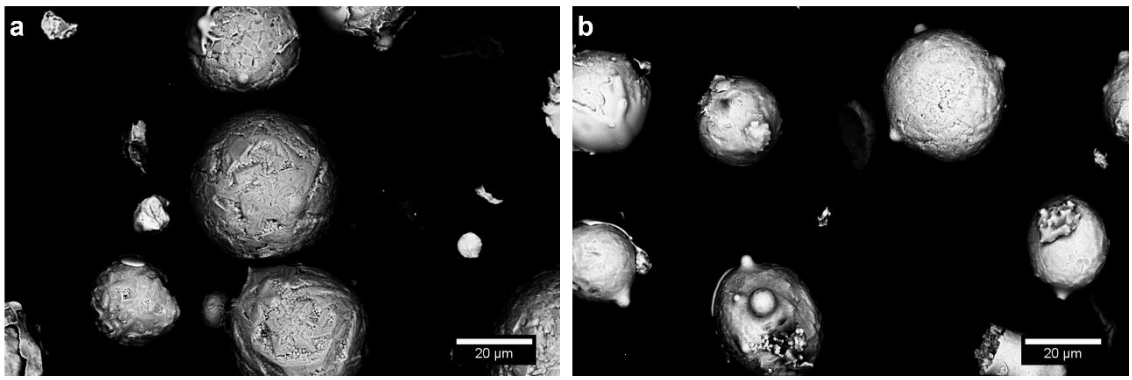


*Figure 4: Recovered powder after deposition: a) CRC-410; b) CRC-425.*

In zones of high impact rate, it is possible to see locations where the incoming particles interacted with the few adhered particles at the substrate surface. When these interactions occur, the adhered particles either get dislodged from the substrate leaving an indentation or get fractured. This lack of ductility also makes the incoming particle unable to adhere to a previously deposited particle. Consequently, the creation of a second layer of particles is limited, preventing coating build-up. Figure 5 shows a few particles that have been impacted by incoming particles: the particles are fractured and show minor level of plastic deformation.

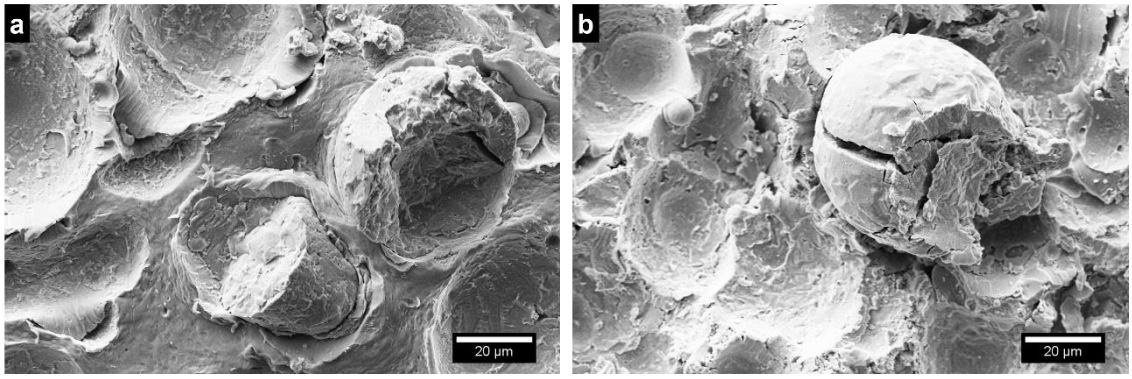


*Figure 5: Adhered particles fractured by incoming particles: a) CRC-410; b) CRC-425.*

The overall spraying outcome of this kind of particles (with low ductility) is similar to the deposition of ceramics, where a particle gets embedded in the soft substrate, and is almost instantly eroded by the incoming particles leaving small embedded sections on the substrate. This is confirmed by substrate cross-sections where several layers were tentatively sprayed. Figure 6 (a) shows particles that have been impacted by a second wave of incoming particles and shows eroded and fractured sections, while Figure 6 (b) shows the final substrate after several of these layers were tentatively sprayed, with only traces of particles remaining on a highly deformed surface.

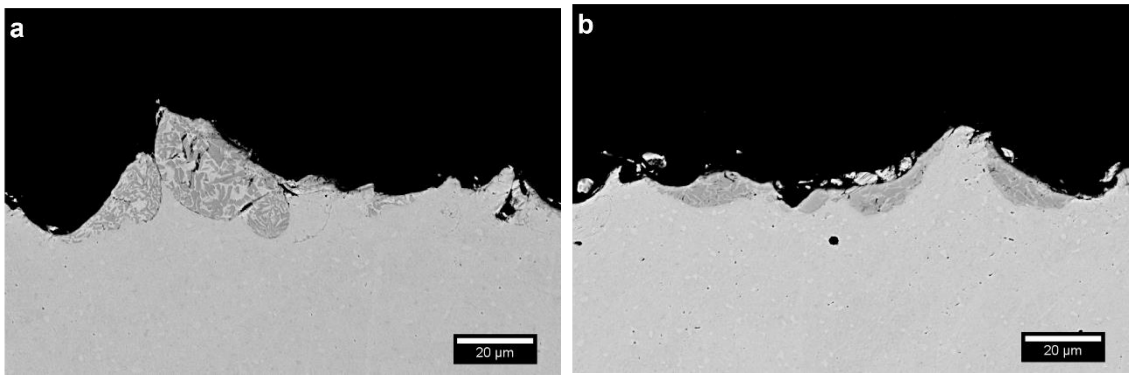


*Figure 6: Cross-section of interrupted spray tests in zones with multiple impacts: a) Two layers tentatively sprayed; b) Several layers tentatively sprayed.*

Another phenomenon observed from the interrupted spray test images is related to the NiCr layer found at the surface of some of the particles mentioned previously. When these particles hit the substrate surface it appears that this layer can achieve bonding with the substrate as several of these particles sections were found at the surface of the test samples. Some of these sections are presented in Figure 7. This NiCr mantle was always found without the inner particle suggesting that this outer layer has no strong bonding with the particle itself. This observation is another indication that the particle does not adhere due to the lack of ductility. Since these layers are metallic, they have the ductility required to deform and adhere to the substrate while the hard particles do not show this ductility, bouncing back upon impact.

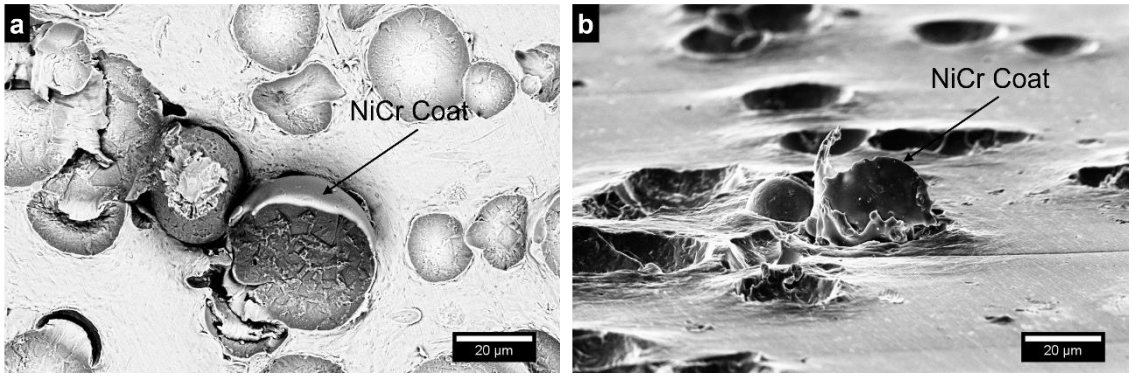


*Figure 7: Details of remaining NiCr shells seen after the interrupted spray tests.*

Finite element analysis helps to further explain the reasons behind the powders deposition behavior. The particles were cross-sectioned, and several representative particles were digitalized and exported to Abaqus/Explicit in order to perform impact simulation. Figure 8 shows some of the digitalized particles that were used in the simulation. The NiCr and $Cr_3C_2$ phases were also traced based on the images contrasts in order to represent the internal microstructure of the particles. It is worth mentioning that a particle coated with a NiCr layer (mantle) was digitalized and it is represented by particle D in Figure 8, The mantle was modeled as a separate element from the particle and it was assumed that no attachment exists between these parts. From the figure, one can notice the difference in NiCr composition between particles A and B (CRC-410) versus particle C and D (CRC-425), as the latter ones contain a higher amount of the metallic phase. For the finite element analysis, a total of three particles per powder type were digitalized. The substrate temperature was evaluated at 192°C using thermal imaging and particle velocity was measured at an average of 435 m/s for CRC-410 particles and 430m/s for CRC-425 particles.

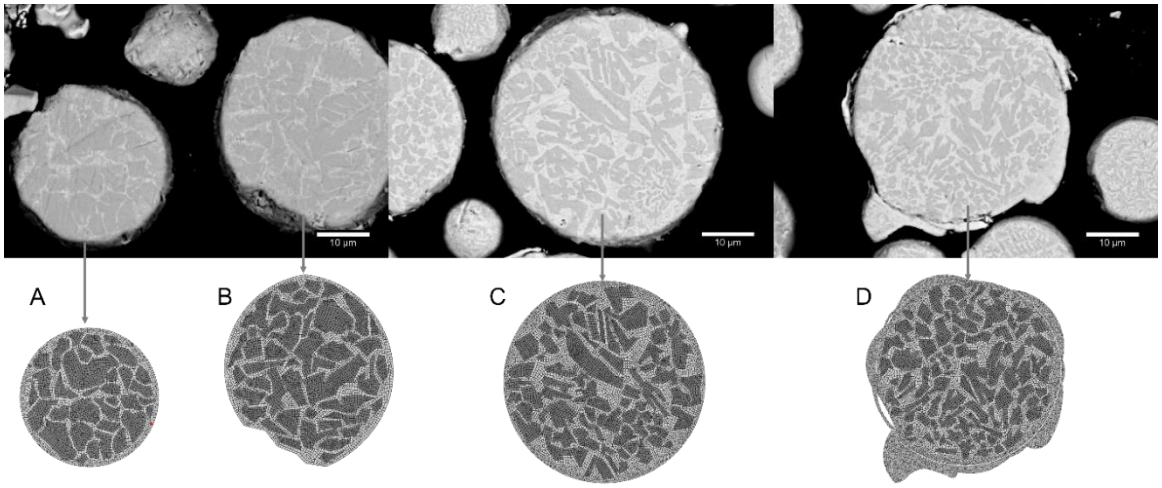


*Figure 8: Digitalization of particles used in the simulations. Particles A and B are from powder CRC-410 and C and D from powder CRC-425.*

Similar to the results observed experimentally, the finite element analysis also shows a limited degree of particle deformation, as presented in Figure 9. Even in the case of the CRC-425 powder particles, where higher metallic content is present, the analysis displays very little deformation of the particle. However, the substrate experienced a high degree of deformation showing the origins of the deep indentations seen in the experimental results.

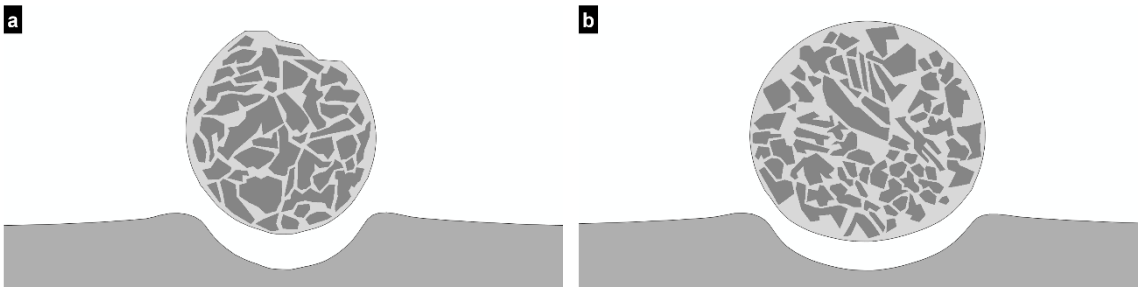


*Figure 9: FEA results of impacts of: a) CRC-410 particle; b) CRC-425 particle, 1µs after rebound.*

This behavior is explained by the uniformly distributed ceramic phase inside the particles. Figure 10 shows the modeled stress distributions during the particle impacts. It is observed that the highest stresses are found in the particles ceramic phase. These ceramic zones redistribute the stresses uniformly across the particles enhancing their strength and inhibiting their ductility. As such, the lower stress levels experienced by the ductile phase is insufficient to induce shear instability that is usually responsible for particle deformation and bonding in cold spray.

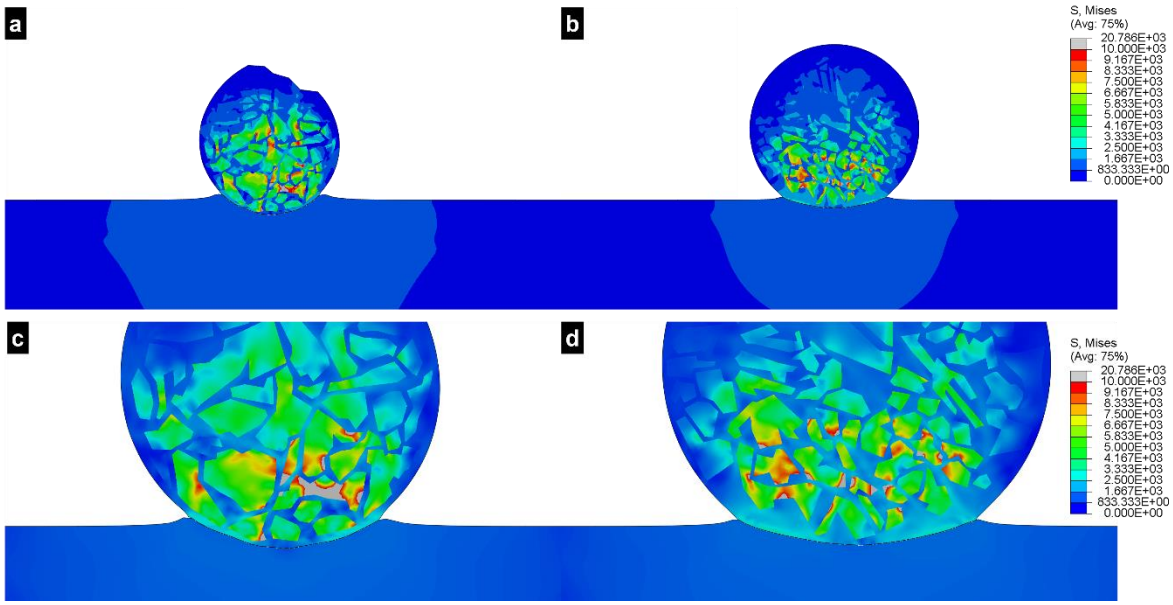


*Figure 10: Overall and details of stress distributions upon impact of particles: a) and c) CRC-410 particle; b) and d) CRC-425 particle.*

This stress redistribution mechanism was corroborated by comparing the modeled deformation states of the particles used for this study with a simulation of a particle consisting of the metallic phase only. The results are presented in Figure 11. This figure clearly shows the impact that the ceramic elements have on the deformation behavior of the particles and the stress redistribution due to the ceramic

particles. Figure 11 c) and d) shows the stress field in the particles during the impact, where the ceramic phase was removed from the image in order to directly compare the metallic phases stress

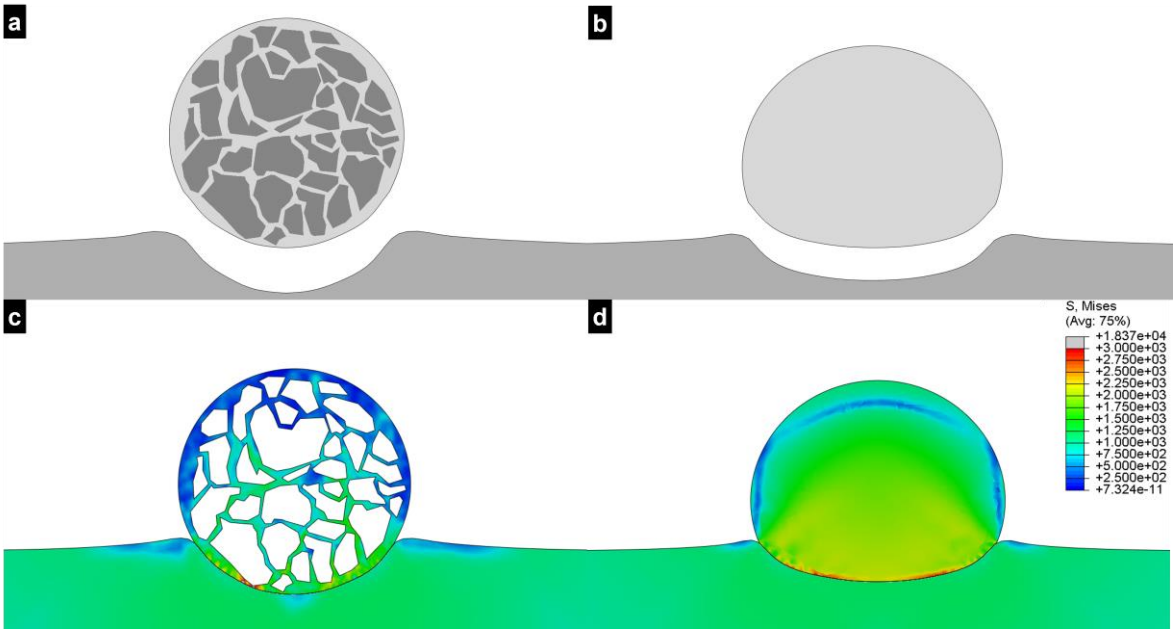


*Figure 11: Comparison of particles: a) With ceramic; b) Only metallic; c) Stress distribution of particle with ceramics; d) Stress distribution of only metallic particle.*

This strengthening mechanism is the same as the one behind the enhanced strength and hardness of cermet materials and is the reason why cermets are good candidates for abrasion resistant materials. This mechanism is also the reason behind the lower DE exhibited by these particles compared to the ones made of solely the metallic phase and explains why they are less suitable to be sprayed by cold spray. Since cold spray is a solid state process that relies on extensive plastic deformation to obtain adhesion, these cermet particles are too densely distributed in the matrix, and under the spray conditions used they were no able to reach the deformation level needed to adhere to the substrate, and therefore cause erosion. It is possible that at higher particle impact velocity and temperature that can be reached with high-pressure cold spray equipment, these particles can meet the conditions to obtain the adiabatic shear instability needed for bonding. This should be explored in further investigation.

The impact modeling of the coated NiCr mantle showed a different behavior where a high degree of deformation of the mantle is observed. Figure 12 (a), shows three stages of the particle undergoing impact. The first stage shows the particle an instant before the impact. During the second stage, the

substrate and mantel are undergoing large plastic deformations, and the mantle starts delaminating from the particle core. Finally, the last stage, a few moments after the impact, shows that the inner particle has bounced off and that the mantle is still in contact with the substrate. This result closely resembles the one seen in Figure 7. Figure 12 (b) shows the computed equivalent plastic deformation (PEEQ) during the last stage. It is important to notice the high amount of plastic deformation experienced by the mantle while the particle core did not show any significant deformation. By undergoing a high amount of plastic deformation, the mantle has larger probabilities to adhere to the substrate, this was simulated by not allowing separation between the mantle and the substrates in the FEA model. These modeling results support and help to explain the presence of similar structures found at the surface of interrupted spray tests substrates.

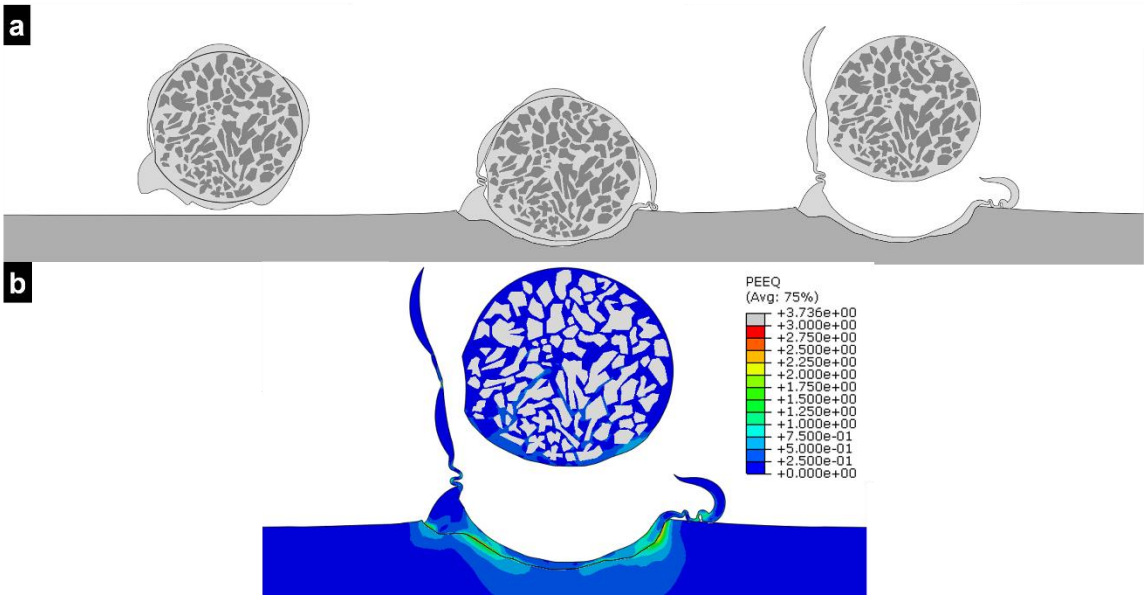


*Figure 12: FEA results of particle showing NiCr mantle: a) Deformation behavior/stages; b) Equivalent plastic deformation.*

## Porous Agglomerated and Sintered Morphology

Based on its morphology, the CRC-300 powder was identified as porous agglomerated and sintered. Figure 13 (a) and (b) show an overview of the powder size and morphology as well as details of the surface of this powder. One can observe that the powder particles are porous and the ceramic particles appear to have fused during the sintering process. In these powders, the NiCr component act as a binder for the ceramic particle, gluing sections of fused ceramic particles rather than a metallic matrix containing the ceramic phase as found in the previous powders (CRC-410 and CRC-425). The powder

internal microstructure is presented in Figure 13 (C) and (D) were cross-sections of the powders are shown and porosity better revealed.

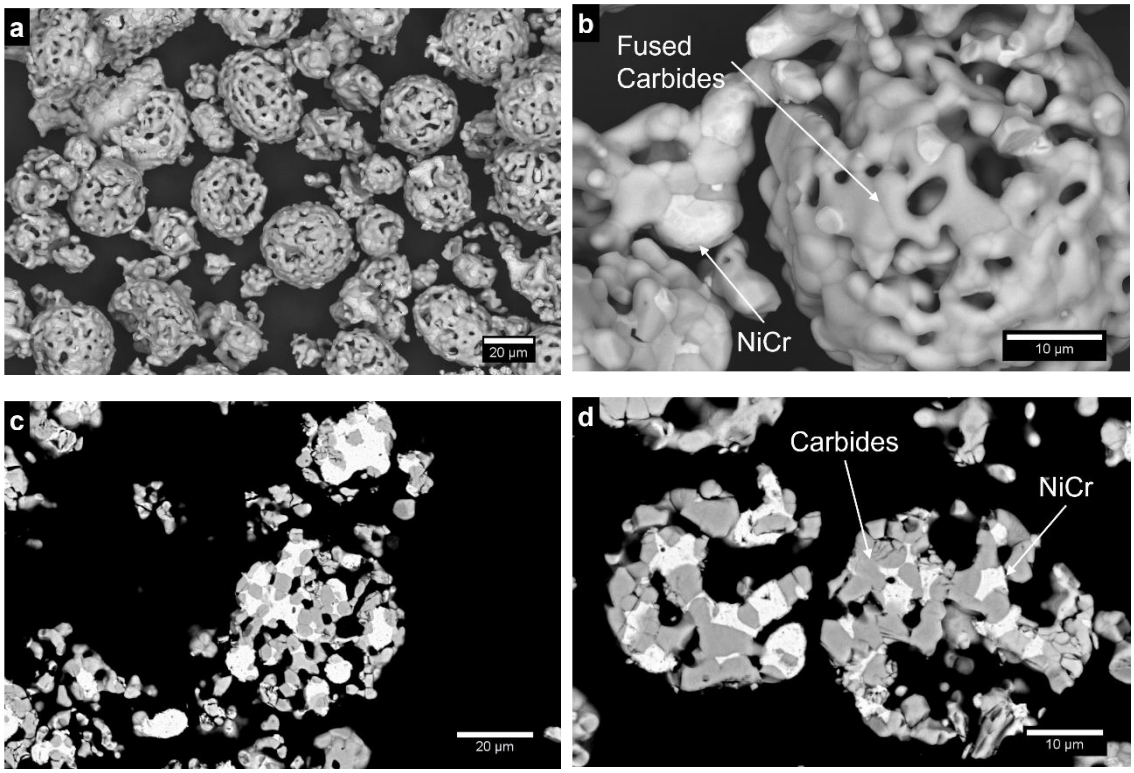


*Figure 13: a) Overview of CRC-300 powders; b) Superficial details of the particles; c) and d) Cross-sections of particles.*

The deposition efficiency of this powder was evaluated at 1.7%. Despite this low value, a coating was successfully sprayed. It is important to note that during deposition sections of the built coating flaked off, due to low adhesion. The DE was calculated without considering these flaked sections. Cross-sections of these coatings are shown in Figure 14, revealing several horizontal cracks. This might be a result of the feedstock powder porosity combined with a lack of plasticity or deformation of the particles upon impact. It is hypothesized that these cracks and the flaking off of some parts of the coatings while spraying are linked. When the coating is being built, cracks propagate until they can no longer sustain the stresses of the deposition and consequently the stream of gas delaminates a section of the coating. The coatings ceramic/metal ratio was evaluated using EDS and an increase in the metallic content from 25wt.% of NiCr in the powder to 41wt.% in the coating was found.

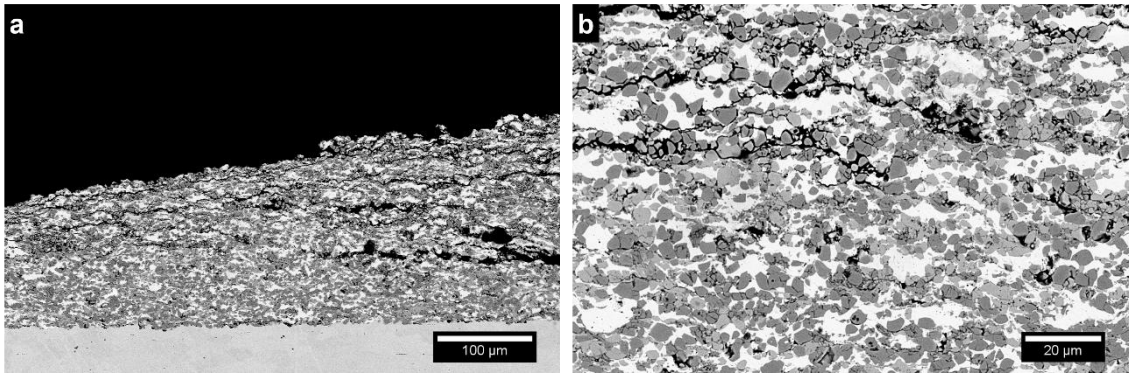


*Figure 14: Cross-sections of CRC-300 coatings.*

Interrupted spray test results confirmed the fracture of the particles upon impact. Figure 15 shows some of the first particles that arrived at the substrates and confirms that they have been fractured upon impact. It also reveals that some particles did lose a section of the original particle as it is possible to see NiCr particle components still adhered to the substrate and mixed with ceramic particles on top. Besides the fractured particles, the tests also revealed several craters created by the particles without any particle bonding. The exact bonding mechanism was not revealed by these images, but it is hypothesized that it is a combination of mechanical and metallurgical bonding depending on the particles impacting surface.

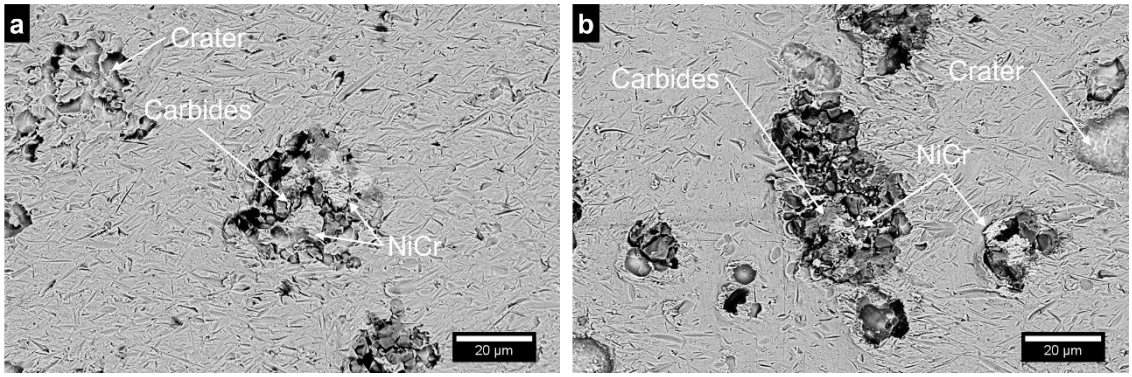


*Figure 15: Top view of single particle impact showing a fractured CRC-300 particle.*

This particle fracturing upon impact can also be confirmed upon inspection of the recovered non-adhered particles. It can be observed from Figure 16 that almost all particles that did no adhere to the substrate fractured upon impact. Even when full particles are found, as presented in Figure 16 (b), these particles are severely cracked in the sections where the ceramic particles were fused. These

sections of the particles are weak and brittle locations that promote fracture upon the stresses caused by the impact. This is also supported by the amount of small ceramic particles found in the recovered powder. Upon impact, when a particle cracks and fractures, several of these ceramic particles will be lost, due to the weak bonding between them, and will be blown away by the cold spray gas stream, explaining the increment of the NiCr phase in the coatings.

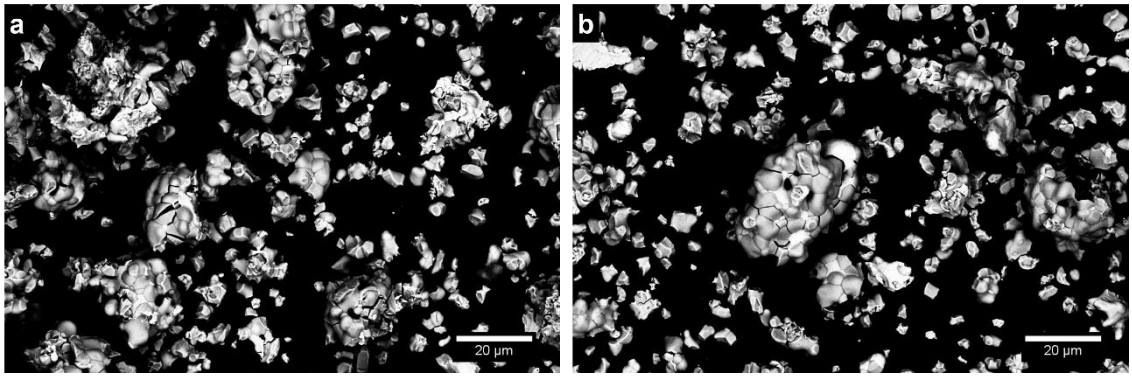


*Figure 16: Overview of non-adhered recovered CRC-300 powder a) fractured particles; and b) full particles cracked in ceramic sections.*

As particles keep adhering to the surface of the previously deposited and cracked particles, the coating keeps building up. This combines with the intrinsic porosity of the feedstock particles and creates porous zones that evolve into cracks. Figure 17 shows a cross-section and overview image of the second layer of particles adhering to the substrate. It is easy to see the gap between the particles and the inherent porosity of the particles contributing to the coating porosity. This lack of structural integrity finally results in coating delamination or in the long horizontal cracks present in the coatings cross-sections.

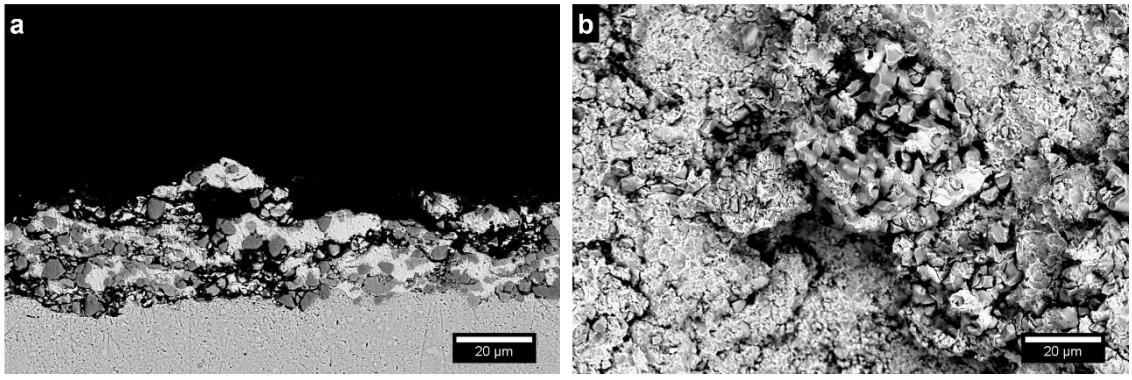


*Figure 17: a) Cross-section; b) Top view, of the second layer of adhering CRC-300 particles.*

Finite element analysis helped to assess the deformation behavior and adhesion mechanism of these porous particles. Some cross-sectioned particles were digitalized and imported to Abaqus/explicit for impact modeling. Figure 18 shows the digitalized particles used in the finite element analysis. The fused ceramic particles were assumed to behave as a continuous particle. After the simulations, the stress in the fused ceramic contact zones was inspected in order to conclude if the stresses at these locations were enough to explain the cracking observed experimentally. The substrate temperature was evaluated at 199ºC and the average particle velocity was measured at 451 m/s.

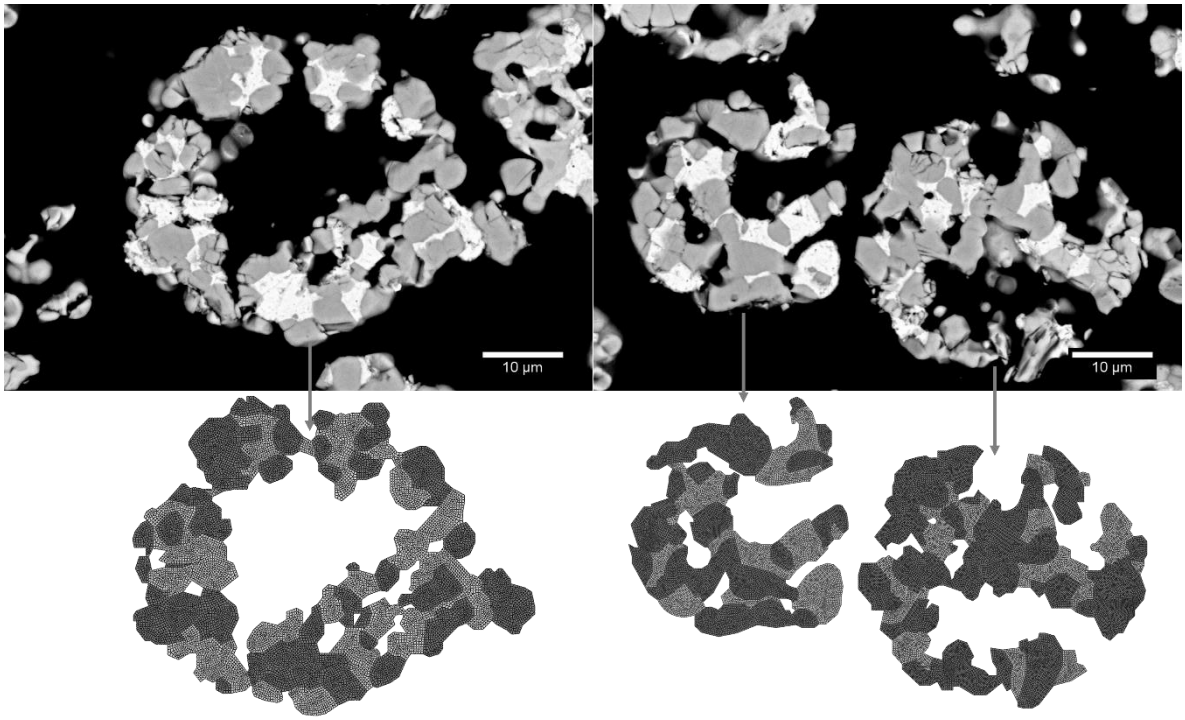


*Figure 18: Particle digitalization for CRC-300 powders.*

Figure 19 shows the particles deformation at three different stages of the impact. The time steps were defined depending on the kinetic energy of the simulation. Figure 19(a) corresponds to the particles before the impact, when the kinetic energy is the highest. Figure 19(b) represent the midpoint between the highest and the lowest point in kinetic energy, and finally, Figure 19(c) is the position with the lowest kinetic energy. This last frame is when the particle is at its highest deformation, and before the elastic energy stored in the particle is released. It can be seen that even at this highest deformation point a single particle does not have enough energy to close the pores originally present in the particles, as all figures show some remnant porosities. This is confirmed experimentally when comparing these images with Figure 17 (a).

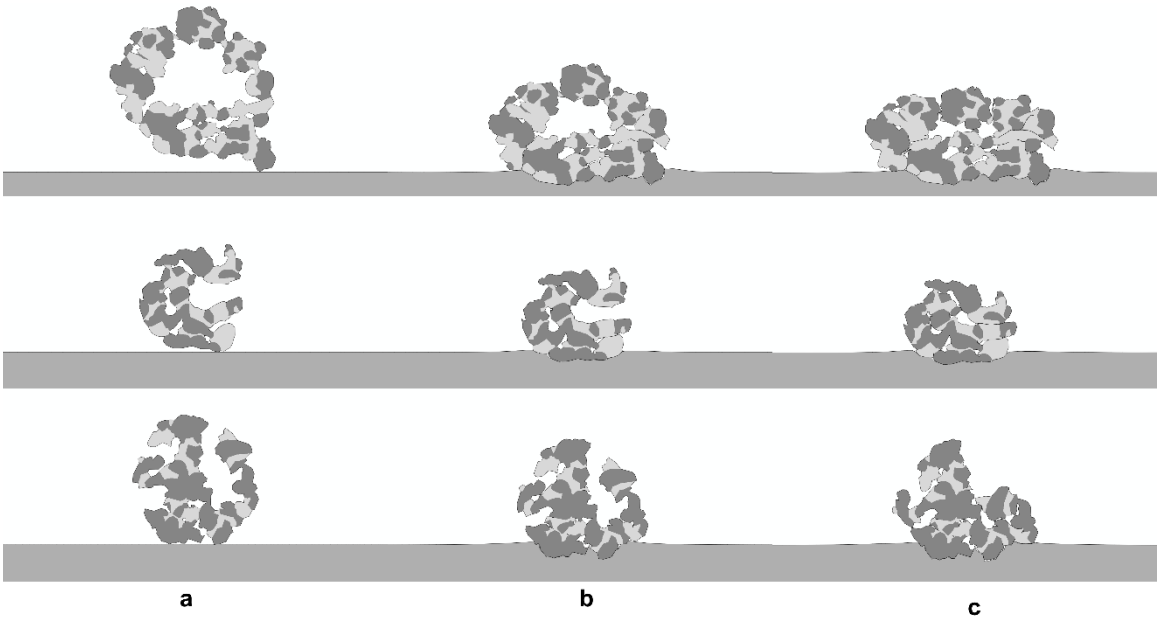


*Figure 19: Evolution of 3 CRC-300 particles deformation at different kinetic energy levels: a) Highest kinetic energy level; b) Midpoint; c) Lowest kinetic energy level.*

Even though these simulations were done without considering damage or fracture of the brittle phase, it is still possible to find insight on the impact mechanism by analyzing stresses and plastic strains experienced by the particles. Figure 20 shows the stress field in two selected particles at the location of the lowest kinetic energy. The display of the stresses has been limited to a minimum of 5 GPa in tension, with this value considerably higher than the flexural strength of $Cr_3C_2$ particles of these dimensions [51]. Therefore there is no doubt that the stresses due to impact might fracture these particles. The locations where the stresses are higher (colored sections) are located exclusively inside the ceramic particles and concentrated at fused zoned between ceramic particles. Due to the high stresses, it is expected that these sections should experience fracture of the ceramic particles, leading to the results observed in the interrupted spray tests, where several fracture zones were identified. This can be the reason behind the numerous horizontal cracks seen in Figure 14 and the peeling of the coatings during deposition.

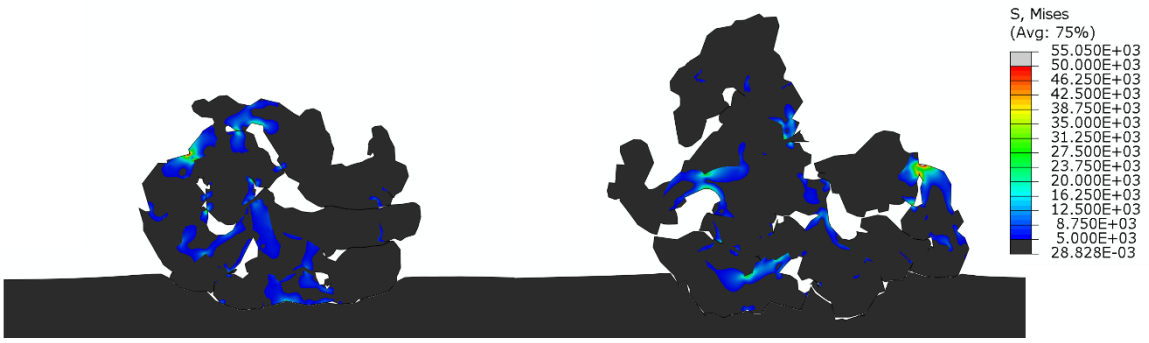


*Figure 20: FEA results: Stress fields in two selected CRC-300 Particles.*

## Dense Agglomerated and Sintered Morphology

The third category of powder includes H.C. Starck, Amperit 584 and Amperit 587 powders. Both powders are produced by agglomeration and sintering, but their morphology differs from the CRC-300 powder, as can be seen from Figure 21. This is true even for Amperit 584 powder (Figure 21 (a)) that contains 25wt.% of NiCr, similarly to the previous studied powder CRC-300. This is a result of the powder production techniques used. Different agglomeration techniques, pressures, initial particle sizes and sinterization temperatures can lead to different final morphologies. Figure 21 reveals less apparent porosity than the previously studied agglomerated and sintered powder (CRC-300). Amperit 587, Figure 21 (b) and (d) shows more superficial NiCr than Amperit 584. This is expected due to its higher NiCr content (35wt.%). Cross-sections of both powders, presented in Figure 21 (c) and (d) show that these powders are mostly dense, with some porosity found inside some of the particles.

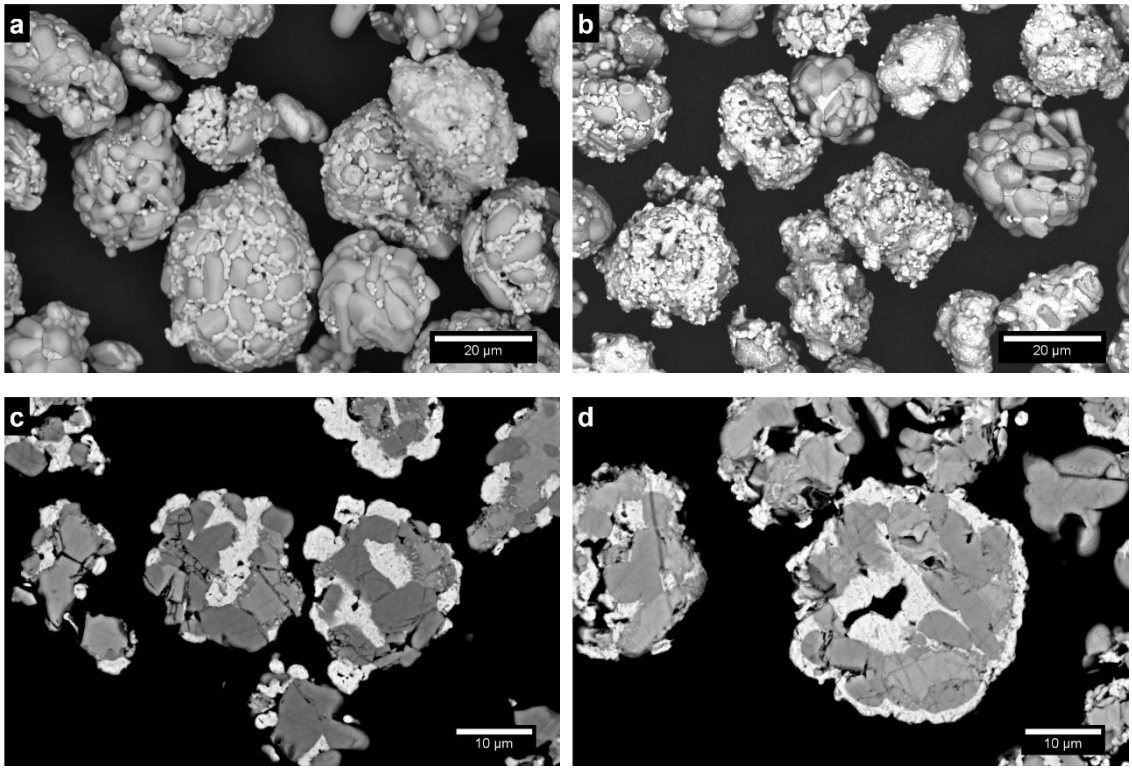


*Figure 21: Overview and cross-sections of powders: a) and (c) Amperit 584; b) and d) Amperit 587.*

Even though these powders morphology appears to be similar, their behavior during cold spray deposition differed greatly. The DE of Amperit 584 was evaluated at -0.1, therefore resulting in a slight erosion of the substrate, while the DE of Amperit 587 was evaluated at 4.0%. This difference is attributed to the higher metallic phase content in Amperit 587. The higher amount of NiCr makes the particles more likely to deform and adhere to the substrate. Figure 22, shows a cross-section of one of the coatings obtained with the Amperit 587 powder. The coating is dense and does not show any trace of horizontal cracks. The NiCr content of the coatings measured with EDS was evaluated as 60wt.% NiCr. This value is remarkably high when compared with the original feedstock powder composition (35wt.%).

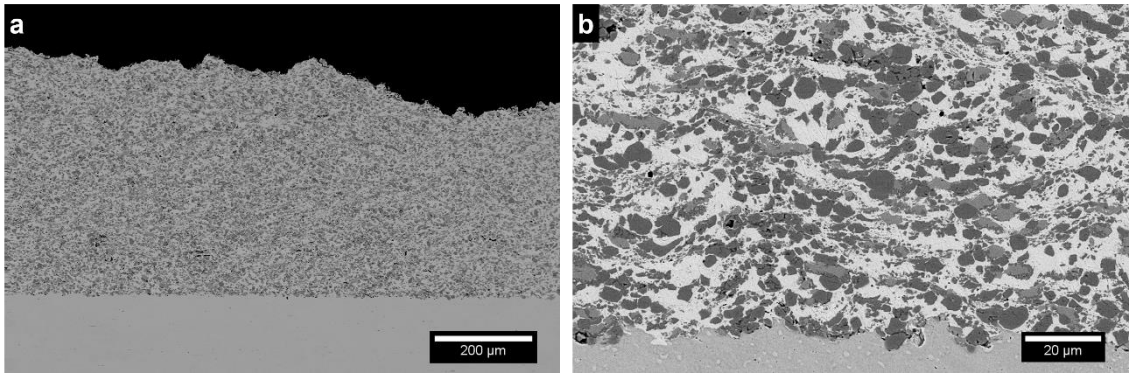


*Figure 22: Coatings cross-sections obtained with Amperit 587: A) Overview; b) Details at the interface.*

Interrupted spray test results gave some indications of the reasons behind this large difference in deposition behavior between the two powders. Even though Amperit 584 resulted in erosion, the tests revealed that the first particles impacting the substrates adhere to it. Figure 23 (a) shows several particles, some fragmented by the impact and others intact. As the spray progresses, the particles do not adhere and eventually start eroding the first layer and the substrate, as can be seen in Figure 23 (b). This effect is also shown in cross-sections of the tests substrates, where single particles can be found, as illustrated in Figure 23 (c). But when a second particle impacts the adhered particle, both fracture and lose some material leaving just a fragment of the original particles in the substrate, as shown in Figure 23 (d).

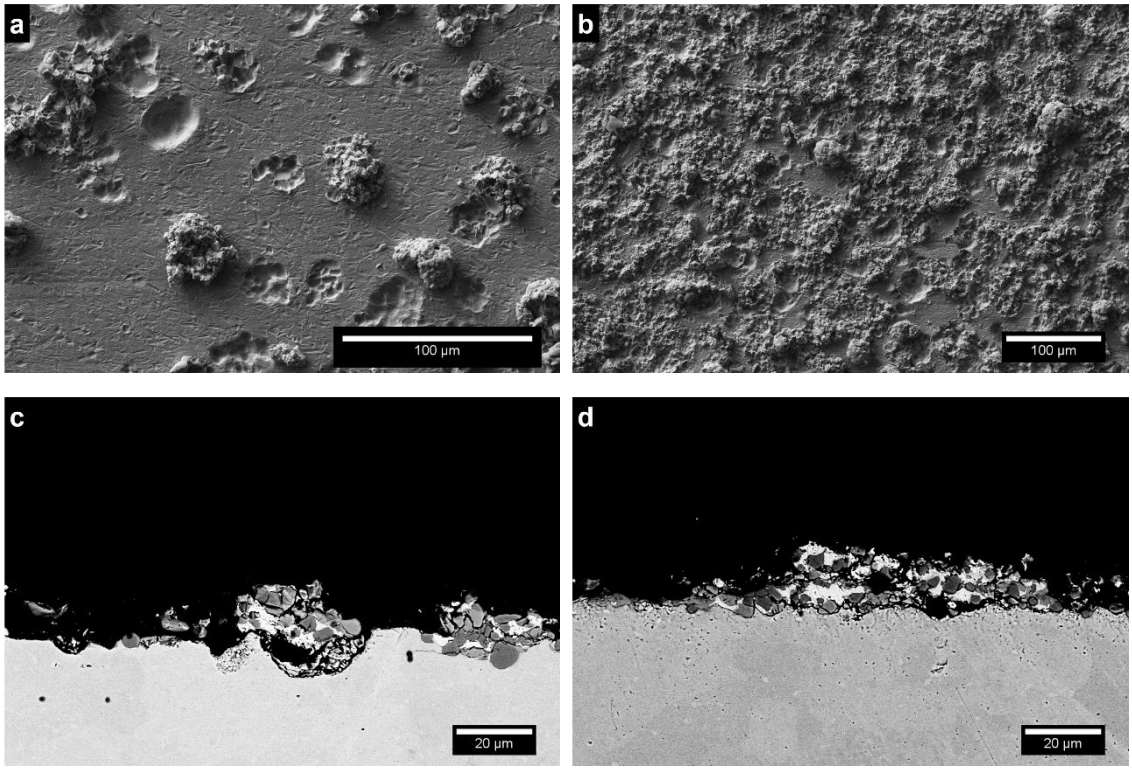


*Figure 23: Interrupted spray test of Amperit 584: a) and b) Top views; c) and d) Cross-sections.*

Amperit 587 powder shows a similar behavior in the interrupted spray tests. Some of the first particles arriving at the substrate fractured upon impact or left an indentation without adhering. However, the tests also revealed that some particles impact and leave lumps of NiCr at the substrate surface with some ceramic particles adhered to it. These particles are likely the ones with high NiCr content at the surface. An example of the traces left on the substrate can be seen in Figure 24 (a). These particles with high metallic content at the surface can also deposit without fracturing as shown in Figure 24 (b). This behavior is confirmed by the cross-sections images in Figure 24 (c) and (d), where the particles are found to have a high NiCr content and just a few ceramic particles. This behavior gets repeated as particles keep depositing. This difference in deposition behavior results in the difference in DE compared to Amperit 584. While the Amperit 584 powder deposited the first particles carrying a high ceramic content, it resulted in the erosion of the adhered particles when new incoming particles impacted on the first particles deposited. For the case of Amperit 587 feedstock powder, it deposits preferentially when the metallic phase of the particle impacts the substrate. This allows for the next particles to have a ductile surface to adhered to and allow building the coating. However, this deposition mechanism comes at the cost of low DE and the requirement of limited ceramic content.

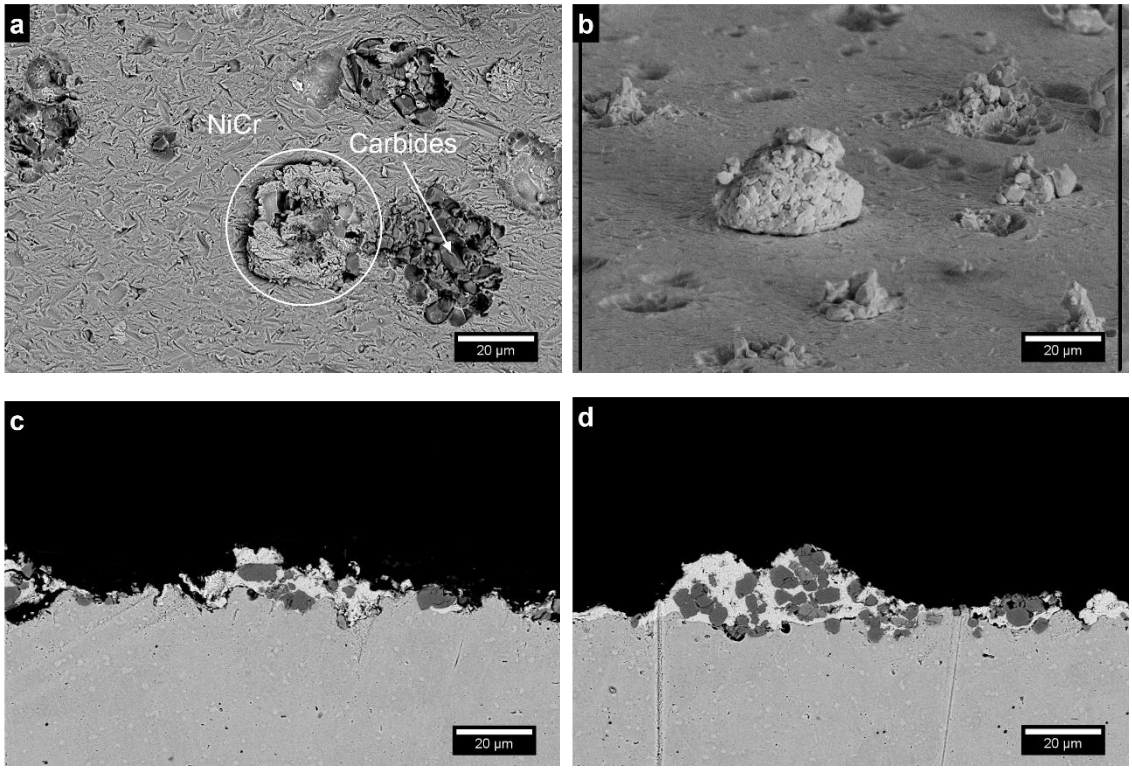


*Figure 24: Interrupted spray test of Amperit 587: a) and b) Top view;c) and d) cross-sections.*

The fracturing of the particles observed in the interrupted spray tests results is confirmed by analyzing the particles that did not adhere to the substrate. Figure 25 shows the powder recovered after spray, and reveals a high amount of small ceramic particles and also particles fractured in half, possibly as a result of the high stress in this section of the particles. This high amount of ceramic particles is in line with the reduction in coating ceramic content observed when comparing the coatings with the feedstock powders.

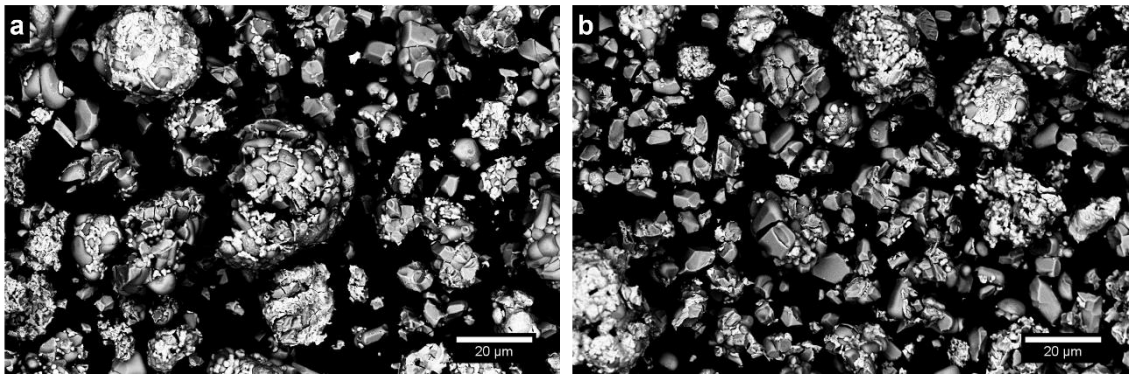


*Figure 25: Overview of non-adhered powders: a) Amperit 584;b) Amperit 587.*

For the FEA some cross-sectioned particles were digitalized and imported to Abaqus/explicit. Figure 26 shows some of the digitalized particles used in the finite element analysis. The substrate temperature was evaluated at 195°C and the average particle velocity measured was 499 m/s for Amperit 584 and 509 m/s for Amperit 587.

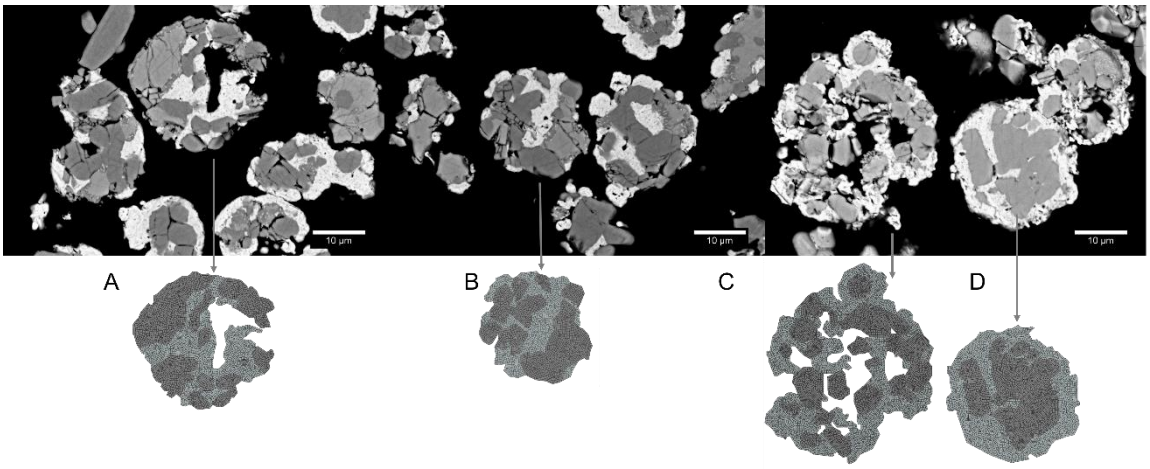


*Figure 26: Digitalization of selected particles: A and B Amperit 584 powders. C and D Amperit 587 powders.*

Figure 27 shows the deformation of some selected particles for each powder at three different kinetic energy levels. Figure 27 (a) shows the particles just before the impact with the substrate, at the highest kinetic energy level, Figure 27 (b) midway to the minimum kinetic energy level, and Figure 27 (c) at its lowest kinetic energy level. It is easy to see that these particles do not experience much plastic deformation upon impact. This is a consequence of their high density and the strengthening effect of the ceramic particles. Figure 28 displays PEEQ and it is possible to see that particles with a NiCr outer layer present a higher degree of deformation upon impact at the substrate contact and have a larger area of contact between metal in the particle and the substrate. This allows the superficial metallic layer of the particle to adhere to the substrate. If the ceramic content is not well adhered to the superficial metal, a result as the one shown in Figure 24 (a) can be obtained where just remains of NiCr are found in the substrates. In the case the ceramic layer adheres well adheres to the metal, a result as illustrated in Figure 24 (b) can be obtained, where the full particle adheres to the substrate. Another feature to observe is the amount of plastic deformation of the substrate that can accommodate or promote particle embedment even if not enough plastic deformation is seen in the particle.

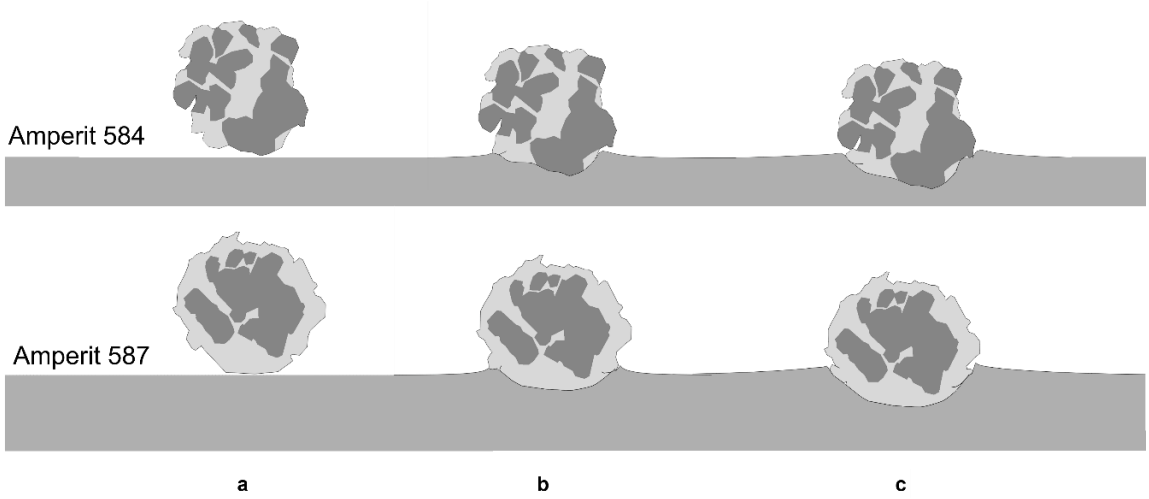


*Figure 27: Evolution of particle deformation at different kinetic energy levels: a) Highest energy level; b) Midpoint ;c) Lowest kinetic energy for selected particles, Amperit 584 and Amperit 587.*

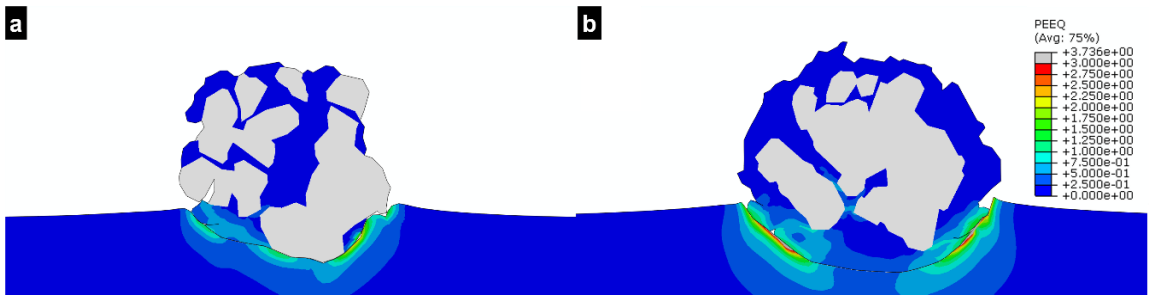


*Figure 28: Plastic deformation field of selected particles: a) Amperit 584;b) Amperit 587.*

## Blended Powders

Diamalloy 3004 was classified as blended powder.This powder is a commercial blending made with atomized 25wt.% NiCr and 75wt.% chromium carbide. This morphology is shown in Figure 29 (a) and (b). A large range in ceramic particle size is observed, ranging from 5um to 25 um in size. Deposition of this powder was successful, obtaining dense coatings shown in Figure 29 (c) and (d). The DE of this powder was measured at 4.2%, slightly higher that Amperit 587. The coating metallic content measured by EDS was 69wt.% NiCr. This value is remarkably higher than the feedstock powder at 25wt.% of NiCr. This behavior has been previously reported in investigations when the consolidation of blended cermet powders by cold spray has been studied [26, 29, 52–54]. These investigations have covered in general aluminum based cermets, and it has been seen that the ceramic weight percentage in the coatings reduced approximately to half of the powder content. It is important

to note that this study used completely different materials and obtained a low DE compared with the investigation of Al-based cermets, but the reduction in ceramic content seen after deposition is in the same range (from 75wt.% in the feedstock powder to 31wt.% of carbide in the coatings).

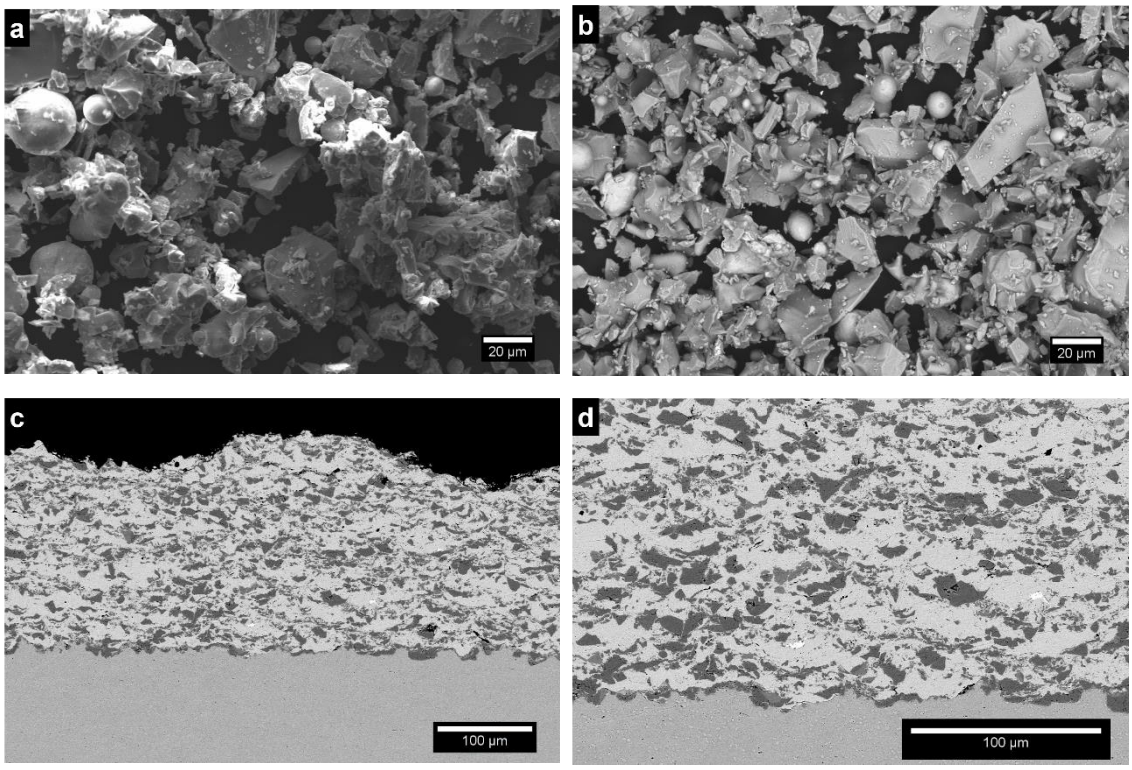


*Figure 29: (a) and (b) Overview of Diamalloy 3004; (c) and (d) Cross-sections of coatings obtained.*

Interrupted spray tests reveal the deposition behavior of this powder. Figure 30 (a) shows that ceramic particles hit and deeply embed the substrates, while Figure 30 (b) shows that NiCr particles deform upon impact, adhering to the substrates. As the deposition continues, the ceramic particles act as peening agent, hitting and deforming the previously deposited material. Figure 30 (c) shows a NiCr particle that has been severely deformed by these peening particles. Figure 30 (d) shows a top view of the coating obtained with this powder, where just a few ceramic particles can be identified on the surface. This suggests that ceramic particles have lower probabilities of adhering to the substrate that the metallic particles.

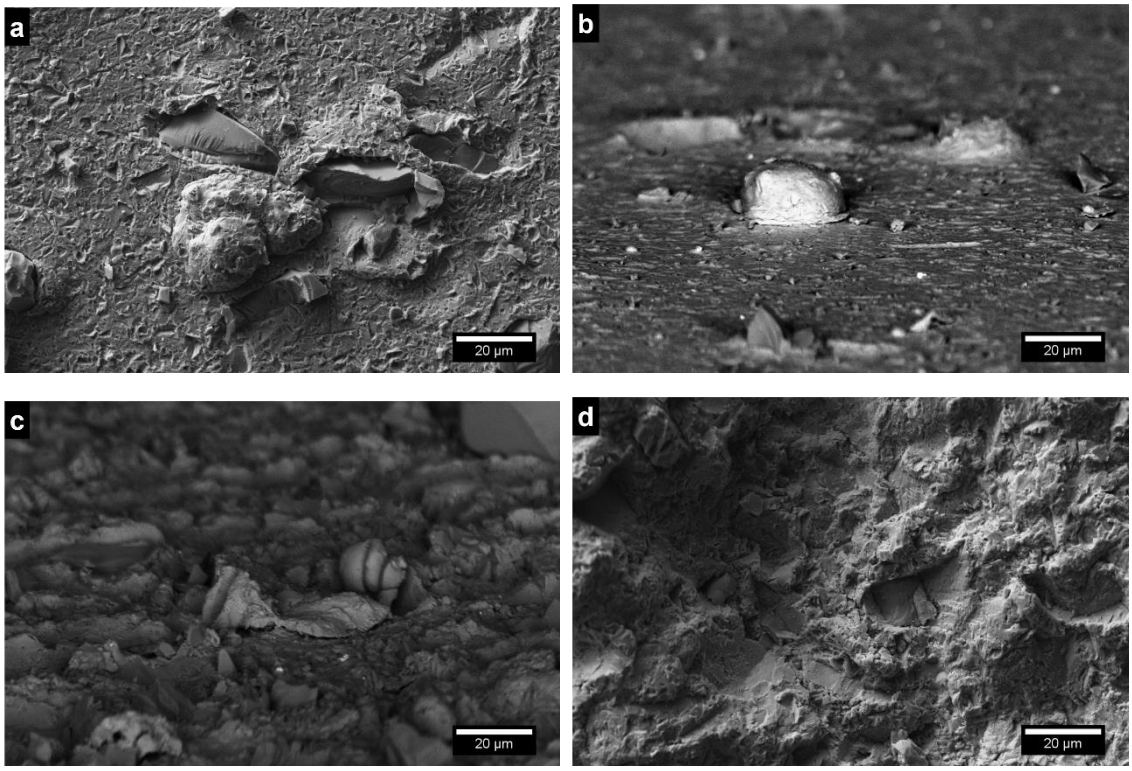


*Figure 30: Interrupted spray test results of Diamalloy 3004: a) NiCr particle and embedded ceramics; b) NiCr particles; c) Peened NiCr particle;d) Top view of coating.*

In addition, when the powders that did not adhere to the substrate (Figure 31) are analyzed, it is easy to see that most of these particles are ceramic particles. One can also observe that several ceramic particles appear to be fractured. In addition, as expected, the metallic particles recovered appear to be severely deformed.

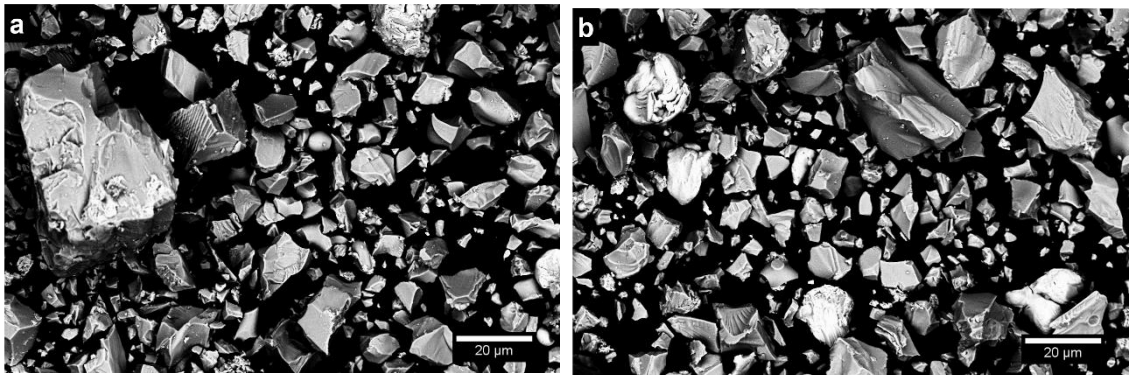


*Figure 31: Overview of Diamalloy 3004 non-adhered powder particles.*

FEA was also done for this powder, and three cross-sections of the carbides and three cross-sections of NiCr powders were digitalized and imported to Abaqus/explicit. Figure 32 shows some selected digitalized particles used in the finite element analysis. The substrate temperature was evaluated at 190°C and the average particle velocity measured was 471 m/s.

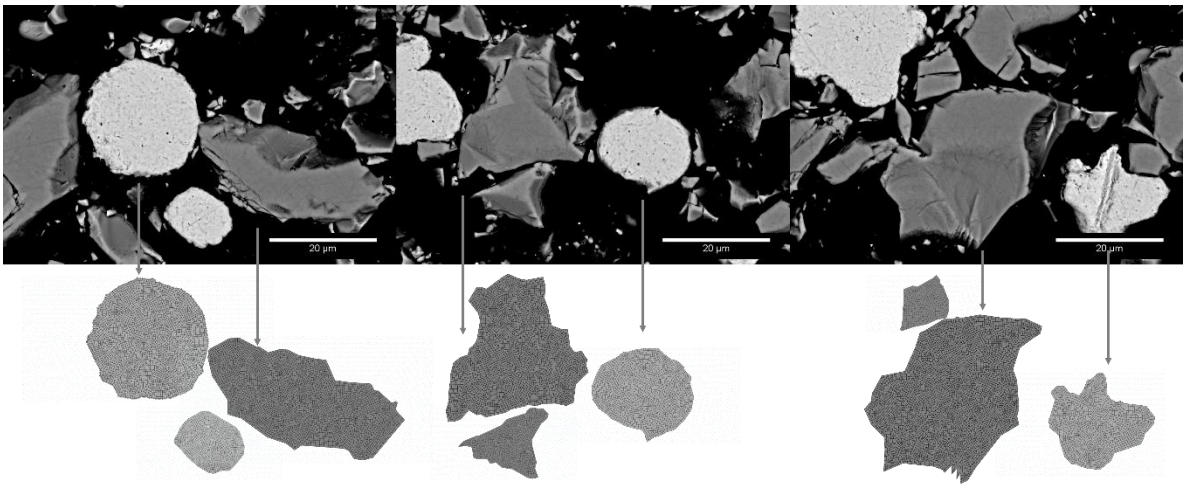


*Figure 32: Ceramic and metallic particle digitalizations used for FEA for Diamalloy 3004.*

Figure 33 shows the result of the FEA for some selected particles. The deformation seen in the NiCr particles is characteristic of impacts of spherical metallic particles in cold spray, and it is comparable with result found in the interrupted spray tests (Figure 30 (b)). Figure 33 (c) and (d) shows the FEA results of the ceramic particles. It is important to note the indentation depth of the ceramic particles, leading to particle embedment seen in Figure 30 (a). From the FEA analysis, it is clear the ceramic particles do not embed completely into the substrate, the exposed part of the ceramic particle leaving them vulnerable to breaking by following impacts with incoming particles. When this happens, part of the ceramic particle remains deeply embedded in the substrate and the fractured part flies away as the one seen in Figure 31. Figure 34 shows an example of the particles that remain embedded in the substrate after fracturing.

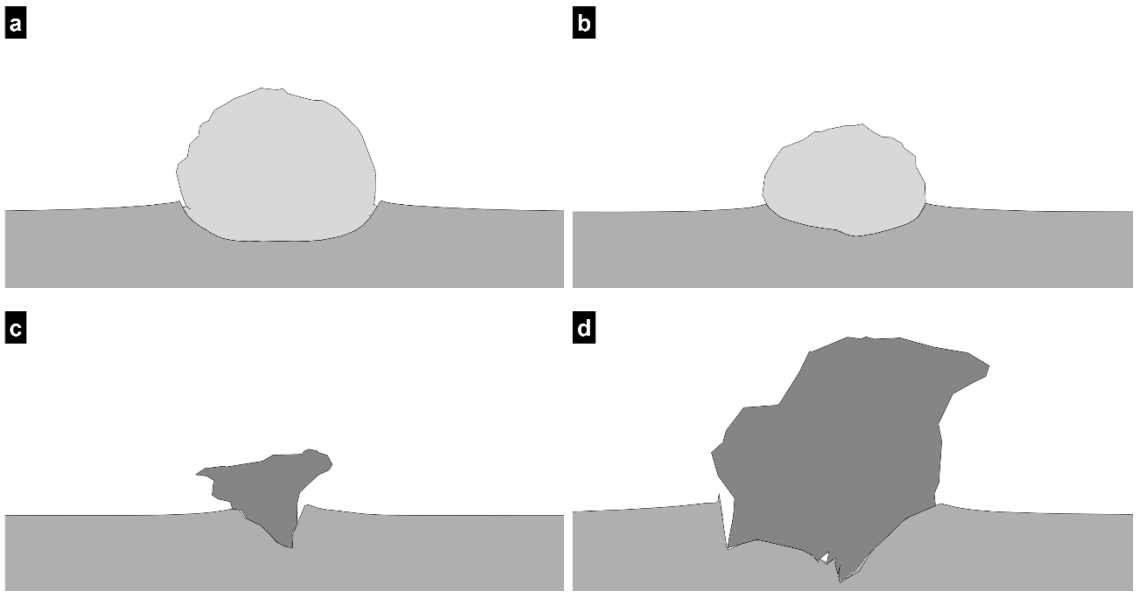


*Figure 33: FEA results for selected Diamalloy 3004 particles: (A) and (B) Metallic particles; (C) and (D) Ceramic particles.*

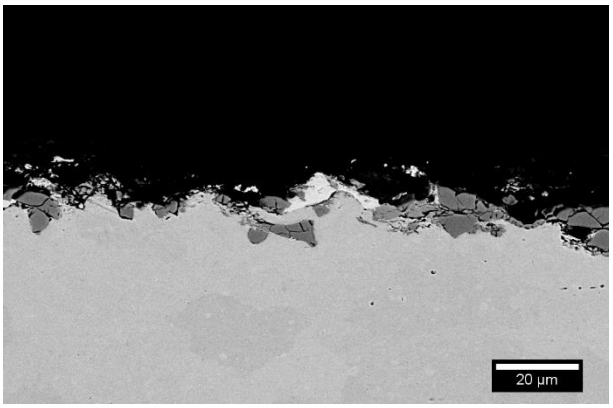


*Figure 34: Fractured chromium carbide particles embedded in the substrate.*

## Summary of Results

Table 6 summarizes the obtained results. It presents the powders used with their respective DE and the ceramic content of the coatings, when coatings were obtained. It is important to note that in all coatings, the ceramic composition was reduced. This is a general outcome seen by other investigations in cermets by cold spray [26, 29, 52–54]. It is important to mention that DEs of these powders are remarkably low. This is a result of the low deposition parameters and the use of nitrogen combined with the hardness of the materials.

*Table 6: Summary of Powders Used.*

| Commercial name | Morphology | Powder Composition wt.% Carbide/Metal | DE | Coating Composition wt.% Carbide/Metal |
|---|---|---|---|---|
| Praxair CRC-410 | Spherical | 70/30 | -0.6% ± 0.2% | No deposition |
| Praxair CRC-425 | Spherical | 60/40 | -0.4% ± 0.1% | No deposition |
| Praxair CRC-300 | Porous Agglomerated and sintered | 75/25 | 1.7% ± 0.9% | 59/41 |
| H.C. Starck Amperit 584 | Dense Agglomerated and sintered | 75/25 | -0.1% ± 0.1% | No deposition |
| H.C. Starck Amperit 587 | Dense Agglomerated and sintered | 65/35 | 4.0% ± 0.8% | 48/52 |
| Oerlikon Diamalloy 3004 | Atomized with crushed | 75/25 | 4.2% ± 0.7% | 31/69 |

# Conclusion

From the six CrC-NiCr commercially available powders tested in this investigation, three of them produced successful coatings, but only two produced dense coatings. The analysis performed allowed identifying that powder morphology has a large impact on the feedstock powder deposition behavior. Both spherical cermets, CRC-410 and CRC-425 led to substrate erosion, the dense particle morphologies leading to low plasticity by redistributing the stresses inside the particles. This lack of ductility is responsible for the low deposition efficiency of these particles. Porous feedstock powder morphologies as the one seen in the CRC-300 powder led to successful coatings, but several internal cracks were found, leading to coating peeling during deposition. Porous feedstock powder structure with fused ceramic particles at the outside of the particles led to particle fracture upon impact.

Ceramic and metallic contents was also found to be an important factor in the deposition behavior of the particles. Amperit 584 and Amperit 587, both with the same morphology showed different deposition behaviors. Amperit 587 resulted in a dense coating due to its higher metallic content. These particles left metallic traces in the substrate upon impact which helped to build the coatings. Feedstock powders made of metal-ceramic blend also produced successful dense coatings, even though severe fracturing of the ceramic particles upon impact were observed as well as a high decrease of ceramic content in the coatings. Further studies focusing on this decrease of ceramic content should be done with more accurate methods than EDS. This will allow understanding the structural changes that may happen to the ceramic particles and the potential effect on the coating properties. More studies should

be done to characterize and optimize the morphology of cermet powders and tailor them for cold spray in order to widen the spectrum of materials sprayable using this process.

# References


1. Picas J a., Punset M, Menargues S, et al (2015) Microstructural and tribological studies of as-sprayed and heat-treated HVOF Cr3C2–CoNiCrAlY coatings with a CoNiCrAlY bond coat. Surf Coatings Technol 268:317–324. doi: 10.1016/j.surfcoat.2014.10.039

2. Ji G-C, Li C-J, Wang Y-Y, Li W-Y (2006) Microstructural characterization and abrasive wear performance of HVOF sprayed Cr3C2–NiCr coating. Surf Coatings Technol 200:6749–6757. doi: 10.1016/j.surfcoat.2005.10.005

3. Poirier D, Legoux J-GG, Lima RS (2013) Engineering HVOF-Sprayed Cr 3 C 2 -NiCr Coatings: The Effect of Particle Morphology and Spraying Parameters on the Microstructure, Properties, and High Temperature Wear Performance. J Therm Spray Technol 22:280–289. doi: 10.1007/s11666-012-9833-3

4. Yun E, Lee S (2005) Correlation of microstructure with hardness and wear resistance in Cr3C2/stainless steel surface composites fabricated by high-energy electron beam irradiation. Mater Sci Eng A 405:163–172. doi: 10.1016/j.msea.2005.05.081

5. Baiamonte L, Marra F, Gazzola S, et al (2015) Thermal sprayed coatings for hot corrosion protection of exhaust valves in naval diesel engines. Surf Coatings Technol. doi: 10.1016/j.surfcoat.2015.10.072

6. Y. Ding, T. Hussain, D. G. McCartney High-temperature oxidation of HVOF thermally sprayed NiCr–Cr 3 C 2 coatings: microstructure and kinetic. J Mater Sci. doi: 10.1007/s10853-015-9238-z

7. Picas JA, Forn A, Matthäus G (2006) HVOF coatings as an alternative to hard chrome for pistons and valves. Wear 261:477–484. doi: 10.1016/j.wear.2005.12.005

8. Kunioshi CT, Correa O V., Ramanathan L V. (2006) High temperature oxidation and erosion–oxidation behaviour of HVOF sprayed Ni–20Cr, WC–20Cr–7Ni and $Cr_3C_2$–Ni–20Cr coatings. Surf Eng 22:121–127. doi: 10.1179/174329406X98403

9. Bu Qian Wang, Luer K (1994) The erosion-oxidation behavior of HVOF Cr3C2-NiCr cermet

coating. Wear 174:177–185. doi: 10.1016/0043-1648(94)90100-7

10. Wang BQ, Shui ZR (2002) The hot erosion behavior of HVOF chromium carbide-metal cermet coatings sprayed with different powders. Wear 253:550–557. doi: 10.1016/S0043-1648(02)00049-2

11. Matthews S (2014) Compositional Development as a Function of Spray Distance in Unshrouded/Shrouded Plasma-Sprayed Cr3C2-NiCr Coatings. J Therm Spray Technol 24:515–533. doi: 10.1007/s11666-014-0212-0

12. Matthews N, Jones R, Sih GC (2013) Application of supersonic particle deposition to enhance the structural integrity of aircraft structures. Sci China Physics, Mech Astron 57:12–18. doi: 10.1007/s11433-013-5367-z

13. Yuan J, Ma C, Yang S, et al (2015) Improving the wear resistance of HVOF sprayed WC-Co coatings by adding submicron-sized WC particles at the splats' interfaces. Surf Coatings Technol. doi: 10.1016/j.surfcoat.2015.11.017

14. Alidokht SA, Manimunda P, Vo P, et al (2016) Cold spray deposition of a Ni-WC composite coating and its dry sliding wear behavior. Surf Coatings Technol 308:424–434. doi: 10.1016/j.surfcoat.2016.09.089

15. Yuan J, Zhan Q, Huang J, et al (2013) Decarburization mechanisms of WC–Co during thermal spraying: Insights from controlled carbon loss and microstructure characterization. Mater Chem Phys 142:165–171. doi: 10.1016/j.matchemphys.2013.06.052

16. Myalska H, Moskal G, Szymański K (2014) Microstructure and properties of WC–Co coatings, modified by sub-microcrystalline carbides, obtained by different methods of high velocity spray processes. Surf Coatings Technol 260:303–309. doi: 10.1016/j.surfcoat.2014.07.097

17. Dykhuizen RCC, Smith MFF (1998) Gas Dynamic Principles of Cold Spray. J Therm Spray Technol 7:205–212. doi: 10.1361/105996398770350945

18. Tokarev a. O (1996) Structure of aluminum powder coatings prepared by cold gasdynamic spraying. Met Sci Heat Treat 38:136–139. doi: 10.1007/BF01401446

19. Alkhimov AP, Papyrin AN, Kosarev VF, et al (1995) Method and device for coating.

20. Assadi H, Gärtner F, Stoltenhoff T, Kreye H (2003) Bonding mechanism in cold gas spraying. Acta Mater 51:4379–4394. doi: 10.1016/S1359-6454(03)00274-X

21. Schmidt T, Assadi H, Gärtner F, et al (2009) From particle acceleration to impact and bonding in cold spraying. J Therm Spray Technol 18:794–808. doi: 10.1007/s11666-009-9357-7

22. Grujicic M, Saylor JR, Beasley DE, et al (2003) Computational analysis of the interfacial bonding between feed-powder particles and the substrate in the cold-gas dynamic-spray process. Appl Surf Sci 219:211–227. doi: 10.1016/S0169-4332(03)00643-3

23. Hussain T, McCartney DG, Shipway PH, Zhang D (2009) Bonding mechanisms in cold spraying: The contributions of metallurgical and mechanical components. J Therm Spray Technol 18:364–379. doi: 10.1007/s11666-009-9298-1

24. Dykhuizen RCC, Smith MFF, Gilmore DLL, et al (1999) Impact of High Velocity Cold Spray Particles. J Therm Spray Technol 8:559–564. doi: 10.1361/105996399770350250

25. Samson T, MacDonald D, Fernández R, Jodoin B (2015) Effect of Pulsed Waterjet Surface Preparation on the Adhesion Strength of Cold Gas Dynamic Sprayed Aluminum Coatings. J Therm Spray Technol 24:984–993. doi: 10.1007/s11666-015-0261-z

26. Irissou E, Legoux J-G, Arsenault B, Moreau C (2007) Investigation of Al-Al2O3 Cold Spray Coating Formation and Properties. J Therm Spray Technol 16:661–668. doi: 10.1007/s11666-007-9086-8

27. Sova a., Papyrin A, Smurov I (2009) Influence of Ceramic Powder Size on Process of Cermet Coating Formation by Cold Spray. J Therm Spray Technol 18:633–641. doi: 10.1007/s11666-009-9359-5

28. Wang Q, Spencer K, Birbilis N, Zhang M-X (2010) The influence of ceramic particles on bond strength of cold spray composite coatings on AZ91 alloy substrate. Surf Coatings Technol 205:50–56. doi: 10.1016/j.surfcoat.2010.06.008

29. Shkodkin a., Kashirin A, Klyuev O, Buzdygar T (2006) Metal Particle Deposition Stimulation by Surface Abrasive Treatment in Gas Dynamic Spraying. J Therm Spray Technol 15:382–386. doi: 10.1361/105996306X124383

30. Finnie I, McFadden DH (1978) On the velocity dependence of the erosion of ductile metals

by solid particles at low angles of incidence. Wear 48:181–190. doi: 10.1016/0043-1648(78)90147-3

31. Ang ASM, Berndt CC, Cheang P (2011) Deposition effects of WC particle size on cold sprayed WC–Co coatings. Surf Coatings Technol 205:3260–3267. doi: 10.1016/j.surfcoat.2010.11.045

32. Jafari M, Enayati MH, Salehi M, et al (2014) Influence of Nickel-Coated Nanostructured WC-Co Powders on Microstructural and Tribological Properties of HVOF Coatings. J Therm Spray Technol 23:1456–1469. doi: 10.1007/s11666-014-0171-5

33. Lima R., Karthikeyan J, Kay C., et al (2002) Microstructural characteristics of cold-sprayed nanostructured WC–Co coatings. Thin Solid Films 416:129–135. doi: 10.1016/S0040-6090(02)00631-4

34. Wolfe DE, Eden TJ, Potter JK, Jaroh AP (2006) Investigation and Characterization of Cr3C2-Based Wear-Resistant Coatings Applied by the Cold Spray Process. J Therm Spray Technol 15:400–412. doi: 10.1361/105996306X124400

35. Singh H, Sidhu TS, Karthikeyan J, Kalsi SBS (2014) Development and Characterization of Cr 3 C 2 –NiCr Coated Superalloy by Novel Cold Spray Process. Mater Manuf Process 1–7. doi: 10.1080/10426914.2014.973599

36. MacDonald D, Fernández R, Delloro F, Jodoin B (2016) Cold Spraying of Armstrong Process Titanium Powder for Additive Manufacturing. J Therm Spray Technol 1–12. doi: 10.1007/s11666-016-0489-2

37. Johnson GR, Cook WH (1983) A constitutive model and data for metals subjected to large strains, high strain rates and high temperatures. In: Proc. 7th Int. Symp. Ballist. The Hague, The Netherlands, pp 541–547

38. Choi H-J, Lee M, Lee JY (2010) Application of a cold spray technique to the fabrication of a copper canister for the geological disposal of CANDU spent fuels. Nucl Eng Des 240:2714–2720. doi: 10.1016/j.nucengdes.2010.06.038

39. Yin S, Xie Y, Suo X, et al (2015) Interfacial bonding features of Ni coating on Al substrate with different surface pretreatments in cold spray. Mater Lett 138:143–147. doi:

10.1016/j.matlet.2014.10.016

40. Cormier Y, Dupuis P, Jodoin B, Ghaei A (2015) Finite Element Analysis and Failure Mode Characterization of Pyramidal Fin Arrays Produced by Masked Cold Gas Dynamic Spray. J Therm Spray Technol 24:1549–1565. doi: 10.1007/s11666-015-0317-0

41. Wang X, Feng F, Klecka MA, et al (2015) Characterization and modeling of the bonding process in cold spray additive manufacturing. Addit Manuf 8:149–162. doi: 10.1016/j.addma.2015.03.006

42. King PC, Bae G, Zahiri SH, et al (2010) An Experimental and Finite Element Study of Cold Spray Copper Impact onto Two Aluminum Substrates. J Therm Spray Technol 19:620–634. doi: 10.1007/s11666-009-9454-7

43. Ghelichi R, Bagherifard S, Macdonald D, et al (2014) Experimental and numerical study of residual stress evolution in cold spray coating. Appl Surf Sci 288:26–33. doi: 10.1016/j.apsusc.2013.09.074

44. Abdel-Aal HA (2000) On the Influence of Thermal Properties on Wear Resistance of Rubbing Metals at Elevated Temperatures. J Tribol 122:657. doi: 10.1115/1.555417

45. Lide DR (2003) CRC Handbook of Chemistry and Physics, 84th Edition. Taylor & Francis

46. Bauccio M (1994) ASM engineered materials reference book. ASM International

47. Chase MWJ (1998) NIST-JANAF Thermochemical Tables. American Inst. of Physics

48. Uhlmann E, von der Schulenburg MG, Zettier R (2007) Finite Element Modeling and Cutting Simulation of Inconel 718. CIRP Ann - Manuf Technol 56:61–64. doi: 10.1016/j.cirp.2007.05.017

49. Steinberg D (1996) Equation of State and Strength Properties of Selected Materials. Lawrence Livermore National Laboratory

50. Papyrin A, Kosarev V, Klinkov S, et al (2006) Cold Spray Technology. Elsevier Science

51. Chen-Tsu, Fu;Jenn-Ming W (1994) Microstructure and mechanical properties of Cr3C 2 particulate reinforced AI203 matrix composites. J Mater Sci 29:2671–2677.

52. Shockley JM, Descartes S, Vo P, et al (2015) The influence of Al2O3 particle morphology on the coating formation and dry sliding wear behavior of cold sprayed Al–Al2O3 composites. Surf Coatings Technol 270:324–333. doi: 10.1016/j.surfcoat.2015.01.057

53. Sova a., Kosarev VF, Papyrin A, Smurov I (2010) Effect of Ceramic Particle Velocity on Cold Spray Deposition of Metal-Ceramic Coatings. J Therm Spray Technol 20:285–291. doi: 10.1007/s11666-010-9571-3

54. Maev RG, Leshchinsky E (2006) Low Pressure Gas Dynamic Spray : Shear Localization during Particle Shock Consolidation. Therm. Spray 2006 Sci. Innov. Appl.

## 5.4 Cold sprayed Chromium carbide-Nickel Chromium as a replacement and restoration method for Chromium-plated steel and alternatives

This last section of the results had the goal to apply previous results to assess the feasibility of using cold spray as a restoration/replacement method for chrome plating. It targets the research objective "Consolidation of cermet coating by cold spray for an engineering application". The interest in the replacement of this coating comes from the fact that the industry has been pushed to eliminate the use of hard chrome coatings due to the hazardous by products of its production. In this investigation, a cermet coating is considered as a possible replacement of the coating as well as a restoration method. The restoration was done on worn Cr-plated steel as well as in other potential replacement of Chromium coatings. A commercially available cermet powder, chromium carbide-nickel chromium powder (65/35), was used for the coatings. The coatings and restorations were analyzed by SEM and tested by strip rupture, neutral salt spray fog and fluid immersion tests. The adhesion strength of the cold spray coatings was tested as well as their porosity and hardness. The deposition and restoration of coatings were successful. Hard and dense coatings were obtained. The process of restoration of Cr-plating and its alternatives was also achieved, with a clean interface obtained in each case. Coatings and restorations passed strip to rupture test as well as fluid immersion tests with two selected industrial fluids. Neutral salt spray fog tests revealed that the cold spray coatings had some corrosion paths that allows the solution to reach the substrate and start the corrosion process. This was found in a few locations and could be avoided with further investigation in this area. The coatings proved to have potential as an alternative of Cr-plating or to restore damaged hard coatings.

# Cold Sprayed Chromium Carbide-Nickel Chromium as a Replacement and Restoration Method for Chromium-Plated Steel and Alternatives.

Ruben Fernandez, Bertrand Jodoin.

University of Ottawa Cold Spray Research Laboratory, Ottawa, ON, Canada.

## Abstract

Global regulations have pushed the industry to eliminate the use of hard chrome coatings due to the hazardous side products. In this study, a commercially available cermet powder (chromium carbide-nickel chromium powder) was proposed as a coating replacement of chromium plating as well as a restoration for this coating and its alternatives (electroless Ni-plating, and WC-Co-Cr produced by HVOF). The coatings and restorations were analyzed by SEM and evaluated using strip rupture test as well as neutral salt spray fog and fluid immersion tests. The cold spray coatings adhesion strength was evaluated as well as porosity level and hardness. Hard and dense coatings were obtained and chromium-plating restoration and restoration of its alternatives were also achieved. A clean interface was obtained in each case. Coatings and restorations passed strip to rupture tests as well as fluid immersion tests. Neutral salt spray fog tests revealed that the cold spray coatings have some path that allows the solution to reach the substrate, inducing the corrosion process in a few locations, requiring further development work. Nevertheless, the work demonstrate the potential of cold spraying the selected material as an alternative to chromium-plating or to restore damaged hard coatings.

*Keywords: Chromium plating replacement, Cold Spray, CrC-NiCr, Coating restoration.*

## Introduction

Chromium plating is a process heavily used in engineering industries as a surface finish and protective coating that prevent corrosion and increase the durability of a part. It can be divided in decorative plating and hard (wear resistant) plating. Decorative chrome plating is used mainly in consumer goods. This thin coating (0.5 µm to 5 µm) is primarily designed to be aesthetically pleasing, but it also improves the durability and corrosion resistance of the coated piece. Hard plating is a thicker chrome layer, between 8 µm to 250 µm [1, 2]. Due to its thickness, it shows the

inherent hardness of chromium and improves the erosion resistance of the part. Its value for engineering applications relies on its hardness and its low friction coefficient. These coatings are also used for minimizing the seizing of parts and improving corrosion resistance.

The industry has been pushed to eliminate the use of hard chrome. The plating process uses hexavalent chromium $Cr_6$, which is the most toxic form of chromium [1, 3, 4]. Its use has been banned by the European Union since 2006 [5]. It is listed in group 1 of the international agency for research on cancer (IARC) [6]. In the U.S.A., the Environmental Protection Agency (EPA) identifies hexavalent chromium as 1 of 17 high-priority toxic chemicals, and it is heavily regulated. It also lists as a priority pollutant under the Clean Water Act [7, 8] and as a hazardous constituent under the Resource Conservation and Recovery Act [114]. In Canada hexavalent chromium is part of the toxic substances regulated by Canadian Environmental Protection Act since 1999 [9].

Currently, the electroplating industry is focusing its efforts on changing the plating process to use trivalent chromium $Cr_3$, which is less toxic than $Cr_6$. This compound has the potential of replacing $Cr_6$ but the coatings produced with it have proven to be more expensive, difficult to control and have not reached the same performance than $Cr_6$ [1, 10]. Another disadvantage of this plating process is its inability to be repaired. When a chrome plated part gets damaged, it is necessary to remove the coating completely from every part of the piece, clean it and then plate it again [1]. This restoration method is highly inefficient, time consuming and expensive. For these reasons, there is a strong need to find a suitable replacement and repair method for hard chrome plating. Different alternatives for its replacement have been examined and tested and just a few alternatives have shown some potential, but they also present some disadvantages. Electroless nickel plating [11, 12] is an excellent alternative to provide corrosion protection of the base material and has good repairability, but does not meet hardness requirements and has low building rates. PVD coatings [13] offer superior corrosion resistance and adequate hardness levels, but offer no reparability, have low building rates. Furthermore, it is an expensive process thus is still far from becoming widely used in industrial applications. HVOF coatings have been proposed as an alternative as they have shown potential as hard coatings. WC-Co coating produces by HVOF can match the hardness of the chromium plating, have shown similar wear resistance, and good building rates. Consequently, these coatings are the most promising alternatives so far. However, they do not offer good corrosion protection and cannot be easily repaired [3, 4, 14].

The lack of reparability of HVOF coatings comes from the residual stresses in the coatings produced. It is known and well documented that regular thermal spray techniques such as plasma

spray or HVOF induce tensile stresses in the coating due to the thermal mismatch between the sprayed particle (hot and melted) and the substrate (cold) [15]. These tensile stresses can be harmful if the coated parts are subjected to fatigue or when the goal of the spray is the restoration of a pre-existing coating. These tensile stresses pull the coating away of the pre-existing coating, leaving weak interfaces that can be subjected to corrosion or abrasion.

Cold spray is a thermal spray process that uses kinetic energy instead of thermal energy to deposit a coating. The cold spray process accelerates feedstock powders (usually metals) in a supersonic gas stream produced by a convergent-divergent nozzle (de Laval) [16–18]. Due to the low gas temperatures used in addition to the rapid gas expansion in the nozzle, the feedstock powders remain solid throughout their flight making cold spray a solid state process [19–21]. The particles impact the substrate and experience extensive plastic deformation prior to bonding to the substrate either mechanically or metallurgically if enough plastic deformation is obtained [16, 19, 22–26]. Since cold spray is a solid state process with low working temperatures and the deposition mechanism is based on deformation (and not melting), the resulting residual stresses are typically compressive instead of tensile [27–30] This makes cold spray a potential solution for coating restoration. The compressive residual stresses should result in deposited coatings pushing against the preexisting coatings, thus closing any gap and sealing the repair. This could also provide the coatings a longer fatigue life.

Chromium carbide-nickel chromium coatings (CrC-NiCr) are cermet coatings that offer good wear and erosion protection due to their high hardness and provide good corrosion/oxidation protection to the base metal. Investigations have shown that these coatings can operate in harsh environments at room and elevated temperatures [4, 31–34]. These properties make this material ideal for chrome plating replacement. These coatings have started to gain attention, and have been produced and studied when applied using HVOF [4]. Cold spray can offer some advantages over HVOF to spray CrC-NiCr coatings as it is expected to create compressive stresses that benefit the repairability of coatings while minimizing the probability of decarburization, a potential problem when spraying cermet coatings by HVOF [35–37].

This study presents CrC-NiCr coatings produced with cold spray as a potential replacement for chromium-plating on steel. In addition, cold spray is presented as a restoration method for damaged chromium-plating and its alternatives, namely electroless nickel plating and WC-Co-Cr HVOF coatings. Microstructure analysis, adhesion strength and hardness test were performed for the coatings produced. The coatings and restorations were also evaluated using strip rupture, neutral

salt spray fog and fluid immersion test to verify this process and material as feasible replacement/restoration method for chromium-plating and its alternatives.

# Experimental Procedures

## Feedstock Materials and Substrates

The CrC-NiCr powder used for in this investigation was the commercially available Amperit 587 (H.C. Starck, Munich, Germany). This is an agglomerated and sintered powder containing 35wt.% NiCr, with a particle size range between 10 to 45 µm. An overview of the powder is presented in Figure 1, revealing the powder morphology. The darker phase represents the chromium carbide, while the whiter phase is the metallic phase. It can be seen that some particles present a high metallic content at the surface while other showed just carbides at the surface.

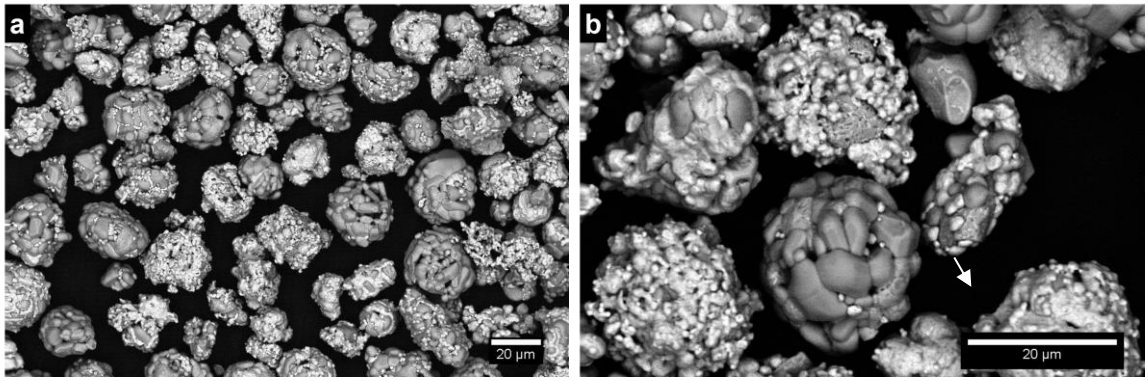


*Figure 1: Overview of H.C. Starck Amperit 587 feedstock powder:a)Overview; b)Detail.*

For the coating production and evaluation, substrates made of AISI 4340 steel were used. This substrate material was chosen as it is one typical material plated with chromium to improve its surface durability. The restorations were done on simulated damages on three different materials: chromium-plated AISI 4340 steel, electroless nickel-plated AISI 4340 steel, and HVOF WC-Co-Cr coated AISI 4340 steel. To simulate damages a section of steel was masked before the original coating procedure, thus hindering the original coating building process and creating a section with the substrate steel exposed.

## Cold Spray Deposition

The cold spray system used was the commercial EP Series SST Low Pressure Cold Spray System (Centerline Ltd., Windsor, Ontario, Canada). The system consists of a 15 kW heater with a maximum gas temperature of 500°C and a maximum gas pressure of 3.8 MPa. The de Laval nozzle

used for this work is made of WC and has a throat diameter of 2 mm and a diverging section length and exit diameter of 120 mm and 6.35 mm, respectively. The powder was fed to the nozzle using a commercially available rotatory feeder (Model AT-1200HP, Thermach Inc., Appleton, WI, USA). All sprays were performed using the parameters given in Table 1.

*Table 1: Cold Spray Parameters Used.*

| Parameter | Value |
|---|---|
| Gas Temperature | 500 °C |
| Gas Pressure | 3.8 MPa |
| Gas Nature | Nitrogen |
| Traverse Speed | 5 mm/s |
| Step | 2 mm |
| Feed rate | 13.2 g/min |
| Standoff Distance | 10 mm |

The deposition efficiency (DE) was calculated, based on the powder feed rate and the mass gain after deposition. To do this measurement, a precision scale Sartorius Extend—model ED124S, with a readability of 1mg, was used. It is important to note that this value was calculated just for the cold spray coating production and not for the restorations, as the simulated damaged coatings might interfere with the process and alter the results.

## Coatings Characterization and Adhesion Tests

The coatings produced were cross-sectioned and analyzed using optical microscopy (VHX-1000, Keyence Corporation, Osaka, Japan) and scanning electron microscopy (SEM, model EVO MA-10, Carl Zeiss AG, Oberkochen, Germany). The coatings ceramic composition was analyzed by energy-dispersive X-ray spectroscopy (EDS, model INCA X-Act, Oxford Instruments, Oxford, England). The coatings porosity level was evaluated using contrast analysis and hardness values were obtained using a Duramin-10 (Struers ApS, Denmark) equipped with a Vickers indenter using a load of 0.5 kgf.

The coatings adhesion strength were measured following the ASTM C-633 standard. Cylinders made of AISI 4340 steel were coated, and a thermally cured elastomeric adhesive (FM-1000) was used to glue the coatings to counter cylinders. The samples were placed in an oven at 175°C for 2 hours to ensure the adhesive had properly cured. The testing was done using a universal tensile testing machine. Four different substrate surface preparations prior to spray were tested: polished with an aluminum oxide buffing wheel, sanded with 130 paper, and sandblasted with two different

blasting media (80 grit alumina and 20 grit ferrosilicate using nitrogen at 1 MPa). The substrate preparation with the highest adhesion value was used for the remaining of the investigation.

## Coatings Restoration and Testings

To investigate restoration of damaged coatings, the simulated damaged coatings were cross-sectioned, and the damaged area was analyzed using optical microscopy and SEM. This allowed identifying features in the damaged area that might interfere with the restoration of the coating and to address these features adequately. The damaged coatings were restored using cold spray and the selected feedstock material and machined back to size using a surface grinder. The restored coatings were cross-sectioned and analyzed to inspect the interfaces between the cold spray repairs and the original coatings. Vicker microhardness measurements were done on the restored coatings as well as the original coatings (chromium-plated, nickel-plated and HVOF WC-Co-Cr).

To evaluate if the repaired coatings are prone to peeling, strip rupture tests (MIL-DTL-83488D) were performed. These tests consist in bending the coated part back and forth until the coating and substrate break. The coating interface is then inspected closely for evidence of peeling and flaking. The specimen dimension used in this test were 25.4 mm x 154.4 mm x 6.35 mm, with a 10 mm zone of simulated damage along the center of the specimen. Figure 2 shows a schematic of the samples used in this test. A V-notch was machined (by electro-discharge machining) at the back of the restored specimens in order to perform this test. The tip of the notches were located 1 mm from the surface of the repaired coatings. These test were performed in the restored coatings (chromium-plated, nickel-plated and HVOF WC-Co-Cr) as well as in fully cold spray coated substrates.

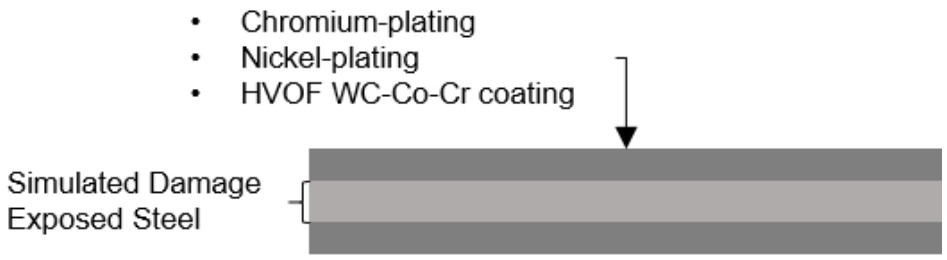


*Figure 2: Schematic of specimen (top view) to be restored and used in strip rupture test and fluid immersion test.*

Corrosion performance was evaluated for each of the restored coatings. The evaluations followed the neutral salt spray fog test specified in the ASTM B117 standard. The tests were performed using 101.6 mm x 154.4 mm x 6.35 mm samples with a 40 mm wide damaged strip. An undamaged nickel plated sample was used as a reference for comparison. The sides and the back of the samples were sealed with a polymeric tape in order to protect the exposed steel and not interfere with the tests. The samples were left for four weeks in the salt spray fog chamber and were photographed every week for visual inspection and to find evidence of corrosion products.

Fluid immersion tests were performed using a modified version of ASTM F483 standard. The fluid immersion test measures the compatibility of coatings with selected maintenance chemicals. Visual inspection of the samples was done after an exposure of 24 and 168 hours. Each specimen was photographed before and after the test. These tests were performed on 25.4 mm x 154.4 mm x 6.35 mm samples as the one showed in Figure 2. This test was done on restored coatings as well as on fully cold spray coated substrates. The fluids used in the tests were the industrial cleaner and degreasers Calla solve 120 (Aviall Toronto, Mississauga, Ontario, Canada) and the high performance liquid runway deicer Gen3 (LNT solutions Inc, Tillsonburg, Ontario, Canada). Visual inspection was done looking for evidence of discoloration of the coating, restoration and interface with the original coating. The sides and back of the samples were sealed with a polymeric tape in order to protect the exposed steel that might interfere with the test.

# Results and Discussion

Successful coatings were produced using the Amperit 587 feedstock powder at the specified spray parameters. Figure 3 shows an overview of a coating and the coating/substrate interface. The coating is dense, and the substrate/coating interface looks clean with no indication of potential delamination. The coatings porosity was evaluated as less than 1% as this value is the limit of the evaluation technique used. The coatings hardness value was measured at 746 ± 81 $HV_{0.5}$. This high hardness value is typical of cermet materials as the ceramic particles help to redistribute the stresses, thus strengthening the material. Nevertheless, this hardness value is high for coatings sprayed with cold spray using nitrogen as process gas. The deposition efficiency was evaluated at 4.0% ± 0.8%, even though this value is low, cermet powders typically lead to erosion of the substrate when sprayed with cold spray at this conditions. EDS was used to evaluate the coatings composition. This was used to estimate the coatings metallic and ceramic contents. The coatings metallic content was evaluated at 52wt% NiCr, revealing that some ceramic particle is lost during deposition as the original feedstock powder metallic content was 35wt%. When cermet particle are sprayed, they

fracture upon impact to the substrate. During this process ceramic and metallic content of the particle can be lost. It is expected that the metallic component of the powder will be more likely to adhere to the substrate than ceramic particles, therefore changing the composition obtained in the coating.

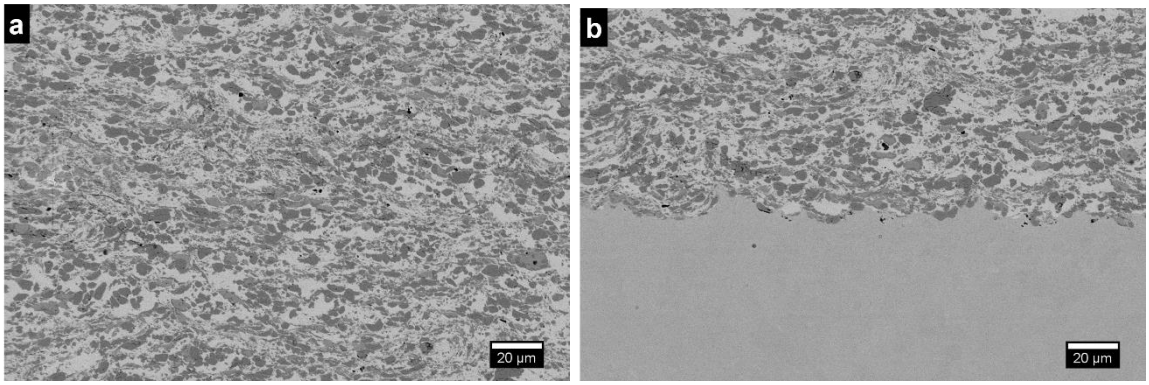


*Figure 3: Overview of Amperit 587 cold spray coating and interface with 4340 steel substrate*

The adhesion strength results are shown in Figure 4 for each of the substrate preparation method used. Sand blasting with 20 grit ferrosilicates gave the highest adhesion strength at 27.2 ± 3.2 MPa. All other substrate preparations gave similar adhesion strength, around 18 MPa (polished: 17.6 ± 2.5 MPa, sanded: 18.6 ± 2.0 MPa, and sand blasted 80 grit: 19.1 ± 2.9 MPa). Since the feedstock powder is considerably harder than the substrate, it is expected that as it deposits the particles impacting the substrate surface will potentially create a new surface preparation (referred to as surface activation [38, 39]). Therefore, if the substrate preparation is not aggressive enough, the feedstock powder particles will 'erase' any prior preparation and the adhesion of the coatings will stabilize to a specific value (18 MPa in this case). For the rest of the study, sand blasting with 1MPa nitrogen and 20 grit ferrosilicates was used as it generated the highest adhesion values.

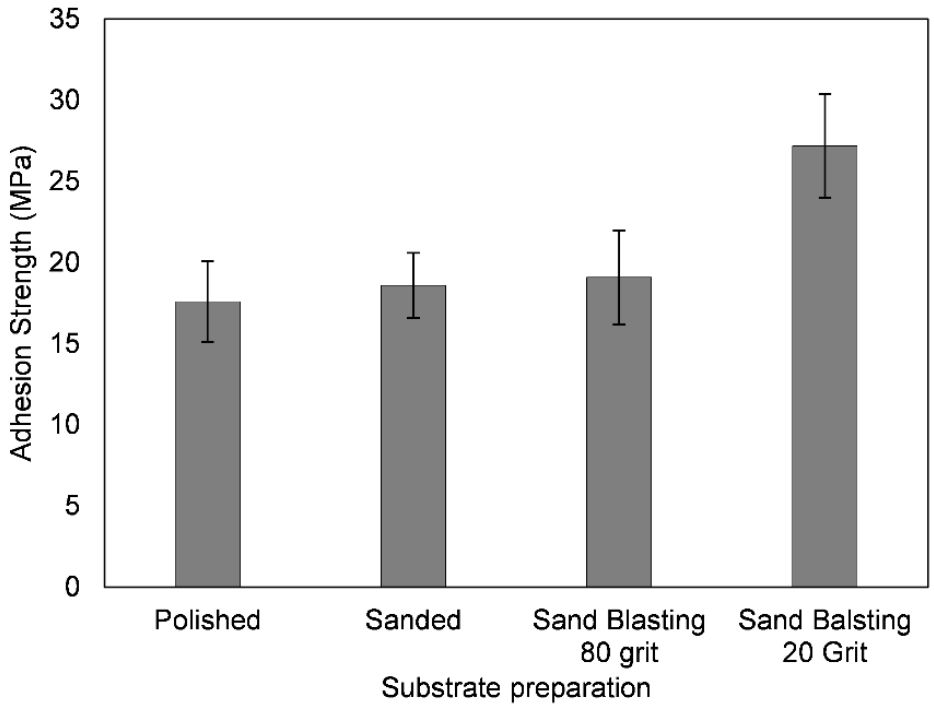


*Figure 4: Adhesion strength results for different substrate preparations.*

## Damaged Coatings Restoration

### *Chrome-plated steel restoration*

The cross-sections of the chromium plating and the simulated damaged zone (prior to repair) can be seen in Figure 5. The damaged zone presents a smooth slope with a width of approximately 600µm from the original coating to the bare substrate.

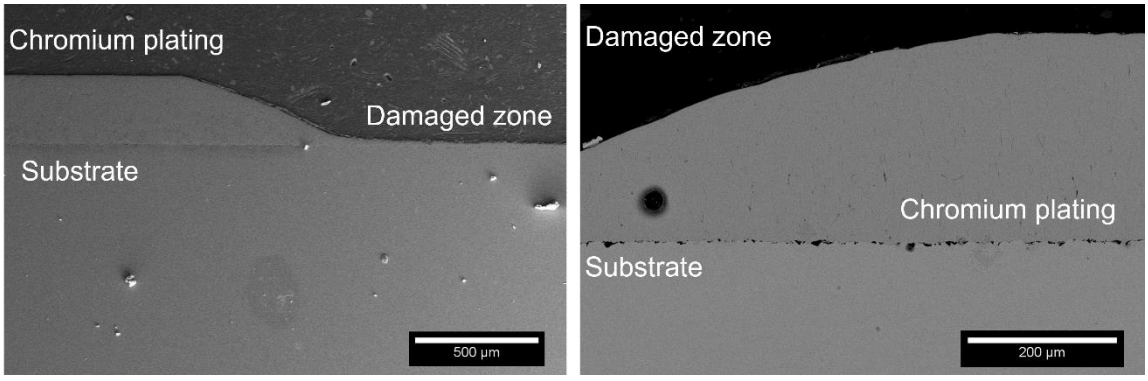


*Figure 5: Damaged chromed plated steel: the zone to be restored (labelled damaged) is shown.*

The specimens were sand blasted and cleaned with acetone in an ultrasonic bath before deposition.The cold spray deposition was successful but peeling was observed in the transition zone of the original chromium coating to the simulated damage, as can be seen in Figure 6. From this figure, it is clear that the issue comes from a low adhesion between the cold spray repair and the original chromium plating. Chromium is a hard and brittle material and these properties makes it a challenging substrate for cold spray of hard materials, were ductility is usually needed in order to obtain a good bonding. To avoid this problem during the restoration, the slope in the transition zone was removed, this prevented to spray directly on top of the chromium plating where the adhesion was low, and therefore avoiding delamination.

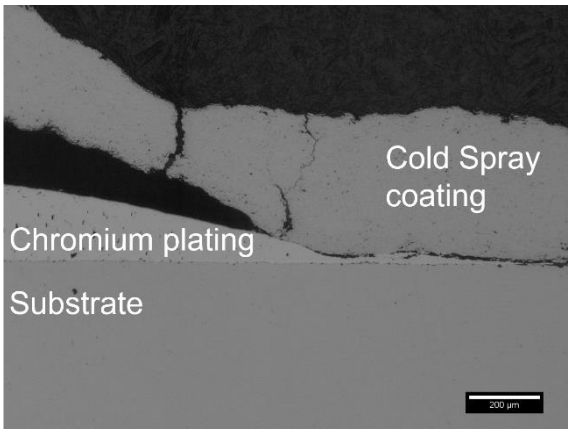


*Figure 6: Failed restoration of chrome plating steel. Delamination is observed at the original coating surface.*

To remove this slope in the transition zone, the chromium layer was milled in this section. This creates a sharper edge therefore avoiding to spray onto the original chromium coated zone. The damaged specimen was then sand blasted, and cleaned in acetone prior to deposition. The cold spray repair sprayed successfully and adhered well to the original coating as well as to the substrate using this surface preparation method. The repaired area was cross-sectioned and is presented in Figure 7. The restoration shows a clean interface between the chromium plating and the cold spray repair, as well as between the cold spray repair and the substrate. No interfacial pores are observed and no sign of delamination is detected form these images. It is important to note that even though the edge of the chrome plating was machined squared, the erosion caused by cold spray particles onto the chromium edges created a slope at the interface, this slope is sharper than the original one.

Another aspect to note is that some particles were found at the interface between the chromium plating and the steel substrates. These particles are not a result of the restoration process, as they can be found at the interface even before machining as can be seen by examining Figure 5. EDS was used to identify the particles as aluminum oxide. It is likely that these particles were embedded prior to plating the samples.

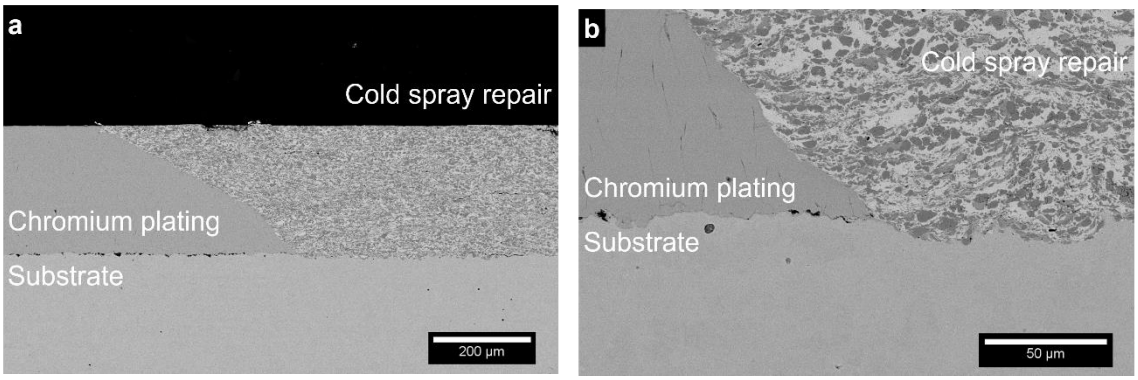


*Figure 7: Successful coating restoration of chrome-plated steel; a) Overview; b) Interface.*

### *Electroless Nickel-plated Steel Restoration*

The restoration of nickel-plated steel also needed special substrate preparation before spraying. Figure 8 shows the simulated damaged zone of nickel-plated steel substrates. The first characteristic to note is a protuberance at the interface between the Ni-plating and the simulated damage. This lapel covers part of the exposed steel, and would disallow proper deposition on this section as cold spray is a line-of-sight coating process.

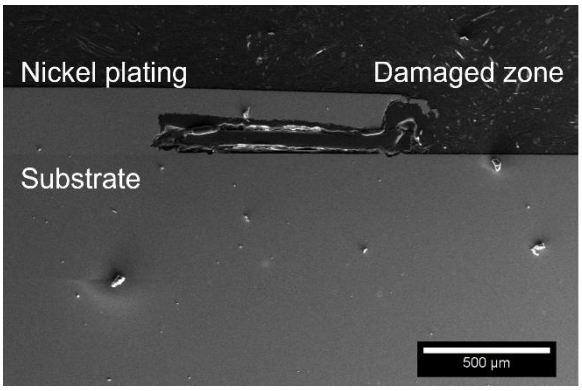


*Figure 8: Simulated damaged nickel-plated steel at the zone to be restored.*

To properly prepare the substrate for deposition, the elimination of this lapel is required. Since pure nickel is a soft metal, the removal can be achieved by polishing this edge using a buffering wheel. Although, this creates a wide slope between the nickel plating and the damaged zone, nickel is soft and thus a suitable substrate for cold spray coatings. As such, no delamination (such as the one seen in the chromium plating) was expected. After polishing the lapels, the substrates were sandblasted and cleaned with acetone in and ultrasonic bath prior to deposition. The coating restorations were successful, and Figure 9 shows an overview of the coating restoration, and the interface between the nickel-plating, the cold spray restoration, and the steel substrate. A well defined interface is seen without pores and no sign of delamination.

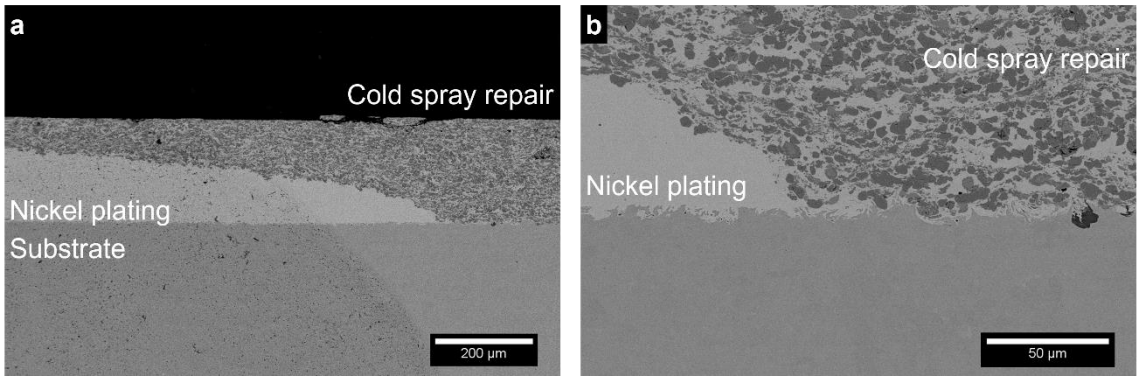


*Figure 9: Successful coating restoration of nickel-plated steel, a) Overview; b) Interface.*

### *HVOF WC-Co-Cr Coated Steel Restoration*

Figure 10 shows a cross-section of the HVOF coating to be repaired, including the simulated damaged zone. It is important to note that the WC-Co-Cr coating shows some degree of porosity. The simulated damaged zone appears to be fit for deposition, as it presents a narrow slope. The substrates were sandblasted and cleaned with acetone in an ultrasonic bath prior to deposition.

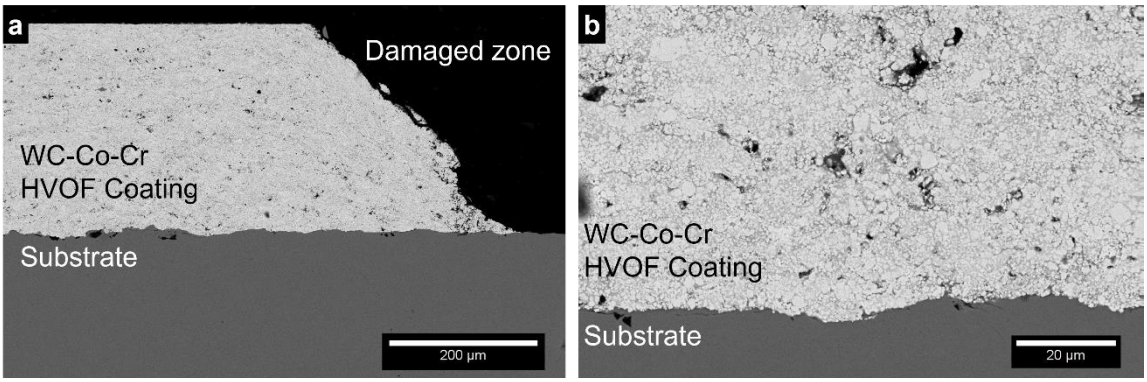


*Figure 10: Simulated damaged HVOF WC-Co-Cr coated steel at the zone to be restored.*

The cold spray coating repairs obtained were dense and without any sign of delamination. Figure 11 shows an overview of the coating restoration as well as a detail of the interface between the HVOF coating, cold spray repair and substrate. The interface is well defined and without the presence of pores or sign of delamination. It is important to note that some embedded grit particles were found under the HVOF coatings. These embedded particles were not induced by the cold spray restoration process as this area was never exposed during the process. It is suspected that these particles were embedded during substrate preparation for the HVOF coating as they were also found prior to the repair process, as can be observed in Figure 10.

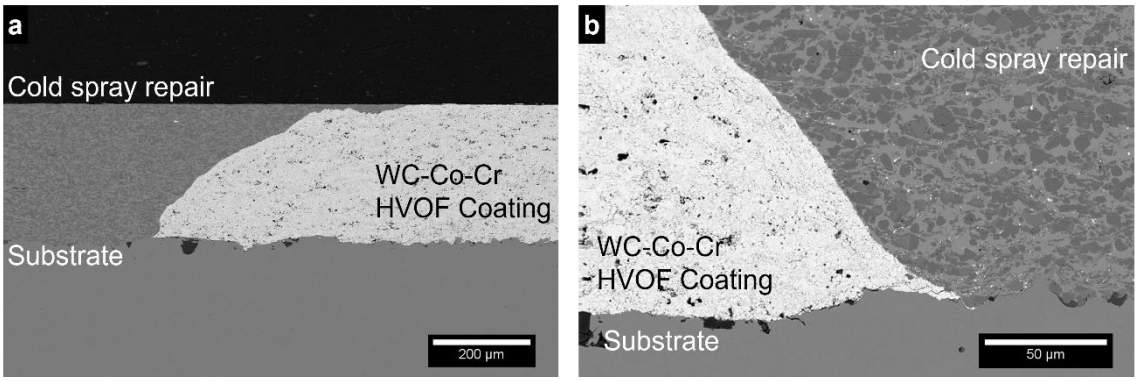


*Figure 11: Successful coating restoration of HVOF-coated steel by cold spray; a) Overview; b) Interface.*

## Hardness and Strip Rupture Test

Hardness values of chromium-plating, nickel-plating, and HVOF coatings were evaluated in order to compare with the values obtained for the cold spray coatings. The results are presented in Table 2. It can be seen that the cold spray coating repair is softer than chrome plating and HVOF coating but is nevertheless in a close range. However, nickel-plating shows to be considerably softer with a hardness value less than a quarter of the chromium-plating hardness. The hardness value of coatings is directly related to its resistance to erosion. Even though electroless nickel-plating is considered as a potential replacement of chromium-plating, its benefit to the base materials are not related to the erosion protection or the superficial hardness that the coating can provide, but rather with its corrosion resistance. This similar hardness between the cold spray coating repair and the chromium plating makes the proposed cold spray coating repair a good candidate for its replacement by potentially offering similar erosion protection to the based metal. The value is high for a cold spray coating sprayed with nitrogen at low spray parameters. This high value is due to the ceramic particles as they help to redistribute the stresses, thus strengthening the material.

*Table 2: Hardness value of damaged coatings and CrC-NiCr cold spray coating.*

| **Coating** | **Hardness ($HV_{0.5}$)** |
|---|---|
| CrC-NiCr Cold spray coating | 746 ± 81 |
| Chromium-Plating | 850 ± 30 |
| Nickel-Plating | 198 ± 2 |
| HVOF WC-Co-Cr coating | 931 ± 120 |

Strip rupture tests were performed on the cold spray coatings and on the restored specimens. All sample passed the tests, as no sign of delamination were found between the repaired coatings and the substrate in the ruptured zone as can be seen in Figure 12. This result is in line with the results of adhesion tests. Adhesion strengths of 27 MPa were achieved and this value is high enough to ensure a proper adhesion between the coatings and the substrates.

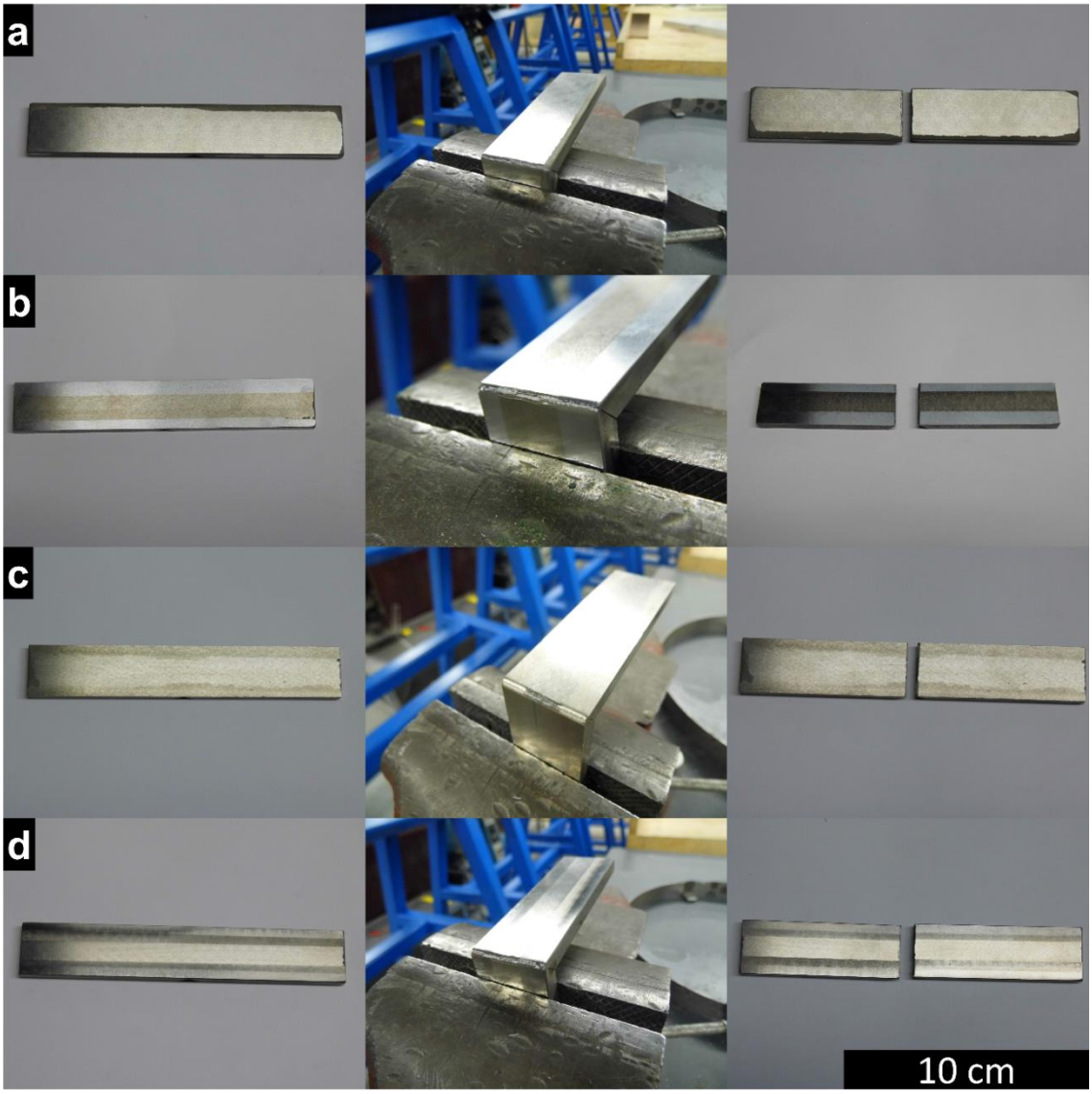


*Figure 12: Selected strip rupture test results for cold spray CrC-NiCr coatings/restorations on: a) Cold spray coating; b) Chromium-plating restoration; c) Nickel-plating restoration; d) HVOF WC-Co-Cr coating restoration.*

## Neutral Salt Spray Fog Tests

Neutral salt spray fog tests were performed following the ASTM-B117 standard. The test was applied for each of the restored coatings as well as to a reference undamaged nickel-plated steel. Figure 13 shows the progression of the corrosion tests week by week, starting with the reference specimen. As can be seen in the figure, the reference plate did not show

any sign of corrosion products even after 4 weeks in the test chamber. The absence of red corrosion products indicates a proper corrosion protection of the steel substrate.

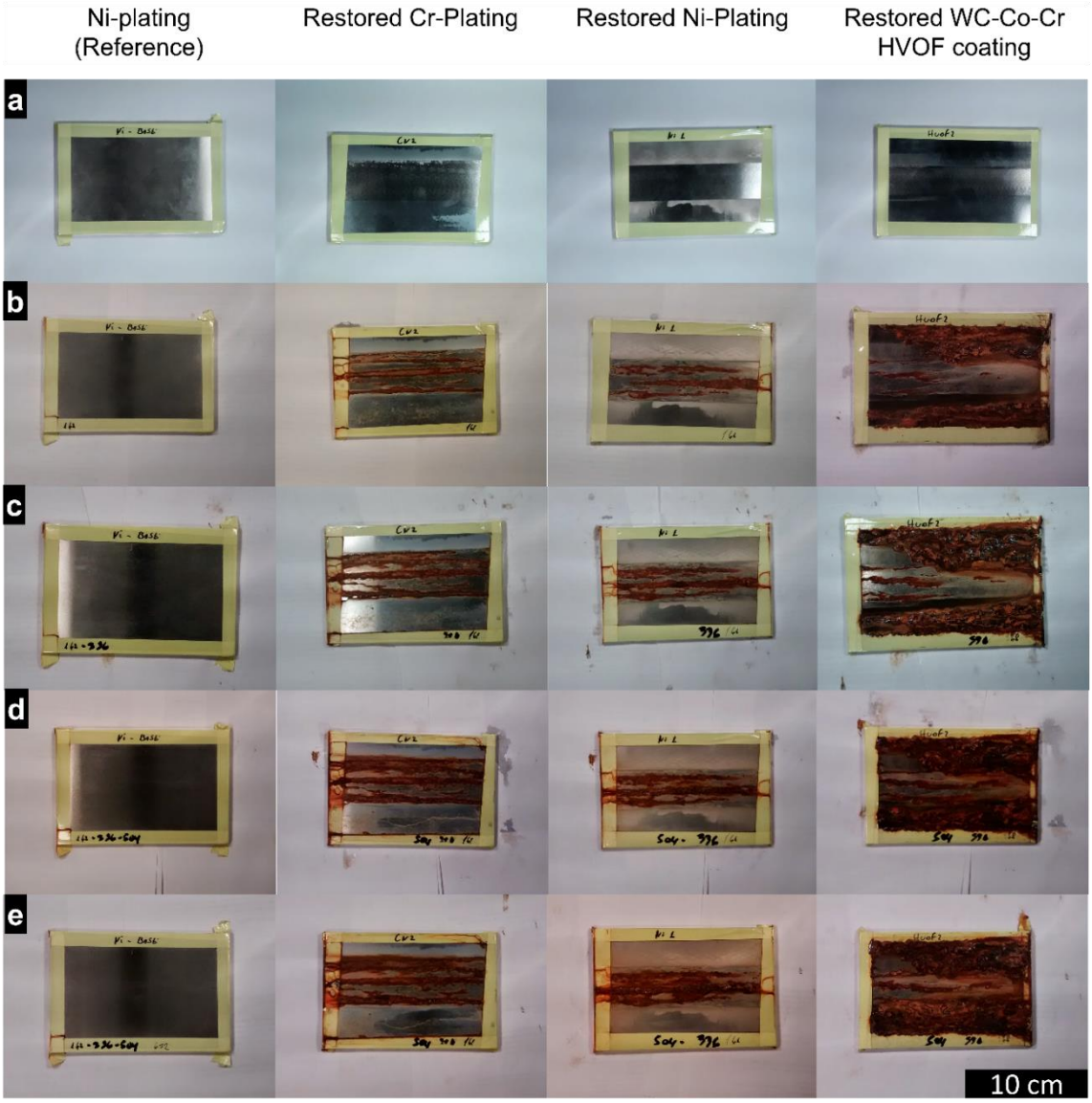


*Figure 13: Neutral salt spray test results of reference and restored sample at: a) 0 hours; b) 168 hours; c) 336 hours; d) 504 hours; e) 672 hours.*

The results of neutral salt fog tests on the restored chromium-plated steel can be seen in the second column of Figure 13. After the first week red corrosion appears at the interface of the original coating and the cold spray repaired zone as well as inside the cold spray repaired zone. Some pitting was also detected in the original chrome-plating. In the following weeks, the corrosion progressed

slowly, and no considerable change in the corrosion products was observed. Red corrosion is a direct indication that the solution reached the steel substrate. It is suspected that the solution could penetrate through the interface between the chrome plating and the cold spray repair. This can result in a possible path for the solution to reach the steel substrate. Similar corrosion products appear in the central zone of the cold spray repair. It is possible that the corrosion was made possible by connected porosities too small to be detected by optical means or SEM imaging. However, the corrosion progresses slowly, and the damage did not extend further than this possible path. This is an indication that the sprayed material has a good potential for corrosion protection.

For the restoration of nickel-plated steel, third column of Figure 13, the interface between the cold spray repair and the nickel-plated coatings showed no indication of corrosion. This presents a difference with the previous case, where corrosion products appeared between the chromium plating and the cold spray restoration. This suggests that the cold spray repair achieves a better bonding to the nickel plating than the chromium plating. This difference can be explained by the difference in hardness of the plating materials. Nickel, being soft ductile material, would deform during the cold spray process, and the interface will adapt and deform with the impacting CrC-NiCr particles helping to seal this joint through what is expected to be mechanical bonding. However, chromium is a hard brittle material that potentially erodes when impacted by the CrC-NiCr particles. Consequently, no plastic deformation can contribute to sealing this interface, and thus it is more likely that a micro path may exist at this interface.

Although the joint between the cold spray repair and the nickel plating did not show corrosion products, red corrosion appears after the first week at the center of the cold spray repair. In the following weeks, the corrosion progressed slowly and no change in the corrosion behavior was observed. This is an indication that the coating can permeate the solution by connected microporosities. Despite the solution reaching the substrate, the corrosion did not extended further.

Finally, neutral salt fog test results for the HVOF WC-Co-Cr coated steel are presented in the last column of Figure 13.The first thing to be noticed in these samples is the poor corrosion resistance of the HVOF coatings. The HVOF coatings appear to be extremely corroded after the first week, providing no protection to the base material, and progressing fast in the following weeks. This results have been shown in other investigations where HVOF WC-Co-Cr showed no corrosion protection in this test [14]. Despite the low corrosion protection of the HVOF coating, the cold spray repair behaved as with the previous specimens with some red corrosion appearing at the

center of the cold spray repair after the first week. This corrosion progressed slowly in the following weeks.

Specimens of each restoration were further analyzed to obtain some insight on the corrosion mechanisms. Samples were first cleaned of corrosion product with a wire brush and inspected for locations where the corrosion could have originated. Figure 14 shows the specimens after the cleaning of the corrosion products. It can be seen that in the case of the chromium-plated steel restoration, only specific spots of the cold spray repair and the interface appeared to be subjected to corrosion. In the case of the nickel plating restoration, the center of the cold spray repair can be identified as a possible infiltration point and presents delamination. It is suspected that below this zone, corrosion products accumulated and resulted in delamination of a section of the cold spray repair.


*Figure 14: Cleaned restored samples after neutral salt spray fog test: a) Chromium-plating; b) Nickel-plating; c) HVOF coating.*

Finally, the restoration of HVOF coated steel showed some corrosion spot in the cold spray repair and several ones in the HVOF coating. The HVOF coating showed sections were it blistered and delaminated form the steel, as shown in Figure 15. It is expected that this blistering occured due to severe accumulation of corrosion products at the interface of HVOF coating and the steel. This accumulation can force the coating to blister.

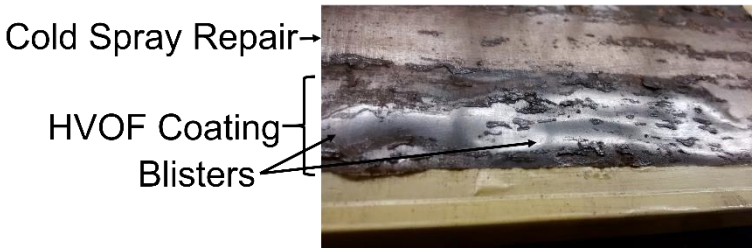


*Figure 15: Blistering found in WC-Co-Cr section of the restored HVOF coated steel.*

The specimens were cross-sectioned for SEM analysis. Figure 16 shows a cross-section of the cold spray repair zones. From these images, it is difficult to observe any direct infiltration path that the solution might have taken, but pockets of corrosion products were found. These pockets of corrosion products were at a different location in different specimens, but always in the cold spray repair. These zones suggest that a corrosion paths actually exist and is most likely three-dimensional channels, therefore the images taken captured just a cross section of these paths. It is believed that few defects might have occurred during deposition, these become weak points for the solution to infiltrate and to reach the substrate, creating these paths.

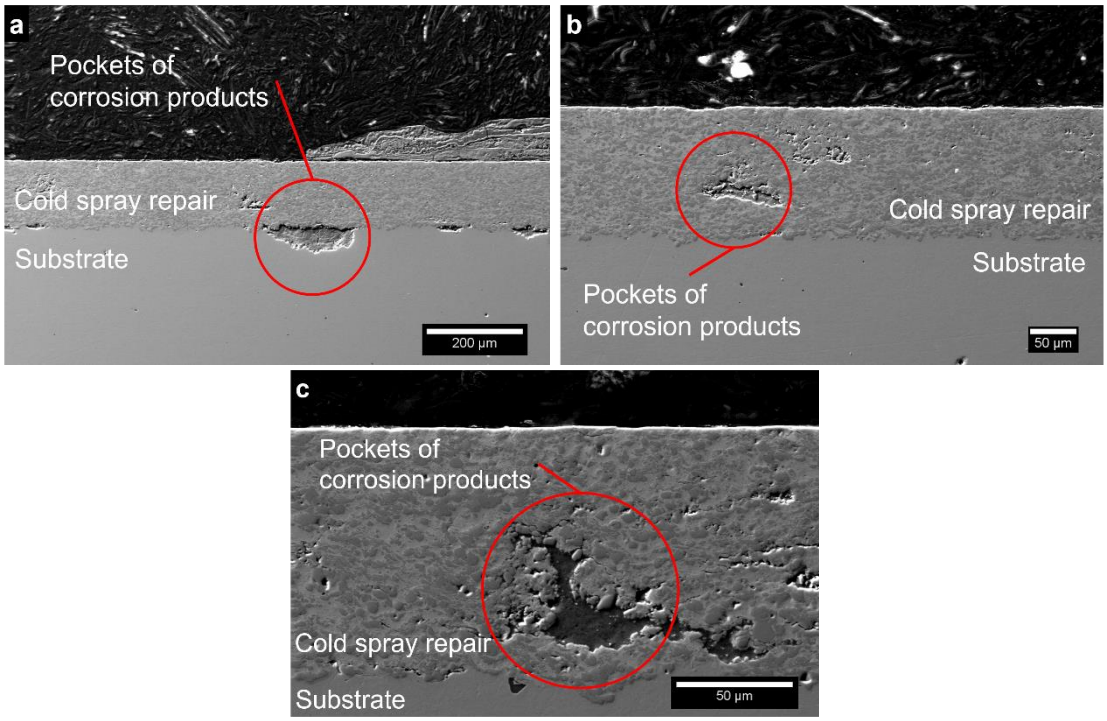


*Figure 16: Selected cross-sections after neutral salt spray fog tests showing pockets of corrosion products in cold spray repairs: a) Chromium plating repair; b) Nickel-plating repair; c) HVOF coating repair.*

Figure 17 a) shows a cross section centered on the interface between the chromium plating and cold spray repair after the neutral salt spray fog tests. Surprisingly, no corrosion product were found in this intersection. This area was identified as a weak spot during the test due to corrosion product accumulation. The cross section shows a clean interface without evidence of infiltration of the solution to the substrate.

Figure 17 b) shows a cross-section of the deamination found in the cold spray repair section of the nickel-plating restoration. It easy to see the accumulation of corrosion products at the base of the substrate, forcing delamination of the cold spray repair.

Finally, Figure 17 c) shows a blistering section of the HVOF coating, corrosion product accumulated below the WC-Co-Cr coating forcing it to delaminate, and blistering the whole section. In addition, a severe attack of the substrate can be seen. This blistering occurred in all HVOF specimens tested, in several spots of the HVOF coating. It is possible that the coating has multiple paths for the solution to permeate, reach the substrate, and start the attack, propagating preferentially at the interface between the substrate and this coating.

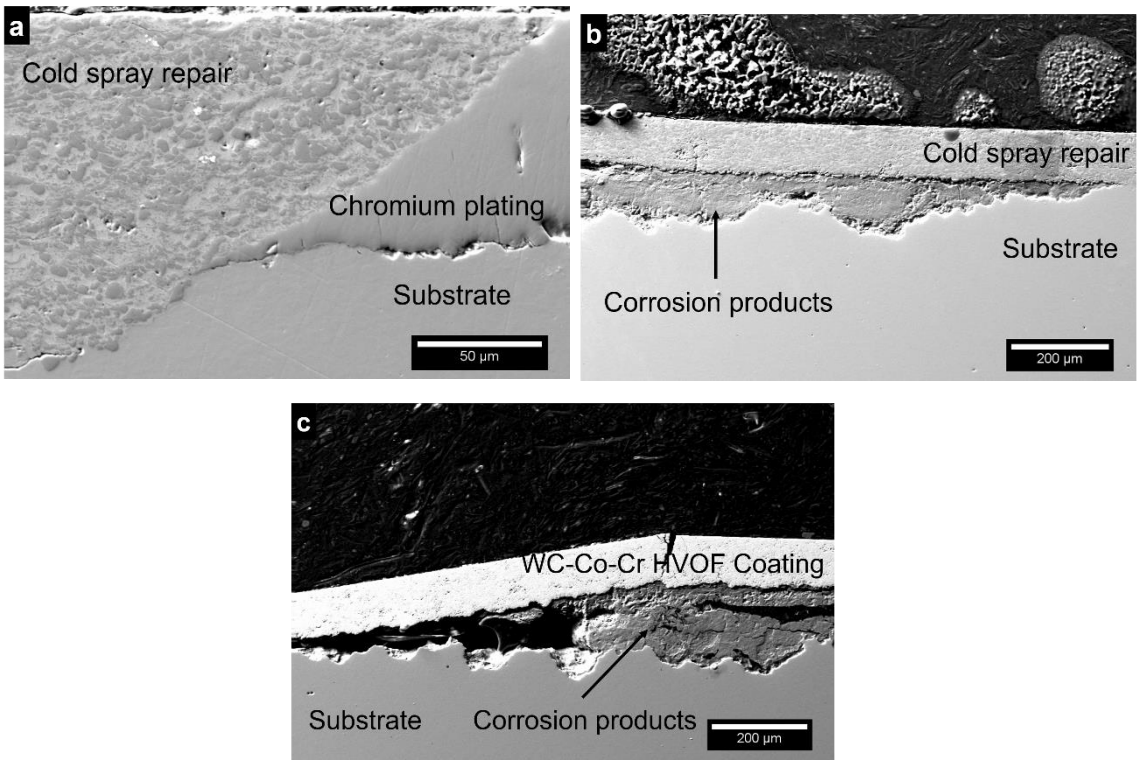


*Figure 17: Selected cross-sections of repairs after neutral salt spray fog tests: a) Chromium-plating-cold spray repair interface; b) Delamination of cold spray section in Nickel-plating repair; c) blistering in WC-Co-Cr HVOF coating.*

## Fluid Immersion Tests

The fluid immersion tests were performed using a modified version of ASTM F483. Figure 18 shows the results after 168 hours for the cold spray coatings and the repairs. The images also include a reference coating (not immersed in fluid) in order to inspect for decoloration by comparison. It

can be clearly appreciated that the fluids do not have any influence on the cold spray coatings or the repairs, qualifying this coating and the restoration to safely work with these fluids.

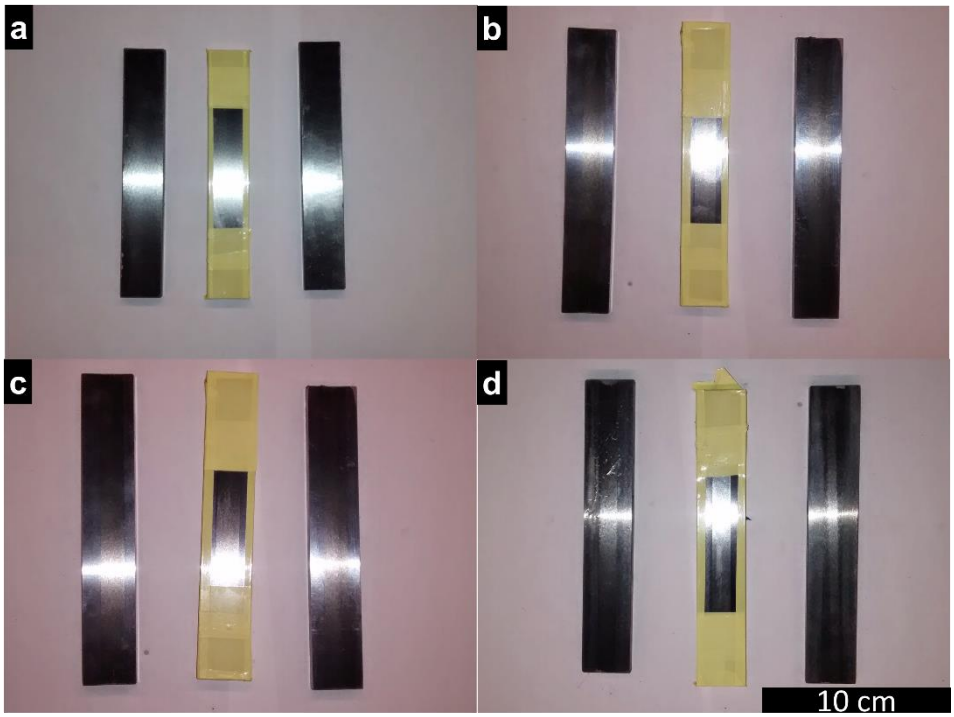


*Figure 18: Fluid immersion results in cold spray coatings and repairs. Each image contains: reference sample, sample immersed in Gen3 fluid and sample immersed in Calla solve 120 fluid for: a) Cold spray coating; b)Chromium plating repair; c) Nickel plating repair; d) WC-Co-Cr HVOF coating repair.*

# Conclusions

This investigation is a first approach to the replacement and restoration of chromium-plating by cold spray using CrC-NiCr feedstock powder. Cold spray has the benefit of typically inducing compressive residual stresses in the coatings, which makes it ideal for the restoration of preexisting coatings and is a feature not shared with other thermal spray processes. If a cermet is sprayed, the coatings obtained can have high hardness, in addition, the low temperatures avoid the degradation of the materials involved. In this study, the deposition of CrC-NiCr powder was successful, resulting in hard and dense coatings with an average hardness of 746Hv and porosity levels below 1%. The substrate preparation method was studied and an adhesion strength of 27MPa was obtained. Besides producing a coating, a step by step process was investigated for the restoration of simulated damaged chromium-plating as well as its alternatives electroless nickel-plating and

HVOF WC-Co-Cr coatings. Cold spray coating as a replacement of chromium-plating as well as a restoration method passed the strip rupture peeling tests as well as the fluid immersion tests. Neutral salt spray fog tests revealed that the coating does not provide a corrosion protection as good as nickel-plating and that some paths, not detectable by SEM, could exist inside the coating. Further investigation is recommended to identify and prevent defects that can create paths, or to seal the coatings through sintering. Overall this kind of coating show potential for the replacement and restoration of chromium-plating and alternatives, as it shows similar hardness than chromium-plating, and considerably higher than nickel-plating, and shows potential to be corrosion resistant if the coating is sealed, this potential is not offered by HVOF coatings.

# References

1. Dennis JK, Such TE (1993) Nickel and Chromium Plating. Elsevier

2. Nriagu JO, Nieboer E (1988) Chromium in the Natural and Human Environments. John Wiley & Sons

3. Ibrahim A, Berndt CC (2007) Fatigue and deformation of HVOF sprayed WC–Co coatings and hard chrome plating. Mater Sci Eng A 456:114–119. doi: 10.1016/j.msea.2006.12.030

4. Picas JA, Forn A, Matthäus G (2006) HVOF coatings as an alternative to hard chrome for pistons and valves. Wear 261:477–484. doi: 10.1016/j.wear.2005.12.005

5. REACH (2006) Regulation (EC) No 1907/2006 - REACH - Safety and health at work - EU-OSHA. In: 1907. https://osha.europa.eu/en/legislation/directives/regulation-ec-no-1907-2006-of-the-european-parliament-and-of-the-council. Accessed 24 Nov 2015

6. IARC (2012) IARC Monographs on the Evaluation of Carcinogenic Risks to Humans 100E. IARC

7. US EPA, OA, OP, ORPM R (1976) Summary of the Resource Conservation and Recovery Act.

8. US EPA, OA, OP, ORPM R (1972) Summary of the Clean Water Act.

9. CEPA (1999) Canadian Environmental Protection Act, 1999 (CEPA 1999). http://www.ec.gc.ca/lcpe-cepa/default.asp?lang=En&n=26A03BFA-1. Accessed 24 Nov 2015

10. Manty BA, Weis ML, Cavanaugh JH Advanced Techniques for Replacing Hexavalent Chrome Plating. 1–6.

11. Ambat R, Zhou W (2004) Electroless nickel-plating on AZ91D magnesium alloy: effect of substrate microstructure and plating parameters. Surf Coatings Technol 179:124–134. doi: 10.1016/S0257-8972(03)00866-1

12. VOORWALD H, PADILHA R, COSTA M, et al (2007) Effect of electroless nickel interlayer on the fatigue strength of chromium electroplated AISI 4340 steel. Int J Fatigue 29:695–704. doi: 10.1016/j.ijfatigue.2006.07.004

13. Navinšek B, Panjan P, Milošev I (1999) PVD coatings as an environmentally clean alternative to electroplating and electroless processes. Surf Coatings Technol 116–119:476–487. doi: 10.1016/S0257-8972(99)00145-0

14. Agüero A, Camón F, García de Blas J, et al (2011) HVOF-Deposited WCCoCr as Replacement for Hard Cr in Landing Gear Actuators. J Therm Spray Technol 20:1292–1309. doi: 10.1007/s11666-011-9686-1

15. Bergmann CP, Vicenzi J (2011) Protection against Erosive Wear Using Thermal Sprayed Cermet. Prot against Erosive Wear Using Therm Sprayed Cermet 89. doi: 10.1007/978-3-642-21987-0

16. Dykhuizen RCC, Smith MFF (1998) Gas Dynamic Principles of Cold Spray. J Therm Spray Technol 7:205–212. doi: 10.1361/105996398770350945

17. Tokarev a. O (1996) Structure of aluminum powder coatings prepared by cold gasdynamic spraying. Met Sci Heat Treat 38:136–139. doi: 10.1007/BF01401446

18. Alkhimov AP, Papyrin AN, Kosarev VF, et al (1995) Method and device for coating.

19. Assadi H, Gärtner F, Stoltenhoff T, Kreye H (2003) Bonding mechanism in cold gas spraying. Acta Mater 51:4379–4394. doi: 10.1016/S1359-6454(03)00274-X

20. Schmidt T, Assadi H, Gärtner F, et al (2009) From particle acceleration to impact and bonding in cold spraying. J Therm Spray Technol 18:794–808. doi: 10.1007/s11666-009-9357-7

21. Grujicic M, Saylor JR, Beasley DE, et al (2003) Computational analysis of the interfacial bonding between feed-powder particles and the substrate in the cold-gas dynamic-spray process. Appl Surf Sci 219:211–227. doi: 10.1016/S0169-4332(03)00643-3

22. Hussain T, McCartney DG, Shipway PH, Zhang D (2009) Bonding mechanisms in cold spraying: The contributions of metallurgical and mechanical components. J Therm Spray Technol 18:364–379. doi: 10.1007/s11666-009-9298-1

23. Dykhuizen RCC, Smith MFF, Gilmore DLL, et al (1999) Impact of High Velocity Cold Spray Particles. J Therm Spray Technol 8:559–564. doi: 10.1361/105996399770350250

24. Samson T, MacDonald D, Fernández R, Jodoin B (2015) Effect of Pulsed Waterjet Surface Preparation on the Adhesion Strength of Cold Gas Dynamic Sprayed Aluminum Coatings. J Therm Spray Technol 24:984–993. doi: 10.1007/s11666-015-0261-z

25. Koivuluoto H, Vuoristo P (2010) Structural Analysis of Cold-Sprayed Nickel-Based Metallic and Metallic-Ceramic Coatings. J Therm Spray Technol 19:975–989. doi: 10.1007/s11666-010-9481-4

26. Grujicic M, Zhao CL, Tong C, et al (2004) Analysis of the impact velocity of powder particles in the cold-gas dynamic-spray process. Mater Sci Eng A 368:222–230. doi: 10.1016/j.msea.2003.10.312

27. Luzin V, Spencer K, Zhang MX (2011) Residual stress and thermo-mechanical properties of cold spray metal coatings. Acta Mater 59:1259–1270. doi: 10.1016/j.actamat.2010.10.058

28. Spencer K, Luzin V, Matthews N, Zhang MX (2012) Residual stresses in cold spray Al coatings: The effect of alloying and of process parameters. Surf Coatings Technol 206:4249–4255. doi: 10.1016/j.surfcoat.2012.04.034

29. Saleh M, Luzin V, Spencer K (2014) Evaluation of the Residual Stress in the Cold Spray Technique Using Smooth Particle Hydrodynamics Modelling and Neutron Diffraction. Mater Sci Forum 777:205–212. doi: 10.4028/www.scientific.net/MSF.777.205

30. Ghelichi R, Bagherifard S, Macdonald D, et al (2014) Experimental and numerical study of residual stress evolution in cold spray coating. Appl Surf Sci 288:26–33. doi:

10.1016/j.apsusc.2013.09.074

31. Y. Ding, T. Hussain, D. G. McCartney High-temperature oxidation of HVOF thermally sprayed NiCr–Cr 3 C 2 coatings: microstructure and kinetic. J Mater Sci. doi: 10.1007/s10853-015-9238-z

32. Kunioshi CT, Correa O V., Ramanathan L V. (2006) High temperature oxidation and erosion–oxidation behaviour of HVOF sprayed Ni–20Cr, WC–20Cr–7Ni and Cr $_3$ C $_2$ –Ni–20Cr coatings. Surf Eng 22:121–127. doi: 10.1179/174329406X98403

33. Bu Qian Wang, Luer K (1994) The erosion-oxidation behavior of HVOF Cr3C2-NiCr cermet coating. Wear 174:177–185. doi: 10.1016/0043-1648(94)90100-7

34. Wang BQ, Shui ZR (2002) The hot erosion behavior of HVOF chromium carbide-metal cermet coatings sprayed with different powders. Wear 253:550–557. doi: 10.1016/S0043-1648(02)00049-2

35. Alidokht SA, Manimunda P, Vo P, et al (2016) Cold spray deposition of a Ni-WC composite coating and its dry sliding wear behavior. Surf Coatings Technol 308:424–434. doi: 10.1016/j.surfcoat.2016.09.089

36. Yuan J, Zhan Q, Huang J, et al (2013) Decarburization mechanisms of WC–Co during thermal spraying: Insights from controlled carbon loss and microstructure characterization. Mater Chem Phys 142:165–171. doi: 10.1016/j.matchemphys.2013.06.052

37. Yuan J, Ma C, Yang S, et al (2015) Improving the wear resistance of HVOF sprayed WC-Co coatings by adding submicron-sized WC particles at the splats' interfaces. Surf Coatings Technol. doi: 10.1016/j.surfcoat.2015.11.017

38. Donner K-R, Gaertner F, Klassen T (2010) Metallization of Thin Al2O3 Layers in Power Electronics Using Cold Gas Spraying. J Therm Spray Technol 20:299–306. doi: 10.1007/s11666-010-9573-1

39. Klinkov S V., Kosarev VF (2012) Cold spraying activation using an abrasive admixture. J Therm Spray Technol 21:1046–1053. doi: 10.1007/s11666-012-9778-6

# Chapter 6

# Conclusions and Future work

The general objective of this thesis was to deepen the understanding of the manufacturing of cermets coatings produced by cold spray. This was done by exploring the fundamentals of the deposition process, investigating the coatings mechanical properties and exploring possible applications of cold spray cermet coatings. This was accomplished by establishing clear research objectives, careful experimentation, and numerical modeling.

This work gives some insights on the production of cermet coatings and helps to understand behaviors previously reported in other investigations that did not carry any rigorous and in depth analysis but rather stated some possible mechanisms. The deposition behavior and effect of feedstock powder ceramic content on the deposition efficiency of aluminum deposited by cold spray were studied. Three mechanisms briefly suggested in the literature were investigated. The interaction of ceramic and metallic particles upon impact was evaluated using a finite element analysis approach, showing that an impinging ceramic particle on an aluminum particle in the vicinity of the substrate leads to an increment of pressure, plasticity, and temperature at the substrate-particle interface, which result in more favorable conditions for deposition of the metallic particle. However, a probabilistic analysis showed that the event is unlikely and thus can be considered negligible. The two other possible mechanisms were studied, namely the effect of asperities and oxide removal/cleaning. This was done by designing an experiment enabling the measurements of the deposition efficiency of a single layer of pure aluminum over coatings previously deposited with different aluminum/alumina feedstock powder compositions. This test allowed to gauge the effect of asperities while removing the influence of oxide cleaning. Results indicated that both asperity

creation and oxide layer removal mechanisms have a major influence in the increment of DE during deposition.

These results were also supported by a study done spraying mixtures with different ceramic morphologies. It investigated the effect of the ceramic morphology on blended aluminum-alumina feedstock powder deposition efficiency. Aluminum particles mixed with spherical alumina or angular alumina particles have been used. The deposition efficiency obtained when spraying with spherical alumina decreased as the alumina content increases. This contrasted with coatings sprayed with angular alumina particles where an increment in DE was observed in samples with low alumina content, followed by a consistent decrease as the alumina content increased. The cause of this difference was identified by the low partial DE of spherical alumina particles. In addition, using the single layer deposition efficiency test, it was determined that the effect of asperities is suppressed in coatings sprayed with spherical alumina.

The retention of ceramic into the coatings was also studied and it was determined to be considerably lower in coatings produced with spherical alumina than the ones sprayed with angular alumina. The retention obtained was assessed to be lower than 10wt.% of the injected amount in the case of spherical alumina and 50wt.% for angular alumina. Mechanical properties of the coatings produced with aluminum-alumina blends were also investigated using two morphologies of ceramic particles and numerous feedstock powder compositions. Wear resistance of coatings sprayed with spherical alumina showed no improvement when compared with cold sprayed pure aluminum coatings. This effect is strictly related to ceramic content as coatings sprayed with angular alumina with similar ceramic content also showed no improvement in wear resistance. For coatings containing 22wt.% of alumina or less, no significant benefit was seen over pure aluminum coatings, while at higher values, a consistent increase in wear resistance is seen until 39wt.% of alumina. Coatings with higher alumina content did not show an increment in wear resistance. Coatings hardness is also affected by ceramic content, with a consistent increase in hardness with the ceramic content. For similar ceramic compositions, coatings sprayed with spherical alumina produced harder coatings that coatings sprayed with angular alumina. This behavior was attributed to more work hardening induced by the low DE of spherical alumina. Adhesion was shown to increase drastically as the ceramic content increased in the feedstock powder. In addition, coatings sprayed with spherical alumina showed a faster rate of increase of adhesion strength than the ones sprayed with angular ceramic. The former reached the limit of the test (glue failure) in coatings sprayed with powders

containing 40wt.% of spherical alumina, while coatings sprayed with angular alumina also achieved this limit but with powders containing 80wt.%. Cross-sections and single particle impact tests revealed that the adhesion increments are caused by different mechanisms. While it was shown that the presence of asperities and oxide-free surfaces are the mechanism that leads to a higher adhesion in coatings sprayed with angular alumina, in the case of spherical alumina the increase appeared to be driven by a peening effect of the ceramic into the first layer of aluminum particles. This high deformation leads to swirling at the interface strengthening the bonding between the coating and the substrate. In addition to the consolidation of cermet coatings by spraying blended powder, the morphology of cermet powders was studied to understand their deposition behavior and to assess the feasibility of consolidating cermets coatings. In this study, a Nickel-Chromium alloy was used as the metal phase and Chromium-Carbide as the ceramic component. Six commercially available powders were tested with different morphologies and metal/ceramic ratios. The morphology of the powders shows to have a major effect on the deposition behavior. Atomized cermet powders did not deposit and lead to erosion of the substrate independently of the metal/ceramic ratio. Detailed FEA study showed that its dense morphology leads to low plasticity by redistributing the impact stresses inside the particles. It was theorized that this lack of ductility is responsible for the low deposition efficiency of these particles. Agglomerated and sintered powders with a porous microstructure led to successful coatings but severally cracked. FEA showed extremely high stress in the ceramic particles, which might have resulted in the fracture of the particles upon impact. In agglomerated and sintered powder with a denser microstructure, the metal/ceramic ratio showed to have a major influence on the deposition behavior. The powder with 25wt.% metal composition leads to substrate erosion while the powder containing 35 wt.% of metallic phase produced successfullydense coatings. Metal ceramic blended also produced successfully dense coatings. Severe fracturing of the ceramic particles upon impact was observed as well as an important decrease of ceramic content between the feedstock powder and the coatings.

The dense agglomerated and sintered powder that produced coatings was proposed as a possible replacement and/or restoration coating for Cr-plating. The coatings exhibited a hardness of 746Hv and a porosity level below 1%, which is ideal for the replacement of Cr-platings. Adhesion strengths of 27MPa were obtained. Besides the replacement of Cr-plating, the restoration of its alternatives was investigated, namely electroless Ni-plating and HVOF WC-Co-Cr coatings. The restoration made with cold spray passed the strip rupture peeling tests as well as the fluid immersion tests using

two selected fluids. Neutral salt spray fog test revealed that the corrosion resistance of the coatings is not as good as Ni-plating and that some corrosion paths, not detectable by SEM, could exist inside the coatings, revealing that further investigations need to be done to avoid defects that can create these paths. Overall this study offers an alternative for replacement and restoration of Cr-plating and alternatives providing a good balance between hardness, adhesion and corrosion resistance that compete with the current alternatives of Cr-plating.

## 6.1 Future Work

More work is recommended to increase the understanding of bonding mechanism in cold sprayed particles and the effect that ceramic particles might have in the process. It is also recommended to focus the effort in applied investigation that uncovers to the potential that cold spray deposition process has in the production of cermet powders, exploiting its comparative advantages, such as the production of compressive stresses, high building rates and solid-state deposition. Some specifics of future investigations proposed to complement this study is listed below.

- To generalize the results uncovered in this research, several materials should be used to investigate the effect of ceramic in the deposition behavior of blended cermets. Several particle sizes should be study as well as different hardness of metallic and ceramic particles. These studies should also be conducted at several cold spray parameter to reach a full understanding of the influence of various parameters on the mechanism of deposition and bonding in blended cermet

- A study focusing on proving in a direct way the oxide cleaning effect has in the deposition efficiency may lead to a better understanding of the bonding mechanism, not just of cermets but of all cold spray powders. The results of such study might be applied to different aspects of material science and engineering, such as cold welding, galling, explosion welding and other phenomena where high-strain rate plastic deformation occur in contacts between metals.

- Coatings sprayed with spherical alumina had high hardness and excellent adhesion combined with low ceramic content. It is possible to extrapolate this results and hypothesizes a blending feedstock powder that produce a pure metallic coating with all the benefit brought by the presence of ceramic particles but without contamination. For such a study different particle

size and material could be used in the blending to achieve this result.

- FEA simulation was used to draw some conclusion in the deposition behavior of cermet powders by comparing them with interrupted spray test. This FEA model with metal-ceramic it is novel and has not been found in the literature. This this can be improved by adding damage evolution to the model, as well as specific bonding condition with the substrate. The adherence between metal and ceramic can also be investigated in order to include it in the model.

- The study with cermet powders revealed that for particle with the same morphology, the superficial metallic content might have a major influence on the deposition behavior of powders. This result suggests that successful coating might be achieved if ceramic particles covered with metal and sprayed. This could potentially create hard cermet coatings with higher DE that the one obtained in this investigation.

- Finally, some work is needed to improve the corrosion resistant of CrC-NiCr coating for the replacement and restoration of Cr-plating and its alternatives. The coating obtained was dense, hard and had a good interface with the substrate and the damaged coatings. But some paths for corrosion products were present inside the coating that could not be detected by SEM. This means the paths are very narrow. Therefore there are prospects of improving the coating by heat treating and sintering these paths and consequently, sealing the coating. Since the path is narrow the time needed to sinter and sealed the coating is expected to be short.

# Bibliography


[1] A.J. Zuckerwar. *Handbook of the Speed of Sound in Real Gases*. Elsevier Science, 2002.

[2] Tobias Schmidt, Hamid Assadi, Frank Gärtner, Horst Richter, Thorsten Stoltenhoff, Heinrich Kreye, and Thomas Klassen. From particle acceleration to impact and bonding in cold spraying. *J. Therm. Spray Technol.*, 18(5-6):794–808, 2009.

[3] Frank Gärtner, Thorsten Stoltenhoff, Tobias Schmidt, and Heinrich Kreye. The Cold Spray Process and Its Potential for Industrial Applications. *J. Therm. Spray Technol.*, 15(2):223–232, June 2006.

[4] John L. Ellis and Claus G. Goetzel. Cermets. In *ASM Handb. Vol. 2 Prop. Sel. Nonferrous Alloy. Spec. Mater. - ASM Int.*, chapter Cermets, page 1328. ASM International, 1990.

[5] A.P. Alkhimov, A.N. Papyrin, V.F. Kosarev, N.I. Nesterovich, and M.M. Shushpanov. Gas-dynamic spraying method for applying a coating, April 12 1994. US Patent 5,302,414.

[6] Julio Villafuerte, editor. *Modern Cold Spray*. Springer International Publishing, Cham, 2015.

[7] J. Pattison, S. Celotto, A. Khan, and W. O'Neill. Standoff distance and bow shock phenomena in the Cold Spray process. *Surf. Coatings Technol.*, 202(8):1443–1454, January 2008.

[8] T. Schmidt, F. Gaertner, and H. Kreye. New Developments in Cold Spray Based on Higher Gas and Particle Temperatures. *J. Therm. Spray Technol.*, 15(4):488–494, 2006.

[9] KeeHyun Kim, Makoto Watanabe, and Seiji Kuroda. Bonding mechanisms of thermally softened metallic powder particles and substrates impacted at high velocity. *Surf. Coatings Technol.*, 204(14):2175–2180, 2010.

[10] B. Broll. *Microcosmos: Discovering the World Through Microscopic Images from 20 X to Over 22 Million X Magnification*. Firefly Books, Limited, 2010.

[11] Leonardo Ajdelsztajn, Bertrand Jodoin, George E. Kim, Julie M. Schoenung, Bertrand Jodoin, George E. Kim, and Julie M. Schoenung. Cold Spray Deposition of Nanocrystalline Aluminum Alloys. *Metall. Mater. Trans. A*, 36A(3):657–666, March 2005.

[12] A. List, F. Gärtner, T. Schmidt, and T. Klassen. Impact Conditions for Cold Spraying of Hard Metallic Glasses. *J. Therm. Spray Technol.*, 21(3-4):531–540, February 2012.

[13] Peter C. King, Christian Busch, Teresa Kittel-Sherri, Mahnaz Jahedi, and Stefan Gulizia. Interface melding in cold spray titanium particle impact. *Surf. Coatings Technol.*, 239:191–199, 2014.

[14] Patrick Trahan. *Corrosion Protection of Friction Stir Welded Al 7075 Panel for use in Aerospace Applications using Cold Gas Dynamic Spray By*. PhD thesis, University of Ottawa, 2013.

[15] Heui-Joo Choi, Minsoo Lee, and Jong Youl Lee. Application of a cold spray technique to the fabrication of a copper canister for the geological disposal of CANDU spent fuels. *Nuclear Engineering and Design*, 240(10):2714–2720, oct 2010.

[16] V. Champagne and D. Helfritch. Critical Assessment 11: Structural repairs by cold spray. *Mater. Sci. Technol.*, 31(6):627–634, 2015.

[17] Aleksandra Nastic. *Repair of Aluminum Alloy Aerospace Components and Cold Gas Dynamic Spray Flow Distribution Investigation*. PhD thesis, University of Ottawa, 2015.

[18] Guillaume Archambault. *Lay-up Moulding of a Carbon Fiber Reinforced Polymer Composite on a Cold Sprayed Metallic Layer*. PhD thesis, University of Ottawa, 2015.

[19] T. Stoltenhoff, C. Borchers, F. Gärtner, H. Kreye, T. Stoltenhoff, J. Voyer, H. Kreye, S. Riekehr, and M. Koçak. Mechanical properties of cold-sprayed and thermally sprayed copper coatings. *Surf. Coatings Technol.*, 200(24):6770–6782, apr 2006.

[20] a. Shkodkin, A. Kashirin, O. Klyuev, and T. Buzdygar. Metal Particle Deposition Stimulation by Surface Abrasive Treatment in Gas Dynamic Spraying. *J. Therm. Spray Technol.*, 15(3):382–386, 2006.

[21] Eric Irissou, Jean-Gabriel Legoux, Bernard Arsenault, and Christian Moreau. Investigation of Al-Al2O3 Cold Spray Coating Formation and Properties. *J. Therm. Spray Technol.*, 16(5-6):661–668, oct 2007.

[22] Qiang Wang, Kevin Spencer, Nick Birbilis, and Ming-Xing Zhang. The influence of ceramic particles on bond strength of cold spray composite coatings on AZ91 alloy substrate. *Surf. Coatings Technol.*, 205(1):50–56, sep 2010.

[23] J.M. Shockley, S. Descartes, P. Vo, E. Irissou, and R.R. Chromik. The influence of Al2O3 particle morphology on the coating formation and dry sliding wear behavior of cold sprayed Al-Al2O3 composites. *Surf. Coatings Technol.*, 270:324–333, may 2015.

[24] Sulzer Metco. Thermal Spray Materials Guide, 2015.

[25] James R. Tinklepaugh. *Cermets*. Reinhold Publishing Corporation, 1960.

[26] R.C. C Dykhuizen and M.F. F Smith. Gas Dynamic Principles of Cold Spray. *J. Therm. Spray Technol.*, 7(2):205–212, 1998.

[27] Y. Xu and I.M. Hutchings. Cold spray deposition of thermoplastic powder. *Surf. Coatings Technol.*, 201(6):3044–3050, dec 2006.

[28] REACH. Regulation (EC) No 1907/2006 - REACH - Safety and health at work - EU-OSHA, 2006.

[29] J.A. Picas, A. Forn, and G. Matthäus. HVOF coatings as an alternative to hard chrome for pistons and valves. *Wear*, 261(5-6):477–484, sep 2006.

[30] V. Luzin, K. Spencer, and M. X. Zhang. Residual stress and thermo-mechanical properties of cold spray metal coatings. *Acta Mater.*, 59(3):1259–1270, 2011.

[31] a. O. Tokarev. Structure of aluminum powder coatings prepared by cold gasdynamic spraying. *Met. Sci. Heat Treat.*, 38(3):136–139, mar 1996.

[32] A.P. Alkhimov, V.F. Kosarev, and A.N. Papyrin. A method of cold gas dynamic deposition. *Sov. Phys. Dokl.*, 35(12):1047–1049, 1990. translation from the American Institute of Physics, 1991.

[33] A.P. Alkhimov, A.N. Papyrin, V.F. Kosarev, N.I. Nesterovich, and M.M. Shushpanov. Method and device for coating, 1995.

[34] S.H. Thurston. Method of impacting one metal upon another., August 12 1902. US Patent 706,701.

[35] Rocheville Charles F. Device for treating the surface of a workpiece. US Patent 3,100,724.

[36] Anatolii N. Papyrin. *Cold Spray Technology*. Elsevier, 2007.

[37] Tobias Schmidt, Frank Gärtner, Hamid Assadi, and Heinrich Kreye. Development of a generalized parameter window for cold spray deposition. *Acta Mater.*, 54(3):729–742, February 2006.

[38] A.H. Shapiro. *The dynamics and thermodynamics of compressible fluid flow*. Number v. 1 in The Dynamics and Thermodynamics of Compressible Fluid Flow. Ronald Press Co., 1953.

[39] B. Jodoin. Cold Spray Nozzle Mach Number Limitation. *J. Therm. Spray Technol.*, 11(4):496–507, 2002.

[40] A.P. Alkhimov, V.F. Kosarev, and S.V. Klinkov. The Features of Cold Spray Nozzle Design. *J. Therm. Spray Technol.*, 10(2):375–381, June 2001.

[41] C B Henderson. Drag coefficients of spheres in continuum and rarefied flows. *Aiaa*, 14(6):2, 2003.

[42] Wen-Ya Li, Chang-Jiu Li, Hong-Tao Wang, Cheng-Xin Li, and Hee-Seon Bang. Measurement and Numerical Simulation of Particle Velocity in Cold Spraying. *J. Therm. Spray Technol.*, 15(4):559–562, 2006.

[43] Wen-Ya Li and Chang-Jiu Li. Optimal Design of a Novel Cold Spray Gun Nozzle at a Limited Space. *J. Therm. Spray Technol.*, 14(3):391–396, 2005.

[44] M. Karimi, a. Fartaj, G. Rankin, D. Vanderzwet, W. Birtch, and J. Villafuerte. Numerical Simulation of the Cold Gas Dynamic Spray Process. *J. Therm. Spray Technol.*, 15(4):518–523, 2006.

[45] M. Grujicic, C. L. Zhao, C. Tong, W. S. DeRosset, and D. Helfritch. Analysis of the impact velocity of powder particles in the cold-gas dynamic-spray process. *Mater. Sci. Eng. A*, 368(1-2):222–230, 2004.

[46] Peter C. King and Mahnaz Jahedi. Relationship between particle size and deformation in the cold spray process. *Appl. Surf. Sci.*, 256(6):1735–1738, January 2010.

[47] Hirotaka Fukanuma, Naoyuki Ohno, Bo Sun, and Renzhong Huang. In-flight particle velocity measurements with DPV-2000 in cold spray. *Surf. Coatings Technol.*, 201(5):1935–1941, 2006.

[48] Anatolii N. Papyrin. Preface. In *Cold Spray Technology*, pages x–xii. Elsevier, 2007.

[49] H. Katanoda, M. Fukuhara, and N. Iino. Numerical study of combination parameters for particle impact velocity and temperature in cold spray. *J. Therm. Spray Technol.*, 16(5-6):627–633, 2007.

[50] B. Jodoin, D. MacDonald, and S. Robert. The Lure of Nozzle Design and Deposition Efficiency. In *North Am. Cold Spray Conf.*, 2014.

[51] Hamid Assadi, Frank Gärtner, Thorsten Stoltenhoff, and Heinrich Kreye. Bonding mechanism in cold gas spraying. *Acta Mater.*, 51(15):4379–4394, September 2003.

[52] M. Grujicic, J.R. Saylor, D.E. Beasley, W.S. DeRosset, and D. Helfritch. Computational analysis of the interfacial bonding between feed-powder particles and the substrate in the cold-gas dynamic-spray process. *Appl. Surf. Sci.*, 219(3-4):211–227, December 2003.

[53] Peter C. King, Gyuyeol Bae, Saden H. Zahiri, Mahnaz Jahedi, and Changhee Lee. An Experimental and Finite Element Study of Cold Spray Copper Impact onto Two Aluminum Substrates. *J. Therm. Spray Technol.*, 19(3):620–634, 2010.

[54] P.C. King, S.H. Zahiri, and M. Jahedi. Focused ion beam micro-dissection of cold-sprayed particles. *Acta Mater.*, 56(19):5617–5626, November 2008.

[55] M. Grujicic, C.L L. Zhao, W.S S. DeRosset, and D. Helfritch. Adiabatic shear instability based mechanism for particles/substrate bonding in the cold-gas dynamic-spray process. *Mater. Des.*, 25(8):681–688, December 2004.

[56] T. Hussain, D. G. McCartney, Philip H. Shipway, and D. Zhang. Bonding mechanisms in cold spraying: The contributions of metallurgical and mechanical components. *J. Therm. Spray Technol.*, 18(3):364–379, 2009.

[57] R.C. C Dykhuizen, M.F. F Smith, D.L. L Gilmore, R.a. A Neiser, X. Jiang, and S. Sampath. Impact of High Velocity Cold Spray Particles. *J. Therm. Spray Technol.*, 8(4):559–564, 1999.

[58] K. T. Ramesh. High Strain Rate and Impact Experiments. In W.N. Sharpe, Jr., editor, *Handbook of Experimental. Solid Mechanics*, chapter 33. D, pages 1–31. Springer, 2008.

[59] Saeed Rahmati and Abbas Ghaei. The use of particle/substrate material models in simulation of cold-gas dynamic-spray process. *J. Therm. Spray Technol.*, 23(3):530–540, 2014.

[60] Gordon R Johnson and William H Cook. A constitutive model and data for metals subjected to large strains, high strain rates and high temperatures. In *Proceedings of the 7th International Symposium on Ballistics*, volume 21, pages 541–547. The Hague, The Netherlands, 1983.

[61] Dean L. Preston, Davis L. Tonks, and Duane C. Wallace. Model of plastic deformation for extreme loading conditions. *J. Appl. Phys.*, 93(1):211–220, 2003.

[62] T. Samson, D. MacDonald, R. Fernández, and B. Jodoin. Effect of Pulsed Waterjet Surface Preparation on the Adhesion Strength of Cold Gas Dynamic Sprayed Aluminum Coatings. *J. Therm. Spray Technol.*, 24(6):984–993, July 2015.

[63] Richard Feynman, Robert Leighton, and Matthew Sands. *The Feynman Lectures on Physics*, volume 1. Addison-Wesley, Boston, second edition, 1963.

[64] A. Kiejna and K.F. Wojciechowski. *Metal Surface Electron Physics*. Elsevier, 1996.

[65] Yang Lu, Jian Yu Huang, Chao Wang, Shouheng Sun, and Jun Lou. Cold welding of ultrathin gold nanowires. *Nat. Nanotechnol.*, 5(3):218–224, 2010.

[66] a Merstallinger and M Sales. Assessment of Cold Welding between Separable Contact Surfaces due to Impact and Fretting under Vacuum. *ESA Sci. . . .*, 2009.

[67] L. Ajdelsztajn, a. Zúñiga, B. Jodoin, and E.J. Lavernia. Cold gas dynamic spraying of a high temperature Al alloy. *Surf. Coatings Technol.*, 201(6):2109–2116, 2006.

[68] D.L. L Gilmore, R.C. C Dykhuizen, R.a. A Neiser, T.J. J Roemer, and M.F. F Smith. Particle Velocity and Deposition Efficiency in the Cold Spray Process. *J. Therm. Spray Technol.*, 8(4):576–582, 1999.

[69] T.H. H. Van Steenkiste, J.R. R. Smith, and R.E. E. Teets. Aluminum coatings via kinetic spray with relatively large powder particles. *Surf. Coatings Technol.*, 154(2-3):237–252, May 2002.

[70] Chang-Jiu Li, Wen-Ya Li, and Hanlin Liao. Examination of the Critical Velocity for Deposition of Particles in Cold Spraying. *J. Therm. Spray Technol.*, 15(2):212–222, June 2006.

[71] T. Stoltenhoff, H. Kreye, and H.J. Richter. An Analysis of the Cold Spray Process and Its Coatings. *J. Therm. Spray Technol.*, 11(4):542–550, 2002.

[72] T. Klassen, F. Gärtner, T. Schmidt, J.-O. Kliemann, K. Onizawa, K.-R. Donner, H. Gutzmann, K. Binder, and H. Kreye. Basic principles and application potentials of cold gas spraying. Bindemechanismen und potenzielle Anwendungen des Kaltgasspritzens. *Materwiss. Werkstttech.*, 41(7):575–584, 2010.

[73] C.-J. Li, H.-T. Wang, Q. Zhang, G.-J. Yang, W.-Y. Li, and H. L. Liao. Influence of Spray Materials and Their Surface Oxidation on the Critical Velocity in Cold Spraying. *J. Therm. Spray Technol.*, 19(1-2):95–101, November 2009.

[74] Wen-Ya Li, Chang-Jiu Li, and Hanlin Liao. Significant influence of particle surface oxidation on deposition efficiency, interface microstructure and adhesive strength of cold-sprayed copper coatings. *Appl. Surf. Sci.*, 256(16):4953–4958, June 2010.

[75] A. Concustell, J. Henao, S. Dosta, N. Cinca, I.G. Cano, and J.M. Guilemany. On the formation of metallic glass coatings by means of Cold Gas Spray technology. *J. Alloys Compd.*, 651:764–772, December 2015.

[76] E. Calla, D.G. McCartney, and P.H. Shipway. Effect of Deposition Conditions on the Properties and Annealing Behavior of Cold-Sprayed Copper. *J. Therm. Spray Technol.*, 15(2):255–262, 2006.

[77] K. Balani, a. Agarwal, S. Seal, and J. Karthikeyan. Transmission electron microscopy of cold sprayed 1100 aluminum coating. *Scr. Mater.*, 53(7):845–850, 2005.

[78] Christine Borchers, Frank Gärtner, Thorsten Stoltenhoff, and Heinrich Kreye. Formation of persistent dislocation loops by ultra-high strain-rate deformation during cold spraying. *Acta Mater.*, 53(10):2991–3000, June 2005.

[79] C. Borchers, F. GaÌˆrtner, T. Stoltenhoff, and H. Kreye. Microstructural bonding features of cold sprayed face centered cubic metals. *J. Appl. Phys.*, 96(8):4288, 2004.

[80] Yu Zou, Wen Qin, Eric Irissou, Jean Gabriel Legoux, Stephen Yue, and Jerzy a. Szpunar. Dynamic recrystallization in the particle/particle interfacial region of cold-sprayed nickel coating: Electron backscatter diffraction characterization. *Scr. Mater.*, 61(9):899–902, 2009.

[81] M. Oksa and J. Metsäjoki. Optimizing NiCr and FeCr HVOF Coating Structures for High Temperature Corrosion Protection Applications. *J. Therm. Spray Technol.*, 24(3):436–453, 2014.

[82] a.C. Hall, D.J. Cook, R.a. Neiser, T.J. Roemer, and D.a. Hirschfeld. The Effect of a Simple Annealing Heat Treatment on the Mechanical Properties of Cold-Sprayed Aluminum. *J. Therm. Spray Technol.*, 15(2):233–238, 2006.

[83] P. Richer, A. Zúñiga, M. Yandouzi, and B. Jodoin. CoNiCrAlY microstructural changes induced during Cold Gas Dynamic Spraying. *Surf. Coatings Technol.*, 203(3-4):364–371, November 2008.

[84] K. Balani, T. Laha, a. Agarwal, J. Karthikeyan, and N. Munroe. Effect of carrier gases on microstructural and electrochemical behavior of cold-sprayed 1100 aluminum coating. *Surf. Coatings Technol.*, 195(2-3):272–279, 2005.

[85] Daniel A Macdonald. *Restoration of Aluminum Aerospace Parts and Coatings using Cold Gas Dynamic Spraying By*. PhD thesis, University of Ottawa, 2014.

[86] E. Irissou, D. Poirier P. Vo, P. Keech, and J. G. Legoux. Cold sprayed corrosion protection coating for nuclear waste repository canister. In *Cold sprayed Corros. Prot. Coat. Nucl. waste Repos. canister.*, Worcester, 2012. North American Cold Spray Conference, Worcester Polytechnic Institute.

[87] T Sonoda, T Kuwashima, and T Saito. Super Hard WC Cermet Coating by Low Pressure Cold Spray Based on Optimization of Powder Properties. In *Therm. Spray 2013*, pages 241 – 245 (5). ASM International, 2013.

[88] M. Yandouzi, E. Sansoucy, L. Ajdelsztajn, and B. Jodoin. WC-based cermet coatings produced by cold gas dynamic and pulsed gas dynamic spraying processes. *Surf. Coatings Technol.*, 202(2):382–390, nov 2007.

[89] H. Myalska, G. Moskal, and K. SzymaÅ„ski. Microstructure and properties of WC–Co coatings, modified by sub-microcrystalline carbides, obtained by different methods of high velocity spray processes. *Surf. Coatings Technol.*, 260:303–309, 2014.

[90] Hyung-jun Kim, Chang-hee Lee, and Soon-young Hwang. Superhard nano WC–12% Co coating by cold spray deposition. *Mater. Sci. Eng. A*, 391:243–248, 2005.

[91] N. M. Melendez, V. V. Narulkar, G. a. Fisher, and a. G. McDonald. Effect of reinforcing particles on the wear rate of low-pressure cold-sprayed WC-based MMC coatings. *Wear*, 306(1-2):185–195, 2013.

[92] J.C. Lee, H.J. Kang, W.S. Chu, and S.H. Ahn. Repair of Damaged Mold Surface by Cold-Spray Method. *CIRP Annals - Manufacturing Technology*, 56(1):577–580, 2007.

[93] M. Yandouzi, S. Gaydos, D. Guo, R. Ghelichi, and B. Jodoin. Aircraft Skin Restoration and Evaluation. *Journal of Thermal Spray Technology*, 23(8):1281–1290, aug 2014.

[94] M. Faccoli, G. Cornacchia, D. Maestrini, G. P. Marconi, and R. Roberti. Cold Spray Repair of Martensitic Stainless Steel Components. *Journal of Thermal Spray Technology*, 23(8):1270–1280, aug 2014.

[95] Timothy J Eden and D Ph. Cold Spray Repair of the F-18 AMAD Strategic DoD Relationship. In CTMA, editor, *CTMA Symposium*. CTMA, 2012.

[96] N. Matthews, R. Jones, and G. C. Sih. Application of supersonic particle deposition to enhance the structural integrity of aircraft structures. *Science China Physics, Mechanics and Astronomy*, 57(1):12–18, dec 2013.

[97] A. Sova, S. Grigoriev, A. Okunkova, and I. Smurov. Potential of cold gas dynamic spray as additive manufacturing technology. *The International Journal of Advanced Manufacturing Technology*, 69(9-12):2269–2278, aug 2013.

[98] Yannick Cormier, Philippe Dupuis, Bertrand Jodoin, and Antoine Corbeil. Net Shape Fins for Compact Heat Exchanger Produced by Cold Spray. *Journal of Thermal Spray Technology*, 22(7):1210–1221, jul 2013.

[99] Xian-Ming Meng, Jun-Bao Zhang, Wei Han, Jie Zhao, and Yong-Li Liang. Influence of annealing treatment on the microstructure and mechanical performance of cold sprayed 304 stainless steel coating. *Appl. Surf. Sci.*, 258(2):700–704, 2011.

[100] Yannick Cormier, Philippe Dupuis, Bertrand Jodoin, and Abbas Ghaei. Finite Element Analysis and Failure Mode Characterization of Pyramidal Fin Arrays Produced by Masked Cold Gas Dynamic Spray. *Journal of Thermal Spray Technology*, 24(8):1549–1565, dec 2015.

[101] Michael Saleh, Vladimir Luzin, and Kevin Spencer. Evaluation of the Residual Stress in the Cold Spray Technique Using Smooth Particle Hydrodynamics Modelling and Neutron Diffraction. *Materials Science Forum*, 777:205–212, 2014.

[102] Gyuyeol Bae, Yuming Xiong, S. Kumar, Kicheol Kang, and Changhee Lee. General aspects of interface bonding in kinetic sprayed coatings. *Acta Materialia*, 56(17):4858–4868, 2008.

[103] Wen Ya Li, Hanlin Liao, Chang Jiu Li, Hee Seon Bang, and C. Coddet. Numerical simulation of deformation behavior of Al particles impacting on Al substrate and effect of surface oxide films on interfacial bonding in cold spraying. *Applied Surface Science*, 253(11):5084–5091, 2007.

[104] Wen Ya Li, Hanlin Liao, Chang Jiu Li, Gang Li, Christian Coddet, and Xiaofang Wang. On high velocity impact of micro-sized metallic particles in cold spraying. *Applied Surface Science*, 253(5):2852–2862, 2006.

[105] Shuo Yin, Xiao Fang Wang, W. Y. Li, and Hong En Jie. Effect of substrate hardness on the deformation behavior of subsequently incident particles in cold spraying. *Applied Surface Science*, 257(17):7560–7565, 2011.

[106] a. Sova, A. Papyrin, and I. Smurov. Influence of Ceramic Powder Size on Process of Cermet Coating Formation by Cold Spray. *J. Therm. Spray Technol.*, 18(4):633–641, jul 2009.

[107] a. Sova, V. F. Kosarev, A. Papyrin, and I. Smurov. Effect of Ceramic Particle Velocity on Cold Spray Deposition of Metal-Ceramic Coatings. *J. Therm. Spray Technol.*, 20(1-2):285–291, oct 2010.

[108] R. Gr. Maev and V. Leshchynsky. Air Gas Dynamic Spraying of Powder Mixtures: Theory and Application. *J. Therm. Spray Technol.*, 15(2):198–205, 2006.

[109] Ha Yong Lee, Se Hun Jung, Soo Yong Lee, Young Ho You, and Kyung Hyun Ko. Correlation between Al2O3 particles and interface of Al-Al2O3 coatings by cold spray. *Appl. Surf. Sci.*, 252(5):1891–1898, dec 2005.

[110] K. Spencer, D.M. Fabijanic, and M.X. Zhang. The use of Al-Al2O3 cold spray coatings to improve the surface properties of magnesium alloys. *Surf. Coatings Technol.*, 204(3):336–344, oct 2009.

[111] C. Feng, V. Guipont, M. Jeandin, O. Amsellem, F. Pauchet, R. Saenger, S. Bucher, and C. Iacob. B4C/Ni Composite Coatings Prepared by Cold Spray of Blended or CVD-Coated Powders. *J. Therm. Spray Technol.*, 21(3-4):561–570, mar 2012.

[112] Andrew Siao Ming Ang, Christopher C. Berndt, and Philip Cheang. Deposition effects of WC particle size on cold sprayed WC-Co coatings. *Surf. Coatings Technol.*, 205(10):3260–3267, feb 2011.

[113] Douglas E. Wolfe, Timothy J. Eden, John K. Potter, and Adam P. Jaroh. Investigation and Characterization of Cr3C2-Based Wear-Resistant Coatings Applied by the Cold Spray Process. *J. Therm. Spray Technol.*, 15(3):400–412, sep 2006.

[114] R.S Lima, J Karthikeyan, C.M Kay, J Lindemann, and C.C Berndt. Microstructural characteristics of cold-sprayed nanostructured WC-Co coatings. *Thin Solid Films*, 416(1-2):129–135, sep 2002.

[115] Jianhui Yuan, Chunwei Ma, Shanglei Yang, Zhishui Yu, and Hua Li. Improving the wear resistance of HVOF sprayed WC-Co coatings by adding submicron-sized WC particles at the splats' interfaces. *Surf. Coatings Technol.*, nov 2015.

[116] J. K. Dennis and T. E. Such. *Nickel and Chromium Plating*. Elsevier, 1993.

[117] Jerome O. Nriagu and Evert Nieboer. *Chromium in the Natural and Human Environments*. John Wiley & Sons, 1988.

[118] A. Ibrahim and C.C. Berndt. Fatigue and deformation of HVOF sprayed WC-Co coatings and hard chrome plating. *Mater. Sci. Eng. A*, 456(1-2):114–119, may 2007.

[119] IARC. IARC Monographs on the Evaluation of Carcinogenic Risks to Humans 100E. Technical report, IARC, 2012.

[120] RMD US EPA, OA, OP, ORPM. Summary of the Clean Water Act, 1972.

[121] RMD US EPA, OA, OP, ORPM. Summary of the Resource Conservation and Recovery Act, 1976.

[122] CEPA. Canadian Environmental Protection Act, 1999 (CEPA 1999), 1999.

[123] Brian A Manty, Melissa L Weis, and John H Cavanaugh. Advanced Techniques for Replacing Hexavalent Chrome Plating.

[124] Rajan Ambat and W Zhou. Electroless nickel-plating on AZ91D magnesium alloy: effect of substrate microstructure and plating parameters. *Surf. Coatings Technol.*, 179(2-3):124–134, feb 2004.

[125] H Voorwald, R Padilha, M Costa, W Pigatin, and M Cioffi. Effect of electroless nickel interlayer on the fatigue strength of chromium electroplated AISI 4340 steel. *Int. J. Fatigue*, 29(4):695–704, apr 2007.

[126] B. Navinšek, P. Panjan, and I. Milošev. PVD coatings as an environmentally clean alternative to electroplating and electroless processes. *Surf. Coatings Technol.*, 116-119:476–487, sep 1999.

[127] Iain Finnie. Erosion of surfaces by solid particles. *Wear*, 3(2):87–103, mar 1960.

[128] J.G.A. Bitter. A study of erosion phenomena part I. *Wear*, 6(1):5–21, jan 1963.

[129] J.H. Neilson and A. Gilchrist. Erosion by a stream of solid particles. *Wear*, 11(2):111–122, feb 1968.